New insights from electronic transport into superconducting sub-gap states

Vivien Perrin

Thèse de doctorat

NNT : 2022UPASP151

université PARIS-SACLAY

New insights from electronic transport into superconducting sub-gap states

Etude du transport électronique dans les états liés intra-gap au sein de supraconducteurs

Thèse de doctorat de l'université Paris-Saclay

École doctorale n°564 , Physique en Ile-de-France (PIF)
Spécialité de doctorat: Physique
Graduate School: Physique

Thèse préparée au **Laboratoire de Physique des Solides (Université Paris-Saclay, CNRS)**, sous la direction de **Pascal SIMON**, Professeur des universités, la co-direction de **Marcello CIVELLI**, Maître de conférences

Thèse soutenue à Paris-Saclay, le 12 Décembre 2022, par

Vivien PERRIN

Composition du jury

Membres du jury avec voix délibérative

Marco APRILI Directeur de recherche, CNRS (LPS Orsay)	Président
Alfredo LEVY YEYATI Professeur, Université autonome de Madrid	Rapporteur & Examinateur
Jérôme RECH Chargé de recherche, HDR, CNRS (CPT Marseille)	Rapporteur & Examinateur
Deung-Jang CHOI Chercheuse associée, Materials Physics Center, San Sebastian	Examinatrice

université PARIS-SACLAY

ÉCOLE DOCTORALE
Physique en Île-de-France (PIF)

Titre: Etude du transport électronique dans les états liés intra-gap au sein de supraconducteurs.
Mots clés: Supraconductivité; Etats liés; Transport quantique; Fermions de Majorana.

Résumé: Dès la fin des années soixante, il fut démontré qu'un unique spin classique placé au sein d'un supraconducteur conventionnel est capable de générer un état lié, localisé, dont l'énergie se trouve dans le gap BCS. Il s'agit d'un état lié de Yu-Shiba-Rusinov (YSR), en l'honneur de ses découvreurs. Pour une concentration finie d'impuretés magnétiques, ces états s'hybrident et forment une bande de Shiba dans le gap BCS. Récemment, il a été théoriquement proposé qu'une chaîne unidimensionnelle d'impuretés magnétiques déposées sur un substrat supraconducteur en onde s puisse réaliser un supraconducteur topologique supportant des fermions de Majorana à ses extrémités. Cette proposition a suscité un regain d'intérêt pour les états liés de YSR, dans le but de les assembler en structures plus complexes. Dans ce manuscrit, nous revisitons le transport électronique dans les états de YSR et montrons que les propriétés de transport, mesurées par microscopie/spectroscopie à effet tunnel (STM/STS), contiennent des informations précieuses sur les propriétés de ces états.

Tout d'abord, nous montrons qu'une unique impureté magnétique induit localement des corrélations de paires non conventionnelles dites odd-frequency, à l'emplacement de l'impureté. En analysant les fonctions de Green locales, nous déduirons que la partie imaginaire de cette fonction d'appariement non-conventionnelle est proportionnelle à la composante paire de la densité d'état locale, directement mesurable par spectroscopie à effet tunnel standard. En utilisant ce résultat, nous proposons une méthode pour extraire la fonction d'appariement non conventionnelle des données STS. Nous l'appliquons ensuite à des données STS mesurées sur une mono-couche de Pb/Si(111) pour prouver l'existence d'appariement odd-frequency au voisinage des états de YSR.

Deuxièmement, motivés par le développement récent de la spectroscopie à effet tunnel, nous avons utilisé la technique de Keldysh pour calculer les fluctuations du courant dans les états de YSR. Nous montrons que ce bruit contient des signatures claires des réflexions d'Andreev résonnantes et des processus incohérents à une seule particule dans les états de YSR. Nous comparons nos prédictions théoriques avec les données expérimentales mesurées par nos collègues du LPS et montrons que notre modèle théorique, simple, capture correctement les caractéristiques importantes du bruit de courant. De l'accord quantitatif entre théorie et expérience, nous extrayons le taux de relaxation intrinsèque d'un l'état de YSR, inaccessible par spectroscopie de courant standard. De plus, nos résultats indiquent clairement la présence concomitante de réflexions d'Andreev et de processus à une seule particule dans les états de YSR.

Enfin, nous étendons le modèle précédent pour analyser le bruit de grenaille au voisinage de tous types d'états liés supraconducteurs dans le gap, couvrant ainsi les états de YSR, les états liés d'Andreev mais aussi les fermions de Majorana topologiques. En combinant des méthodes analytiques et numériques, nous démontrons que la tomographie du bruit de courant au voisinage de fermions triviaux et de fermions de Majorana présentent des différences marquées permettant de distinguer ces deux types d'états liés. Sur la base d'un modèle effectif de basse énergie, nous montrons que ces différences ont un caractère universel dont l'origine n'est autre que la symétrie particule-trou intrinsèque de la fonction d'onde de Majorana.

université PARIS-SACLAY | ÉCOLE DOCTORALE Physique en Île-de-France (PIF)

Title: New insights from electronic transport into superconducting sub-gap states.
Keywords: Superconductivity; Bound-states; Quantum transport; Majorana fermions.

Abstract: In the late sixties, it was shown that a single classical spin immersed in a conventional superconductor is able to generate a localized bound-state inside the BCS of the superconducting substrate. These states were named after their discoverers Yu-Shiba-Rusinov (YSR) bound states. For a finite concentration of magnetic impurities, these states hybridize and form Shiba bands inside the BCS gap. Recently, it was theoretically proposed that a one-dimensional chain of magnetic ad-atoms deposited on an s-wave superconducting substrate can realize a topological superconductor supporting Majorana edge modes at its ends. Since this proposition, YSR bound-states have attracted renewed interest with an eye to building more complex structures. In this manuscript, we will revisit electronic transport in YSR states and show that transport properties, measured by scanning tunneling microscopy/spectroscopy (STM/STS), contain valuable insights into the properties of these states.

First, we shall show that a single magnetic impurity locally induces unconventional odd-frequency pair correlations at the impurity location. Analyzing the local Green's functions, we show that the imaginary part of the odd-frequency pairing function is proportional to the even component of the local density of state, directly measured in standard tunneling spectroscopy. Using this result, we propose a method to extract the unconventional pairing function from STS data, apply it to STS data measured on a Pb/Si(111) monolayer, and prove the occurrence of odd-frequency pairing around YSR states.

Second, motivated by the recent development of scanning tunneling spectroscopy, we used Keldysh techniques to calculate the current shot-noise in YSR states. We show that the shot-noise contains clear signatures of resonant Andreev reflections and incoherent single-particle tunneling processes in YSR states. We compare our theoretical predictions with experimental data measured by our LPS colleagues and show that our simple theoretical model correctly captures the important features of shot noise. From the quantitative agreement between theory and experiment, we extract the intrinsic relaxation rate of the YSR state, which is inaccessible by differential conductance spectroscopy. Moreover, our results clearly indicate the concomitant presence of Andreev and single-particle processes in YSR states.

Finally, we extend the former model to analyze the scanning tunneling shot-noise in the vicinity of any superconducting sub-gap states, including YSR impurity states, Andreev bound-states, and topological Majorana zero-modes. Combining analytical and numerical methods, we demonstrate that shot-noise tomography reveals key distinctive features that allow one to distinguish trivial zero-energy fermions from Majorana zero-modes. Based on a low-energy effective model, we show that these sharp differences have a universal character that is rooted in the intrinsic particle-hole symmetry of the MZM wavefunction.

New insights from electronic transport into superconducting sub-gap states

by
Vivien Perrin

A document submitted in partial fulfillment of the requirements for the degree of

Doctor of Philosophy in Physics

at

Université Paris-Saclay

To my lovely grandfather, Camille.

Camille Perrin
26 Juin 1939 – 08 Juillet 2015

Remerciements

Mes trois années de thèse furent riches en émotions et enseignements, tant du point de vue scientifique que sur le plan humain. Mon parcours doctoral ne m'a pas seulement permis de m'épanouir en tant que physicien mais a aussi été l'occasion de gagner confiance en moi, de mûrir, de m'affirmer et d'acquérir une certaine indépendance. C'est pour quoi je tiens à remercier toute les personnes qui ont pris part à cette aventure.

Tout d'abord je tiens à adresser mes sincères remerciements à mes deux encadrants de thèse Pascal Simon et Marcello Civelli sans qui cette aventure n'aurait pas été possible. Grâce à leur pragmatisme et leur sens physique aiguisé, ils ont su m'aiguiller dans mes recherches et mes choix tout en me laissant une grande liberté et en m'exposant à un large panel de sujets. Je remercie particulièrement Pascal pour sa disponibilité et ses encouragements.

J'aimerais aussi remercier les membres de mon jury: Alfredo Levy Yeyati, Deung-Jang Choi, Jérôme Rech et Marco Aprili, pour avoir accepter de participer à ma soutenance. Je remercie plus particulièrement Alfredo Levy Yeyati et Jérôme Rech pour avoir accepter la lourde tâche de rapporteur de ce travail.

Bien que cette thèse fut menée en grande partie à distance, depuis mes Vosges natales, je remercie tous les membres du groupe Théorie du LPS pour leur accueil chaleureux et toutes les discussions scientifiques lors des pauses cafés. En particulier, je souhaite remercier Andrej Mesaros pour ses conseils et sa collaboration lors de nombreux projets durant ma thèse. Je remercie aussi mes collègues de bureau Étienne Fayen et Rodolfo Rocco pour leur bonne humeur quotidienne et Ansgar Graf pour les bons moments passés en sa compagnie à Cargèse. En passant, je tiens à remercier Marie-France Mariotto et Véronique Thieulart pour leur aide précieuse concernant les nombreuses démarches administratives et l'organisation de mon séjour à Cargèse.

En dehors du cercle du groupe Théorie, il me tient à coeur de remercier mes collaborateurs scientifiques. Premièrement je remercie Mircea Trif, pour sa collaboration lors de projets non présentés dans ce manuscrits. Deuxièmement, je tient à remercier Tristan Cren et Cristophe Brun pour leur collaboration sur le sujet des corrélations de paires impaires en fréquence. Enfin je suis très reconnaissant envers mes collègues expérimentateurs du LPS: Marco Aprili, Freek Massee, Umamahesh Thupakula et Alexandra Palacio-Morales, sans qui mes travaux théoriques sur les fluctuations du courant dans les états de Yu-Shiba-Rusinov n'aurait pu être confrontés à la réalité expérimentale. Je tiens à les féliciter pour la prouesse expérimentale qu'ils ont accompli. Je remercie plus particulièrement Marco, qui a aussi été mon parrain de thèse, ainsi que Freek pour leurs questions et remarques qui ont nourri ma curiosité et m'ont poussé à approfondir mes travaux. Je tiens à préciser en passant que mon travail sur la tomographie de bruit des états liés de Majorana, n'aurait pas vu le jour sans une brillante remarque de Freek.

Pour finir, je tiens à remercier chaleureusement mes proches. Tout d'abord mes grand-parents Marie-Claude et Christian pour l'intérêt qu'ils ont porté à mes travaux, leur soutien et tous les moments de joie partagés avec eux. Je remercie aussi mon frère, Jules, pour sa joie de vivre, son soutien dans les moments les plus difficiles et

son empathie. *Juju*, j e suis sûr que ton grand coeur et ton sens de l'écoute feront de toi un médecin hors pair. Je n'oublie pas non plus de remercier ma belle-soeur Jeanne, dit *Jeannette* pour son humour et sa joie.

Mes parents ont bien évidemment joué un rôle très important durant mon parcours étudiant et plus particulièrement durant ma thèse. Aussi, je leur suis infiniment reconnaissant pour leur soutien infaillible. Ce sont eux qui m'ont poussé à faire du mieux que je le pouvais durant tout mon parcours, et ce depuis ma tendre enfance. Leur bienveillance, leur attention et leur amour m'ont permis de m'épanouir et furent salvateurs dans les moments difficiles de cette thèse. *Paps, Mams,* je vous dois beaucoup, et je veux vous dire mille fois merci. Votre éducation a éveillé ma curiosité pour les sciences, me menant jusqu'à la thèse. Les valeurs que vous m'avez transmises: rigueur, persévérance, et humilité, m'ont permis de la mener à bien et de devenir Docteur.

Enfin et surtout je veux remercier la personne qui partage mon quotidien, ma fiancée, Alizé. C'est elle qui fut en première ligne durant les dernières années de cette thèse et qui a su écouter mes complaintes, me supporter et me remotiver dans les moments de doute. Je la remercie pour sa patience infinie et la joie qu'elle apporte dans ma vie. Je ne peux trouver de mots pour dire à quel point je lui suis reconnaissant de m'avoir offert le plus beau cadeau du monde, mon fils, Côme. Ce petit bonhomme, qui ne cesse de m'émerveiller, a été mon moteur durant la rédaction de ce manuscrit. J'espère que nous épanouïerons ensemble, tous les trois, pendant encore de nombreuses années.

Synthèse:

La supraconductivité est une phase de la matière caractérisée par l'absence de résistance électrique et l'expulsion parfaite des lignes de flux magnétiques de son intérieur. La découverte de la supraconductivité remonte à 1911, lorsque H. Kammerlingh-Onnes et son équipe à Leyde observent que la résistance électrique d'un échantillon de mercure s'annule de manière abrupte lorsque l'échantillon est refroidi en dessous de 4.2K [1]. La seconde caractéristique de l'état supraconducteur, le diamagnétisme parfait, ne fut observé que vingt ans plus tard, en 1933, par Meissner et Ochsenfeld [2]. Ce phénomène fut par la suite nommé effet Meissner-Ochsenfeld en l'honneur de ses découvreurs. Les deux phénomènes précédents n'apparaissent qu'en dessous d'une certaine température, nommée température critique, et qui dépend du matériau supraconducteur. Pour les métaux purs étudiés jusqu'au milieu des années soixante-dix, la température critique est de l'ordre de quelques degrés Kelvin, proche du zéro absolu ($-273,15°$C).

Dès la découverte expérimentale de la supraconductivité, d'importants efforts ont été mis en oeuvre pour comprendre l'origine de ce phénomène et établir une théorie de l'effet supraconducteur. Néanmoins, la supraconductivité est resté un casse-tête pour les théoriciens, et ce n'est qu'en 1957 que J. Bardeen, L. N. Cooper et J. R. Schrieffer proposèrent la première théorie microscopique de la supraconductivité: la célèbre théorie BCS [3, 4]. Dans cette théorie, la transition vers la phase supraconductrice est expliquée par la formation d'un condensat de paires d'électrons dont l'énergie est proche du niveau de Fermi, appelées paires de Cooper. Ce condensat de paires est bien séparé de ses états excités par une bande d'énergie interdite ou *gap*, noté Δ et appelé *gap de BCS* ou *gap supraconducteur*. De manière générale, Δ est un nombre complexe et joue le rôle du paramètre d'ordre supraconducteur au sens de la théorie des transitions de phase de Ginzburg-Landau [5].

Comme tous les matériaux, en réalité, les supraconducteurs ne sont pas parfaitement purs et contiennent des impuretés dont la présence pourrait potentiellement modifier leurs propriétés électroniques de façon drastique. C'est pourquoi, comprendre comment les impuretés sont susceptibles d'affecter les propriétés électroniques de matériaux donnés est un sujet central de la physique de la matière condensée. En 1959, P.W. Anderson a montré que la présence d'impuretés non-magnétiques, préservant la symétrie par renversement du temps, ne modifie pas les propriétés des supraconducteurs conventionnels en onde s [6], un résultat aujourd'hui connu comme le théorème d'Anderson. À contrario, la concurrence apparente entre la supraconductivité et le magnétisme, bien illustrée par l'effet Meissner-Ochsenfeld, suggère que le désordre magnétique, qui brise la symétrie par renversement du temps pourrait affecter l'état supraconducteur. En effet, dans un article pionnier, A. Abrikosov et L. P. Gor'kov ont montré que la présence d'un désordre magnétique dans les supraconducteurs à ondes s réduit la magnitude du *gap* supraconducteur ainsi que la température critique et pourrait à terme détruire la cohérence de l'état supraconducteur pour des concentrations d'impuretés suffisamment importantes [7]. Quelques années plus tard, L. Yu, H. Shiba et A. I. Rusinov démontrèrent, de manière indépendante, qu'un unique moment magnétique *classique*, isolé, immergé dans un supraconducteur en onde s agit de manière effective comme

un potentiel de brisure de paires et génère un unique état lié, localisé, dont l'énergie se trouve dans le *gap* supraconducteur [8, 9, 10]. Ces états liés sont aujourd'hui nommés états de Yu-Shiba-Rusinov en l'honneur de leurs découvreurs. En présence d'une concentration finie d'impuretés magnétiques, les états de YSR ayant un recouvrement fini s'hybrident et donne naissance à une bande de Shiba dans le *gap* supraconducteur [9].

Bien que l'existence des états de Yu-Shiba-Rusinov ait été prédite dès la fin des années soixante, leur observation et caractérisation expérimentale resta longtemps balbutiante en raison, notamment, de la fine résolution spatiale et spectrale requise. Ainsi, ce n'est qu'en 1997 que A. Yazdani et ses collaborateurs rapportent la première observation expérimentale, directe, d'états de Yu-Shiba-Rusinov, par spectroscopie à effet tunnel [11]. Cette prouesse expérimentale fut permise par les récents progrès technologiques permettant la préparation de surfaces supraconductrices propres et la déposition d'atomes magnétiques sous ultra-vide et à basse température. Ainsi que par le développement de la spectroscopie à effet tunnel permettant l'étude de ses surfaces avec un haut niveau de résolution spatiale et spectrale à des températures ultra-basses, bien en dessous de la température critique. Plus récemment, le domaine a connu un regain d'intérêt, principalement motivé par la possibilité de manipuler des chaînes d'états de Yu-Shiba-Rusinov pour induire une phase supraconductrice topologique dans les bandes Shiba [12].

Pour être bref, la topologie est une branche des mathématiques qui s'intéresse aux propriétés d'objets géométriques qui sont préservées lors de déformations continues de ces objets. De telles propriétés sont appelées invariants topologiques. En physique du solide, les matériaux topologiques sont caractérisés par la présence de modes d'énergie nulle localisé au bords de l'echantillon. Ces derniers ne peuvent être éliminés lors de déformations continues du système. L'exemple le plus célèbre de phase topologique en matière condensée est certainement l'effet Hall quantique entier [13], pour lequel la présence d'états de bord chiraux, topologiquement protégés, donnent lieu à une conductance de Hall transverse quantifiée [14]. Dans le cas de supraconducteurs topologiques, les modes de bord topologiques sont des quasiparticules de Majorana qui ont la propriété particulière d'être leurs propres antiparticules. Ces quasiparticules possèdent des caractéristiques avantageuses pour le calcul quantique. Premièrement, le caractère non-local de ces quasiparticules les rend robustes à la présence de désordre local préservant le gap supraconducteur. De plus, les modes de bord de Majorana possèdent une statistique d'échange non abélienne. De ce fait l'état quantique de qbits de Majorana peut être manipulé en échangeant les modes de Majorana. Ces deux propriétés font des modes de Majorana des candidats idéaux pour la réalisation de futurs ordinateurs quantiques topologiques tolérants aux erreurs [15]. Depuis leur prédiction théorique [16], les modes de Majorana sont devenus le *Saint Graal* de la physique de la matière condensée et constitue l'un des thèmes de recherche les plus actifs du domaine. Au cours de la dernière décennie, des travaux théoriques ont montré qu'une chaîne unidimensionnelle (1D) d'impuretés magnétiques ,déposées à la surface d'un supraconducteur conventionnel en onde *s*, possède une phase supraconductrice topologique 1D abritant des modes de bord de Majorana à ses extrémités [12]. Néanmoins, afin de concevoir de telles chaînes d'impuretés magnétiques, une compréhension profonde et détaillée des propriétés de la brique de base, l'état de Yu-Shiba-Rusinov, est nécessaire. Ainsi, les états de Yu-Shiba-Rusinov ont suscité un engouement particulier durant la dernière décennie au sein de la communauté scientifique de la matière condensée [17]. Les propriétés spectrales ainsi que la dépendance spatiale des états de Yu-Shiba-Rusinov ont ainsi fait l'objet d'une caractérisation expérimentale approfondie et sont aujourd'hui bien comprises [10, 18, 19]. Au contraire, le temps de relaxation intrinsèque de ces états de Yu-Shiba-Rusinov, élément crucial pour la réalisation de structures plus complexes telles que les chaînes, a reçu moins d'attention et reste encore difficile à caractériser expérimentalement.

C'est pourquoi, cette thèse a pour but de revisiter les propriétés de transport électronique des états de Yu-Shiba-Rusinov et plus généralement des états liés intra-gap au sein de supraconducteurs. Afin d'établir un lien direct avec les résultats expérimentaux, nous porterons une attention particulière aux observables locales qui peuvent être mesurées par microscopie/spectroscopie à effet tunnel. En effet, grâce à sa haute résolution spatiale et énergétique, cette technique expérimentale est largement utilisée pour caractériser les états liés localisés intra-gap tels que les états de Yu-Shiba-Rusinov [17] ou les modes de Majorana topologiques [20]. Dans un premier temps, nous montrerons que l'état de Yu-Shiba-Rusinov modifie localement l'état supraconducteur du matériau hôte et induit des paires de Cooper non conventionnelles, dont l'état de spin est triplet et possèdent une symétrie impaire en fréquence. De plus, nous verrons que la spectroscopie à effet tunnel conventionnelle du coeur des états de Yu-Shiba-Rusinov contient des signatures de la présence d'appariement impaire en fréquence au voisinage de l'impureté magnétique. Nous montrerons alors, de manière explicite, comment la partie imaginaire de la fonction d'appariement impaire en fréquence peut être extraite directement du spectre de conductance différentielle. Deuxièmement, motivés par le développement, très récent, de la spectroscopie à effet tunnel du bruit de grenaille [21, 22], nous montrerons que l'analyse des fluctuations du courant tunnel dans les états de Yu-Shiba-Rusinov fournit des informations précieuses sur la nature des processus de transfert de charge sous-jacents. De plus, cette analyse permet d'estimer le temps de relaxation intrinsèque des états de Yu-Shiba-Rusinov. Enfin, en étendant les résultats précédents au cas d'états liés supraconducteurs arbitraires, nous montrons que la tomographie du bruit de grenaille, d'ores et déjà réalisable [21, 22], possède des caractéristiques bien distinctes déterminées par la nature de l'état lié sondé. Plus particulièrement, ces différences qualitatives très prononcées permettent de distinguer des énergies nulles triviales états fermioniques des modes zéro de Majorana. Le manuscrit présenté ici comprend cinq chapitres, deux chapitres introductifs suivis de trois chapitres dédies aux résultats originaux obtenus pendant cette thèse. Ces chapitres sont organisés comme suit:

- **Chapitre. 1: Théorie de champ moyen des supraconducteurs et topologie**
  Le but de ce premier chapitre introductif est de présenter le formalisme théorique qui sera utilisé tout au long de le manuscrit pour décrire les propriétés électroniques des supraconducteurs à des températures bien inférieures à la température critique. Ce formalisme, connu sous le nom de formalisme de Bogoliubov-de-Gennes, n'est autre qu'une description de champs moyen de la supraconductivité, qui peut être vue comme une généralisation de la théorie de BCS. Nous commencerons ce chapitre par un bref rappel de la théorie de champ moyen de BCS [3]. Ensuite, nous généraliserons cette théorie en autorisant la présence de paires de Cooper de symétries arbitraires et présenterons ainsi le formalisme de Bogoliubov-de-Gennes [23]. Enfin, nous discuterons la classification topologique des phases supraconductrices [24] ainsi que les propriétés des modes de Majorana qui apparaissent au bords de certains supraconducteurs topologiques [25].

- **Chapitre. 2: Introduction au formalisme des fonctions de Green hors-équilibre**
  Dans ce second chapitre introductif, nous introduirons le formalisme théorique des fonctions de Green hors-équilibre sur le contour de Keldysh [26]. Cet outil théorique puissant est parfaitement adapté à l'étude du transport électronique. Ainsi, il permet de décrire de manière pratique la microscopie/spectroscopie à effet tunnel des états de sous-gap supraconducteurs et de comparer directement nos résultats aux données expérimentales. Tout d'abord, nous poserons les bases de la technique des fonction de Green hors-équilibre et introduirons le concept de contour temporel, pierre angulaire du formalisme [27]. Ensuite, nous nous concentrerons sur le contour de Keldysh, un contour spécifiquement adapté à l'étude

des régimes stationnaires [26]. Enfin, nous appliquerons le formalisme de Keldysh à la modélisation des expériences de spectroscopie à effet tunnel, dans lesquelles une pointe métallique sonde un échantillon supraconducteur présentant potentiellement un état lié intra-gap. Plus particulièrement nous montrerons de manière explicite comment la conductance différentielle peut être calculée via la technique de Keldysh. Aussi, nous appliquerons nos résultats au cas d'un supraconducteur conventionnel parfait, pour lequel la conductance peut être calculée analytiquement et met en évidence le concept de réflexion d'Andreev [28].

- **Chapitre. 3: Appariement impaire en fréquence au voisinage d'impuretés magnétiques**
  Ce chapitre est le premier chapitre dédié aux résultats originaux obtenu lors de cette thèse. Ici, nous montrerons qu'un état de Yu-Shiba-Rusinov convertit localement les paires de Cooper conventionnelles, en onde s, singlets de spin et paires en fréquence, du matériau hôte en paires de Cooper non-conventionnelles, en onde s, triplets de spin et impaires en fréquence. Tout d'abord, nous présenterons brièvement le concept d'appariement impaire en fréquence [29]. Après un bref tour d'horizon historique de ce dernier concept, nous passerons en revue les propriétés spectrales et spatiales bien connues des états Yu-Shiba-Rusinov [10, 18, 17]. Ensuite, nous calculerons explicitement les fonctions d'appariement au cœur de l'état de Yu-Shiba-Rusinov et montrerons que la densité électronique locale, directement mesurable par spectroscopie à effet tunnel, est proportionnelle à la partie imaginaire de la fonction d'appariement impaire en fréquence. En se basant sur ce dernier résultat, nous proposerons une méthode pour extraire la partie imaginaire de la fonction d'appariemment impaire en fréquence à partir de spectres de conductance différentielle expérimentaux, mesurés par spectroscopie à effet tunnel. Enfin, nous appliquerons notre méthode à un jeux de données mesurées par G. C. Ménard, et ses collaborateurs à l'Institut des Nanosciences de Paris. Les résultats ainsi obtenus montrent des signatures expérimentales de l'occurrence d'appariement impaire en fréquence au vosinage des états de Yu-Shiba-Rusinov. Ce chapitre est basé sur l'article suivant : [30], paru dans *Physical Review Letters*.

- **Chapitre. 4: Spectroscopie à effet tunnel du bruit de grenaille des états de Yu-Shiba-Rusinov**
  Dans ce chapitre, motivé par le développement récent de la spectroscopie à effet tunnel du bruit de grenaille, nous nous baserons sur le formalisme de Keldysh pour construire un modèle théorique du transport électronique dans les états de Yu-Shiba-Rusinov. Tout d'abord, nous décrirons le dispositif expérimental considéré et construirons un modèle théorique simplifié décrivant le transport électronique à basse énergie dans les états de Yu-Shiba-Rusinov situés dans le gap supraconducteur. Ensuite, nous utiliserons le formalisme de Keldysh, introduit au Chapitre. 1, pour calculer le courant électronique traversant la jonction tunnel ainsi que le bruit de grenaille associé aux fluctuations de courant. Du point de vue théorique, il est aisé de montrer qu'en présence de relaxation, le courant tunnel au travers d'un état de Yu-Shiba-Rusinov provient de deux types distincts de processus de transfert de charge microscopique: des processus tunnel à une seule particule et des réflexions d'Andreev [31]. Récemment, M. Ruby et ses collaborateurs ont mesuré le courant tunnel dans les états de Yu-Shiba-Rusinov grâce à un microscope à effet tunnel sondant le coeur de l'impureté magnétique. Les résultats expérimentaux combinés à une modélisation théorique suggèrent que le courant provient majoritairement des processus à une particule pour de grandes distances pointe/échantillon. Au contraire, les processus d'Andreev deviennent majoritaires lorsque la distance pointe approche l'échantillon [32]. Ces résultats suggèrent que les processus à une particule et ceux d'Andreev opèrent de manière simultanée dans les états de Yu-Shiba-Rusinov [32],

en accord avec les prédictions théoriques antérieures [31]. Néanmoins, cette conclusion est sujette à interprétation et ne constitue pas une preuve irréfutable de la présence de processus d'Andreev. À ce jour, la spectroscopie de courant standard ne nous a pas livré de signatures directes et non-ambiguës de l'occurence de processus d'Andreev dans les états de Yu-Shiba-Rusinov. Ici, nous montrerons qu'au contraire, la spectroscopie de bruit de grenaille fournit des preuves directes de la présence concomittante de processus d'Andreev et des processus à un seule particule, dans les états de Yu-Shiba-Rusinov. Enfin, en comparant nos prédictions théoriques aux mesures expérimentales du bruit de grenaille obtenues par U. Thupakula et ses collaborateurs au LPS, nous montrerons que notre modèle capture correctement les principales caractéristiques qualitatives du bruit de grenaille, oservées experimentalement dans les états de Yu-Shiba-Rusinov. De plus, nous montrerons qu'il est possible d'atteindre un accord quantitatif entre mesures et théorie en utilisant le taux de relaxation de l'état de Yu-Shiba-Rusinov comme seul paramètre libre. Grâce à l'accord quantitatif ainsi obtenu, nous estimerons le taux de relaxation des états de Yu-Shiba-Rusinov. Le taux de relaxation typique ainsi estimé est de l'ordre du microélectronvolt, bien en dessous de l'énergie d'agitation thermique, de l'ordre de quelques centaines de microélectronvolts. Ainsi, nos résultats montrent que la spectrocopie du bruit de grenaille permet d'accéder à des échelle d'energie et de temps inaccessible par spectroscopie conventionnelle, dont la résolution est limité par l'élargissement thermique. Pour finir, notre analyse théorique des données expérimentales indique clairement la présence concomitante de processus à une seule particule et de processus d'Andreev. Ce chapitre est basé sur la publication suivante : [33], parue dans *Physical Review Letters*.

- **Chapitre. 5 : Tomographie du bruit de grenaille, un nouvel outil pour identifier les modes de Majorana**
  Dans ce chapitre, nous montrons que la tomographie à bruit de fond révèle des caractéristiques distinctives clés qui permettent de distinguer les états fermioniques triviaux à énergie nulle, comme les états YSR, des modes zéro de Majorana. Dans un premier temps, nous décrirons brièvement la plateforme expérimentale la plus mature pour l'ingénieurie de phase supraconductrice topologique arborant des modes de bord de Majorana: les nanofils de Rashba. Un nanofil de Rashba est une hétérostructure hybride constituée d'un nanofil semiconducteur présentant un fort couplage spin-orbit intrinsèque, le pus souvent de l'Indium ou l'Arsenide déposé à la surface d'un supraconducteur conventionnel, le plus souvent de l'Aluminium. En présence d'un champ magnétique parallèle à l'axe du nanofil une phase supraconductrice topologique est induite dans le nanofil, à condition que le champs soit suffisamment fort. La nature topologique de la phase supraconductrice se traduit alors par la présence de deux modes de Majorana, chacun localisé à une extrémité du nanofil. En combinant l'étude d'un modèle analytique effectif à basse énergie et des simulations numériques exactes, nous montrerons que le facteur de Fano au voisinage de modes de Majorana ne présente pas de dépendance spatiale et reste égal à un, indépendemment de la position sondée. En revanche, le facteur de Fano au voisinage des états liés fermioniques triviaux présente des oscillations spatiales bien marquées qui excédent largement un, pour certaines positions. En construisant un modèle effectif à basse énergie, nous montrerons que ces différences marquées ont un caractère universel trouvant son origine dans la symétrie particule-trou caractéristique de la fonction d'onde d'un mode de Majorana isolé. Ce chapitre est basé sur la publication suivante: [34].

- **Chapitre. 6 : Conclusion générale**
  Nous finirons ce manuscrit par un chapitre de conclusion générale où nous resumerons les principaux

résultats, discuterons les limites de nos travaux ainsi que les perspectives possibles. Ci-dessous nous donnons une traduction condensée de cette conclusion générale.

Dans cette thèse, nous avons revisité les propriétés de transport électronique des états liés intr-gap au sein de supraconducteurs. Plus particulièrement, nous avons montré que la mesure du courant tunnel et du bruit de grenaille associé, au moyen de microscopes à effet tunnel, fournit des informations précieuses sur les propriétés des états sub-gap supraconducteurs et leurs propriétés. Ceci inclut la présence d'un appariement non conventionnel, le temps de relaxation intrinsèque des états liés, ou encore l'asymétrie particule-trou de leur fonction d'onde.

Premièrement nous avons montré que les états de Yu-Shiba-Rusinov induisent de manière locale un appariement non-conventionnel, impair en fréquence. De plus nous proposons un protocole permettant d'extraire la partie imaginaire de la fonction d'appariement impaire en fréquence à partir du spectre de conductance différentielle mesurée au coeur de l'impureté et obtenons ainsi des signatures expérimentales de la présence de correlation impaire en fréquence au voisinage d'impureté magnétiques [30]. Lors d'une collaboration avec F. L. N. Santos et ses collaborateurs, que nous n'avons pas présenté dans ce manuscrit, nous avons pu étendre les résultats précédents au cas d'une concentration finie d'impuretés magnétiques dans la limite diluée [35].

Dans un second temps nous nous sommes intéressés à la spectroscopie à effet tunnel de bruit de grenaille, une technique expérimentale très récente et prometteuse [21, 22]. En utilisant le formalisme de Keldysh nous avons pu montrer que la mesure du bruit de grenaille à l'échelle atomique montre de manière claire et direte que le courant au travers d'états de Yu-Shiba-Rusinov provient à la fois de processus d'Andreev et de processus à un seule particule opérant simultanément. De plus, cette technique permet d'estimer le taux de relaxation intrinsèque des états de Yu-Shiba-Rusinov habituellement masqué par les effets thermiques.

Il est important de rappler que les résultats précédents sont basés sur un modèle classique de l'impureté magnétique. Ainsi, il serait intéressant de comprendre dans quelles mesures les fluctuations quantiques du spin de l'impureté magnétique affectent nos résultats. Ce point pourrait être abordé dans un futur proche, mais nécessiterait l'utilisation d'outils théoriques pointus et sophistiqués, adaptés à la description d'électrons fortement corrélés, tel que la théorie du champ moyen dynamique hors-équilibre [36].

Pour finir, en étendant notre moèdele théorique du bruit de grenaille au voisinnage des états de Yu-Shiba-Rusinov à des états liés intra-gap de nature arbitraire, nous avons pu montré que la tomographie du bruit de courant est un outil prometteur pour l'identification de mode de Majorana isolés et le développement de technologie quantique basées sur les qubits de Majorana. Sur la base d'un modèle effectif à basse énergie, nous avons montré, de manière ananlytique, que dans le régime de couplage tunnel fort, où la contribution des processus incohérents à une seule particule peut être négligée devant les réflexions d'Andreev, le facteur de Fano est essentiellement déterminé par l'asymétrie locale particule-trou de la fonction d'onde de l'état lié. Ceci suggère que la tomographie du facteur de Fano peut être utilisée pour distinguer les fermions triviaux des fermions de Majorana. Nos simulations numériques de la tomographie du facteur de Fano nous a permis de confirmer les résultats analytiques obtenus par l'approximation de basse énergie. Plus précisément, nous avons montré qu'au voisinage d'un mode de Majorana spatialement isolé, le facteur de Fano ne présente pas de dépendance spatiale significative, reste constant et égal à un. Ce comportement contraste fortement avec les fortes oscillations supérieures à un observées au voisinage d'états liés triviaux. De plus, les résultats analytiques obtenus par l'approximation de basse énergie indiquent que ces fortes oscillations trouvent leur origine dans l'asymétrie particule-trou locale (c'est-à-dire la charge locale) de l'état lié sondé. Ainsi, bien que la tomographie du facteur de Fano est incapable de sonder directement nature topologique du coeur de l'échantillon, elle est sensible

l'asymétrie particule-trou locale de l'état lié sondé et donc au recouvrement des fonctions d'onde de Majorana le composant. Cette technique pourrait donc jouer un rôle clé dans le développement de technologies quantiques basées sur les qubits de Majorana, motivant ainsi l'utilisation de la spectrocopie à effet tunnel de bruit de grenaille pour l'étude des fermions de Majorana et, plus généralement, de la matière topologique.

Nous noterons en passant que notre étude numérique traite un modèle minimal des nanofils hybrides semiconducteurs/superconducteurs. Ce modèle minimal peu être raffinés afin d'obtenir un description plus réaliste des nanofils. Par exemple l'effet du désordre, la présence de bandes mutliples ou encore l'environnement électrostatique du nanofil peuvent être pris en compte et potentiellement modifié nos résultats. Néanmoins, puisque la signature particulière des modes de Majorana isolé, observée dans la tomographie du facteur de Fano, est ancrée dans la symétrie particule-trou intrinsèque de leur fonction d'onde, nos résultats ont un caractère universel. Ainsi, il est raisonnable de supposer que nos résultats ne sont pas affecter significativement par les détails microscopiques du modèle. Corrollairement, nos résultats peuvent être appliqués pour identifier des modes de Majorana isolés dans des sytèmes différents des naofils de Rashba. Plus spécifiquement, nous espérons que la tomographie du facteur de Fano soit un outil pertinent pour étudier les modes de Majorana putatifs, localisés au cœur de vortex au sein des supraconducteurs à base de fer, qui font aujourd'hui l'objet d'un examen expérimental intensif. Très récemment, le bruit de grenaille a été mesuré au cœur d'un vortex dans le $\mathrm{FeTe_{0,55}Se_{0,45}}$ [37], ouvrant ainsi la voie à la tomographie du bruit de fond au voisinage des cœurs de vortex. Par conséquent, dans un avenir proche, il sera intéressant d'étendre nos travaux et d'étudier, par des moyens numériques, les variations spatiales du facteur de Fano au voisinage de cœurs de vortex dans les supraconducteurs à base de fer, en se basant sur des modèles multibandes réalistes. En effet, bien que de récentes études théoriques ont étudié le courant et le bruit de grenailles au cœur du vortex [38], l'étude détaillée et complète de la tomographie du facteur de Fano fait encore défaut.

En guise de remarque finale, il est important de souligner que ce manuscrit ne constitue pas une revue exhaustive de tous les sujets abordés au cours des trois dernières années de cette thèse de doctorat. Bien que ce manuscrit se concentre sur le transport électronique dans les états liés intra-gap, qui est déterminé par la dynamique du transfert de charge à travers la jonction tunnel, une autre voie prometteuse pour étudier les propriétés des états de Yu-Shiba-Rusinov est de sonder directement la dynamique du spin de l'impureté magnétique. Ainsi, nous avons étudié la dynamique des ondes de spin dans une chaîne 1D d'atomes magnétiques placée à la surface d'un supraconducteur conventionnel en présence d'un couplage spin-orbite. Un tel système présente des modes de Majorana localisés à chacune de ses extrémités qui sont susceptibles d'affecter la dynamique des ondes de spin se propageant le long de la chaîne. Au moyen de la théorie des perturbations, nous avons pu montré que l'absorption du mode uniforme d'onde de spin dépend de la parité du qubit de Majorana. Ceci suggère ainsi que la spectrcopie des ondes de spin pourrait être utilisée comme une sonde de la parité des Majoranas. Ces résultats préliminaires encourageant devront être approfondis dans un futur proche.

Contents

List of Figures

List of Tables

Introduction

Superconductivity is a state of matter characterized by a vanishing electrical resistance and the expulsion of magnetic flux fields from its interior. The discovery of the superconducting state dates back to 1911 when H. Kammerlingh-Onnes and its team in Leyde observed that the electrical resistance of solid mercury abruptly vanishes when the temperature decreases below 4.2 K [1]. The second characteristic was observed twenty years later, in 1933, by Meissner and Ochsenfeld [2], and was named after its discoverers, the Meissner-Ochsenfeld effect. These two phenomena only occur below a given temperature, called the critical temperature, which depends on the superconducting materials. For pure metals studied before the mid-seventies, the critical temperature is of the order of a few Kelvins.

Great efforts have been made to understand the origin of superconductivity and construct a theory of superconductivity. Nevertheless, it was only in 1957 that J. Bardeen, L.N. Cooper, and J. R. Schrieffer proposed the first truly microscopic theory of superconductivity: the BCS theory [3]. In this theory, the superconducting transition is understood as the formation of a condensate of pairs of electrons around the Fermi level, known as Cooper pairs. This condensate is well-separated from its excited states by an energy gap named the BCS or superconducting gap Δ. This plays the role of the superconducting order parameter in the Landau-Ginzburg theory of phase transitions [5].

As any materials, realistic superconductors are not perfectly pure and do contain impurities that could potentially modify their electronic properties dramatically. That is why understanding how impurities are likely to affect the electronic properties of given materials has always been a central topic in condensed matter physics. In 1959, P.W. Anderson showed that the presence of non-magnetic disorder preserving the time-reversal symmetry does not alter the properties of *conventional* s-wave superconductors [6], a result that is nowadays known as the Anderson theorem. However, the apparent competition between superconductivity and magnetism, as exemplified by the Meissner-Ochsenfeld effect, suggests that magnetic disorder, which breaks the time-reversal symmetry, might affect the superconducting state. Indeed, in a seminal work, A. Abrikosov and L. P. Gor'kov showed that the presence of magnetic disorder in s-wave superconductors reduces the superconducting gap and critical temperature and could ultimately destroy the coherence of the superconducting state for a sufficiently high concentration of impurities [7]. A few years later, L. Yu, H. Shiba, and A. I. Rusinov independently showed that [8, 9, 10] an isolated classical spin immersed in an s-wave superconductor acts as a pair breaking potential and generates a single localized bound-state inside he superconducting gap. These bound states are known as Yu-Shiba-Rusinov (YSR) states. For finite concentrations of magnetic impurities, the YSR states hybridize and form Shiba bands inside the superconducting gap [**?**].

Despite their early theoretical predictions in the late sixties, because of the high spatial and energy resolution required, the first experimental observation of YSR states was reported thirty years later by A. Yazdani *et al.* [11] thanks to scanning tunneling spectroscopy. More recently, the field experienced a renewed interest,

mainly motivated by the possibility of engineering chains of YSR states to induce topological superconductivity in the Shiba bands.

To be brief, topology is a branch of mathematics that study the characteristics of geometrical objects preserved by continuous deformations, called topological invariants. In solid-state physics, topological materials are characterized by the presence of zero-energy edge modes that cannot be removed by continuous deformations of the system. The most famous example of a topological phase of matter is the Integer Quantum Hall state [13], in which protected chiral edge states give rise to a quantized transverse Hall conductance [14]. In topological superconductors, the topological edge modes are Majorana quasiparticles which are their own antiparticles. Because they are topologically protected against local noise and exhibit exotic exchange statistics, Majorana zero modes (MZMs) are ideal building blocks of forthcoming fault-tolerant topological quantum computers [15].

Since their theoretical predictions [16], the search for Majorana zero modes is one of the most active research topics in condensed matter physics. During the last decade, it was proposed that one-dimensional (1D) chains of magnetic impurities placed on top of an s-wave superconductor could realize a 1D topological superconductor exhibiting MZMs at its ends [12]. Therefore, before engineering such chains of magnetic impurities, a complete and detailed understanding of their building block, the YSR state, is highly required. Thus, the Yu-Shiba-Rusinov states have known a renewed during the last decade [17]. The spectral properties as well as the spatial dependence of these bound-states have been thoroughly investigated by theoretical and experimental means, and are nowadays rather well understood [10, 18, 39, 17]. On the contrary, the intrinsic relaxation time of these Yu-Shiba-Rusinov states, a crucial element for the realization of structures such as chains, has received less attention and its experimental characterization remains challenging.

That is why, in this thesis, we will revisit the electronic properties of YSR states. In order to make a direct connection with experiments, we will pay special attention to local observables that can be measured by scanning tunneling microscopy/spectroscopy (STM/STS). Indeed, because of its high spatial and energy resolution, STM/STS is the most widely used experimental technique to study localized sub-gap states such as YSR [17] or topological MZMs [20]. First, we will show that the YSR state locally modifies the superconducting state of the host material and induces unconventional odd-frequency spin-triplet Cooper pairs. In addition, we shall see that conventional tunneling spectroscopy of the YSR core allows one to show experimental evidence of the occurrence of the odd-frequency pairing in these systems and explicitly extract the pairing function from the data. Second, motivated by the recent development of scanning tunneling shot-noise spectroscopy [22, 21], we will show that the analysis of current fluctuations in YSR states provides valuable insight into the underlying charge transfer processes and allows us to estimate the intrinsic relaxation time of YSR states. Finally, extending the previous results to arbitrary superconducting sub-gap states, we show that shot-noise tomography, which is currently feasible [22, 21], reveals key distinctive features that allow one to distinguish trivial zero-energy fermionic states from Majorana zero modes. The present manuscript is constructed as follows:

- **Chapter. 1: Mean-field theory of superconductors and topology**
  In this chapter, we introduce the generalized mean-field theory of superconductors that is used throughout the manuscript to describe the electronic properties of superconducting systems. We start with a brief reminder of the BCS theory [3]. Then we extend the standard BCS theory to include Cooper pairs with arbitrary symmetry and present the so-called Bogoliubov-de-Gennes formalism [23]. Finally, we present the topological classification of superconductors [24] and the properties of the topologically protected Majorana edge modes [25].

- **Chapter. 2: Introduction to non-equilibrium Green's functions technique**
  In this chapter, we present the non-equilibrium Green's functions technique on the Keldysh contour [26]. This powerful theoretical tool is perfectly suited to the study of electronic transport. Therefore, it allows us to describe conveniently scanning tunneling microscopy/spectroscopy of superconducting sub-gap states and directly compare our results to experimental data. First, we lay the foundations of the non-equilibrium Green's function technique and introduce the time-contour idea [27]. Then, we focus on the Keldysh contour that is well-suited for the study of steady-state regimes [26]. Finally, we focus on the modeling of scanning tunneling spectroscopy experiments where a metallic tip probes a superconducting substrate that can exhibit sub-gap states and show how to compute the current and differential conductance thanks to the Keldysh technique. We conclude this chapter with a concrete application to the case of a clean BCS superconductor. In this case the differential conductance can be computed analytically and allows us to introduce the concept of Andreev reflections [28].

- **Chapter. 3: Odd-frequency pairing around magnetic impurities**
  In this chapter, we show how a YSR state locally converts the *conventional* even-frequency spin-singlet s-wave Cooper pairs of the BCS substrate into *unconventional* odd-frequency spin-triplet s-wave Cooper pairs. First, we briefly introduce the concept of odd-frequency pairing [29]. After a brief historical review of the field, we review the well-known spectral and spatial properties of the YSR states [10, 18, 17]. Then, we explicitly compute the pairing functions at the YSR core and show that the local electronic density of state, directly measured in STS experiments, is proportional to the imaginary part of the odd-frequency pairing function. Using these results, we propose a method to extract the imaginary part of the odd-frequency pairing function from STS data. Finally, we illustrate our method for STS data measured by G. C. Ménard, *et al.* at the Institut des Nanosciences de Paris. Our results show experimental evidence of the occurrence of the odd-frequency pairing around YSR states. This chapter is based on the following publication: [30].

- **Chapter. 4: Scanning tunneling shot-noise spectroscopy of Yu-Shiba-Rusinov states**
  In this chapter, motivated by the recent development of scanning tunneling shot-noise spectroscopy, we use the Keldysh technique to analyze the electronic transport into YSR sub-gap states theoretically. First, we describe the experimental set-up that we consider and construct a simplified model describing the low-energy electronic transport into YSR sub-gap states. Second, we use the Keldysh technique to compute the current across the STM junction and its shot-noise. It is already known that the current is carried by single-particle tunneling and Andreev reflection processes [31]. Nevertheless, even if some tantalizing signatures of a transition from single-electron dominated tunnelling to Andreev processes have been reported [32], the standard current spectroscopy does not exhibit clear signatures of Andreev processes. Here, we show that, on the contrary, the shot-noise spectroscopy provides direct evidences for Andreev processes and single-particle processes. Finally, comparing our theoretical predictions to experimental noise data measured by U. Thupakula *et al.*, we show that our model correctly captures the main features of the shot noise in YSR states. From the quantitative agreement between experiment and theory, we can estimate the YSR relaxation rate, which is inaccessible by differential conductance spectroscopy, whose resolution is thermally limited. In addition, our theoretical analysis of the experimental data clearly indicates the concomitant presence of single-particle and Andreev processes. This chapter is based on the following publication: [33].

- **Chapter. 5: Shot-noise tomography: a new tool to identify Majorana zero modes**
  In this chapter, we show that shot-noise tomography reveals key distinctive features that allow one to distinguish trivial zero-energy fermionic states, like YSR states, from Majorana zero modes. First, we briefly describe the most promising solid-state platform exhibiting MZMs: the superconducting Rashba nanowires. By employing numerical and analytical methods, we show that the Fano factor in the vicinity of Majorana zero modes is spatially constant and equal to one. In sharp contrast, the Fano factor of trivial fermionic bound-states is strongly spatially dependent and exceeds one. Based on a low-energy effective model, we show that these sharp differences have a universal character that is rooted in the intrinsic particle-hole symmetry of the MZM wavefunction. This chapter is based on the following publication: [34]

- **Chapter. 6: General conclusion** In this chapter, we briefly summarize the original results obtained in this thesis and draw a general conclusion.

Chapter 1

Mean-field theory of superconductors and topology

In this chapter, we introduce the theoretical framework that we used hereinafter to describe the electronic properties of superconducting systems: the well-known Bogoliubov-de-Gennes formalism. This formalism is nothing but a generalized version of the famous Bardeen-Cooper-Schrieffer theory [3, 4]. The standard BCS theory, which might be interpreted as a mean-field theory of the superconducting state, successfully describes many fundamental aspects of all the superconductors known before until the mid-seventies, named *conventional* superconductors. However, in 1976, *unconventional* superconductors exhibiting a superconducting order parameter with symmetries that are not allowed by the standard BCS theory, was experimentally observed. This discovery motivated the extension of the BCS theory to superconducting order parameters with arbitrary symmetries. It gave rise to the generalized mean-field theory of the superconducting state, the so-called Bogoliubov-de-Gennes (BdG) formalism.

The chapter is constructed as follows: In the first section, we briefly introduce the standard BCS theory, then we extend the standard BCS theory to Cooper pairs of arbitrary symmetry and present the BdG formalism. Finally, based on the symmetry properties of the single-particle BdG Hamiltonian, the topological classification of superconductors is presented with an emphasis on the Majorana edge-states arising in finite-size topological superconductors.

1.1 Standard BCS theory

In 1957, Bardeen Schrieffer and Cooper proposed the first truly microscopic theory for superconductivity[3, 4], which is based on three key concepts. The first one is due to Cooper, who showed, in 1956, that in the presence of a weak electronic attraction, a Fermi sea is unstable to the formation of a bound pair of electrons. This pair, named a Cooper pair, is the central building block of the BCS theory.

However, electrons carry a negative charge, and they repel each other because of the Coulomb repulsion, preventing them to form pairs. Even if screening effects render the Coulomb repulsion short-ranged in metals, it remains repulsive. Hence it is necessary to elucidate how an electronic attraction can arise in metals. Here comes the second cornerstone of the BCS theory. In a nutshell, BCS showed that the coupling of the electrons with the displacements of the ion cores lattice, the well-known phonons, effectively generates an attractive

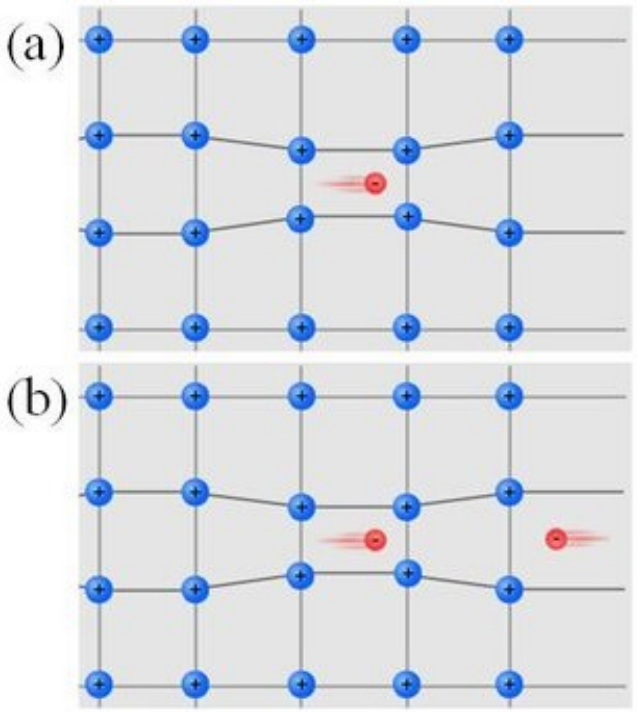

Figure 1.1: Schematic illustration of phonon-mediated attraction and Cooper pair formation in the BCS theory. (a) a first electron interacts with the surrounding positive ion cores, creating an excess positive charge. (b) The excess positive charge attracts the second electron with opposite spin, moving in the opposite direction. The 2 electrons are locked together, forming a Cooper pair.

interaction between electrons. The physical idea is that a first electron polarizes the background medium by attracting the positive ions. In turn, the excess positive charge created attracts a second electron resulting in an effective electronic interaction as depicted in Fig.1.1. Using a jellium model, D. Pines concretely showed that the phonon-mediated interaction is attractive in a narrow energy range of the order of the Debye energy $\hbar\omega_D$, and has the same order of magnitude as the Coulomb repulsion [40]. Hence it seems reasonable to assume that the phonon-mediated interaction overrides the Coulomb repulsion resulting in a net attractive interaction between electrons providing a microscopic mechanism for Cooper formation [3, 4, 41].

Finally, since the Fermi sea is unstable against the formation of a Cooper pair when the net interaction is attractive, one expects that these pairs will condense until a certain equilibrium where the binding energy of an additional pair becomes zero. That is the last key idea of the BCS theory, where the groundstate of the system is found to be a condensate of Cooper pairs.

Following the review by M. Sigrist [23], we will now briefly derive the main results of the BCS theory starting from a simplified model introduced by BCS. Here, for convenience, we employ a mean-field technique rather than the variational method originally used by BCS.

1.1.1 The reduced BCS model

Because the Debye energy is much smaller than the Fermi energy in typical metals, the attractive interaction is only present in a narrow energy window around the Fermi energy. Therefore, it seems reasonable to describe the electronic properties of the normal metal within a low-energy model. Assuming that there is only one conduction band crossing the Fermi level, the Hamiltonian describing the system reads,

$$\mathcal{H} = \sum_{\boldsymbol{k},\sigma} c^\dagger_{\boldsymbol{k}\sigma}\xi(k)c_{\boldsymbol{k}\sigma} + \sum_{\boldsymbol{k},\boldsymbol{k'},\boldsymbol{q}} \frac{1}{2}V(\boldsymbol{q})c^\dagger_{\boldsymbol{k}+\boldsymbol{q}\sigma}c^\dagger_{\boldsymbol{k'}-\boldsymbol{q}\sigma'}c_{\boldsymbol{k'}\sigma'}c_{\boldsymbol{k}\sigma}, \tag{1.1}$$

with $V(\boldsymbol{q})$ the net effective interaction resulting from the Coulomb repulsion and phonon-mediated interaction, $\xi(k) = \epsilon(k) - \mu$, $\epsilon(k)$ the band dispersion of the metal, which we assume to be isotropic for simplicity, and $c_{\boldsymbol{k}\sigma}$ the operator annihilating an electron of spin σ and momentum $\hbar\boldsymbol{k}$.

Because of screening effects in metals, both the Coulomb repulsion and phonon-mediated attraction are very short-ranged. Consequently, it seems legitimate to replace momentum dependent interaction $V(\boldsymbol{q})$ by an effective contact interaction $V_{\text{eff}}(\boldsymbol{q}) = g$. Therefore, following Bardeen, Cooper and Schrieffer, we consider the reduced BCS model [42],

$$\mathcal{H} = \sum_{\boldsymbol{k},\sigma} c^\dagger_{\boldsymbol{k}\sigma}\xi(k)c_{\boldsymbol{k}\sigma} + g\sum_{\boldsymbol{k},\boldsymbol{k'},\boldsymbol{q}} c^\dagger_{\boldsymbol{k}+\boldsymbol{q}\uparrow}c^\dagger_{\boldsymbol{k'}-\boldsymbol{q}\downarrow}c_{\boldsymbol{k'}\downarrow}c_{\boldsymbol{k}\uparrow}, \tag{1.2}$$

with g the strength of the effective contact interaction. Note that, since the interaction potential is a Dirac's delta in real space, the interaction term only involves pair of electrons with opposite spin, due to Pauli exclusion principle. If the phonon-mediated interaction dominates the Coulomb repulsion $g < 0$, the interaction is attractive and provides a pairing mechanism.

Based on phase-space argument, one can argue that the relevant scattering processes are the ones involving pairs of electrons in the states $|\boldsymbol{k}\uparrow\rangle$ and $|-\boldsymbol{k}\downarrow\rangle$, possessing a zero total momentum and spin [4, 42]. Other scattering processes can be treated as perturbation [4]. Thus it is legitimate to use the reduced Hamiltonian,

$$\mathcal{H} = \sum_{\boldsymbol{k},\sigma} c^\dagger_{\boldsymbol{k}\sigma}\xi(k)c_{\boldsymbol{k}\sigma} + g\sum_{\boldsymbol{k},\boldsymbol{k'}} c^\dagger_{\boldsymbol{k}\uparrow}c^\dagger_{-\boldsymbol{k}\downarrow}c_{-\boldsymbol{k'}\downarrow}c_{\boldsymbol{k'}\uparrow}. \tag{1.3}$$

In their original paper, J. Bardeen L. N. Cooper and J. R. Schrieffer used a variational method to find the ground-state of this Hamiltonian. Here, we will obtain the same results within a mean-field approach yielding directly the spectrum of excitations of the superconductor known as *Bogoliubov quasiparticle* or simply *bogoliubons*.

1.1.2 Mean-field treatment

In the mean-field version of the BCS theory, it is assumed that the $U(1)$ symmetry of $\mathcal{H}$ is spontaneously broken. Therefore, the pair annihilation operators $b_{\boldsymbol{k}} = c_{-\boldsymbol{k}\downarrow}c_{\boldsymbol{k}\uparrow}$ can have a finite expectation value $\langle b_{\boldsymbol{k}}\rangle$, where $\langle ...\rangle \equiv \text{Tr}[\exp(-\beta\mathcal{H})...]/\,\text{Tr}[\exp(-\beta\mathcal{H})]$ and $\beta = 1/(k_BT)$. $\langle b_{\boldsymbol{k}}\rangle$ may be interpreted as the wavefunction of Cooper pairs in momentum space. Writing $b_{\boldsymbol{k}} = \langle b_{\boldsymbol{k}}\rangle + \delta b_{\boldsymbol{k}}$ and neglecting terms $\propto \delta^2$ the original interacting Hamiltonian $\mathcal{H}$ becomes the quadratic mean-field Hamiltonian $\mathcal{H}_{\text{mf}}$,

$$\mathcal{H}_{\text{mf}} = \sum_{\boldsymbol{k}} c^\dagger_{\boldsymbol{k}\sigma}\xi(k)c_{\boldsymbol{k}\sigma} + \Delta c^\dagger_{\boldsymbol{k}\uparrow}c^\dagger_{-\boldsymbol{k}\downarrow} + \Delta^* c_{-\boldsymbol{k}\downarrow}c_{\boldsymbol{k}\uparrow} - \frac{|\Delta|^2}{g}, \tag{1.4}$$

where $\Delta \equiv g\langle\sum_{\boldsymbol{k}'} b_{\boldsymbol{k}'}\rangle = |\Delta|e^{i\varphi}$ is the superconducting order parameter (also called *gap*) and has to be computed self-consistently. Then introducing the 2-component Nambu-spinor $\Psi(\boldsymbol{k}) \equiv (c_{\boldsymbol{k}\uparrow}, c^\dagger_{\boldsymbol{k}\downarrow})^T$, the Hamiltonian adopts a matrix form,

$$\mathcal{H}_{\rm mf} = \sum_{\boldsymbol{k}} \Psi^\dagger(\boldsymbol{k}) H_{BCS}(\boldsymbol{k}) \Psi(\boldsymbol{k}) + \sum_{\boldsymbol{k}} \xi(k) - \frac{|\Delta|^2}{g}, \tag{1.5}$$

$$\text{with } H_{BCS}(\boldsymbol{k}) = \exp\Big[-i\frac{\varphi}{2}\tau_z\Big](\xi(k)\tau_z + |\Delta|\tau_x)\exp\Big[i\frac{\varphi}{2}\tau_z\Big], \tag{1.6}$$

where τ_i are Pauli matrices acting in particle-hole space. It is easy to show that

$$H_{BCS}(\boldsymbol{k}) = \exp\Big\{i\frac{\varphi}{2}\tau_z\Big\}\exp\Big\{-i\frac{\theta_k}{2}\tau_y\Big\}E(k)\tau_z\exp\Big\{i\frac{\theta_k}{2}\tau_y\Big\}\exp\Big\{-i\frac{\varphi}{2}\tau_z\Big\}, \tag{1.7}$$

where $\theta_{\boldsymbol{k}} = \arccos\frac{\xi(k)}{E(k)}$ and $E(k) = \sqrt{|\Delta|^2 + \xi^2(k)}$. Thus, $\mathcal{H}_{\rm mf}$ can be diagonalized by means of a Bogoli-

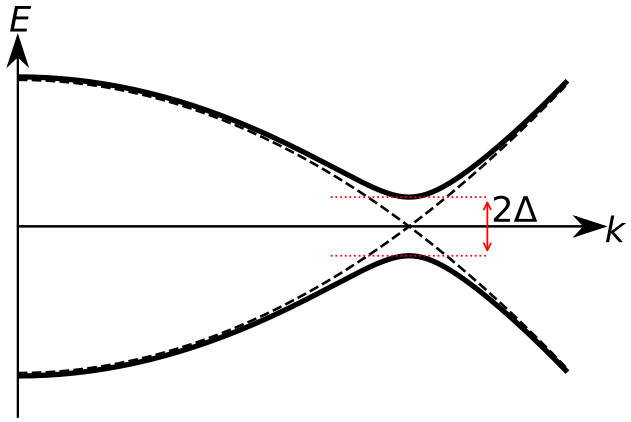

Figure 1.2: Schematic quasiparticle spectrum of $\hat{H}_{BCS}(k)$. The solid lines correspond to the energy of electron-like quasiparticles $E(k)$ and the energy of hole-like quasiparticles $-E(k)$ for $\Delta = 0.2E_F$ with E_F the Fermi energy. The dashed lines represent the electron and hole energies, respectively, $\xi(k)$ and $-\xi(k)$, when $\Delta = 0$. When $\Delta = 0$, the electron and hole bands cross the zero energy at the k_F. When $\Delta \neq 0$ the bands hybridize, opening a gap at k_F.

ubov transformation,

$$\mathcal{H}_{\rm mf} = \sum_{\boldsymbol{k}} E_k(\gamma^\dagger_{\boldsymbol{k}\uparrow}\gamma_{\boldsymbol{k}\uparrow} + \gamma^\dagger_{\boldsymbol{k}\downarrow}\gamma_{\boldsymbol{k}\downarrow}) + \xi(k) - E(\boldsymbol{k}) - \frac{|\Delta|^2}{g}, \tag{1.8}$$

$$a_{\boldsymbol{k}\uparrow} = u_{\boldsymbol{k}}c_{\boldsymbol{k}\uparrow} - v_{\boldsymbol{k}}c^\dagger_{-\boldsymbol{k}\downarrow}, \tag{1.9}$$

$$a_{-\boldsymbol{k}\downarrow} = v_{\boldsymbol{k}}c^\dagger_{\boldsymbol{k}\uparrow} + u_{\boldsymbol{k}}c_{-\boldsymbol{k}\downarrow}, \tag{1.10}$$

with $u(k) = \sqrt{\frac{E(k)+\xi(k)}{2E(k)}}$, and $v(k) = \sqrt{\frac{E(k)-\xi(k)}{2E(k)}}e^{i\phi}$. Since $u^2(k) + v^2(k) = 1$, the operators $a_{\boldsymbol{k}\sigma}$ are fermionic operators satisfying the anticommutation relation, $\{a^\dagger_{\boldsymbol{k}\sigma}, a_{\boldsymbol{k}'\sigma'}\} = \delta_{\boldsymbol{k}\boldsymbol{k}'}\delta\sigma\sigma'$. These operators are

linear superpositions of electron and hole operators, which annihilate a quasiparticle *excitation* named a *bogoliubon* with spin σ, momentum $\hbar\boldsymbol{k}$ and energy $E(k) > 0$. The quasiparticle spectrum is gapped as a result of the hybridization between electrons and holes (see Fig. 1.2). Note that the two quasiparticle energy branches are degenerated due to the time-reversal symmetry of the BCS Hamiltonian. To conclude, within the BCS theory, a superconductor is equivalent to a gas of free fermionic quasiparticles named *bogoliubons*, therefore all electronic properties of a standard BCS superconductor are completely determined by the *bogoliubons* and their energies.

1.1.3 BCS groundstate

With $\mathcal{H}_{\text{mf}}$ written in its diagonal form, given by (1.8), the groundstate $|\psi_{BCS}\rangle$ is readily obtained as the vacuum of *bogoliubons*,

$$\gamma_{\boldsymbol{k}\sigma}\,|\psi_{BCS}\rangle = 0,\ \forall \boldsymbol{k}, \sigma. \tag{1.11}$$

It is convenient to express the BCS grounstate, $|\psi_{BCS}\rangle$ from the vacuum of original fermions $c_{\boldsymbol{k},\sigma}$, denoted $|vac\rangle$ here. After some algebra, one obtains [43, 42],

$$|\psi_{BCS}\rangle = \prod_{\boldsymbol{k}} \left(u_{\boldsymbol{k}} + v_{\boldsymbol{k}} c^{\dagger}_{\boldsymbol{k}\uparrow} c^{\dagger}_{-\boldsymbol{k},\downarrow}\right) |vac\rangle\,. \tag{1.12}$$

The functions $u_{\boldsymbol{k}}$, and $v_{\boldsymbol{k}}$ depends on Δ which is self-consistently defined through, $\Delta \equiv g\langle\sum_{\boldsymbol{k}'} b_{\boldsymbol{k}'}\rangle$. In the $T = 0$ limit, inserting equations (1.9), and (1.10) into the self-consistent we obtain,

$$\Delta = -g \sum_{\boldsymbol{k}} \frac{\Delta}{2E(k)}. \tag{1.13}$$

If $g > 0$ this equation only admits the trivial solution $\Delta = 0$. In that case, there is no superconductivity, and the groundstate corresponds to the Fermi sea, $|FS\rangle$. Indeed, in that case, $u_{\boldsymbol{k}} = \Theta(k - k_F)$ and $v_{\boldsymbol{k}} = e^{i\phi}(1 - \Theta(k - k_F))$, with Θ the Heaviside step-function, hence $|\psi_{BCS}\rangle \propto \prod_{\boldsymbol{k},k<k_f} c^{\dagger}_{\boldsymbol{k}\uparrow} c^{\dagger}_{-\boldsymbol{k},\downarrow} |vac\rangle = |FS\rangle$. Hereinafter we assume $g < 0$. In that case, the self-consistent equation admits a non-trivial solution $\Delta \neq 0$ with minimal energy [42, 41]. In this case, $u_{\boldsymbol{k}}$ is always non-zero, and we can write the groundstate as,

$$|\psi_{BCS}\rangle = \frac{1}{\mathcal{N}} \prod_{\boldsymbol{k}} \exp\left\{\frac{v_{\boldsymbol{k}}}{u_{\boldsymbol{k}}} c^{\dagger}_{\boldsymbol{k}\uparrow} c^{\dagger}_{-\boldsymbol{k}\downarrow}\right\} |vac\rangle\,, \tag{1.14}$$

with $\mathcal{N}$ a normalization factor. Written in this form, it is obvious that the BCS groundstate is a coherent state of Cooper pairs with a well-defined phase. In analogy with the Bose-Einstein condensation, the BCS groundstate is therefore interpreted as a condensate of Cooper pairs where a macroscopic number of Cooper pairs condense in the same state. Note that for non-trivial solutions, the self-consistent equation can be written as:

$$1 = -g \sum_{\boldsymbol{k}} \frac{1}{2\sqrt{|\Delta|^2 + \xi(k)^2}} \tag{1.15}$$

The phase, ϕ of the BCS gap Δ, does not appear in the equation, and an infinite number of solutions exist. Therefore, the groundstate is not unique, and there exist infinitely many degenerate groundstates of $\mathcal{H}_{\text{mf}}$ (see [43, 42] for a detailed discussion of it).

1.1.4 Critical temperature

Let us briefly investigate the role of temperature in the BCS theory. Because the gap Δ is self-consistently determined, it depends on the temperature T. When T increases, Δ decreases to zero. The critical temperature corresponding to the transition from the superconducting to the normal metallic state, T_c, is thus defined as $\Delta(T_c) = 0$. Again, inserting equations (1.9), and (1.10) into the self-consistent definition, $\Delta \equiv g\langle\sum_{\boldsymbol{k}'} b_{\boldsymbol{k}'}\rangle$, the gap equation at finite T, reads:

$$\Delta = -g\sum_{\boldsymbol{k}} \frac{\Delta}{2E(k)} \tanh\frac{\beta E(k)}{2} \;\Rightarrow\; 1 = -g\sum_{\boldsymbol{k}} \frac{1}{2E(k)} \tanh\frac{\beta E(k)}{2}, \tag{1.16}$$

where $\beta = 1/(k_B T)$. In principle, (1.16) has to be solved self-consistently by a numerical approach to obtain the exact $|\Delta|(T)$. When $T \to T_c^-$ it is legitimate to assume that $|\Delta| \to 0$ and make a Taylor expansion of (1.16) with respect to $|\Delta|$ to obtain:

$$1 \simeq -g\int_{-\infty}^{\infty} \mathrm{d}\xi \frac{\nu(\xi)}{2\xi} \tanh\frac{\xi}{2k_B T_c}, \tag{1.17}$$

with $\nu(\xi)$ the normal-state density of states. The integral in the right member is diverging, and we need to introduce a cut-off energy to regularize it. In other words, we shall remember that the attractive interaction is only present in a narrow energy window around the Fermi energy. Recalling that the attractive interaction is phonon-mediated, the Debye energy $\hbar\omega_D$ is a natural energy cut-off for the interaction. It is assumed that $\hbar\omega_D$ is much smaller than the typical electronic energy scale, *i.e.* the Fermi energy E_F. Hence, it seems legitimate to employ the wide-band approximation, $\nu(\xi) \simeq \nu(0) \equiv \nu_0$. Within these approximations, the gap equation can be solved analytically,

$$1 \simeq -g\nu_0 \int_0^{\hbar\omega_D} \mathrm{d}\xi \frac{1}{\xi} \tanh\frac{\xi}{2k_B T_c} = -g\nu_0 \int_0^{\frac{\hbar\omega_D}{k_B T_C}} \mathrm{d}x \frac{1}{x} \tanh\frac{x}{2} \simeq -g\nu_0 \ln\frac{\hbar\omega_D 1.13}{k_B T_c}. \tag{1.18}$$

Inverting the last equality, one obtains the critical temperature T_c,

$$T_c = \frac{1.13\hbar\omega_D}{k_B} \exp\left(\frac{1}{g\nu_0}\right). \tag{1.19}$$

Note that the critical temperature is cut-off dependent.

The superconducting gap in the zero-temperature limit, $|\Delta|(T = 0) \equiv \Delta_0$ can be computed within the same approximations. Using the self-consistent relation at $T = 0$, one obtains,

$$-\frac{1}{g\nu_0} = \int_0^{\hbar\omega_D} \mathrm{d}\epsilon \frac{1}{\sqrt{\Delta_0^2 + \epsilon^2}} = \sinh^{-1}\frac{\hbar\omega_D}{\Delta_0}. \tag{1.20}$$

Assuming $0 < -g\nu_0 \ll 1$ which corresponds to the weak-coupling limit, the previous equation reads:

$$\Delta_0 = \hbar\omega_D \exp\left(\frac{1}{g\nu_0}\right). \tag{1.21}$$

Therefore, the ratio $\frac{\Delta_0}{k_B T_c}$ is universal for the weak-coupling superconductors and satisfies,

$$\frac{\Delta_0}{k_B T_c} = 1.764. \tag{1.22}$$

This is a signature of the weak-coupling approximation where physical quantities can be expressed independently of the cut-off energy once T_c is known.

1.1.5 Limits of the standard BCS theory

The standard BCS theory successfully describes the low-T_c superconductors known before the mid-seventies. In these superconductors, Cooper pairs are s-wave spin-singlet. This type of Cooper pair is named *conventional*. But one can imagine different kinds of pairs, named *unconventional* pairs, which are beyond the scope of the standard BCS theory.

Let us restrict our attention to Cooper pairs with zero center of mass momentum, which are pairs of degenerated electrons with opposite momentum $\hbar\boldsymbol{k}$ and $-\hbar\boldsymbol{k}$ and spin σ, and σ'. In absence of spin-orbit coupling, their wavefunction in real space, $\boldsymbol{\psi}(\boldsymbol{r}, \sigma; \boldsymbol{r'}, \sigma')$ can thus be decomposed as, $\boldsymbol{\psi}(\boldsymbol{r}, \sigma; \boldsymbol{r'}, \sigma') = f(\boldsymbol{r} - \boldsymbol{r'})\chi(\sigma, \sigma')$. As electrons are fermions, the wavefunction has to satisfy, $\boldsymbol{\psi}(\boldsymbol{r}, \sigma; \boldsymbol{r'}, \sigma') = -\boldsymbol{\psi}(\boldsymbol{r'}, \sigma'; \boldsymbol{r}, \sigma)$. Assuming full rotation invariance of the metal, $f(\boldsymbol{r} - \boldsymbol{r'})$ can be decomposed into a radial and angular part belonging to the spherical harmonics, the irreducible representations of the group of orbital rotations, characterized by their angular momentum $L = 0, 1, 2, ...$ The behavior of $\boldsymbol{\psi}$ under the exchange of spatial coordinates of the electrons is consequently dictated by the parity of L. To build a Cooper pair wavefunction, one combines a spherical harmonic with one of the four basis states of two spin-$1/2$ systems: the antisymmetric singlet state with total spin $S = 0$ and the 3 symmetric triplet states with $S = 1$, such that the total wavefunction is antisymmetric under exchange of fermions coordinates. Therefore it is theoretically possible to form Cooper pairs with odd (respectively even) angular momentum L in a spin-triplet state (respectively spin-singlet). Superconducting states made of Cooper pairs with $L \neq 0$ are thus named *unconventional* superconductors. For crystalline materials, the previous statement remains valid if we replace the spherical harmonics with the irreducible representations of the appropriate point symmetry group.

The discovery of superfluid ^{3}He in 1976, where Cooper pairs have a $L = 1$ angular momentum, showed that *unconventional* superconductors are not only theoretical speculations but do exist in nature. With this discovery, the field of *unconventional* superconductivity boomed, shedding new light on superconductivity. Because the *conventional* phonon-mediated attraction proposed in the standard BCS theory is short-range, the attractive interaction is felt by electrons only if they have a finite probability of being found at the same spot. Consequently, it inevitably leads to the formation of *conventional* s-wave Cooper pairs. Hence, *unconventional* superconductors are due to microscopic pairing mechanisms different from the *conventional* phonon-mediated interaction. Numerous alternative mechanisms were studied, including spin-fluctuation mediated interactions or long-range Coulomb repulsion, to list a few. The microscopic origin of the pairing mechanism and its consequence on the symmetry of the order parameter is beyond the scope of this thesis, and the interested reader is invited to read the excellent review by Sigrist [44] for a pedagogical introduction.

As a last remark, we stress that both the BdG and standard BCS theories are mean-field approximations and therefore fail to describe strongly-correlated materials such as the high-T_c cuprates. More advanced theoretical tools, such as the famous Dynamical Mean-Field Theory, are required to correctly and quantitatively understand the complex phase diagram of these materials.

The present manuscript is focused on the electronic properties of hybrid heterostructures made of magnetic or spin-active regions in contact with *conventional* superconductors, conveniently described by mean-field approximation. Consequently, the BdG formalism, detailed below, conveniently describes the electronic properties of the systems studied throughout this manuscript, and it will be employed everywhere in what follows. Additionally, hereinafter, it is always assumed that the superconductor is sufficiently robust to be unaffected by the other parts of the system and acts as a macroscopic reservoir of Cooper pairs. Therefore, the microscopic origin of the superconductivity in the bulk superconductor is beyond the scope of the discussion.

At the interface between the superconducting and magnetic materials, superconductivity is induced by proximity effects. In principle, the induced superconducting gap at the interface should be self-consistently determined and requires the microscopic description of the coupling between the bulk superconductor and the interface. However, this induced superconducting gap can be experimentally measured. Thus, hereinafter, we will consider the induced gap as an adjustable input parameter of the model rather than a self-consistently determined parameter.

1.2 Generalized mean-field theory of superconductors

1.2.1 Bogoliubov-de-Gennes (BdG) formalism

For the sake of simplicity, we consider a uniform electronic system and assume that the electrons have a single internal degree of freedom, their spin[1]. Since we want to construct a generic mean-field theory, we do not specify any particular pairing mechanism nor symmetry of the metal. Thus, our starting point is the generic Hamiltonian, including an attractive electron-electron interaction,

$$\mathcal{H} = \sum_{\boldsymbol{k},\sigma} c^\dagger_{\boldsymbol{k}\sigma} \mathrm{h}^0_{\sigma,\sigma'}(\boldsymbol{k}) c_{\boldsymbol{k}\sigma'} + \frac{1}{2} \sum_{\substack{\boldsymbol{k},\boldsymbol{k'},\boldsymbol{q} \\ \sigma_1,\sigma_2,\sigma_3,\sigma_4}} V_{\sigma_1,\sigma_2,\sigma_3,\sigma_4}(\boldsymbol{k},\boldsymbol{k'}) c^\dagger_{\boldsymbol{k}\sigma_1} c^\dagger_{-\boldsymbol{k}+\boldsymbol{q}\sigma_2} c_{-\boldsymbol{k'}+\boldsymbol{q}\sigma_3} c_{\boldsymbol{k'}\sigma_4}. \tag{1.23}$$

Next, assuming that the dominant superconducting instability corresponds to Cooper pairs with zero center of mass momentum, the most relevant scattering processes are the ones connecting such pairs. Neglecting other scattering processes, the Hamiltonian can be further simplified:

$$\mathcal{H} = \sum_{\boldsymbol{k},\sigma} c^\dagger_{\boldsymbol{k}\sigma} \mathrm{h}^0_{\sigma,\sigma'}(\boldsymbol{k}) c_{\boldsymbol{k}\sigma'} + \frac{1}{2} \sum_{\substack{\boldsymbol{k},\boldsymbol{k'} \\ \sigma_1,\sigma_2,\sigma_3,\sigma_4}} V_{\sigma_1,\sigma_2,\sigma_3,\sigma_4}(\boldsymbol{k},\boldsymbol{k'}) c^\dagger_{\boldsymbol{k}\sigma_1} c^\dagger_{-\boldsymbol{k}\sigma_2} c_{-\boldsymbol{k'}\sigma_3} c_{\boldsymbol{k'}\sigma_4}. \tag{1.24}$$

Then using a mean-field approximation, the interaction can be decoupled in the Cooper channel to obtain a quadratic Hamiltonian. Concretely, one introduce the pair annihilation operators, $b_{\boldsymbol{k},\sigma,\sigma'} = c_{-\boldsymbol{k},\sigma} c_{\boldsymbol{k},\sigma'}$ and decompose them as $b_{\boldsymbol{k},\sigma,\sigma'} = \langle b_{\boldsymbol{k},\sigma,\sigma'} \rangle + \delta b_{\boldsymbol{k},\sigma,\sigma'}$. Inserting this definition in the Hamiltonian and neglecting all terms $\propto \delta^2$, we obtain the quadratic Hamiltonian,

$$\mathcal{H}_{mf} = \sum_{\substack{\boldsymbol{k} \\ \sigma,\sigma'}} c^\dagger_{\boldsymbol{k}\sigma} \mathrm{h}^0_{\sigma,\sigma'}(\boldsymbol{k}) c_{\boldsymbol{k}\sigma'} + \frac{1}{2} \sum_{\substack{\boldsymbol{k} \\ \sigma,\sigma'}} \tilde{\Delta}_{\sigma,\sigma'}(\boldsymbol{k}) c^\dagger_{\boldsymbol{k}\sigma} c^\dagger_{-\boldsymbol{k}\sigma'} + \left[\tilde{\Delta}_{\sigma,\sigma'}(\boldsymbol{k})\right]^* c_{-\boldsymbol{k}\sigma'} c_{\boldsymbol{k}\sigma} + K, \tag{1.25}$$

[1] including additional internal degrees of freedom such as orbital or band indices is straightforward and does not introduce conceptual difficulties

where K is a constant. The gap functions $\tilde{\Delta}_{\boldsymbol{k}}^{\sigma,\sigma'}$ are self-consistently defined,

$$\tilde{\Delta}_{\boldsymbol{k}}^{\sigma,\sigma'} \equiv \sum_{\substack{\boldsymbol{k'} \\ \sigma_1,\sigma_2}} V_{\sigma,\sigma',\sigma_1,\sigma_4}(\boldsymbol{k},\boldsymbol{k'})\langle c_{\sigma_1-\boldsymbol{k'}} c_{\sigma_2\boldsymbol{k'}}\rangle, \tag{1.26}$$

and $\langle ... \rangle$ denotes the thermal average with respect to $\mathcal{H}_{\rm mf}$. Since we are not interested in the ground-state energy of the superconductor, the constant K can be ignored, and we neglect it hereinafter.

$\mathcal{H}_{\rm mf}$ contains non-diagonal terms coupling the two spin sectors. Hence, to write it in a matrix form, it is necessary to use a mathematical trick and describes electron and hole operators redundantly. Namely, we define the four component Nambu-spinor $\psi_{\boldsymbol{k}} = [c_{\boldsymbol{k}\uparrow}, c_{\boldsymbol{k}\downarrow}, c^\dagger_{-\boldsymbol{k},\downarrow}, -c^\dagger_{-\boldsymbol{k}\uparrow}]^T$, which allow us to write:

$$\mathcal{H}_{\rm mf} = \frac{1}{2}\sum_{\boldsymbol{k}} \psi^\dagger_{\boldsymbol{k}} \begin{bmatrix} \hat{\rm h}^0(\boldsymbol{k}) & \hat{\Delta}(\boldsymbol{k}) \\ \hat{\Delta}^\dagger(\boldsymbol{k}) & -\sigma_y \left[\hat{\rm h}^0(-\boldsymbol{k})\right]^* \sigma_y \end{bmatrix} \psi_{\boldsymbol{k}} = \frac{1}{2}\sum_{\boldsymbol{k}} \psi^\dagger_{\boldsymbol{k}} \hat{H}(\boldsymbol{k}) \psi_{\boldsymbol{k}}, \tag{1.27}$$

where σ_i are Pauli matrices acting in spin space, and $\hat{\Delta}_{\boldsymbol{k}}$ is a matrix in spin space defined as $\hat{\Delta}(\boldsymbol{k}) = -i\tilde{\Delta}(\boldsymbol{k})\sigma_y$.

A straightforward diagonalization of the Bogoliubov-de-Gennes Hamiltonian, $\hat{H}(\boldsymbol{k})$, thus gives access to the single-particle excitation energy of the superconductor and the corresponding quasiparticle. Therefore from a mean-field perspective, a superconductor is equivalent to a gas of free particles, and the BdG Hamiltonian $\hat{H}$ might be interpreted as a single-particle Hamiltonian.

However, because of the redundant description of electron and hole degrees of freedom, some special care is needed to avoid double counting when interpreting the eigenstates and eigenvalues of $\hat{H}(\boldsymbol{k})$ in terms of quasiparticle operators. This delicate point is the topic of the next subsection.

1.2.2 Constrained particle-hole symmetry of BdG Hamiltonians

The inherent redundancy of the BdG formalism, imposes the BdG Hamiltonian $\hat{H}_{\boldsymbol{k}}$ to fulfill a particular relationship named *particle-hole* (PH) *constraint*, for reasons which will become clear in the next section of this manuscript. To show it, we first remark the Nambu spinors $\psi_{\boldsymbol{k}}$ and $\psi_{-\boldsymbol{k}}$ are not independent and obey the relationship,

$$\sigma_y\tau_y\psi_{\boldsymbol{k}} = (\psi^\dagger_{-\boldsymbol{k}})^T, \tag{1.28}$$

highlighting the redundancy of the formalism. This relationship imposes a constraint on the BdG Hamiltonian:

$$\begin{aligned}
\mathcal{H}_{\rm mf} &= \frac{1}{2}\sum_{\boldsymbol{k}} \psi^\dagger_{\boldsymbol{k}} \hat{H}(\boldsymbol{k}) \psi_{\boldsymbol{k}}, \\
&= \frac{1}{2}\sum_{\boldsymbol{k}} (\sigma_y\tau_y\psi_{-\boldsymbol{k}})^T \hat{H}(\boldsymbol{k}) (\psi^\dagger_{-\boldsymbol{k}}\sigma_y\tau_y)^T, \\
&= \frac{1}{2}\sum_{\boldsymbol{k}} \psi^T_{-\boldsymbol{k}}\sigma_y\tau_y \hat{H}(\boldsymbol{k})\tau_y\sigma_y (\psi^\dagger_{-\boldsymbol{k}})^T, \\
&= -\frac{1}{2}\sum_{\boldsymbol{k}} \psi^\dagger_{-\boldsymbol{k}} \left[\sigma_y\tau_y \hat{H}(\boldsymbol{k})\tau_y\sigma_y\right]^T \psi_{-\boldsymbol{k}} + \frac{1}{2}\sum_{\boldsymbol{k}} tr\hat{H}(\boldsymbol{k}), \\
&= -\frac{1}{2}\sum_{\boldsymbol{k}} \psi^\dagger_{-\boldsymbol{k}}\sigma_y\tau_y \left[\hat{H}(\boldsymbol{k})\right]^* \tau_y\sigma_y\psi_{-\boldsymbol{k}},
\end{aligned} \tag{1.29}$$

where we used $\sigma_y\tau_y = \tau_y\sigma_y = (\sigma_y\tau_y)^T$, $\hat{H}(\boldsymbol{k}) = \hat{H}^\dagger(\boldsymbol{k})$ and the fermionic anticommutation rules. Consequently, the BdG Hamiltonian satisfies the following relationship,

$$C^{-1}\hat{H}(\boldsymbol{k})C = -\hat{H}(-\boldsymbol{k}), \tag{1.30}$$

where $C = \tau_y \otimes \sigma_y\mathcal{K}$, with $\mathcal{K}$ the complex conjugation operator. Since C is an anti-unitary operator that anti-commutes with the BdG Hamiltonian, it corresponds to a PH symmetry defined in the next section(1.43). It is important to notice that (1.30) is a *built-in* constraint of the BdG formalism and does not require any physical symmetries of the system. Consequently, it will be named a *constraint* to contrast with the notion of conventional *symmetries*, which are not imposed by formalism.

The *particle-hole constraint* has important consequences on the spectrum of the BdG Hamiltonian $\hat{H}(\boldsymbol{k})$. Indeed, if an $|\phi_{\boldsymbol{k}}\rangle$ is an eigenstate of $\hat{H}(\boldsymbol{k})$ with energy $E_{\boldsymbol{k}}$, $|\bar{\phi}_{\boldsymbol{k}}\rangle = C\,|\phi_{\boldsymbol{k}}\rangle$ is an eigenstate of $\hat{H}(-\boldsymbol{k})$ with energy $-E_{\boldsymbol{k}}$. Hence, the energies and eigenvectors of $\hat{H}(\boldsymbol{k})$ and $\hat{H}(-\boldsymbol{k})$ are not independent. It directly follows that $\hat{H}(\boldsymbol{k})$ can be written as:

$$\hat{H}_{\boldsymbol{k}} = U_{\boldsymbol{k}}\mathrm{diag}\left[E_+(\boldsymbol{k}), E_-(\boldsymbol{k}), -E_-(-\boldsymbol{k}), -E_+(-\boldsymbol{k})\right]U_{\boldsymbol{k}}^\dagger, \tag{1.31}$$

$$\text{with, } U_{\boldsymbol{k}} = \begin{bmatrix} u_{\boldsymbol{k}\uparrow+} & u_{\boldsymbol{k}\downarrow+} & v_{\boldsymbol{k}\downarrow+} & -v_{\boldsymbol{k}\uparrow+} \\ u_{\boldsymbol{k}\uparrow-} & u_{\boldsymbol{k}\downarrow-} & v_{\boldsymbol{k}\downarrow-} & -v_{\boldsymbol{k}\uparrow-} \\ v^*_{-\boldsymbol{k}\uparrow-} & v^*_{-\boldsymbol{k}\downarrow-} & u^*_{-\boldsymbol{k}\downarrow-} & -u^*_{-\boldsymbol{k}\uparrow-} \\ v^*_{-\boldsymbol{k}\uparrow+} & v^*_{-\boldsymbol{k}\downarrow+} & u^*_{-\boldsymbol{k}\downarrow+} & -u^*_{-\boldsymbol{k}\uparrow+} \end{bmatrix}. \tag{1.32}$$

Introducing the set of fermionic operators,

$$\begin{bmatrix} a_{\boldsymbol{k}+} & a_{\boldsymbol{k}-} & a^\dagger_{-\boldsymbol{k}-} & a^\dagger_{-\boldsymbol{k}+} \end{bmatrix}^T = U_{\boldsymbol{k}}^\dagger\psi_{\boldsymbol{k}}, \tag{1.33}$$

up to a constant shift, the mean-field Hamiltonian reads,

$$\mathcal{H}_{\mathrm{mf}} = \sum_{\boldsymbol{k}} E_{\boldsymbol{k}+}a^\dagger_{\boldsymbol{k}+}a_{\boldsymbol{k}+} + E_{\boldsymbol{k}-}a^\dagger_{\boldsymbol{k}-}a_{\boldsymbol{k}-}. \tag{1.34}$$

This equation clearly shows that, from a mean-field point of view, superconductors are equivalent to free fermions gases, and their electronic properties are easily accessible. The above equation clearly shows that the many-body Hamiltonian can be diagonalized using only the two energy bands $E_\pm(\boldsymbol{k})$ and their eigenstates $|\phi_{\boldsymbol{k}\pm}\rangle$. Thus, the band-structure of $\hat{H}(\boldsymbol{k})$, named the *quasiparticle spectrum* throughout this manuscript, contains redundant information and is said *doubled*. Indeed a single fermionic degree of freedom described by the operators $a_{\alpha\boldsymbol{k}}$ is associated with a pair of opposite energies in the *qasiparticle spectrum*.

To make it more clear, we introduce a new set of fermionic operators:

$$\tilde{a}_{\boldsymbol{k}\pm} = \begin{cases} a_{\boldsymbol{k}\pm}, & \text{if} E_\pm(\boldsymbol{k}) \geq 0 \\ a^\dagger_{\boldsymbol{k}\pm}, & \text{if} E_\pm(\boldsymbol{k}) < 0 \end{cases}. \tag{1.35}$$

With this definition, $\tilde{a}_{\boldsymbol{k}\pm}$ necessarily has a positive energy $|E_\pm(\boldsymbol{k}|$ and thus corresponds to the annihilation operator of a *quasiparticle excitation*. Hence only the positive energies and eigenstates of the *quasiparticle spectrum* describe *quasiparticle excitations* above the groundstate. The negative energies are simply an artifact due to the redundancy of the BdG formalism.

1.2.3 $U(1)$ spin rotation symmetry and reduced BdG formalism

In the mean-field theory of superconductors, the $U(1)$ spin rotation symmetry along a given axis, chosen as the spin-quantization axis $\boldsymbol{e}_z$, has a particularly important role. When this symmetry is present, the electronic spin projection along $\boldsymbol{e}_z$, $\hat{S}_z$, is conserved and the 4×4 BdG Hamiltonian $\hat{H}(\boldsymbol{k})$ is diagonal in spin space. Therefore, one can take advantage of the block-diagonal form of $\hat{H}(\boldsymbol{k})$ and write the many-body Hamiltonian $\mathcal{H}_{\rm mf}$ as,

$$\mathcal{H}_{mf} = \sum_{\boldsymbol{k}} \Psi^{\dagger}(\boldsymbol{k}) \hat{H}^{\uparrow}(\boldsymbol{k}) \Psi(\boldsymbol{k}), \tag{1.36}$$

with $\Psi(\boldsymbol{k}) = (c_{\uparrow}(\boldsymbol{k}), c^{\dagger}_{\downarrow}(-\boldsymbol{k}))^T$ and $\hat{H}^{\uparrow}(\boldsymbol{k})$ the projection of $\hat{H}(\boldsymbol{k})$ in the $\uparrow$-spin sector. In fact, we already encounter this situation in the standard BCS theory. In such situations, it is thus unnecessary to use the redundant BdG formalism and we find it more convenient to work with the 2-component Nambu spinor $\Psi(\boldsymbol{k})$ and the *reduced* BdG Hamiltonian $\hat{H}^{\uparrow}(\boldsymbol{k})$ which is a 2×2 matrix acting in particle-hole space.

It is important to note that the *reduced* formalism, is not *particle-hole redundant*. Indeed, all Nambu-spinors $\Psi(\boldsymbol{k})$ are independent one from each other and the *reduced* BdG Hamiltonian is not *PH constrained*. As a consequence, the band-structure of $\hat{H}^{\uparrow}(\boldsymbol{k})$ is not a *doubled* spectrum and its eigenstates are in one to one correspondence with *bogoliubons*. Denoting the 2 eigenvalues of $\hat{H}^{\uparrow}(\boldsymbol{k})$, $E_1(\boldsymbol{k})$, and $E_2(\boldsymbol{k})$ and their respective eigenstates $|u_{1\boldsymbol{k}}\rangle$, and $|u_{2\boldsymbol{k}}\rangle$ we can diagonalize $\mathcal{H}_{\rm mf}$,

$$\mathcal{H}_{\rm mf} = \sum_{\boldsymbol{k}} \left[E_1(\boldsymbol{k}) a_1^{\dagger}(\boldsymbol{k}) a_1(\boldsymbol{k}) + E_2(\boldsymbol{k}) a_2^{\dagger}(\boldsymbol{k}) a_2(\boldsymbol{k}) \right], \tag{1.37}$$

where indices $1, 2$ denotes the quasiparticle bands, and we introduced the new set of fermionic operators,

$$a_1(\boldsymbol{k}) = \langle u_{1\boldsymbol{k}} | \, \Psi(\boldsymbol{k}), \tag{1.38}$$

$$a_2(\boldsymbol{k}) = \langle u_{2\boldsymbol{k}} | \, \Psi(\boldsymbol{k}). \tag{1.39}$$

Note that $E_1(\boldsymbol{k})$ and $E_2(\boldsymbol{k})$ are not necessarily positive. Hence, operators $a_1(\boldsymbol{k})$, $a_2(\boldsymbol{k})$ corresponding to negative energies should be physically interpreted as creation (rather than annihilation) operators of *quasiparticle excitations*. Hereinafter, we always use the *reduced* BdG formalism when $U(1)$ spin-rotation symmetry is present. Therefore, we will indifferently denote the 4-component and 2-component Nambu spinors by $\psi(\boldsymbol{k})$. Similarly, the 4×4 *full* BdG Hamiltonian and the 2×2 *reduced* one are both denoted $\hat{H}(\boldsymbol{k})$. This convention avoids cumbersome notations without any confusion since the formalism used is clear from the context.

1.3 Symmetry protected topological superconductors

1.3.1 A brief introduction to topology

During the last decades, considerable progress has been made in understanding the topological phases of quantum matter. Many phases of condensed matter, such as ferromagnetism or superconductivity, can be understood from the Landau-Ginzburg framework of spontaneous symmetry breaking [45]. On the contrary, topological phases can not be distinguished from topologically trivial ones in terms of their symmetries or based on a local order parameter. Instead, nontrivial topological phases are characterized by the existence of robust edge states

at their boundaries. These edge states arise due to a nontrivial quantum mechanical wavefunction topology[2] that can be measured in terms of a quantized topological invariant, which might be observable. Therefore, topological phases are of pure quantum nature.

The most famous example of a topologically nontrivial phase is the Integer Quantum Hall (IQH) state, in which protected chiral edge states give rise to quantized transverse Hall conductance. The IQH state was first discovered experimentally in 1980 when K. von Klitzing *et al.* measured quantized plateaus in the transverse Hall conductance of a two-dimensional electron gas subjected to a strong magnetic field [13]. This discovery earned K. von Klitzing the 1985 Nobel prize in physics. Soon after, it was theoretically understood that the chiral edge states and the quantization of the transverse Hall conductance observed in the IQH state are due to a non-trivial topology of the electronic band characterizing the bulk of the electron gas. This non-trivial topology is characterized by a topological invariant, the Chern number, which is proportional to the Hall conductance [46, 14, 47].

Since the discovery of the IQH state, it has been shown that topological phases of matter appear in electronic insulators and semi-metals, *unconventional* superconductors, and interacting bosonic or fermionic systems. An exhaustive review of the topic is beyond the scope of this thesis, and we restrict our attention to topological phases of non-interacting fermionic matter with a spectral gap, including insulators and gapped superconductors. In this context, the wavefunction topology is defined as follows: two phases are said topologically equivalent if their wavefunctions can be deformed into one another via an adiabatic transformation that preserves the bulk energy gap. Topological phases can thus be categorized into topological classes characterized by a topological invariant. A change in the topological invariant requires a closing of the bulk gap. Hence, topological phase transitions separating two unequivalent topological phase correspond to closings of the bulk gap associated with a change in the topological invariant. The introduction of these new concepts, among others, has been rewarded with the 2016 Nobel Prize in physics awarded to D. J. Thouless, D. Haldane, and J. M. Kosterlitz.

Even if nontrivial topological phases can not be distinguished from trivial ones in terms of their symmetries, symmetries play a central role in the study of topological phases of matter, but in a very different way than in the Landau-Ginzburg framework. Indeed, symmetries may give rise to new topological phases. In the presence of symmetries, the space of possible phases is restricted. Hence, some phases which were connected to the trivial phase in the absence of the symmetries become disconnected from it, as illustrated in Fig. 1.3. In this case, the topological properties of non-trivial phases are protected by the spectral gap and the presence of symmetries. Thus these phases are named *symmetry-protected topological phases* (SPT).

Notice that since topological properties are unaffected by *smooth deformation* that preserves the bulk gap (and the symmetries), a topological phase transition necessarily corresponds to a gap closing. Therefore, if we consider a finite-size topological material, the boundaries of the material are interfaces that connect a trivial topological phase,*i.e.*, the vacuum, to a non-trivial one,*i.e.*, the bulk of the topological material. Since two equivalent phases can not be deformed into one another adiabatically, it directly follows that gapless edge states should exist at the boundaries. This result is known as bulk-edge correspondence. In the case of topological insulators (TIs), these edge states are electronic states. On the contrary, in topological superconductors (TSCs), the edge modes are quasiparticle eigenmodes which are coherent superpositions of electron and hole excitations. Most importantly, as we will show below, because of the *particle-hole constraint* of the BdG formalism, gapless edge modes in topological superconductors contain equal parts of electrons and holes and are, there-

[2]The notion of wavefunction topology will be elucidated below.

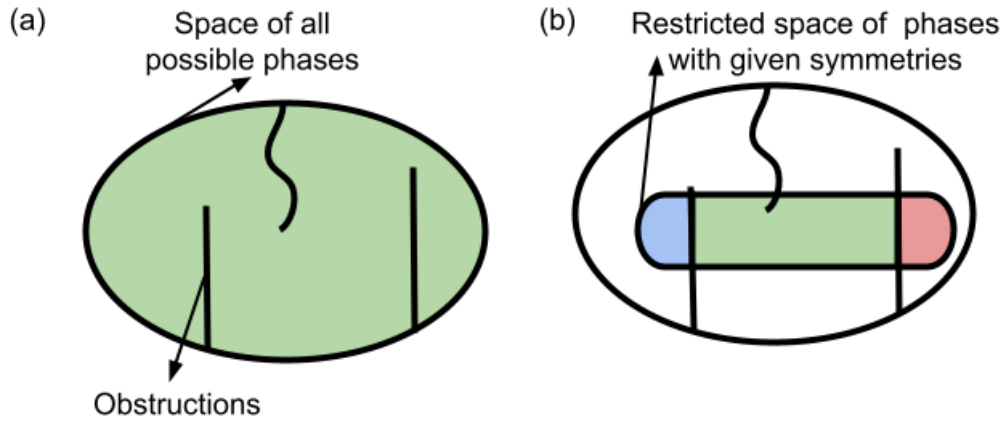

Figure 1.3: Schematic illustration of the notion of symmetry-protected topology. (a) The space of all possible phases is represented by the black ellipse. Black lines denote obstruction in this space to *smooth* mappings. Since all points of the space are connected to the others, all phases are topologically equivalent and trivial. (b) Imposing a given set of symmetries, the space of possible phases is restricted. Some regions of the restricted space become disconnected from the trivial phases (green shaded region), the other giving rise to non-trivial topological classes (red and blue shaded regions).

fore, Majorana particles. These particles could be used as building blocks of topological quantum computers [48], explaining why topological superconductors attracted intensive interest during the last decades.

Below, we will first present the topological classification of topological insulators and superconductors, the famous *ten-fold way*, then we show how topologically protected Majorana modes arise in topological superconductors, and finally, we discuss their exotic properties.

1.3.2 The periodic table of topological superconductors and insulators

In this subsection, we provide a brief introduction to the *ten-fold* topological classification of fully gapped, non-interacting fermionic systems, which includes TIs and fully gapped TSCs. Since we are interested in *symmetry-protected topology*, we should first classify non-interacting systems according to their symmetries. Here, we are interested in topological properties which are protected by non-spatial and global symmetries that are called *fundamental* symmetries. As explained below, there exist three distinct *fundamental* symmetries: the particle-hole (PH), time-reversal (TR), and chiral symmetries.

We recall that symmetries are transformations under which the many-body Hamiltonian describing the system, $\mathcal{H}$ is invariant. According to the Wigner theorem, any symmetry transformation in quantum mechanics can be represented at the many-body level by either a linear and unitary or anti-linear and anti-unitary operator acting on the Hilbert space. Hence, symmetries are generally defined at the many-body level as transformations acting on the many-body Hilbert space [24]. Nevertheless, for non-interacting systems, symmetries can be represented at the single-particle level by a unitary or anti-unitary operator that commutes or anti-commutes with the single-particle Hamiltonian of the system: $\hat{H}$(written in a local basis) [24][3]. Thus, since we only

[3]Notice that $\hat{H}$ designates the BdG Hamiltonian, which acts in Nmabu space for TSCs, or the single-particle, *a.k.a*, first quantized Hamiltonian for TIs, which acts in the single-particle space.

consider non-interacting systems, we directly define symmetries at the *single-particle* level by an operator acting on $\hat{H}$ and a corresponding symmetry condition.

It is important to remark that unitary symmetries that commute with $\hat{H}$ allow us to bring it into a block diagonal form. Hence, we should only discuss the classification of these irreducible blocks, which do not possess any unitary commuting symmetries. We are thus left with three distinct kinds of fundamental symmetries.

First, an anti-unitary operator C that anti-commutes with $\hat{H}$ defines a PH symmetry:

$$C^{-1}\hat{H}C = \hat{H},\ C = U_C\mathcal{K},\ U_C U_C^* = \pm\mathbb{1}, \tag{1.40}$$

Second, an anti-unitary operator T that commutes with $\hat{H}$ defines a TR symmetry :

$$T^{-1}\hat{H}T = \hat{H},\ T = U_T\mathcal{K},\ U_T U_T^* = \pm\mathbb{1}, \tag{1.41}$$

with U_T a unitary matrix and $\mathcal{K}$ the complex conjugation operator.

Third and lastly, the product of the particle-hole and time-reversal symmetry operators: $S = T.C$ defines a unitary operator that commutes with $\hat{H}$, called a chiral symmetry:

$$S^{-1}\hat{H}S = -\hat{H},\ S = U_S,\ U_S^2 = \mathbb{1}, \tag{1.42}$$

where U_S is a unitary matrix. Notice that with the above definitions, the PH and TR symmetries are not uniquely defined, and correspond to *generic* symmetries, which do not necessarily coincide with the *physical* PH and TR symmetries but can also correspond to *effective* symmetries. We will return to this point in Subsection. 5.1.4, where we discuss the topological properties of hybrid semiconducting/superconducting nanowires.

When the system is homogeneous and translation invariant, it is more convenient to use the momentum space representation of $\hat{H}$: $\hat{H}(\boldsymbol{k})$. Since they are non-spatial symmetries, in momentum space, the PH, TR, and chiral fundamental symmetries are defined by [24]:

$$C^{-1}\hat{H}(\boldsymbol{k})C = -\hat{H}(-\boldsymbol{k}),\ C = U_C\mathcal{K},\ U_C U_C^* = \pm\mathbb{1}, \tag{1.43}$$
$$T^{-1}\hat{H}(\boldsymbol{k})T = \hat{H}(-\boldsymbol{k}),\ T = U_T\mathcal{K},\ U_T U_T^* = \pm\mathbb{1}, \tag{1.44}$$
$$S^{-1}\hat{H}(\boldsymbol{k})S = -\hat{H}(\boldsymbol{k}),\ S = U_S,\ U_S^2 = \mathbb{1}. \tag{1.45}$$

Therefore, because of the redundant description of electron and hole degrees of freedom BdG Hamiltonians that describe superconductors are necessarily PH symmetric as explicitly illustrated in Subsection. 1.2.2.

It can be shown that this set of three *fundamental* symmetries is exhaustive. Consequently, without loss of generality, one can assume that there is only a *single* TR symmetry with operator T and a *single* PH symmetry with operator C. A detailed discussion and proof of this statement can be found in the pedagogical review by C. K. Chiu *et al.* [24]. Thus, there are only ten possible different symmetry classes describing how $\hat{H}$ transforms under C, T, and S. First, if we consider T there is three possibilities:

(i) $\hat{H}$ is not TR symmetric, a case which is indicated by "$T = 0$" in Table. 1.1.

(ii) $\hat{H}$ is TR symmetric, and T squares to 1, a case which is indicated by "$T = +$".

(iii) $\hat{H}$ is TR symmetric, and T squares to -1, a case which is indicated by "$T = -$".

Similarly, there is 3 possibility for the behavior of $\hat{H}$ under C, which we write "$C = 0, +, -$". Naively one can think that there are thus 9 symmetry classes describing the behavior of $\hat{H}$ under TR and PH. However, in the absence of both TR and PH symmetries, it is still possible for $\hat{H}$ to be chiral symmetric (denoted by "$S = 1$") or not (denoted by "$S = 0$"). Hence, there exist ten different symmetry classes that are presented in Table. 1.1. This ten-fold symmetry classification of non-interacting systems was first proposed by A. Altland, and M. R. Zirnbauer in 1997 [49] and is nowadays known as the famous *ten-fold way*.

The ten symmetry classes of the ten-fold way are the basic ingredient of the topological classification of TIs and gapped TSCs. Indeed, given the symmetry class and the dimensionality d of a single-particle Hamiltonian $\hat{H}$, it is possible to predict whether non-trivial SPT phases exist or not and when they exist, the nature of their topological invariants (see [50, 51, 52, 53, 24] for detailed proof).

	Symmetries			Dimension		
Class	T	C	S	1	2	3
A	0	0	0	0	$\mathbb{Z}$	0
AIII	0	0	1	$\mathbb{Z}$	0	$\mathbb{Z}$
AI	+	0	0	0	0	0
BDI	+	+	1	$\mathbb{Z}$	0	0
D	0	+	0	$\mathbb{Z}_2$	$\mathbb{Z}$	0
DIII	-	+	1	$\mathbb{Z}_2$	$\mathbb{Z}_2$	$\mathbb{Z}$
AII	-	0	0	0	$\mathbb{Z}_2$	$\mathbb{Z}_2$
CII	-	-	1	$2\mathbb{Z}$	0	$\mathbb{Z}_2$
C	0	-	1	0	$2\mathbb{Z}$	0
CI	+	-	1	0	0	$2\mathbb{Z}$

Table 1.1: The *periodic table* of topological insulators/superconductors. The left-most column indicates the ten symmetry class of the *ten-fold way*. Each class corresponds to the absence or presence of TR (T), PH (C), and chiral (S) symmetries of different types, as indicated by the entries $0, \pm 1$ in the three columns "Symmetries". For a given symmetry class and a given dimensionality of the system, d, the entries "0", "$\mathbb{Z}$", "$2\mathbb{Z}$", and "$\mathbb{Z}_2$" respectively denotes the absence/presence of non-trivial SPT phases and when they exist the nature of their topological invariant. Adapted from [24].

This classification is presented in Table. 1.1. Cases, where non-trivial SPT phases do not exist are indicated by "0" in Table. 1.1. When non-trivial SPT phases exist, the group of the topological invariant that classifies them: $\mathbb{Z}$, $2\mathbb{Z}$, or $\mathbb{Z}_2$ is indicated. However, the table does not explicitly indicate how the topological invariant has to be computed.

Since its discovery, the above-mentioned topological classification has been enriched with *spatial* and *crystalline symmetries*. To contrast with the *strong* SPT presented here, SPT protected by *spatial* symmetries are named *weak* SPT. Moreover, it is also possible to construct a classification for gapped SPT, which is presented in [24].

As a last remark, we stress that the topological classification Table. 1.1 and the corresponding topological invariants are formulated in terms of bulk topological. In finite-size systems, the non-trivial topology of the bulk in dimension d is manifested by the existence of gapless edge modes in dimension $d - 1$, which are topologically protected: they are stable against perturbations preserving the bulk gap and the symmetries. The close

connection between bulk topology and gapless surface states is known as the bulk-edge correspondence. Recently, *Higher-order topological insulators* (HOTIs) and *Higher-order topological superconductors* (HOTSCs) were discovered, where gapless modes live in $d-n$ dimension rather than $d-1$. A detailed study of all possible gapless states arising at the boundaries (or topological defects) of TIs and TSCs according to their symmetry class can be found in [24]. As already stated, for TSCs, the *particle-hole constraint* imposes that the topologically protected gapless modes are coherent superpositions of electrons and holes with equal weight, hence corresponding to Majorana quasiparticles, as discussed below.

1.3.3 The Majorana fermion

The Majorana particle was originally introduced in 1937 by Ettore Majorana in the context of high-energy physics [54]. In its seminal article, Majorana showed that there exist solutions to the Dirac equation, which describes relativistic fermions of spin-$1/2$, which are invariant under charge conjugation. Such solutions, therefore, have a neutral charge and correspond to particles being their own antiparticles. These particles was named after their discoverer Majorana fermions. The Majorana operator γ annihilating a Majorana particle is a self-conjugated operator, which satisfies the following relationships:

$$\{\gamma, \gamma^\dagger\} = 1,\ \gamma = \gamma^\dagger,\ \gamma^2 = (\gamma^\dagger)^2 = 1/2. \tag{1.46}$$

It follows that creating two identical Majorana fermions is allowed but has no effect. Therefore, Majorana fermions are exotic particles that are neither fermions nor bosons but non-Abelian anyons, which can exhibit non-Abelian exchange statistics [15, 55]. To avoid any confusion with Dirac fermions, we try to avoid the name Majorana fermions in this manuscript and instead use the term Majorana particles or simply Majoranas. In addition, we will denote Majorana operators γ_i, with i, any relevant label, to distinguish them from the original fermions c_i and bogoliubons a_i.

Using relativistic notations, the Dirac equation reads:

$$(i\hbar\gamma^\mu\partial_\mu - m)\Psi = 0, \tag{1.47}$$

where Ψ is a Dirac bi-spinor field [4], γ^μ are Dirac matrices, m is the mass of the fermion, and summation over repeated indices ($\mu, \nu = 0, 1, 2, 3$, 0 being time) is understood. The Dirac matrices satisfy the Clifford algebra, $\{\gamma^\mu, \gamma^\nu\} = \mathbb{1}\eta^{\mu\nu}$, where $\eta^{\mu\nu} = diag(1, -1, -1, -1)$ is the metric of a flat spacetime in 3+1D. It is insightful to right explicitly the Dirac equation in the chiral representation[5],

$$\begin{bmatrix} -m & i\hbar\partial_t - \vec{\sigma}.\vec{p} \\ i\hbar\partial_t + \vec{\sigma}.\vec{p} & -m \end{bmatrix} \begin{bmatrix} \psi_L \\ \psi_R \end{bmatrix} = 0, \tag{1.48}$$

where Ψ_L, Ψ_R are respectively the two-components left and right Weyl spinors [25, 56]. Using the minimal coupling prescription, one can show that, in the chiral representation, the charge conjugation acts on Ψ as

[4] Here, Ψ represents a single-particle wavefunction and is not an operator acting in a Fock space.

[5] In this representation the gamma matrices adopt a convenient form,

$$\gamma^0 = \begin{bmatrix} 0 & \mathbb{1} \\ \mathbb{1} & 0 \end{bmatrix},\ \gamma^i = \begin{bmatrix} 0 & \sigma_i \\ -\sigma_i & 0 \end{bmatrix},$$

with σ_i the Pauli matrices.

$\Psi \rightarrow \Psi_c = i\gamma^2\Psi^*$ [25, 56]. Therefore, a Majorana wavefunction Ψ_M should satisfy the *pseudo-reality* condition

$$\Psi_M = i\gamma^2\Psi_M. \tag{1.49}$$

One can already remark that a strong connection exists between Majorana particles of high-energy physics and the BdG formalism in condensed matter theory. First, the Dirac equation, (1.48) can be written,

$$i\hbar\partial_t\Psi(\boldsymbol{r},t) = \hat{H}_{Dirac}\Psi(\boldsymbol{r},t),\ \hat{H}_{Dirac} = \begin{bmatrix} -\boldsymbol{\sigma}.\boldsymbol{p} & m \\ m & \boldsymbol{\sigma}.\boldsymbol{p} \end{bmatrix}, \tag{1.50}$$

and the single-particle Dirac Hamiltonian $\hat{H}_{Dirac}$ has the form of a single-particle BdG Hamiltonian, and the mass term is equivalent to a BCS paring potential [57]. Therefore, the equation of motion governing the dynamics of the Nambu spinor,

$$i\hbar\partial_t\psi(\boldsymbol{r},t) = \hat{H}\psi(\boldsymbol{r},t) \tag{1.51}$$

has the same form as the Dirac equation in its operator version. Second, the condition (1.28) is nothing but an operator version of the *pseudo-reality* condition (1.49). Consequently, the Nambu spinor $\psi(\boldsymbol{r},t)$ is nothing but a Majorana quantum field. Nevertheless, we stress that the pseudo-reality condition (1.28) is satisfied by the entire time-dependent field. On the contrary, as we show below, the stationary solutions of (1.51) ϕ_E with well-defined energies E cannot satisfy the pseudo-reality condition (1.49), unless $E = 0$. Thus it raises questions about the observability of the Majorana character of BdG quasiparticles since they are often probed in the energy domain rather than in the time domain.

Stationary Majorana modes can only arise at zero energy. Indeed, because of the particle-hole constraint (1.30) if ϕ_E is a stationary solution of (1.51) with well-defined energy E, the wavefunction $C\phi_E$ is also a stationary solution of (1.51) with energy $-E$, with C the particle-hole operator $C = \tau_y\sigma_y\mathcal{K}$. Hence, if $E > 0$ ϕ_E and $C\phi_E$ belong to different eigenspace of $\hat{H}$ and are therefore orthogonal. It follows that $\phi_E \neq C\phi_E$. Therefore, the stationary operator $a_E = \int \mathrm{d}\boldsymbol{r}\phi_E^\dagger(\boldsymbol{r})\psi(\boldsymbol{r})$ annihilating a quasiparticle of energy E in the mode ϕ_E is not a self-conjugate $a_E \neq a_E^\dagger$ and is not a Majorana operator. On the contrary, if $E = 0$, ϕ_E and $C\phi_E$ are degenerate and not necessarily orthogonal. It follows that it is possible, but not mandatory, that $\phi_E = C\phi_E$. In this case, the wavefunction ϕ_E satisfies the pseudo-reality condition (1.28) and the operator a_E is a self-conjugate operator $a_E = a_E^\dagger$ and describes a stationary Majorana particle with zero-energy. Consequently, stationary Majorana modes can only emerge at zero energy in superconductors.

In fact, any zero-energy quasiparticle a can be viewed as a pair of Majorana eigenmodes, γ_A and γ_B:

$$a = \frac{\gamma_A + i\gamma_B}{\sqrt{2}},\ \text{with,}\ \gamma_A = \frac{a + a^\dagger}{\sqrt{2}},\ \gamma_B = -i\frac{a - a^\dagger}{\sqrt{2}}. \tag{1.52}$$

Therefore a Majorana particle can be intuitively interpreted as half a Dirac fermion. It seems that the previous transformation is only a mathematical trick. However, it has profound physical consequences if the two Majorana eigenmodes are spatially separated. Indeed, in this case, the single fermionic excitation a splits into two spatially-independent Majorana modes that can be addressed and manipulated separately by local probes. Therefore, the fermionic mode a is a nonlocal and chargeless fermionic mode that is immune to local noise. This can be viewed as an example of *fractionalization*: the separation of an elementary excitation into distinct emergent quasiparticles[58].

Notice that Majorana fermions always come by pairs and that the perfect spatial separation of Majorana modes can only be achieved in infinite-size systems. In realistic finite-size systems, Majorana modes separated by a distance L hybridize due to the finite overlap of their wavefunctions and form a fermionic excitation with finite energy. Nevertheless, for exponentially localized Majorana modes, this energy is exponentially small and decreases with the L as e^{-L/ξ_M}, with ξ_M the localization length of the Majorana modes. Thus, when $L \gg \xi_M$ the overlap between Majorana modes is negligible, and one can consider them as perfectly spatially-separated modes.

To avoid any confusion, it is important to clearly specify the meaning of the terms *Majorana zero mode* and *Majorana bound-states*. **In this manuscript, we will name Majorana zero mode (MZM) any spatially isolated 0D Majorana eigenmode and use the term Majorana bound-state (MBS) to designate any zero-energy fermionic modes corresponding to the superposition of two unpaired MZMs.**

If we consider a trivial superconductor, there is no *a priori* reason for MZMs to appear. However, in a 1D topological superconductor of the D (or BDI) class, the bulk-boundary correspondence imposes the existence of perfectly unpaired MZMs localized at each end of the system, provided that the length of the superconductor L is much larger than the localization length of these modes ξ_M.

To show it, let us first consider the non-realistic case of a semi-infinite topological superconductor. Since the vacuum is a trivial topological superconductor, the extremity of the superconductor separates two topologically nonequivalent phases, which cannot be connected without closing the particle-hole gap. Consequently, there must be a zero-energy mode localized at the extremity of the topological superconductor. This end mode is necessarily a zero-energy Majorana mode. Indeed, let us consider a single end mode with energy E and described by the wavefunction ϕ. Because of the particle-hole symmetry of the BdG Hamiltonian, $C^{-1}\hat{H}C = -\hat{H}$, the wavefunction $C\phi$ is an eigenmode of opposite energy, $-E$. However, since we assumed that there is a single end mode, ϕ necessarily satisfies the pseudo-reality condition $C\phi = \phi$, and its energy must vanish: $E = 0$. Thus the zero-energy end mode is described by a self-adjoint Majorana operator $\gamma = \int \mathrm{d}_b dr \phi^\dagger(\boldsymbol{r})\psi(\boldsymbol{r})$ localized at the end of the superconductor.

Since a finite-size superconductor has two ends, there should be two Majorana modes γ_L and γ_R exponentially localized at the left and right end, respectively. These two modes hybridize due to the finite overlap between their wavefunction and form a fermionic excitation with finite energy $\propto e^{-L/\xi_M}$. Thus, when $L \gg \xi_M$, the overlap between the Majorana modes is negligible, and they do correspond to spatially-isolated MZMs. Hence, the superposition of these two MZMs forms a nonlocal zero-energy fermion: $a_0 = (\gamma_L + i\gamma_R)/\sqrt{2}$, which realizes a MBS.

1.3.4 Exotic properties of Majorana bound-states (MBS)

Since a MBS is a zero-energy fermionic degree of freedom, the groundstate of a system hosting a MBS is necessarily twofold degenerate, and the MBS can be used as a qubit, named a *Majorana qubit*. MBSs and MZMs possess exotic properties which make *Majorana qubit* ideal building blocks for future fault-tolerant quantum computers.

The first interesting property of MBSs that we want to discuss here is their non-locality. Indeed, since a MBS is the superposition of two unpaired MZMs, it is necessarily a non-local object. Therefore, its quantum state cannot be affected by any local perturbation that does not close the particle-hole gap. In other words, the quantum information encoded by a MBs or a *Majorana qubit* is immune to local perturbations.

Second, because they are Majorana particles, MZMs are nonabelian anyons, which exhibit nonabelian exchange statistics. In other words, contrary to the case of bosons and fermions, the quantum many-body ground-state obtained after the exchange of two or more Majorana modes depends on the order in which the exchanges are performed. Therefore, the adiabatic exchange or braiding of Majorana modes is a non-abelian operation equivalent to the multiplication of the many-body ground-state by a unitary matrix U acting in the groundstate manifold. Indeed, a system of $2N$ MZMs possesses a groundstate manifold of dimension $2N$. The exchange operations of MZMs are described by braid groups [59]. It is thus possible to implement some quantum gates (but not all) via braiding operations of MZMs [48]. Such quantum gates present the fundamental advantage since they are topologically protected. Indeed, the results of braiding operations do not depend on the precise details of the adiabatic evolution but only on the order in which MZMs are exchanged. Therefore, *Majorana qubit* can be used to realize topological quantum computation. For a more detailed discussion of the braiding properties of nonabelian anyons, see [48].

It was first proposed to realize braiding operations of MZMs by manipulating and braiding half-quantum vortices in 2D topological superconductors [55]. Indeed, half-quantum vortices allowed in some spin-triplet p-wave superconductors exhibit MZMs localized at their cores. Thus, the adiabatic exchange of such vortices is equivalent to the adiabatic exchange of these MZMs [60, 61, 62]. The adiabatic manipulation of the vortices can be realized thanks to a Josephson junction array by tuning fluxes.

However, braiding MZMs in 1D geometry is not possible because of the inevitable collision of the MZMs. Hence, to realize the braiding of MZMs localized at the end of 1D TSC, it is necessary to use a network of 1D wires. The most straightforward way to exchange MZMs in 1D TSC is to use a junction of three wires, named a *trijunction* or *T-junction*[15]. In such a setup, the boundaries between topological and trivial regions, and hence the MZMs, can be moved by locally tuning the gate voltage [15].

In summary, because of their non-locality and non-abelian braiding statistics, MBS are ideal candidates for fault-tolerant topological quantum computation and constitutes the *Holy Grail* of condensed matter physics.

1.4 The Kitaev chain

1.4.1 Model and symmetries

From a pedagogical point of view, it is insightful to concretely illustrate the topological properties of a toy model capturing the qualitative features of 1D TSCs in the BDI/D class, the famous Kitaev chain. This simplified model was originally introduced by A. Kitaev in 2001 in its seminal paper [16]. It consists of a 1D chain of spinless fermions with p-wave pairing, described by the Hamiltonian,

$$\mathcal{H}_K = -\sum_{j=1}^{N} \mu c_j^\dagger c_j + \sum_{j=1}^{N-1} -t(c_{j+1}^\dagger c_j + c_j^\dagger c_{j+1}) + \Delta c_j c_{j+1} + \Delta^* c_{j+1}^\dagger c_j^\dagger, \tag{1.53}$$

where c_j annihilates a fermion at site j, t is the hopping amplitude between neighboring sites and Δ the pairing potential, and N is the number of sites in the chain. Without loss of generality, we assume that $\Delta \in \mathbb{R}$. Because the fermions are spinless, it is mandatory for Δ to be of the p-wave type. $\mathcal{H}_K$ can be written in a BdG from,

$$\mathcal{H}_K = \Psi^\dagger \hat{H}_K \Psi, \tag{1.54}$$

where we defined the Nambu spinor $\Psi = (c_1, c_1^\dagger, ...c_N, c_N^\dagger)^T$ and $\hat{H}^K$ a $2N \times 2N$ matrix acting in particle-hole$\otimes$position space.

Defining the TR, PH, and chiral operators, $T,\ C$, and S,

$$T = \mathcal{K}, \quad C = \tau_x \mathcal{K}, \quad S = \tau_x, \tag{1.55}$$

one can readily check that,

$$T^{-1}\hat{H}_K T = \hat{H}_K, \quad C^{-1}\hat{H}_K C = -\hat{H}_K, \quad S^{-1}\hat{H}_K S = -\hat{H}_K \tag{1.56}$$

Consequently the Kitaev chain belongs to the BDI class of the *ten fold way* and might possess a non-trivial topological phase.

However, the classification does not predict the parameter range where the Kitaev chain actually possesses non-trivial topological properties. Thus, we should construct the topological phase diagram of the chain by computing its topological invariant.

1.4.2 Closed Kitaev chain, topological invariant and phase diagram

First, let us focus on the bulk properties of the model and construct its topological phase diagram. To that end, we study a closed chain and impose the periodic boundary condition, $c_{N+1} = c_1$. Therefore the system enjoys translation invariance, and $\mathcal{H}_K$ is diagonal in momentum-space,

$$\mathcal{H}_K = \sum_{k \in BZ} (-2t \cos k - \mu) c_k^\dagger c_k + i\Delta \sin k\ c_{-k} c_k - i\Delta \sin k\ c_k^\dagger c_{-k}^\dagger, \tag{1.57}$$

where $c_j = \frac{1}{\sqrt{N}} \sum_{k \in BZ} e^{ikj} c_k$, and BZ is the first Brillouin zone, $BZ = \{0, \frac{2\pi}{N}, ..., \frac{2(N-1)\pi}{N}\}$. Introducing the Nambu spinor $\psi_k = (c_k, c_{-k}^\dagger)^T$, $\mathcal{H}_K$ can be written in a BdG form,

$$\mathcal{H}_K = \frac{1}{2} \sum_{k \in BZ} \psi_k^\dagger \hat{H}_K(k) \psi_k - \mu N, \tag{1.58}$$

$$\hat{H}_K(k) = \boldsymbol{h}(k).\boldsymbol{\tau} = \xi(k)\tau_z + \Delta(k)\tau_y, \tag{1.59}$$

where $\xi(k) = -2t \cos k - \mu,\ \Delta(k) = 2\Delta \sin(k)$, $\boldsymbol{\tau} = (\tau_x, \tau_y, \tau_z)^T$ and $\boldsymbol{h}(k) = (0, \Delta(k), \xi(k))^T$. The Kitaev chain can be characterized by two dimensionless parameters, Δ/t, and μ/t. We can construct its phase diagram in the $(\Delta/t, \mu/t)$ plane.

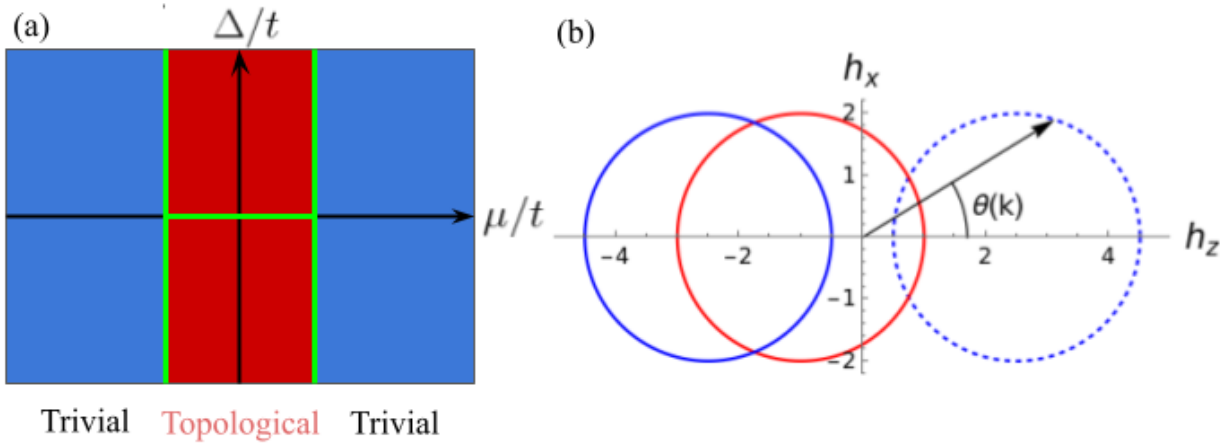

Figure 1.4: Topological properties of the closed Kitaev model. (a) Topological phase diagram. Gapless regions are indicated by the green lines and segments. The topological phase corresponds to the red-shaded area, while trivial regions correspond to the blue-shaded ones. (b) Trajectory of $\boldsymbol{h}(k)$ in the zy-plane when k runs from $-\pi$ to π. The parameters are set to $\Delta = t = 1$, $\mu = 2.5t,\ t,\ -2.5t$ respectively for the blue, red, and blue dashed lines.

According to the *ten-fold way*, the topological properties of the Kitaev chain are characterized by a $\mathbb{Z}$ topological invariant. A brute-force way to obtain the phase diagram would be to compute this topological invariant numerically for every parameter. Here we follow a more educated way. First, we determine the gapless lines of the phase diagram, which might correspond to topological transitions. Second, among the gapless lines, we identify topological phase transitions by computing the change in the topological invariant across each of them.

The quasiparticle spectrum of $\hat{H}_k$ consists of two energy branches $E(k)$ and $-E(k)$, with:

$$E(k) = \sqrt{(-2t\cos(k) - \mu)^2 + |\Delta(k)|^2}. \tag{1.60}$$

The corresponding eigenvectors $\phi_\pm(k)$ are given by, $\phi_+(k) = (u(k), v(k))^T$, and $\phi_-(k) = C\phi_+(-k)$, where,

$$u(k) = \frac{1}{\sqrt{2E(k)}}\sqrt{E(k) + \xi(k)}, \tag{1.61}$$

$$v(k) = \frac{1}{\sqrt{2E(k)}}\frac{\Delta(k)}{|\Delta(k)|}\sqrt{E(k) - \xi(k)}. \tag{1.62}$$

Introducing the fermionic operators $a_k = u_k^* c_k + v_k^* c_k^\dagger$, $\mathcal{H}_K$ is equivalent to a free fermions gas,

$$\mathcal{H}_K = \sum_{k \in BZ} E_k a_k^\dagger a_k \tag{1.63}$$

Note that a_k annihilates a *bogoliubon* of momentum k. Once the expression of $E(k)$ is known, we can identify the region of the phase diagram where $\hat{H}(k)$ is gapless. Let us first study the special case $\Delta = 0$. In this case, the model is a metallic chain of spinless fermions with trivial topology. Its spectrum is gapless when $|\mu| \leq 2t$

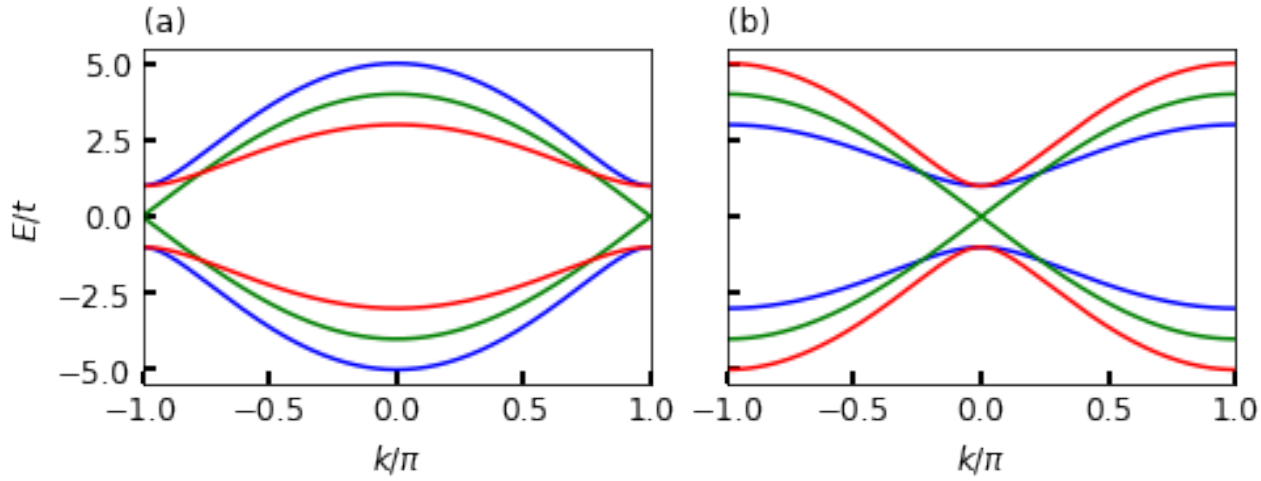

Figure 1.5: Quasiparticle spectrum of the Kitaev model with periodic boundary conditions: energies of $\hat{H}_K(k)$, $\pm E(k)$, in units of t as a function of k for $\Delta = t$. (a): Blue, green and red lines correspond to $\mu/t = -3,\ -2,\ -1$, respectively. (b): Blue, green and red lines correspond to $\mu/t = 1,\ 2,\ 3$, respectively.

and gapped $|\mu| > 2t$. Since the sign of Δ does not change the topological properties of the chain, the gapless segment where $\Delta = 0$, and $|\mu| \leq 2t$, can not corresponds to a topological phase transition (TPT).

We now turn to the more interesting case, $\Delta \neq 0$. In that case, we find two gapless lines. When $\mu = -2t$, $E(k = 0) = 0$, while when $\mu = -2t$, $E(k = \pi) = 0$, as illustrated in Fig. 1.5. These gapless lines and segments are indicated by green lines in Fig. 1.4 (a).

Next, we show that these lines are indeed TPT associated with a change in the topological invariant. To that end, we need to define the topological invariant of the Kitaev model. Topological invariants are generally based on a mapping from the Brillouin Zone ($(\mathbb{S}^1)^d$) to the space of eigenvectors of $\hat{H}(\boldsymbol{k})$. The detailed construction of the different topological invariants is beyond the scope of this manuscript and can be found in [24]. For the Kitaev chain, the topological invariant is based on the mapping from the Brillouin zone to the unit circle $\mathbb{S}^1$ defined by the unit vector $\boldsymbol{n}(k) = \frac{\boldsymbol{h}(k)}{|\boldsymbol{h}(k)|}$ (which entirely determines the eigenvectors),

$$\boldsymbol{n} : \mathbb{S}^1 \to \mathbb{S}^1 \tag{1.64}$$

$$k \to \boldsymbol{n}(k). \tag{1.65}$$

There exist topologically distinct mappings of this kind, classified by the homotopy group $\pi_1(\mathbb{S}^1) = \mathbb{Z}$. Topologically distinct maps are characterized by the topological invariant ν, named the winding number [24]. It is defined as:

$$\nu = \frac{1}{2\pi} \oint_{\mathcal{C}} \mathrm{d}\theta(k) = \frac{1}{2\pi} \int_{BZ} \partial_k \theta(k) \mathrm{d}k. \tag{1.66}$$

Where $\theta(k) = \arg[n_z(k) + i n_y(k)]$ and $\mathcal{C}$ the curve described by the arrow of $\boldsymbol{n}(k)$ when k runs over the whole Brillouin zone. In other words, ν counts the number of times $\boldsymbol{h}(k)$ (or equivalently $\boldsymbol{n}(k)$) encircles the origin when k runs over the entire Brillouin zone, thus $\nu \in \mathbb{Z}$. In Fig. 1.4 (b), the trajectory of $\boldsymbol{h}(k)$ in the yz-plane is plotted, for $\Delta = 1$ and $\mu = -2.5, 1, 2.5$. From this figure, it is obvious that $\nu = 1$ when $\mu < 2t$ and

zero otherwise. Therefore, the red-shaded region of the phase diagram, Fig. 1.4 (a), is topologically non-trivial, while the two other blue-shaded regions are trivial.

To finish, we stress that, like any quantum phase transition, each TPT corresponds to a change in the ground-state $|g\rangle$. Using (1.63), it is obvious that $|g\rangle$ is the vacuum of *bogoliubons*. The $k = 0$ and $k = \pi$ points may be treated carefully. Indeed, $c_{-0} = c_0$ and $c_{-\pi} = c_\pi$, and the pairing potential is ineffective at these points. Thus $a_0 = c_0$ if $\mu < -2t$, $a_0 = c_0^\dagger$ otherwise, and $a_\pi = c_\pi$ if $\mu < 2t$, $a_\pi = -c_\pi^\dagger$ otherwise. Therefore,

$$|g\rangle \propto \Big(\prod_{\pi>k>0} a_k a_{-k}\Big)\left(\begin{cases} 1, & \text{if } \mu < -2t \\ c_0^\dagger, & \text{if } -2t < \mu < 2t \\ c_0^\dagger c_\pi^\dagger, & \text{if } \mu > 2t \end{cases}\right)|0\rangle \tag{1.67}$$

where $|0\rangle$ is the vacuum of original fermions. The fermionic parity $\hat{P} = (-1)^{\sum_j c_j^\dagger c_j}$ is conserved by $\mathcal{H}_K$, therefore, $|g\rangle$ has a well-defined fermionic parity. Notice that the TPTs are associated with a change in ground-state fermionic parity. Indeed straightforward algebra yields,

$$\langle g|\,\hat{P}\,|g\rangle = \begin{cases} -1, \text{ if } |\mu| < 2t \\ +1, \text{ otherwise} \end{cases} . \tag{1.68}$$

This link between fermionic parity and the presence of a non-trivial topological phase is, however, non-universal and depends on the parity of N and the boundary conditions [63].

1.4.3 Majorana zero modes in the open Kitaev chain

According to the bulk-boundary correspondence, Majorana zero modes (MZMs) should be localized at the extremities of an open Kitaev chain in the topological regime. Here, we illustrate the bulk-boundary correspondence by explicitly showing that a non-trivial open Kitaev chain exhibits MZMs localized at its ends. In addition, we will show that the presence of the MZMs.

Imposing open boundary conditions to the Kitaev chain (1.53), we introduce a Majorana representation of $\mathcal{H}_K$. Introducing the new set of $2N$ Majorana operators, γ_j^A, γ_j^B, such that,

$$c_j = \frac{\gamma_j^A + i\gamma_j^B}{\sqrt{2}}, \quad c_j^\dagger = \frac{\gamma_j^A - i\gamma_j^B}{\sqrt{2}}. \tag{1.69}$$

These operators satisfy the anticommutation relation,

$$\{\gamma_j^A, \gamma_{j'}^B\} = 0, \ \{\gamma_j^A, \gamma_{j'}^A\} = \{\gamma_j^B, \gamma_{j'}^B\} = \delta_{j,j'}. \tag{1.70}$$

In this Majorana representation, $\mathcal{H}_K$ becomes,

$$\mathcal{H}_K = i\sum_{j=1}^{N-1}(\Delta - t)\gamma_j^A\gamma_{j+1}^B + (\Delta + t)\gamma_j^B\gamma_{j+1}^A - i\mu\sum_{j=1}^{N}\gamma_j^A\gamma_j^B. \tag{1.71}$$

As already stated, the topological properties can not be changed by smooth local perturbations without closing the gap. Therefore, we can illustrate the topological properties of the non-trivial and trivial phases at two well-chosen points of the phase diagram. We choose the point $\Delta = 0$, $t = 0$ and $\mu \neq 0$ to illustrate the trivial

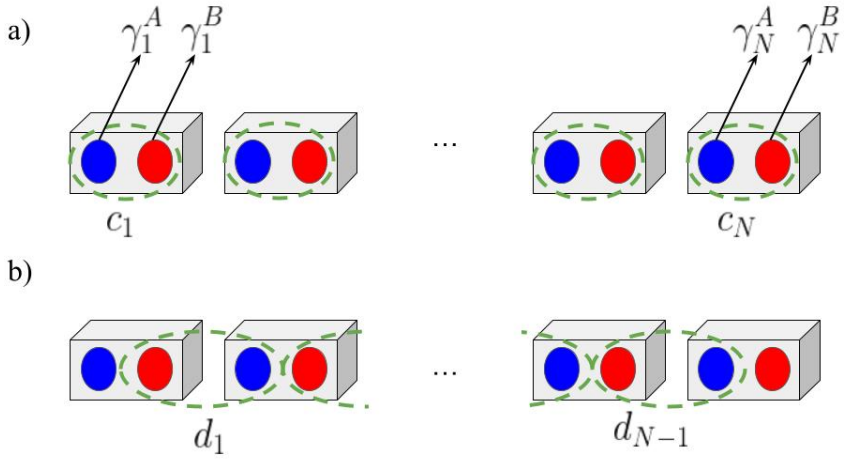

Figure 1.6: Schematic illustration of an open Kitaev chain in the Majorana chain regimes. The grey boxes indicate physical sites, while blue and red dots, respectively, indicate Majorana operators of type A and B. (a): An open Kitaev chain for $\Delta = t = 0$, and $\mu \neq 0$. Majorana operators γ_j^A, γ_j^B, belonging to the same physical site, are paired together as indicated by the green dashed circle. Each on-site pair corresponds to the original Dirac fermion operators c_j.(b): An open Kitaev chain for $\Delta = t \neq 0$, and $\mu = 0$. Majorana operators γ_j^B, γ_{j+1}^A, belonging to adjacent physical sites, are paired together as indicated by the green dashed circle. Each pair corresponds to the gapped Dirac fermion operators d_j. The two Majorana operators at the left and right edges are left unpaired and form a non-local zero-energy Dirac fermion d_0. Figure inspired by [64].

phase and $\Delta = t \neq 0,\ \mu = 0$ to illustrate the topological phase. In each case, the Kitaev chain is conveniently described by a chain of Majorana fermions, and we refer to these cases as the two *Majorana chain* regimes. In the first *Majorana chain* regime, when $\Delta = 0,\ t = 0$ and $\mu \neq 0$, the Hamiltonian is reduced to,

$$\mathcal{H}_K = -i\mu \sum_{j=1}^{N} \gamma_j^A \gamma_j^B. \tag{1.72}$$

As schematized in Fig. 1.6 (a), Majorana operators belonging to the same physical site are paired together, and there are no Majoranas left unpaired. Consequently, all Majoranas are gapped, and there are no zero energy modes, hence no MZMs. $\Delta = t \neq 0,\ \mu = 0$, $\mathcal{H}_K$ becomes,

$$\mathcal{H}_K = 2it \sum_{j=1}^{N-1} \gamma_j^B \gamma_{j+1}^A. \tag{1.73}$$

In contrast to the previous case, Majoranas operators belonging to adjacent physical sites are paired together, as depicted in Fig. 1.6 (b). Thus, introducing the new set of *complex* fermions, $d_j = \frac{\gamma_j^B - i\gamma_{j+1}^A}{\sqrt{2}}$ for $1 \leq j < N$, $\mathcal{H}_K$ reads,

$$\mathcal{H}_K = 2t \sum_{j=1}^{N} \left(d_j^\dagger d_j - \frac{1}{2} \right). \tag{1.74}$$

It is important to remark that the Majorana operators γ_1^A, γ_{N-1}^B are left unpaired. These Majorana operators do not enter the Hamiltonian. Consequently, they are zero-energy modes. In addition, they are perfectly localized at each end of the chain and thus correspond to MZMs localized at the edges of the chain. Since γ_1^A, γ_{N-1}^B are degenerated, we can construct a zero-energy non-local *complex* fermion $d_0 = \frac{\gamma_N^B - i\gamma_1^A}{\sqrt{2}}$. Consequently, the ground-state of the chain in the non-trivial regime is twofold degenerate. The construction of the two ground-states $|g_0\rangle$, $|g_1\rangle$ for any N is not trivial . Here we simply state the results without demonstration; the interested reader can find a rigorous and detailed proof in [64].

$$|g_0\rangle \propto \prod_{j>0} d_j \, |vac\rangle \,, \qquad |g_1\rangle = \begin{cases} d_0^\dagger \, |g_0\rangle \,, & N \text{ is even} \\ d_0 \, |g_0\rangle \,, & N \text{ is odd} \end{cases} \tag{1.75}$$

These two groundstates can be distinguished by their fermionic parity,

$$\langle g_0 | \, \hat{P} \, | g_0 \rangle = (-1)^{N+1}, \qquad \langle g_1 | \, \hat{P} \, | g_1 \rangle = (-1)^{N}. \tag{1.76}$$

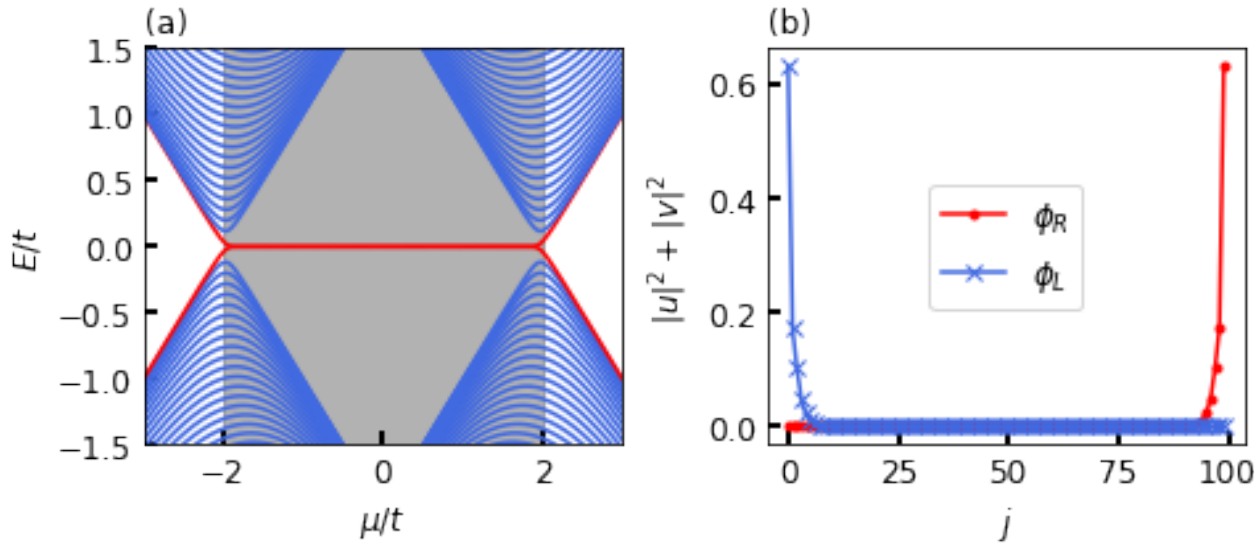

Figure 1.7: Results from numerical diagonalization of a finite size Kitaev chain with $N = 100$ sites and $\Delta/t = 1.3$. (a) Energy spectrum as a function of μ/t. For convenience, we plotted the two lowest energies in red. As it can be observed, the quasiparticle closes and reopens at the two critical points $\mu = \pm 2t$. (b) Square amplitude $|u(j)|^2 + |v(j)|^2$ of the two Majorana wavefunctions ϕ_L and ϕ_R as a function of j for $\Delta/t = 1.3$ and $\mu/t = 1.2$ with $t = 1$.

The pair of MZMs cannot be removed by any local perturbation, which preserves the quasiparticle gap. Therefore, a pair of MZMs should exist in the whole topological phase of the chain. However, away from the analytically soluble point, $\Delta = t$, $\mu = 0$, where the Majorana operators γ_1^A, γ_N^B are exactly zero energy eigenmodes, the eigenstates of the BdG Hamiltonian $\hat{H}_K$ have to be found numerically. In the generic case, the quasiparticle spectrum of $\hat{H}_K$ closes and reopens at the critical points $\mu = \pm 2t$, as observed in Fig. 1.7. In the topological regime, $|\mu| < 2t$, a single pair of eigenstates lies in the middle of the gap at zero energy.

Because of the particle-hole symmetry of $\hat{H}_K$, we can always choose the two zero energy eigenstates $\phi_R,\ \phi_L$ as Majorana eigenmodes satisfying the pseudo-reality condition, $C\phi_{R/L} = \phi_{R/L}$. These two zero-energy Majorana eigenmodes describes two Majorana operators $\gamma_L = \sum_j \phi_A^\dagger(j)\psi(j)$ and $\gamma_R = \sum_j \phi_A^\dagger(j)\psi(j)$. As it can be observed in Fig. 1.7. (b), ϕ_L is localized at the left edge of the nanowire while ϕ_R is localized at the right edge, with the same localization length ξ_M. These two Majorana eigenmodes do not overlap and therefore do correspond to a single pair of MZMs. Their superposition $d_0 = (\gamma_R - i\gamma_L)/\sqrt{2}$ forms a nonlocal zero-energy fermionic bound-state corresponding to a MBS, and the groundstate of the system remains twofold degenerate.

We stress that all the above arguments are only valid when the length of the chain is sufficiently long, $N \gg \xi_M$. Indeed, the Majorana modes decay exponentially towards the bulk $|\phi_L(j)| \propto e^{-n/\xi_M}$, hence their overlap scales as e^{-N/ξ_M}. Because of this overlap, the MZMs hybridize, and the MBS acquire a small energy $E_M \propto e^{-N/\xi_M}$. Consequently, if $N \gg \xi_M$, the energy E_M is negligible, the overlap between the MZMs is negligible, and the non-local fermion d_M is a true MBS. On the contrary, when the size of the chain becomes comparable to ξ_M, the MZMs have a finite overlap, and d_M is no longer a true MBS but a fermionic quasiparticle with finite energy. Notice that, when $\mu = 0$, and $\Delta = t$, $\xi_M = 0$, and the operators γ_L, γ_B and d_M correspond to γ_1^A, γ_N^B and d_0 respectively.

In conclusion, we showed that the non-trivial topology of the bulk of a finite-size Kitaev chain is manifested by the presence of two unpaired MZMs localized at the end of the chain, illustrating the bulk-edge correspondence. The superposition of these MZMs forms a highly nonlocal zero-energy fermionic degree of freedom: a MBS. This fermionic degree of freedom can be used as a *qubit* named *Majorana qubit*, which exhibits highly desirable properties for topological quantum computation (see Subsection.1.3.4).

Chapter 2

Introduction to non-equilibrium Green's function (NEGF)

Throughout this manuscript, we will be interested in the electronic transport through superconducting sub-gap states. More specifically, we want to calculate observables that can be directly measured by means of scanning tunneling microscopy/spectroscopy (STM/STS) techniques. In a typical STM/STS experiment (described in more details in this chapter), the dc voltage bias applied between the tip of the microscope and the sample that is studied maintains the system in an out-of-equilibrium state. Therefore, in order to make a direct connection between our theoretical predictions and experimental data, we should use a theoretical framework that is well-suited for the description of out-of-equilibrium quantum systems.

The non-equilibrium Green's functions (NEGF) technique, a state-of-the-art tool adapted to the description of out-of-equilibrium quantum many-body systems, seems particularly well suited for our purpose. Indeed, this powerful and versatile technique is very well-suited for the study of quantum transport and is nowadays widely used to calculate quantum transport properties in various mesoscopic devices.

The present chapter is dedicated to the introduction of this theoretical tool and is constructed as follows. In the first section, we lay the foundation of the NEGF formalism and introduce its key ingredient, the time contour. In the second section, we focus on the Keldysh contour, a well-suited contour for studying the long-time steady-state regime. We derive the equations obeyed by Green's functions on this contour and the relations relating the different Green's functions. Finally, in the third section, we focus on the theoretical modeling of STS experiments and use the Keldysh technique to compute the electronic current and the differential conductance spectrum.

2.1 The time contour idea

2.1.1 Context

Before entering into the details of the NEGF technique, it is important to define the problem we aim to solve formally. We consider a macroscopic many-body electronic system $\mathcal{S}$ initially in equilibrium in the grand-canonical ensemble at temperature T and chemical potential μ. At the time t_0 an external perturbation $\hat{V}_p(t)$, eventually time-dependent, is applied to the system and drives it out of equilibrium. Our goal is to predict

the results of the measurement of a physical observable $\hat{O}$ at later times, $t > t_0$. For the sake of simplicity, we first assume that the electronic system is not superconducting. We will generalize the NEGF technique to superconducting systems described by BdG Hamiltonians in the last section of this chapter. Without loss of generality, the dynamics of the electronic system in absence of the drive field is described by the many-body Hamiltonian:

$$\mathcal{H} = \mathcal{H}_0 + \mathcal{H}_{int}, \tag{2.1}$$

where $\mathcal{H}_0$ describes free particles and $\mathcal{H}_{int}$ the interactions between them. The NGEF formalism can treat arbitrary initial conditions [65, 27]. Nevertheless, for simplicity, we focus on the case of initial equilibrium in the grand-canonical ensemble at time $t = t_0$. As a consequence, the initial density matrix reads:

$$\hat{\rho} = \frac{e^{-\beta\mathcal{H}_M}}{\mathcal{Z}},\ \mathcal{Z} = \mathrm{Tr}[e^{-\beta\mathcal{H}_M}], \tag{2.2}$$

where $\beta = \frac{1}{k_B T}$, $\mathcal{H}_M = \mathcal{H}_0 + \mathcal{H}_{int} - \mu\hat{N}$, with $\hat{N}$ the particle number operator in the system. For the sake of convenience, the single-particle energies are measured from the chemical potential such that $\mathcal{H}_M = \mathcal{H}$. For time $t > t_0$, the time-evolution of the system is governed by the time-dependent Hamiltonian,

$$\mathcal{H}(t > t_0) = \mathcal{H}_0 + \mathcal{H}_{int} + \hat{V}_p(t) = \mathcal{H}_0 + \hat{V}(t), \tag{2.3}$$

with $\hat{V}(t) = \mathcal{H}_{int} + \hat{V}_p(t)$ the perturbation.

For the present purpose, it is convenient to work with the *Heisenberg picture*. In this picture, the states $|\Psi(t)\rangle$ are time-independent, $|\Psi_H(t)\rangle = |\Psi(t_0)\rangle$, while the operators are time-dependent. The Heisenberg representation $\hat{O}_H(t)$ of an operator $\hat{O}(t)$ is defined by the following equation of motion and the associated initial condition,

$$i\hbar\frac{\mathrm{d}\hat{O}_H(t)}{\mathrm{d}t} = [\mathcal{H}_H(t), \hat{O}_H(t)] + i\hbar\frac{\partial\hat{O}_H(t)}{\partial t},\ \text{with}\ \hat{O}_H(t_0) = \hat{O}(t_0), \tag{2.4}$$

where the subscript H indicates the Heisenberg picture, and the partial derivative notation signifies that only the derivative with respect to the explicit time dependence of $\hat{O}(t)$ must be taken. In this picture, the expectation value at time t of an observable $\hat{O}(t)$ is given by:

$$\langle\hat{O}(t)\rangle = \mathrm{Tr}\Big\{\hat{\rho}\hat{O}_H(t)\Big\}. \tag{2.5}$$

Focusing on single-particle observable, the operator $\hat{O}(t)$ can be written as:

$$\hat{O}(t) = \int \mathrm{d}\boldsymbol{r}\mathrm{d}\boldsymbol{r'}\sum_{\sigma,\sigma'} O_{\sigma,\sigma'}(\boldsymbol{r},\boldsymbol{r'},t)c^\dagger_\sigma(\boldsymbol{r})c_{\sigma'}(\boldsymbol{r'}). \tag{2.6}$$

Hence it is very convenient to introduce the so-called chronological time-ordered Green's function,

$$G^T_{\sigma,\sigma'}(t,\boldsymbol{r};t',\boldsymbol{r'}) = -\frac{i}{\hbar}\,\mathrm{Tr}\Big\{\hat{\rho}\mathcal{T}[c_{\sigma,H}(\boldsymbol{r},t)c^\dagger_{\sigma',H}(\boldsymbol{r'},t')]\Big\} = -i\langle\mathcal{T}[c_\sigma(\boldsymbol{r},t)c^\dagger_{\sigma'}(\boldsymbol{r'},t')]\rangle, \tag{2.7}$$

with $\mathcal{T}$ the chronological time-ordering operator. The action of $\mathcal{T}$ is defined by,

$$\mathcal{T}[\hat{A}(t)\hat{B}(t')] = \begin{cases}\hat{A}(t)\hat{B}(t'),\ t > t' \\ \pm\hat{B}(t')\hat{A}(t), t \le t'\end{cases}, \tag{2.8}$$

where the $+$ and $-$ apply for bosonic and fermionic operators, respectively. Obviously, with $G^T_{\sigma,\sigma'}(t,\boldsymbol{r};t',\boldsymbol{r'})$ in hands, one can compute any single-particle property as $\hbar G^T_{\sigma,\sigma'}(t,\boldsymbol{r};t{+}0^+,\boldsymbol{r'}) = i\langle c^\dagger_{\sigma'}(\boldsymbol{r'},t)c_\sigma(t)\rangle$.

Consequently, our ultimate goal is to compute the time-ordered Green's function. In order to achieve that, it is tempting to follow the strategy of the perturbation technique proposed by Feynman[66] to compute the Green's function in the zero-temperature limit. Namely, we would like to expand $G^T_{\sigma,\sigma'}(t,\boldsymbol{r};t',\boldsymbol{r'})$ in power of the perturbation $\hat{V}_p(t)$. Then we would like to use the famous Wick theorem to decompose the many-particle correlation functions generated into a sum of products of one-particle correlations [67]. This theorem holds if and only if the operators to be averaged evolve with respect to a non-interacting Hamiltonian and the initial density matrix is a non-interacting one-particle density matrix [68]. Hence, if we want to apply the Wick theorem to (2.7), we face two problems, first $\mathcal{H}$ contains interactions, and second, the initial density matrix in (2.7) is a many-body density matrix. The next subsection is devoted to the solution to the first problem.

2.1.2 Time evolution and the round-trip contour

Let us first show how we can solve the first problem with the help of the interaction picture and the idea of a closed-time contour. The idea is to use the *interaction picture* to replace operators evolving with respect to the time-dependent many-body Hamiltonian $\mathcal{H}(t > t_0)$ by operators evolving with respect to the non-interacting and stationary Hamiltonian $\mathcal{H}_0$. Indeed, in the *interaction picture*, the operators evolve in time with respect to

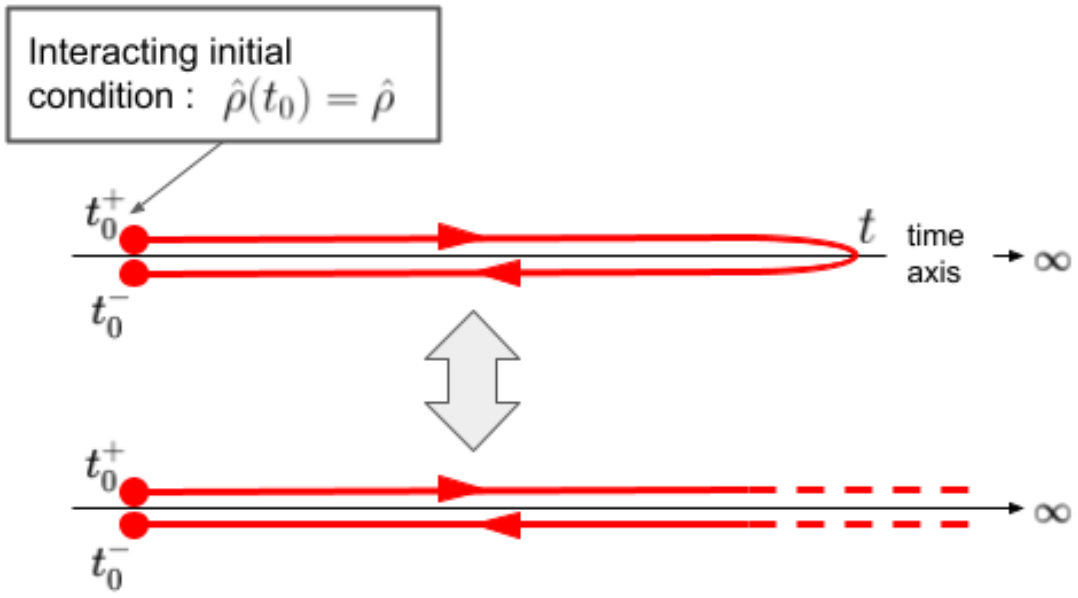

Figure 2.1: Schematic representation of the round-trip contour c. The arrow indicates the time-ordering convention on the contour. On the upper branch ($+$ branch), the time-ordering is chronological, whereas on the lower branch ($-$ branch) the time-ordering is anti-chronological. To be complete, we also indicate the initial condition $\hat{\rho}(t_0) = \hat{\rho}$, with $\hat{\rho}$ the exact many-body density matrix (2.2).

$\mathcal{H}_0$, while the states $|\Psi_I(t)\rangle$ evolves under the action of $\hat{V}_I(t)$, where the subscript I indicates the interaction picture. In other words, in the *interaction picture*, the states and operators obey the following equations of

motion,

$$i\hbar\frac{\mathrm{d}\hat{O}_I(t)}{\mathrm{d}t} = [\mathcal{H}_I(t), \hat{O}_I(t)] + i\hbar\frac{\partial\hat{O}_I(t)}{\partial t}, \text{ with } \hat{O}_I(t_0) = \hat{O}(t_0), \tag{2.9}$$

$$i\hbar\frac{\mathrm{d}\,|\Psi_I(t)\rangle}{\mathrm{d}t} = \hat{V}_I(t)\,|\Psi_I(t)\rangle\,, \text{ with } |\Psi_I(t_0)\rangle = |\Psi(t_0)\rangle\,. \tag{2.10}$$

Note that (2.9) admits the solution,

$$\hat{O}_I(t) = e^{i\mathcal{H}_0\frac{t-t_0}{\hbar}}\hat{O}(t)e^{-i\mathcal{H}_0\frac{t-t_0}{\hbar}}. \tag{2.11}$$

Now, we should express the operators in the *Heisenberg picture* in the *interaction picture*. To do so, we introduce the time-evolution operator $\hat{S}(t_1, t_2)$, defined by the equations,

$$\hat{O}_H(t) = \hat{S}(t_0, t)\hat{O}_I(t)\hat{S}(t, t_0), \tag{2.12}$$

$$\hat{S}(t_1, t_3)\hat{S}(t_3, t_2) = \hat{S}(t_1, t_2), \tag{2.13}$$

$$\hat{S}(t_1, t_1) = \mathbb{1}. \tag{2.14}$$

It is straightforward to show that, $\hat{S}(t, t_0)$ obeys the following equation of motion,

$$i\hbar\frac{\mathrm{d}\hat{S}(t, t_0)}{\mathrm{d}t} = \hat{V}_I(t)\hat{S}(t, t_0). \tag{2.15}$$

Hence, using the initial condition, (2.14) and the identity (2.13), we can formally write $\hat{S}(t_1, t_2)$ as,

$$\hat{S}(t_1, t_2) = \begin{cases} \mathcal{T}[e^{-\frac{i}{\hbar}\int_{t_2}^{t_1}\hat{V}_I(t)\mathrm{d}t}], & t_1 > t_2, \\ \bar{\mathcal{T}}[e^{\frac{i}{\hbar}\int_{t_1}^{t_2}\hat{V}_I(t)\mathrm{d}t}], & t_2 > t_1 \end{cases}, \tag{2.16}$$

with $\mathcal{T}$ the chronological time-ordering operator and $\bar{\mathcal{T}}$ the anti-chronological one defined as,

$$\bar{\mathcal{T}}[\hat{A}(t)\hat{B}(t')] = \begin{cases} \hat{A}(t)\hat{B}(t'), & t < t', \\ \pm\hat{B}(t')\hat{A}(t), & t \geq t', \end{cases} \tag{2.17}$$

where the $+$ and $-$ sign corresponds to the cases of bosonic and fermionic operators, respectively. Defining the round-trip time contour c represented on Fig. 2.1, the equation (2.12) adopts an elegant and compact form,

$$\hat{O}_H(t) = \mathcal{T}_c[e^{-\frac{i}{\hbar}\int_c\hat{V}_I(z)\mathrm{d}z}\hat{O}_I(t)], \tag{2.18}$$

where the time-ordering operator $\mathcal{T}_c$ orders the operators along the round-trip contour c and z is a contour time argument lying on c.

The c contour contains two branches. It runs on the upper branch (the $+$ branch) from $t_0^+ = t_0$ to t and then goes back to $t_0^- = t_0$ on the lower branch (the $-$ branch). On the $+$ branch, the time-ordering is chronological, while on the $-$ branch, it is anti-chronological. The vertical shift between the $+$ and $-$ branch in Fig. 2.1 is only a graphical artifact used for the visibility of each branch. This shift should not confuse the reader, and we stress that both branches lie on the real axis. Since, $\hat{S}(\infty, t)\hat{S}(t, \infty) = \mathbb{1}$, the contour can be expanded to $t = +\infty$

without additional difficulties (see Fig. 2.1). For convenience, we extend the definition of the time-evolution operator to the contour c,

$$S_c(z_2, z_1) = \mathcal{T}_c[e^{-\frac{i}{\hbar}\int_{z_1}^{z_2} \hat{V}_I(z)\mathrm{d}z}], \tag{2.19}$$

where z_1 and z_2 are contour-time arguments lying on c. With this definition, (2.18) becomes,

$$\hat{O}_H(t) = \mathcal{T}_c[S_c(t_0^-, t_0^+)O_I(t)]. \tag{2.20}$$

Therefore, it is straightforward to show that the time-ordered Green's function G^T can be written as:

$$\begin{aligned} G^T_{\sigma,\sigma'}(\boldsymbol{r}, t; \boldsymbol{r}', t') &= -\frac{i}{\hbar}\,\mathrm{Tr}\Big\{\hat{\rho}\mathcal{T}_c[S_c(t_0^-, t^+)c_{I\sigma}(\boldsymbol{r}, t^+)S_c(t^+, t'^+)c^\dagger_{I\sigma'}(\boldsymbol{r}', t'^+)]S_c(t'^+, t_0^+)\Big\} \\ &= \mathrm{Tr}\Big\{\hat{\rho}\mathcal{T}_c[e^{-\frac{i}{\hbar}\int_c \mathrm{d}z V_I(z)}c_{I\sigma}(\boldsymbol{r}, t^+)c^\dagger_{I\sigma'}(\boldsymbol{r}', t'^+)]\Big\}, \end{aligned} \tag{2.21}$$

where we used the fact that the operators inside $\mathcal{T}_c$ commute and $S_c(t_0^-, t^+)S_c(t^+, t'^+)S_c(t'^+, t_0^+) = S_c(t_0^-, t_0^+)$.

Nevertheless, (2.21) is not yet practically useful. Indeed, if we expand the exponential operator, we obtain an infinite series of many-particle correlations involving non-interacting operators. However, in (2.21) the average is performed with respect to the exact many-body density-matrix. Hence the Wick theorem can not be applied. We solve this problem in the next subsection.

2.1.3 Initial correlations and the generalized contour

If we want to use the Wick theorem in (2.21), it is necessary to express the many-body density matrix $\hat{\rho}$ from the non-interacting density matrix $\hat{\rho}_0$,

$$\hat{\rho}_0 = \frac{e^{-\beta\mathcal{H}_0}}{\mathcal{Z}_\prime}, \ \mathcal{Z}_\prime = \mathrm{Tr}[e^{-\beta\mathcal{H}_0}]. \tag{2.22}$$

First, we split off the single-particle density matrix $\hat{\rho}_0$ from $\hat{\rho}$,

$$\hat{\rho} = \hat{\rho}_0\frac{\mathcal{Z}_0}{\mathcal{Z}}e^{\beta\mathcal{H}_0}e^{-\beta\mathcal{H}}. \tag{2.23}$$

Then, we introduce the operator $\hat{S}_{c'}(t_0 - i\hbar\beta, t_0)$,

$$\hat{S}_{c'}(t_0 - i\hbar\beta, t_0) = e^{\beta\mathcal{H}_0}e^{-\beta\mathcal{H}}. \tag{2.24}$$

With this definition, it is straightforward to show that,

$$S_{c'}(t_0 - i\hbar\beta, t_0) = \mathcal{T}_{c'}[e^{-i\int_{t_0}^{\tau} H_{int,I}(\tau')\mathrm{d}\tau'}], \text{ with, } \hat{O}_I(\tau) = e^{i\mathcal{H}_0(\tau - t_0)}\hat{O}(t_0)e^{-i\mathcal{H}_0(\tau - t_0)}, \ \tau \in c', \tag{2.25}$$

where c' is the Matsubara contour defined in Fig. 2.2, $O_I(\tau)$ is the extension of interaction representation of an operator $\hat{O}$ to complex time lying on c', and $\mathcal{T}_{c'}$ is the Matsubara time-ordering operator. $\mathcal{T}_{c'}$ orders the operators along c' according to the direction of the arrow in Fig.2.2,

$$\mathcal{T}_{c'}[\hat{A}(\tau)\hat{B}(\tau')] = \begin{cases} \hat{A}(\tau)\hat{B}(\tau'), \ \tau > \tau' \text{ in } c' \\ \pm\hat{B}(\tau')\hat{A}(\tau), \ \tau' \geq \tau \text{ in } c' \end{cases}. \tag{2.26}$$

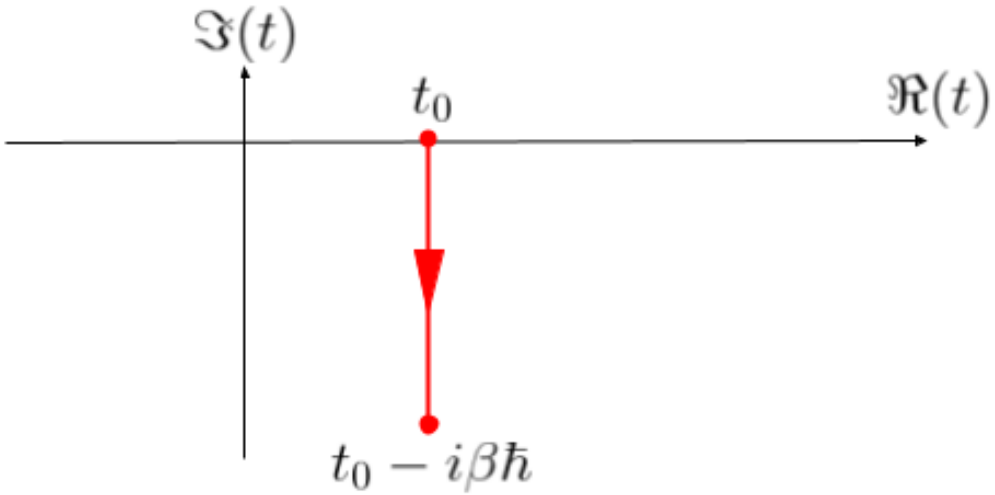

Figure 2.2: Schematic representation of the Matsubara contour c'. The red arrow indicates the time-ordering on c'.

Therefore, we can expand $\hat{\rho}$ in terms of $\hat{\rho}_0$,

$$\hat{\rho} = \frac{\hat{\rho}_0 S_{c'}(t_0 - i\hbar\beta, t_0)}{\mathrm{Tr}\{\hat{\rho}_0 S_{c'}(t_0 - i\beta\hbar, t_0)\}}. \tag{2.27}$$

Inserting the above equation into (2.21) we obtain,

$$G^T_{\sigma\sigma'}(\boldsymbol{r}, t; \boldsymbol{r}', t') = \frac{\mathrm{Tr}\Big\{\rho_0 \hat{S}_{c'}(t_0 - i\beta, t_0)\mathcal{T}_c[S_c(t_0^-, t_0^+)c_{\sigma I}(\boldsymbol{r}, t^+)c^\dagger_{\sigma' I}(\boldsymbol{r}', t'^+)]\Big\}}{\mathrm{Tr}\Big\{\rho_0 \hat{S}_{c'}(t_0 - i\beta, t_0)\Big\}}. \tag{2.28}$$

Noticing the striking similarity between the treatment of the initial density matrix and the time-evolution operator, both being exponential functions, we can combine the two expansions into a single one. To do so, following Wagner[65], we first glue together the contour c and c' and introduce the generalized contour $c^* = c'c$ defined in Fig. 2.3. In addition, we define the time-ordering operator T_{c^*},

$$\mathcal{T}_{c'}[\hat{A}(\tau)\hat{B}(\tau')] = \begin{cases} \hat{A}(\tau)\hat{B}(\tau'), \ z > z' \text{ in } c^* \\ \pm\hat{B}(\tau')\hat{A}(\tau), \ z' \geq z \text{ in } c^* \end{cases}, \tag{2.29}$$

where the contour-times are ordered according to the red arrow in Fig. 2.3. Hence, points lying on c' are always later than the ones lying on c. Lastly, we extend the definition of the time-evolution operator to the c^* contour,

$$S_{c^*}(t_0 - i\hbar\beta, t_0^+) = S_{c'}(t_0 - i\hbar\beta)S_c(t_0^-, t_0^+) = \mathcal{T}_{c^*}[e^{i\int_{c^*}\hat{K}_I(z)\mathrm{d}z}], \tag{2.30}$$

where $\hat{K}_I(z)$ is the perturbation in the interaction picture defined as,

$$\hat{K}_I(z) = \begin{cases} V_I(z), \ z \in c, \\ \mathcal{H}_{int,I}(z), \ z \in c' \end{cases} \tag{2.31}$$

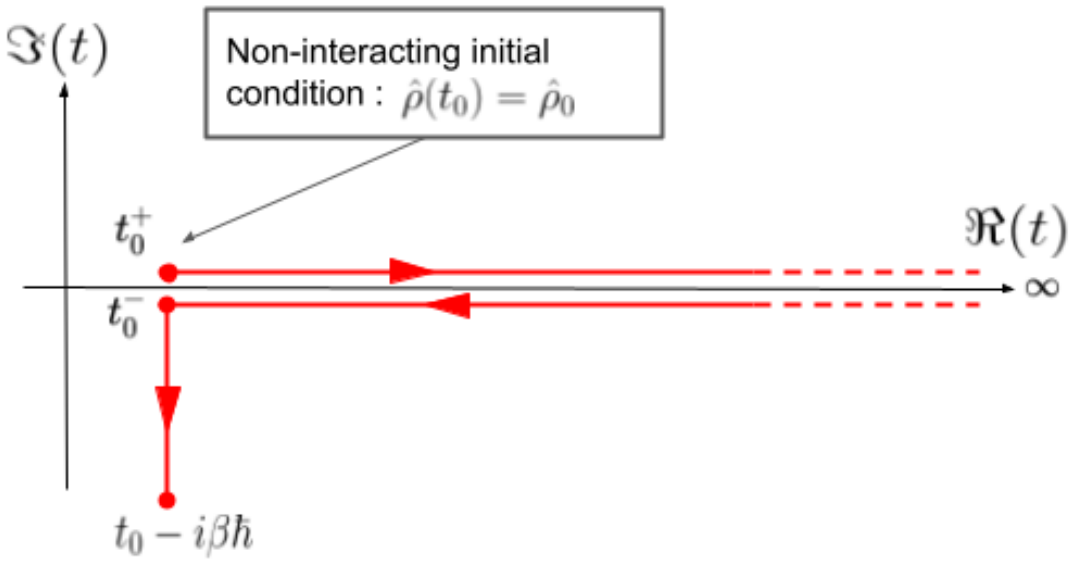

Figure 2.3: Schematic illustration of the generalized contour c^*. The arrow indicates the time-ordering convention on the contour. To be complete, we also indicate the initial condition $\hat{\rho}(t_0) = \hat{\rho}_0$, with $\hat{\rho}_0$ the single-particle density matrix in (2.22).

With all the previous definitions, we obtain the elegant and compact expression,

$$G^T_{\sigma\sigma'}(\boldsymbol{r}, t; \boldsymbol{r}', t') = -\frac{i}{\hbar} \frac{\mathrm{Tr}\Big\{\hat{\rho}_0 \mathcal{T}_{c^*}[e^{-\frac{i}{\hbar}\int_{c^*} \hat{K}_I(z)\mathrm{d}z} c_{\sigma I}(\boldsymbol{r}, t^+) c^\dagger_{\sigma' I}(\boldsymbol{r}', t'^+)]\Big\}}{\mathrm{Tr}\Big\{\hat{\rho}_0 \mathcal{T}_{c^*} e^{-\frac{i}{\hbar}\int_{c^*} d_z V_I(z)}\Big\}} \tag{2.32}$$

$$= -\frac{i}{\hbar} \frac{\langle \mathcal{T}_{c^*}[e^{-i\int_{c^*} d_z \hat{K}(z)} c_\sigma(\boldsymbol{r}, t^+) c^\dagger_{\sigma'}(\boldsymbol{r}', t'^+)]\rangle_0}{\langle \mathcal{T}_{c^*}[e^{-i\int_{c^*} d_z \hat{K}(z)}\rangle_0}, \tag{2.33}$$

where we introduced the short-hand notation:

$$\langle \hat{A}_1(z_1) ... \hat{A}_n(z_n)\rangle_0 = \mathrm{Tr}\Big\{\hat{\rho}_0 \hat{A}_{1,I}(z_1) ... \hat{A}_{n,I}(z_n)\Big\} \tag{2.34}$$

2.1.4 Long-time asymptotic regime and the Keldysh contour

So far we did not make any assumptions and (2.32) is exact on the generalized contour c^*. Using the generalized contour c^* one can take into account the initial correlations and describes the complete dynamics of the system under drive field $\hat{V}_p(t)$ from the early-time transient regime to the long-time asymptotic regime.

In this manuscript, we focus on the long-time steady-state regime reached by the system when a DC drive is applied to it. Therefore, (2.32) and the generalized contour c^* seems unnecessarily complicated for our purpose. Fortunately, in 1964, L. V. Keldysh proposed a simplified contour allowing one to capture the long-time steady-state regime with less computational effort [26]. The idea is that if Green's functions decay rapidly as a function of the difference in times, the system loses its memory of initial correlations after a long time. Under this assumption, the Matsubara contour c' can be neglected. Moreover, neglecting the transient regime,

Figure 2.4: Schematic illustration of the Keldysh contour c_K. c_K is obtained from c^* by neglecting the contour c' which is equivalent to neglecting initial correlations and, discarding the transient regime, setting t_0 to $-\infty$.

we can set t_0 to the infinite past, $t_0 \to -\infty$. We thus end up with the simplified contour defined in Fig. 2.4, known as the Keldysh contour c_K. Hence, we refer to this contour as the Keldysh contour. Using the identity $\mathcal{T}_c[e^{\frac{-i}{\hbar}\int_c V_I(z)\mathrm{d}z}] = \hat{S}(-\infty,\infty)\hat{S}(\infty,-\infty) = \mathbb{1}$, and applying 2.32 to c_K we obtain the simplified equation,

$$G^T_{\sigma\sigma'}(\boldsymbol{r},t;\boldsymbol{r}',t') = -\frac{i}{\hbar}\langle\mathcal{T}_c[e^{-\frac{i}{\hbar}\int_{c_K}\mathrm{d}_z V(z)}c_\sigma(\boldsymbol{r},t^+)c^\dagger_{\sigma'}(\boldsymbol{r}',t'^+)]\rangle_0, \tag{2.35}$$

where $\langle ...\rangle_0$ indicates that the operator evolves with respect to $\mathcal{H}_0$ and that the average is performed with respect to $\hat{\rho}_0$. For non-interacting systems, because the perturbation $\hat{K}_I(z)$ vanishes on c', the Keldysh contour c_K is obviously equivalent to c^* yielding the exact steady-state regime [65].

However, for interacting systems, the validity of the Keldysh contour relies on *thermalization* of the system due to scattering processes. In other words, we expect that, because of the interactions, the initially uncorrelated system has *thermalized* to a correlated state after a long time (see [27, 65] for a detailed discussion). In most cases, this assumption is valid, and the Keldysh contour c_K correctly captures the steady-state regime of interacting systems. Nevertheless, there are some cases where this assumption fails and the steady-state regime depends on the initial correlations. For example, it is the case when interaction can not be thought of as *local perturbation*. This phenomena, called *thermalization breakdown*, has been recently investigated due its experimental relevance [69, 70, 71, 72].

In this manuscript, we focus on non-interacting systems. Hence, for our purpose, the Keldysh contour yields exact results. As a consequence, hereinafter, we strictly use the Keldysh contour c_K and therefore omit the index K to lighten the notations.

2.2 NEGF on the Keldysh contour

2.2.1 Dyson equation on the contour

Expanding the time-evolution operator $e^{-\frac{i}{\hbar}\int_c \mathrm{d}_z V(z)}$ in (2.35), and using Wick's theorem, the exact time-ordered Green's function becomes an infinite geometrical serie of non-interacting Green's functions. Obviously

this serie do not only involve the bare time-ordered Green's function $g^T_{\sigma,\sigma'}(\boldsymbol{r},t;\boldsymbol{r}',t') = -\frac{i}{\hbar}\langle T_c[c_\sigma(\boldsymbol{r},t^+),c_{\sigma'}(\boldsymbol{r}',t'^+)\rangle_0$ but also two-point correlations of the form $\langle T_c[c_\sigma(\boldsymbol{r},z),c_{\sigma'}(\boldsymbol{r}',z')\rangle_0$ with $z = t^\pm$ and $z' = t'^\pm$ lying on the Keldysh contour. It is then convenient to extend the definition of the Green's function to the full contour,

$$G^c_{\sigma\sigma'}(\boldsymbol{r},z;\boldsymbol{r}',z') = -\frac{i}{\hbar}\langle \mathcal{T}_c[c_\sigma(\boldsymbol{r},z),c_{\sigma'}(\boldsymbol{r}',z')]\rangle = -\frac{i}{\hbar}\langle \mathcal{T}_c[e^{-\frac{i}{\hbar}\int_c V(z)\mathrm{d}z}c_\sigma(\boldsymbol{r},z),c_{\sigma'}(\boldsymbol{r}',z')]\rangle_0. \tag{2.36}$$

Similarly to the zero-temperature case G_c can be formally obtained from a power expansion of $e^{-i\int_c V_I(z)\mathrm{d}z}$. Using the Wick theorem, one obtains an infinite serie of products of bare Green's function g_c. Each term in the serie can be conveniently represented by a diagram analogous to the Feynman diagrams in the zero-temperature case[27]. Similarly to the zero-temperature case, the concept of self-energy Σ^c (defined on the Keldsyh contour) naturally arises as the sum of all possible single-particle irreducible diagrams, and the contour-time Green's function obeys the Dyson equation[27],

$$\begin{aligned} G^c_{\sigma\sigma'}(\boldsymbol{r},z;\boldsymbol{r}',z') &= g^c_{\sigma\sigma'}(\boldsymbol{r},z;\boldsymbol{r}',z') \\ &+ \sum_{\gamma,\delta}\int_c \mathrm{d}\boldsymbol{r}_2\mathrm{d}\boldsymbol{r}_3\mathrm{d}z_2\mathrm{d}z_3\; g^c_{\sigma\gamma}(\boldsymbol{r},z;\boldsymbol{r}_2,z_2)\Sigma^c_{\gamma\delta}(\boldsymbol{r}_2,z_2;\boldsymbol{r}_3,z_3)G^c_{\delta\sigma'}(\boldsymbol{r}_3,z_3;\boldsymbol{r}',z'). \end{aligned} \tag{2.37}$$

Using the short-hand notation for the arguments of the contour-time Green's function, $1 \equiv \{\sigma_1,\boldsymbol{r}_1,z_1\}$, eq.(2.37) adopts an elegant and compact form,

$$G^c(1,1') = g^c(1,1') + g^c(1,2)\Sigma^c(2,3)G^c(3,1'), \tag{2.38}$$

where integration over repeated indices is understood.

Nevertheless, physical information is encoded into real-time Green's functions with both time arguments lying on concrete branches of the contour. Hence, G^c is not practically useful, and we find it more convenient to work directly in terms of the *real-time* Green's functions defined in the next subsection.

2.2.2 Real-time Green's functions

Since the Keldysh contour possesses two branches, there are four possible ways to choose the branch of the two-time arguments of G^c. Consequently, the contour-ordered Green's function corresponds to four different real-time Green's functions:

$$G_{\sigma,\sigma'}(\boldsymbol{r},z;\boldsymbol{r}',z') = \begin{cases} G^T_{\sigma,\sigma'}(\boldsymbol{r},t;\boldsymbol{r}',t') = -\frac{i}{\hbar}\langle \mathcal{T}[c_\sigma(\boldsymbol{r},t)c^\dagger_{\sigma'}(\boldsymbol{r}',t')]\rangle & \text{if } z=t^+,\ z'=t'^+ \\ G^{\bar{T}}_{\sigma,\sigma'}(\boldsymbol{r},t;\boldsymbol{r}',t') = -\frac{i}{\hbar}\langle \bar{\mathcal{T}}[c_\sigma(\boldsymbol{r},t)c^\dagger_{\sigma'}(\boldsymbol{r}',t')]\rangle & \text{if } z=t^-,\ z'=t'^- \\ G^{>}_{\sigma,\sigma'}(\boldsymbol{r},t;\boldsymbol{r}',t') = -\frac{i}{\hbar}\langle c_\sigma(\boldsymbol{r},t)c^\dagger_{\sigma'}(\boldsymbol{r}',t')\rangle & \text{if } z=t^-,\ z'=t'^+ \\ G^{<}_{\sigma,\sigma'}(\boldsymbol{r},t;\boldsymbol{r}',t') = \frac{i}{\hbar}\langle c^\dagger_{\sigma'}(\boldsymbol{r}',t')c_\sigma(\boldsymbol{r},t)\rangle & \text{if } z=t^-,\ z'=t'^+ \end{cases} \tag{2.39}$$

It is sometimes convenient to represent G^c in a matrix form $\hat{G}$ containing the four real-times functions, defined as:

$$\check{G}(1,1') = \begin{bmatrix} G^T(1,1') & G^<(1,1') \\ G^>(1,1') & G^{\bar{T}}(1,1') \end{bmatrix}. \tag{2.40}$$

Similarly, we can define a matrix representation $\hat{A}$ for any contour-time function A^c.

It is important to note that the four real-time Green's functions defined in (2.39) are not all independent, namely,

$$G^T + G^{\bar{T}} = G^< + G^>, \tag{2.41}$$

where we omitted the arguments to lighten the notations. The redundancy can be eliminated by a linear transformation of $\check{G}$:

$$\check{G} = \hat{L}\hat{\kappa}_3\check{G}\hat{L}^\dagger = \begin{bmatrix} G^r & G^K \\ 0 & G^a \end{bmatrix}, \ \hat{L} = \frac{1}{\sqrt{2}}(\hat{\kappa}_0 + -i\hat{\kappa}_2), \tag{2.42}$$

where κ_i are the Pauli matrices acting in the space of the contour branch, also called Keldysh space ($\hat{\kappa}_0$ is the identity). G^a, G^r, and G^K are, respectively, the advanced, retarded, and Keldysh Green's function,

$$G^r_{\sigma\sigma'}(\boldsymbol{r}, t; \boldsymbol{r}', t') = -\frac{i}{\hbar}\theta(t - t')\langle\{c_\sigma(\boldsymbol{r}, t), c^\dagger_{\sigma'}(\boldsymbol{r}', t')\}\rangle \tag{2.43}$$

$$G^a_{\sigma\sigma'}(\boldsymbol{r}, t; \boldsymbol{r}', t') = \frac{i}{\hbar}\theta(t' - t)\langle\{c_\sigma(\boldsymbol{r}, t), c^\dagger_{\sigma'}(\boldsymbol{r}', t')\}\rangle \tag{2.44}$$

$$G^K_{\sigma\sigma'}(\boldsymbol{r}, t; \boldsymbol{r}', t') = -\frac{i}{\hbar}\langle[c_\sigma(\boldsymbol{r}, t), c^\dagger_{\sigma'}(\boldsymbol{r}', t')]\rangle \tag{2.45}$$

Obviously, $G^r(1, 1') = G^a(1', 1)^*$, thus, only two Green's function are independent. While $G^{a/r}$ gives information on the particle dynamics and the states of the system G^K gives information about the non-equilibrium occupation of those states.

2.2.3 The Langreth rules

As already mentioned, the Dyson equation (2.37) is not practically useful since it is written in terms of contour-time Green's functions. Hence, we would like to write it directly in terms of real-time Green's functions. In doing so, we need to specify how integrals on the Keldysh contour are translated into integrals on the real-time axis. Let us first consider the convolution product, $C^c(1, 1') = \int_c \mathrm{d}z_2 A^c(1, 2)B^c(2, 1')$. We start

$$\int_c \mathrm{d}z_2 A(1, 2)B(2, 1') = \int_{-\infty}^{\infty} \mathrm{d}t_2 A(1, 2^+)B(2^+, 1') - \int_{-\infty}^{\infty} \mathrm{d}t_2 A(1, 2^-)B(2^-, 1'), \tag{2.46}$$

which can be written in a compact form using the matrix representation,

$$\check{C}(1, 1') = \int_{-\infty}^{\infty} \mathrm{d}t_2 \check{A}(1, 2)\hat{\kappa}_z\check{B}(2, 1'), \tag{2.47}$$

where $\hat{\kappa}_z = \begin{bmatrix} 1 & 0 \\ 0 & -1 \end{bmatrix}$ is the third Pauli matrix acting in the Keldysh space. Equation (2.47) completely specifies the rules to compute contour-time convolution products from real-time convolution products. These rules are known as the Langreth rules. Using eq.(2.47), and equation (2.42), it is easy to obtains the Langreth rules for the retarded, advanced and Keldysh components of $C(1, 1')$,

$$\begin{aligned} \check{C}(1, 1') &= \int_{-\infty}^{\infty} \mathrm{d}t_2 \check{A}(1, 2)\check{B}(2, 1') \\ \Rightarrow C^{r/a}(1, 1') &= \int_{-\infty}^{\infty} \mathrm{d}t_2 A^{r/a}(1, 2)B^{r/a}(2, 1') \qquad (2.48) \\ \Rightarrow C^K(1, 1') &= \int_{-\infty}^{\infty} \mathrm{d}t_2 A^K(1, 2)B^a(2, 1') + A^r(1, 2)B^K(2, 1') \qquad (2.49) \end{aligned}$$

Applying Langreth's rules to the Dyson equation equation (2.37) gives the following closed set of Dyson equations on the real-time axis,

$$G^{r/a} = g^{r/a} + g^{r/a}\Sigma^{r/a}G^{r/a}, \tag{2.50}$$
$$G^{K} = g^{K} + g^{r}\Sigma^{r}G^{K} + g^{r}\Sigma^{K}G^{a} + g^{a}\Sigma^{a}G^{a}, \tag{2.51}$$

where integration/summation over intermediate arguments is understood. It easy to show that the solution of equation (2.51) is,

$$G^{K} = (1 + G^{r}\Sigma^{r})g^{K}(1 + \Sigma^{a}G^{a}) + G^{r}\Sigma^{K}G^{a} \tag{2.52}$$

Thus we obtained a set of closed equations describing out-of-equilibrium states of quantum many-body systems.

Lastly, in electronic transport models, it is often convenient to work directly with the lesser and greater Green's functions directly. These Green's functions functions obey relation similar to (2.52),

$$G^{<} = (1 + G^{r}\Sigma^{r})g^{<}(1 + \Sigma^{a}G^{a}) + G^{r}\Sigma^{<}G^{a} \tag{2.53}$$
$$G^{>} = (1 + G^{r}\Sigma^{r})g^{>}(1 + \Sigma^{a}G^{a}) + G^{r}\Sigma^{>}G^{a}. \tag{2.54}$$

In the case of an interacting system, the self-energy Σ is an infinite serie of one-particle irreducible diagrams which, generally, can not be summed exactly. In the absence of interaction, and if the drive field $V_p(t)$ is quadratic in the electronic field operators, the self-energy is a finite sum of diagrams that can be computed exactly. In that case, the Dyson equations can be solved exactly.

2.3 Application to scanning tunneling spectroscopy

In the previous sections, we presented the technical details of the Keldysh formalism and showed that the Dyson equations could be solved exactly in the absence of interactions. Here, we apply the Keldysh NEGF technique to describe electronic transport in a scanning tunneling spectroscopy (STS) experiment. In such an experiment, a sample that has to be characterized is probed by a tip placed on top of it. Because of the quantum tunneling effect, there is a finite probability for electrons to tunnel from the tip to the sample and vice-versa. In presence of a bias voltage, a charge current flows between the tip and sample. By measuring this current as a function of the applied voltage, one can extract the differential conductance, which, as we will show below, reflects the spectral properties of the sample. Here we focus on STS experiments performed with normal metallic tips on top of superconducting samples. Before applying the NEGF technique, we first have to define Hamiltonian modeling for the STS experiment. This is the aim of the next subsection.

2.3.1 Theoretical modeling

First, it is important to stress that we are interested in biases, $eV \sim \Delta_0$ with Δ_0 the superconducting energy gap in the sample, which is typically much smaller than the Fermi energy. Therefore, the relevant energy interval for the transport properties, which we are interested in, is a narrow energy range around the Fermi energy. Consequently, for our purpose, it is enough to work with a simplified low-energy model describing the tip, the sample, and their coupling. For the sake of simplicity, we assume that the metallic tip and the normal-state

sample have a single-conduction band crossing the Fermi level. Hence focusing on the low-energy physics around the Fermi energy, we neglect orbital and/or band degrees of freedom. For the sake of simplicity, we describe the STS junction as a tunneling junction connecting the single site at the apex of the tip (denoted $\boldsymbol{r_a}$) to the nearest site of the superconducting sample (denoted $\boldsymbol{r_0}$). Since the tunneling probability decreases with the distance between the sites, this tunneling path is expected to be dominant, and it seems legitimate to neglect other tunneling paths. Thus, the STS set-up is conveniently described by the following microscopic Hamiltonian,

$$\mathcal{H} = \mathcal{H}_S + \mathcal{H}_T + t\sum_\sigma \left[c^\dagger_{T\sigma}(\boldsymbol{r_a})c_{S\sigma}(\boldsymbol{r_0}) + c^\dagger_{S\sigma}(\boldsymbol{r_0})c_{T\sigma}(\boldsymbol{r_a})\right] - \mu_T\hat{N}_T - \mu_S\hat{N}_S, \tag{2.55}$$

where $c_{T\sigma}(\boldsymbol{r})$, $c_{S\sigma}(\boldsymbol{r})$ respectively annihilates an electron of spin σ at position $\boldsymbol{r}$ in the tip and sample. $\mathcal{H}_S$, and $\mathcal{H}_T$ are respectively the Hamiltonian describing the isolated sample and tip. $\hat{N}_T$, $\hat{N}_S$ are, respectively, the particle number operators in the tip and sample. μ_T, μ_S are respectively the electrostatic potential of the tip and sample, and their difference account for the voltage bias applied to the STS junction, $\mu_T = \mu_S + eV$. For convenience, we measure the single-particle energies with respect to μ_S, hence $\mu_S = 0$. Lastly, t is the hopping amplitude between the tip and sample, which, without loss of generality, is chosen real.

Remembering that the relevant energies for transport properties lie in a narrow window around the Fermi energy, it seems legitimate to use low-energy effective continuum models to describe the tip and sample. Thus, without loss of generality, the superconducting sample is conveniently described by the following BdG Hamiltonian,

$$\mathcal{H}_S = \frac{1}{2}\int \mathrm{d}\boldsymbol{r}\psi^\dagger_S(\boldsymbol{r})\hat{H}_S(\boldsymbol{r})\psi_S(\boldsymbol{r}), \tag{2.56}$$

$$\hat{H}_S(\boldsymbol{r}) = \begin{bmatrix}\hat{h}_S(\boldsymbol{r}) & \hat{\Delta}(\boldsymbol{r}) \\ \hat{\Delta}^\dagger(\boldsymbol{r}) & -\sigma_y\hat{h}^*_S(\boldsymbol{r})\sigma_y\end{bmatrix}, \tag{2.57}$$

where we defined the Nambu-spinor $\psi^\dagger_S(\boldsymbol{r}) = [c^\dagger_{S\uparrow}(\boldsymbol{r}), c^\dagger_{S\downarrow}(\boldsymbol{r}), c_{S\downarrow}(\boldsymbol{r}), -c^\dagger_{S\uparrow}(\boldsymbol{r})]$, $\hat{h}_S(\boldsymbol{r})$ describes the normal metallic state, and $\hat{\Delta}(\boldsymbol{r})$ describes the pairing potential. Note that (2.56) is not necessarily uniform and can incorporate scattering potentials due to impurities. The precise geometry of the tip is not relevant in the low-energy range we are interested in. Hence, neglecting geometrical effects, we describe the tip as a bulk metal,

$$\mathcal{H}_T = \sum_\sigma \int \frac{\mathrm{d}\boldsymbol{k}}{(2\pi)^d}\epsilon_T(k)c^\dagger_{\sigma T}(\boldsymbol{k})c_{\sigma T}(\boldsymbol{k}), \tag{2.58}$$

with d the dimension of the tip, $c_{\sigma T}(\boldsymbol{k}) = \int \mathrm{d}\boldsymbol{r}e^{-i\boldsymbol{k}.\boldsymbol{r}}c_{\sigma T}(\boldsymbol{r})$ the operator annihilating an electron of the tip with spin σ and momentum $\hbar\boldsymbol{k}$, $\epsilon_T(k)$ the energy-dispersion of the metallic tip. Because the tip is coupled to the superconducting sample, we find it convenient to recast $\mathcal{H}$ in a BdG form,

$$\begin{aligned}\mathcal{H} =& \frac{1}{2}\int \mathrm{d}\boldsymbol{r}\psi^\dagger_S(\boldsymbol{r})\hat{H}_S(\boldsymbol{r})\psi_S(\boldsymbol{r}) + \frac{1}{2}\int \frac{\mathrm{d}\boldsymbol{k}}{(2\pi)^d}\psi^\dagger_T(\boldsymbol{k})\left[\epsilon_T(\boldsymbol{k}) - eV\right]\tau_z\psi_T(\boldsymbol{k}) \\ &+ \frac{t}{2}\psi^\dagger_T(\boldsymbol{r_a})\tau_z\psi_S(\boldsymbol{r_0}) + \mathrm{h.c.}\end{aligned} \tag{2.59}$$

We can now study electronic transport through the STS junction. We define the electronic current operator through the STS junction $\hat{I}(\tau) = -e\frac{\mathrm{d}\hat{N}_T(\tau)}{\mathrm{d}\tau}$, with $\hat{N}_T(\tau)$ the particle number operator in the tip at time τ in the Heisenberg representation. Within our model (2.59), $\hat{I}(\tau)$,

$$\hat{I}(\tau) = \frac{iet}{2\hbar}[\psi_T^\dagger(\boldsymbol{r}_a,\tau)\psi_S(\boldsymbol{r}_0,\tau) - \psi_S^\dagger(\boldsymbol{r}_0,\tau)\psi_T(\boldsymbol{r}_a,\tau)]. \tag{2.60}$$

In the steady-state regime, its average value $\langle\hat{I}(\tau)\rangle$ is time-independent and,

$$I = \langle\hat{I}(\tau)\rangle = \frac{iet}{2\hbar}[\langle\psi_T^\dagger(\boldsymbol{r}_a,\tau)\psi_S(\boldsymbol{r}_0,\tau)\rangle - \langle\psi_S^\dagger(\boldsymbol{r}_0,\tau)\psi_T(\boldsymbol{r}_a,\tau)\rangle], \tag{2.61}$$

where $\langle ...\rangle$ denotes the average value over non-equilibrium states of operators evolving with respect to the Hamiltonian $\mathcal{H}$.

To evaluate these non-equilibrium expectation values, it is convenient to use the Keldysh NEGF introduced in the previous sections of this chapter. It is obvious to show that,

$$I = \frac{et}{\hbar}\sum_\sigma \hbar\{G^<_{ST,\sigma\sigma}(\boldsymbol{r_0}\tau,\boldsymbol{r_a}\tau') - G^<_{TS,\sigma\sigma}(\boldsymbol{r_a},\tau;\boldsymbol{r_0},\tau)\} = 2et\,\mathrm{Re}\Big\{G^<_{ST,\sigma\sigma}(\boldsymbol{r_0}\tau,\boldsymbol{r_a}\tau')\Big\}, \tag{2.62}$$

where $G^<_{\alpha\beta,\sigma\sigma'}(\boldsymbol{r},\tau;\boldsymbol{r'},\tau') = -\langle\mathcal{T}_c[c_{\alpha\sigma}(\boldsymbol{r},\tau^+)c_{\alpha\sigma}(\boldsymbol{r'},\tau'^-)]\rangle$ is the lesser component of the electronic NEGF on the Keldysh contour, $G^c_{\alpha\beta,\sigma\sigma'}(\boldsymbol{r},z;\boldsymbol{r'},z') = -\langle\mathcal{T}_c[c_{\alpha\sigma}(\boldsymbol{r},z)c_{\alpha\sigma}(\boldsymbol{r'},z')]\rangle$. The indices $\alpha = S,T$ and $\beta = S,T$ indicates the sample or tip. In order to compute the Green's functions entering I we consider the coupling between the tip and sample as a perturbation and split the Hamiltonian $\mathcal{H}$ into an unperturbed Hamiltonian $\mathcal{H}_0$ a perturbation $\hat{V}_p$,

$$\mathcal{H} = \mathcal{H}_0 + \hat{V}_p,$$

$$\text{with } \mathcal{H}_0 = \frac{1}{2}\int \mathrm{d}\boldsymbol{r}\psi_S^\dagger(\boldsymbol{r})\hat{H}_S(\boldsymbol{r})\psi_S(\boldsymbol{r}) + \frac{1}{2}\int\frac{\mathrm{d}\boldsymbol{k}}{(2\pi)^d}\psi_T^\dagger(\boldsymbol{k})\left[\epsilon_T(\boldsymbol{k}) - eV\right]\tau_z\psi_T(\boldsymbol{k}), \tag{2.63}$$

$$\text{and } \hat{V}_p = \frac{t}{2}\psi_T^\dagger(\boldsymbol{r_a})\tau_z\psi_S(\boldsymbol{r_0}) + \text{h.c.} \tag{2.64}$$

Then we can use the results of the previous sections and use the perturbative technique on the Keldysh contour.

2.3.2 Superconducting NEGF and their Dyson equations

Because of the pairing potential $\hat{\Delta}(\boldsymbol{r})$ in the superconducting sample, it is easy to realize that the *anomalous* Green's function $-i\langle\mathcal{T}_c[c_{\alpha\sigma}(\boldsymbol{r},z)c_{\beta\sigma}(\boldsymbol{r'},z')]\rangle$ are not necessarily vanishing and couple to the *normal* Green's function $G^c_{\alpha\beta,\sigma\sigma'}(\boldsymbol{r},z;\boldsymbol{r'},z')$. An elegant way to circumvent this problem is to treat electrons and holes on an equal footing and define the superconducting contour-ordered Green's functions $\hat{G}^c_{\alpha\beta}$, as well as their unperturbed counterpart $\hat{g}^c_{\alpha\beta}$,

$$\hat{G}^c_{\alpha\beta}(\boldsymbol{r},z;\boldsymbol{r'},z') = -\frac{i}{\hbar}\langle\mathcal{T}_c\psi_\alpha^\dagger(\boldsymbol{r},z)\otimes\psi_\beta(\boldsymbol{r'},z')\rangle, \tag{2.65}$$

$$\hat{g}^c_{\alpha\beta}(\boldsymbol{r},z;\boldsymbol{r'},z') = -\frac{i}{\hbar}\langle\mathcal{T}_c\psi_\alpha^\dagger(\boldsymbol{r},z)\otimes\psi_\beta(\boldsymbol{r'},z')\rangle_0, \tag{2.66}$$

where the $\hat{}$ symbol indicates that these functions are 4×4 matrices in the particle-hole$\otimes$spin space, and $\alpha,\beta\in\{S,T\}$ indicates the sub-system where the Nambu field acts. We recall that the notation $\langle...\rangle_0$, defined by equation (2.34) indicates equilibrium average with respect to $\hat{\rho}_0=e^{-\beta\mathcal{H}_0}/\operatorname{Tr}\{e^{-\beta\mathcal{H}_0}\}$ of operators evolving with respect to $\mathcal{H}_0$. Since the tip and sample are not coupled by the unperturbed Hamiltonian,

$$\hat{g}^c_{\alpha\beta}(\boldsymbol{r},z;\boldsymbol{r'},z')=\delta_{\alpha,\beta}\hat{g}^c_{\alpha\alpha}(\boldsymbol{r},z;\boldsymbol{r'},z')\equiv\delta_{\alpha,\beta}\hat{g}^c_{\alpha}(\boldsymbol{r},z;\boldsymbol{r'},z') \tag{2.67}$$

Using the perturbation technique (or alternatively the equation of motion), it is straightforward to show that $\hat{G}^c$ satisfies the following Dyson equations,

$$\hat{G}^c_{\alpha\beta}(\boldsymbol{r},z;\boldsymbol{r'},z')=\hat{g}^c_{\alpha\beta}(\boldsymbol{r},z;\boldsymbol{r'},z')+t\int_c \mathrm{d}z_1\hat{g}^c_{\alpha\gamma}(\boldsymbol{r},z;\boldsymbol{r_\gamma},z_1).\tau_z.\hat{G}^c_{\gamma\beta}(\boldsymbol{r_\gamma},z_1;\boldsymbol{r'},z'),\ \gamma\neq\alpha, \tag{2.68}$$

with $\boldsymbol{r}_\gamma=\boldsymbol{r}_0$ if $\gamma=S$ and $\boldsymbol{r}_\gamma=\boldsymbol{r}_a$ if $\gamma=T$. (2.68) is a closed set of equations allowing one to determine exactly $\hat{G}^c_{\alpha\beta}(\boldsymbol{r},z;\boldsymbol{r'},z')$ given the unperturbed Green's functions $\hat{g}^c_{\alpha\beta}(\boldsymbol{r},z;\boldsymbol{r'},z')$.

2.3.3 Exact expression of the average current I

Let us now come back to the expression of the electronic current. With our definition of the Green's functions, it is easy to show that I can be written as

$$I=et\,\mathrm{Re}\Big\{\operatorname{Tr}\Big\{\hat{G}^<_{ST}(\boldsymbol{r_0},\tau;\boldsymbol{r_a},\tau))(\tau_z+\tau_0)\Big\}\Big\}, \tag{2.69}$$

and only depends on $\hat{G}^<_{ST}(\boldsymbol{r_0},\tau;\boldsymbol{r_a},\tau)$. Therefore, for our purpose, it is not necessary to solve the whole set of Dyson equations on the real-time contour, and as we show below, to compute I, it is enough to focus on a reduced set of equations.

First, because $\mathcal{H}$ is time-independent, the real-time Green's functions depend only on the relative time difference, *i.e.* $\hat{G}^\gamma_{\alpha\beta}(\boldsymbol{r},\tau;\boldsymbol{r'},\tau')=\hat{G}^\gamma_{\alpha\beta}(\boldsymbol{r},\boldsymbol{r'},\tau-\tau')$, with $\gamma\in\{r,a,K,>,<\}$. Hence, it is convenient to use the Fourier transform of Green's functions,

$$\hat{G}^\gamma_{\alpha\beta}(\boldsymbol{r},\boldsymbol{r'},\omega)=\int\mathrm{d}\tau e^{\frac{i}{\hbar}\omega\tau}\hat{G}^\gamma_{\alpha\beta}(\boldsymbol{r},\boldsymbol{r'},\tau), \tag{2.70}$$

with $\gamma\in\{r,a,K,>,<\}$. Moreover, as we are interested in the expression of I we can restrict our attention to the set of Green's functions $\hat{G}^{r/a/<}_{\alpha\beta}(\boldsymbol{r_\alpha},t;\boldsymbol{r_\beta},t')$ and **omit the spatial arguments hereinafter**. Applying Langreth's rules to (2.68), it is straightforward to obtain the minimal set of equations determining the current,

$$\hat{G}^<_{ST}(\omega)=t\left[\hat{G}^<_{SS}(\omega)\tau_z g^a_T(\omega)+\hat{G}^r_{SS}(\omega)\tau_z g^<_T(\omega)\right], \tag{2.71}$$

$$\hat{G}^{r/a}_{SS}(\omega)=g^{r/a}_S(\omega)+t^2 g^{r/a}_S(\omega)\tau_z g^{r/a}_T(\omega)\tau_z\hat{G}^{r/a}_{SS}(\omega), \tag{2.72}$$

$$\hat{G}^<_{SS}(\omega)=g^<_S(\omega)+t^2\{g^<_S(\omega)\tau_z g^a_T(\omega)\tau_z\hat{G}^a_{SS}(\omega) \tag{2.73}$$

$$+g^r_S(\omega)\tau_z g^a_<(\omega)\tau_z\hat{G}^a_{SS}(\omega)+g^r_S(\omega)\tau_z g^r_T(\omega)\tau_z\hat{G}^<_{SS}(\omega)\}. \tag{2.74}$$

Thus, to determine the current, we only need the six unperturbed local Green's functions, $g^{r/a/<}_S(\omega)$ and $g^{r/a/<}_T(\omega)$. Noticing that, $\hat{G}^r_{\alpha\beta}(\omega)=[\hat{G}^a_{\beta\alpha}(\omega)]^\dagger$, we have the relations $g^r_{S/T}(\omega)=[g^a_{S/T}(\omega)]^\dagger$. Additionally, the unperturbed tip and sample are in thermodynamic equilibrium, in the grand-canonical ensemble, at their

respective chemical potential, μ_T, and μ_S. Therefore, the unperturbed Green's functions satisfy the so-called fluctuation-dissipation theorem,

$$g_S^<(\omega) = f(\omega)\left[g_S^a(\omega) - g_S^r(\omega)\right] \tag{2.75}$$

$$g_T^<(\omega) = \left[g_T^a(\omega) - g_T^r(\omega)\right].\hat{f}_T(\omega, eV), \tag{2.76}$$

$$\text{with } \hat{f}_T(\omega, eV) = f(\omega - eV)\frac{\tau_0 + \tau_z}{2} + f(\omega + eV)\frac{\tau_0 - \tau_z}{2}, \tag{2.77}$$

and $f(\omega) = 1/(1 + e^{\beta\omega})$ the Fermi-Dirac distribution. Consequently, once $g_T^r(\omega)$ and $g_S^r(\omega)$ specified, the current I is completely determined.

In principle, $g_S^r(\omega)$ and $g_T^r(\omega)$ respectively depends on the Hamiltonians $\mathcal{H}_S$ and $\mathcal{H}_T$. Nevertheless, remembering that we focus on a narrow energy window around the Fermi energy, it seems legitimate to neglect the energy dependence of the density of states (DOS) of the tip. Thus, the Green's functions of the uncoupled metallic tip read,

$$g_T^r(\omega) = -i\pi\nu_T\tau_0 \otimes \sigma_0, \tag{2.78}$$

$$g_T^<(\omega) = 2i\pi\nu_T\sigma_0 \otimes \hat{f}_T(\omega, eV), \tag{2.79}$$

with ν_T the DOS of the tip at the Fermi level. Within this wide-band approximation, the metallic tip is therefore completely characterized by the single parameter ν_T. Injecting the previous equations into (2.71), (2.72) and (2.73) we obtain,

$$I = -\frac{e\Gamma}{2\hbar}\int \mathrm{d}\omega\, \mathrm{Im}\Big\{\mathrm{Tr}\Big\{2\hat{G}_{SS}^r(\omega).f(\omega - eV).(\tau_0 + \tau_z) + \hat{G}_{SS}^<(\omega)(\tau_0 + \tau_z)\Big\}\Big\}, \tag{2.80}$$

$$\hat{G}_{SS}^r(\omega) = g_S^{r/}(\omega) - i\frac{\Gamma}{2}g_S^r(\omega)\hat{G}_{SS}^r(\omega), \tag{2.81}$$

$$\hat{G}_{SS}^<(\omega) = g_S^<(\omega) + i\frac{\Gamma}{2}\left[g_S^<(\omega)\hat{G}_{SS}^a(\omega) + 2g_S^r(\omega)\hat{f}_T(\omega, eV)\hat{G}_{SS}^a(\omega) - g_S^r(\omega)\hat{G}_{SS}^<(\omega)\right], \tag{2.82}$$

with $\Gamma = 2\pi\nu_T t^2$. Obviously, within our theoretical description, the current I is determined by the tunneling rate Γ characterizing the STS junction and $g_S^r(\omega)$, which locally characterize the spectral properties of the sample. Therefore, the current I depends on the local spectral electronic properties of the sample encoded in $g_S^r(\omega)$, as we shall show in the next subsection.

2.3.4 Tunneling regime and linear-response

In the small tunneling rate limit $\Gamma \to 0$, also known as the tunneling regime, it seems legitimate to expand the current in powers of Γ and retain the lowest order term, the linear one. Following this procedure, it is straightforward to show that the current becomes,

$$\begin{aligned} I &\simeq -\frac{e\Gamma}{2\hbar}\int \frac{\mathrm{d}\omega}{2\pi}\,\mathrm{Im}\big\{\mathrm{Tr}\big\{2\hat{g}_S^r(\omega).f(\omega - eV).(\tau_0 + \tau_z) + \hat{g}_S^<(\omega)(\tau_0 + \tau_z)\big\}\big\} \\ &\simeq -\frac{e\Gamma}{2\hbar}\int \frac{\mathrm{d}\omega}{2\pi}\,\mathrm{Im}\{\mathrm{Tr}\{2\hat{g}_S^r(\omega).f(\omega - eV).(\tau_0 + \tau_z) - 2\hat{g}_S^r(\omega)(\tau_0 + \tau_z)f(\omega)\}\} \\ &\simeq \frac{e\Gamma}{\hbar}\int \mathrm{d}\omega\rho_S(\omega).[f(\omega - eV) - f(\omega)], \end{aligned} \tag{2.83}$$

where we defined the local electronic density of states (LDOS) of the isolated sample

$$\rho_S(\omega) = -\frac{1}{2\pi}\,\mathrm{Im}\{\mathrm{Tr}\{g_S^r(\omega)(\tau_0+\tau_z)\}\}. \tag{2.84}$$

This result can also be derived from the Fermi golden rule or linear-response theory. Using equation (2.83) it is straightforward to show that, in the tunneling regime, the differential conductance $G = \frac{\mathrm{d}I}{\mathrm{d}V}$ is given by,

$$G = \frac{e^2\Gamma}{\hbar k_B T}\int \mathrm{d}\omega \rho_S(\omega)\frac{e^{\beta(\omega-eV)}}{\left(1+e^{\beta(\omega-eV)}\right)^2} \underset{T\to 0}{\simeq} \frac{e^2\Gamma}{\hbar}\rho_S(\omega=eV). \tag{2.85}$$

Consequently, the differential conductance spectrum measured by STS at very low temperatures directly yields the LDOS of the sample, provided that the experiment is performed in a tunneling regime. This result proves that the STS technique is well-suited to study spectral electronic properties with good spatial and energy resolution. In practice, the energy resolution is limited by the experimental temperature. Indeed, the convolution product of the LDOS with the Fermi-Dirac derivative in (2.85) broadens the LDOS. Note that this limitation can, however, be circumvented if one uses a superconducting tip instead of a metallic one due to the sharp BCS resonances [32].

2.3.5 Beyond the linear-response the BCS example

In the previous subsection, we show that the Keldysh NEGF technique reproduces the results of the linear response theory in the tunneling regime. However, since the NEGF technique exactly describes non-equilibrium states, it allows us to go beyond the tunneling limit and study non-linear effects. In this subsection, we illustrate the efficiency of the Keldysh technique in the case of a clean BCS sample which allows for exact analytical treatment. In that case, both the sample and the tip have a $U(1)$ spin-rotation invariance. Hence it is convenient to use the *reduced* BdG formalism and write,

$$\begin{aligned}\mathcal{H} = \int \frac{\mathrm{d}\boldsymbol{k}}{(2\pi)^{d_S}}\psi_S^\dagger(\boldsymbol{k})\left[\epsilon_S(k)\tau_z + \Delta\tau_x\right]\psi_S(\boldsymbol{k}) + \int \frac{\mathrm{d}\boldsymbol{k}}{(2\pi)^{d_T}}\psi_T^\dagger(\boldsymbol{k})\epsilon_T(k)\tau_z\psi_T(\boldsymbol{k}) \\ + t\psi_S^\dagger(\boldsymbol{r_0})\psi_T(\boldsymbol{r_a}) + \mathrm{h.c.},\end{aligned} \tag{2.86}$$

with $\psi_\alpha(\boldsymbol{k}) = [c_{\alpha\uparrow}(\boldsymbol{k}), c_{\alpha\downarrow}^\dagger(\boldsymbol{k})]^T$ the Nambu spinor in the sub-system α, the operator annihilating an electron of spin σ and momentum $\hbar\boldsymbol{k}$ in the sub-system α, $\psi_\alpha(\boldsymbol{r_\alpha}) = \int \frac{\mathrm{d}\boldsymbol{k}}{(2\pi)^{d_\alpha}} e^{i\boldsymbol{k}.\boldsymbol{r_\alpha}}\psi_\alpha(\boldsymbol{k})$ and d_α the dimension of the sub-system α. The sample is characterized by its dispersion relation $\epsilon_S(\boldsymbol{k})$ and the BCS gap Δ, which, without loss of generality, is chosen as real and positive.

Because we work within the *reduced* BdG formalism, the contour-ordered superconducting Green's functions defined in (2.65) and (2.66) are, here, 2×2 matrices acting in the particle-hole space. It is easy to show that this modified definition of the superconducting Green's functions does not affect the Dyson equations and that these *reduced* superconducting Green's functions still obey (2.68). On the contrary, one can easily show that the expression of the average current is modified by a factor 2:

$$I = 2\frac{et}{\hbar}\int \frac{\mathrm{d}\omega}{2\pi}\,\mathrm{Re}\,\mathrm{Tr}\{G_{ST}^<(\omega)\}. \tag{2.87}$$

Since the Dyson equations on the contour are unchanged, the current can be calculated thanks to the three equations (2.71), (2.72), (2.73). The Green's functions describing the isolated metallic tip are given by:

$$\hat{g}_T^r(\omega) = -i\pi\nu_T\tau_0, \tag{2.88}$$

$$\hat{g}_T^<(\omega) = 2i\pi\nu_T\hat{f}_T(\omega, eV), \tag{2.89}$$

which corresponds to the projection of (2.88) and (2.89) on the spin-up sector. In order to evaluate the current, we also need the local retarded Green's function of the isolated sample $\hat{g}_S^r(\omega)$. Using the equation of motion of the Nambu spinor $\psi_S(\boldsymbol{k})$, it is straightforward to show that[1]:

$$\hat{g}_S^r(\omega) = \int \frac{\mathrm{d}\boldsymbol{k}}{(2\pi)^{d_S}} \frac{\omega + \epsilon_S(\boldsymbol{k})\tau_z + \Delta\tau_x}{\omega^2 - \epsilon_S^2(\boldsymbol{k}) - \Delta^2} = \int \mathrm{d}\epsilon\nu(\epsilon)\frac{\omega + \epsilon\tau_z + \Delta\tau_x}{\omega^2 - \epsilon^2 - \Delta^2}, \tag{2.90}$$

where in the last equality, we used the normal-state density of states of the BCS sample, $\nu(\epsilon)$, and traded the integral over momentum for an integral over energies. Recalling that the relevant energy range for transport properties is a narrow energy window around the Fermi level. We can safely neglect the energy dependence of $\nu(\epsilon)$ and use the wide-band approximation: $\nu(\epsilon) \simeq \nu_0$ with ν_0 the density of states at the Fermi energy. Therefore, after straightforward algebra, one obtains:

$$\hat{g}_S^r(\omega) = -\pi\nu_0 \frac{\omega + i\eta + \Delta\tau_x}{\sqrt{\Delta^2 - (\omega + i\eta)^2}}, \tag{2.91}$$

with η a small phenomenological energy relaxation rate, accounting for the damping of quasiparticles due to inelastic processes inside the BCS sample. Typical values for η in traditional BCS superconductors is $\eta/\Delta \sim 10^{-2}$ [73]. Thus, η can be viewed as the smallest energy scale of the problem and considered as zero.

Inserting the above-mentioned unperturbed Green's functions into equations (2.71), (2.72), (2.73), one obtains [28]:

$$I = \frac{2e}{h}\int \mathrm{d}\omega T_N(\omega)\left[f(\omega - eV) - f(\omega)\right] + 2R_A(\omega)\left[f(\omega - eV) - f(\omega + eV)\right], \tag{2.92}$$

$$\text{with } T_N(\omega) = \begin{cases} 0 & , \text{ if } |\omega| \leq \Delta \\ 2\alpha\frac{\alpha\left[1-\Delta^2/\omega^2\right]+(2-\alpha)\sqrt{1-\Delta^2/\omega^2}}{\left[\alpha^2+(2-\alpha)\sqrt{1-\Delta^2/\omega^2}\right]^2} & , \text{ if } |\omega| \geq \Delta \end{cases}, \tag{2.93}$$

$$\text{and } R_A(\omega) = \begin{cases} \frac{\alpha^2}{(2-\alpha)^2-4(1-\alpha)\omega^2/\Delta^2} & , \text{ if } |\omega| \leq \Delta \\ \frac{\alpha^2\left[1-\Delta^2/\omega^2\right]+(2-\alpha)\sqrt{1-\Delta^2/\omega^2}}{\left[\alpha^2+(2-\alpha)\sqrt{1-\Delta^2/\omega^2}\right]^2} & , \text{ if } |\omega| \geq \Delta \end{cases}. \tag{2.94}$$

Here $\alpha = \frac{4t^2\pi^2\nu_T\nu_0}{[1+t^2\pi^2\nu_T\nu_0]^2}$ is the normal-state transmission of the STM junction [28]. Let us now give a physical interpretation of this expression. To do so, we inspect the elementary transmission processes that electrons can undergo.

First, an occupied electron in the metallic tip at energy ω can be transmitted into unoccupied quasiparticle states of the sample, transferring a charge equal to e across the junction, as illustrated in Fig. 2.5 (a). Occupied quasiparticles in the sample undergo complementary processes transferring a charge $-e$ across the junction.

[1] see the Supplementary Material of [30] for details

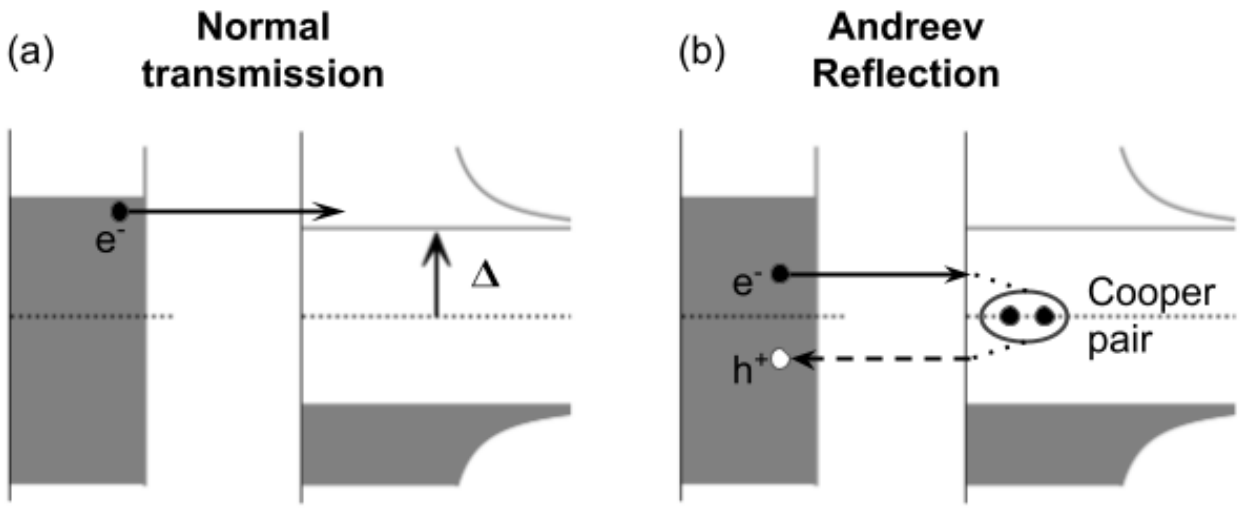

Figure 2.5: Schematic representation of the normal transmission (a) and Andreev reflection (b) processes that take place at the STM junction connecting the metallic tip to the superconducting sample. Notice that contrary to Andreev reflections, which take place at any energy, normal transmission cannot occur at energies ω inside the BCS gap, $|\omega| < \Delta$.

Such processes are nothing but normal transmissions that electrons undergo at the interface between normal metals. Notice that these processes can not occur when $|\omega| < \Delta$, since no quasiparticles are available in this energy range.

Second, due to the presence of a pair condensate in the superconducting sample, occupied electrons in the metallic can be reflected into unoccupied hole states with opposite spin of the metallic tip, transferring a Cooper pair into the condensate, as illustrated in Fig. 2.5 (b). Such a process, known as an Andreev reflection, transfers a charge $2e$ across the sample. Holes undergo complementary processes. Such processes are present at any energy.

Inspecting the occupation factors, one directly identifies the first term in (2.92) as the current produced by normal transmissions and the second one as the current carried by Andreev reflections. Hence, $T_N(\omega)$ is nothing but the probability of normal transmission of electrons at energy ω and $R_A(\omega)$ the probability of Andreev reflections. Therefore, equation (2.92) simply tells us that current is the sum of the probabilities of the different processes weighted by their corresponding charges. The factor 2 in (2.92) comes from the spin-degeneracy.

In the zero-temperature limit, it is straightforward to show that (2.92) directly yields the differential conductance G:

$$G(V) = \begin{cases} \frac{4e^2}{h} \frac{\alpha^2}{(2-\alpha)^2 - 4(1-\alpha)(eV/\Delta)^2} & , \text{ if } |eV| \leq \Delta, \\ \frac{4e^2}{h} \frac{\alpha}{\alpha^2 + (2-\alpha)\sqrt{1-\Delta^2/\omega^2}} & , \text{ if } |eV| \geq \Delta. \end{cases} \tag{2.95}$$

This expression sharply contrasts with the results of the linear-response theory or tunneling theory that predicts a conductance $G(V)$ proportional to the density of the BCS superconductor. Particularly, according to the linear-response theory, $G(V)$ should vanish inside the BCS gap. This is due to the fact that Andreev reflections

require the transfer of two charge carriers across the junction. Hence, their probability is $\propto \alpha^2 \propto t^4$, which cannot be captured by the linear response theory. It is also interesting to remark that for $eV = \pm\Delta$, $G(V)$ is independent of the transmission α. As highlighted by J. C. Cuevas in his thesis [28], this result can not be obtained by finite order perturbation theory with respect to tip-sample coupling and requires summing up all processes up to infinite order. For example, the linear-response theory predicts a diverging conductance due to the coherence peaks in the BCS density of states. Hence, the BCS example clearly shows that the Keldysh theory is a powerful technique that allows one to describe quantum transport phenomena that are not accessible by the standard linear-response, *a.k.a* tunneling theory.

Chapter 3

Odd-frequency pairing around magnetic impurities

The presence of magnetic impurities in a superconductor modifies the superconducting state of the substrate. Hence, magnetic impurities can be used to engineer exotic superconducting phases that are originally absent in the clean superconductor. In this chapter, we will show that a single classical spin immersed in a s-wave superconductor locally breaks the time-reversal symmetry and locally induces *unconventional* s-wave spin-triplet and odd-frequency pair correlations. This chapter is organized as follows: First, we briefly introduce the concept of odd-frequency pairing. Second, after a brief historical review of the field, we discuss the well-known spectral and spatial properties of the YSR states. Then, we explicitly compute the pairing functions at the YSR core and show that the local electronic density of state, directly measured in STS experiments, is proportional to the imaginary part of the odd-frequency pairing function. Using the former result, we propose a method to extract the imaginary part of the odd-frequency pairing function from STS data. Finally, we illustrate our method for STS data measured by G. C. Ménard, *et al.* at the Institut des Nanosciences de Paris. Our results show experimental evidence of odd-frequency pairing around YSR states.

3.1 Introduction to odd-ω pairing

Pairing functions were originally introduced as the chronologically time-ordered anomalous Green's functions, $f^T_{\sigma\sigma',ab}(\boldsymbol{r},t;\boldsymbol{r}',t') = \frac{-i}{\hbar}\langle\mathcal{T}[c_{\sigma a}(\boldsymbol{r},t)c_{\sigma' b}(\boldsymbol{r}',t')]\rangle$, where a,b denote any orbital/band degree of freedom while σ,σ' are spin indices of the 2 fermions. Pairing functions describe how the electrons making up Cooper pairs are correlated to each other. Because of the fermionic anti-commutation relation, any pairing function has to fulfill the symmetry constraint,

$$f^T_{\sigma\sigma',ab}(\boldsymbol{r},t;\boldsymbol{r}',t') = -f^T_{\sigma'\sigma,ba}(\boldsymbol{r}',t';\boldsymbol{r},t). \tag{3.1}$$

Introducing the spin, orbital, spatial coordinates and time coordinates permutation operator S, O, P^*, and T^*, pairing functions must satisfied the relation $SP^*OT^*f_{\sigma\sigma',ab}(\boldsymbol{r},t;\boldsymbol{r}',t') = -f_{\sigma\sigma',ab}(\boldsymbol{r},t;\boldsymbol{r}',t')$, which is symbolically written $SP^*OT^* = -1$ ([29]). This rule is often called the Berezinskii rule [74]. Since $S^2 = O^2 = (P^*)^2 = (T^*)^2 = 1$, there exist $2^3 = 8$ possible pairings, summarized in the 8-fold classification of Table. 3.1. Odd-frequency (odd-ω) pairings refer to all possible pairings which are odd under time argument

S	P^*	O	T^*	Total
-1	1	1	1	-1
1	-1	1	1	-1
1	1	1	-1	-1
-1	-1	1	-1	-1
1	1	-1	1	-1
-1	-1	-1	1	-1
-1	1	-1	-1	-1
1	-1	-1	-1	-1

Table 3.1: Berezinskii classification of the pairing function according to their symmetries properties (adapted from [29]).

permutation T^*. On the contrary, even-frequency pairing denotes any pairing function which is even under T^*. It is important to remark that the Berezinskii classification is based on the chronologically-ordered GF. It is easy to show that the Matsubara pairing function $f^M_{\sigma\sigma',ab}(\boldsymbol{r},\tau;\boldsymbol{r}',\tau')$ is subjected to the exact same Berezinskii constraint than $f^T_{\sigma\sigma',ab}(\boldsymbol{r},t;\boldsymbol{r}',t')$. However, the retarded and advanced pairing functions $f^r_{\sigma\sigma',ab}(\boldsymbol{r},t;\boldsymbol{r}',t')$ and $f^a_{\sigma\sigma',ab}(\boldsymbol{r},t;\boldsymbol{r}',t')$ obey a different constraint,

$$f^r_{\sigma\sigma',ab}(\boldsymbol{r},t;\boldsymbol{r}',t') = -f^a_{\sigma'\sigma,ba}(\boldsymbol{r}',t';\boldsymbol{r},t). \tag{3.2}$$

In conventional low-T_c BCS superconductors, the pairing function is spin-singlet, even under the exchange of spatial coordinates and even under the exchange of time coordinates of the electrons, hence even-frequency.

Odd-ω pairing corresponds to non-local correlations in time, suggesting that electrons must avoid each other in time as they are uncorrelated when their time coordinates are equal. This unconventional pairing was first originally proposed by Berezinskii in 1974 [74], who suggested that the superfluid phase of He^3 a s-wave spin-triplet pairing state arises. In the early nineties, subsequent theoretical studies focused on intrinsic odd-ω in superconductors and the underlying microscopic mechanisms. In 1992, Balatsky *et al.* proposed a new class of spin-singlet odd-ω superconductors, enumerated their physical properties [75], and suggested that the conventional electron-phonon interaction was sufficient to generate odd-ω. However, later studies showed that renormalization effects prevent this [76, 77]. Instead, a generic spin- and frequency-dependent interaction can produce odd-ω pairing states [76, 77]. Such spin-dependent terms might come from antiferromagnetic interactions [76], and spin fluctuations mediated interaction was later proposed as a possible realization of spin-singlet p-wave odd-ω pairing [78]. Odd-ω pairing can also appear in heavy fermion compounds described by a Kondo lattice [79, 80, 81]. An exhaustive review of the possible scenarios realizing intrinsic odd-ω pairing is beyond the scope of the present manuscript. The interested reader is invited to consult the excellent review by J. Linder, and A. V. Balatsky [29].

After a less active period in the late nineties, the field boomed in 2001 when Bergeret *et al.* realized that odd-ω could be engineered in heterostructures made of a conventional s-wave superconductor and a ferromagnet [82, 83]. Oppositely to previous studies, here, the odd-ω pairing is not intrinsically present but originates from the proximity effect of the ferromagnet converting spin-singlet Copper pairs to spin-triplet ones. Thanks to this conversion, Cooper robustly propagates far away in the ferromagnetic, opening the exciting possibility of achieving superconducting spintronics [84, 85]. In fact, odd-ω is rather ubiquitous in hybrid systems and

appears in a wide range of systems as a result of a given symmetry breaking (see [29] and [86] for a comprehensive review). As an example, odd-ω pairing even occurs in the most simple hybrid system one can think of, a junction between a ballistic metal and a *conventional* superconductor. Because the interface locally breaks the spatial inversion symmetry, spin-singlet, even-ω, and s-wave Cooper pairs are converted into spin-singlet, odd-ω, and p-wave ones. More recently, it was shown that Majorana zero modes in superconducting structures are inevitably accompanied by the presence of odd-ω pairings, establishing a strong relation between them [87]. Nevertheless, there is not yet any direct, unambiguous evidence of odd-ω superconductivity, even if spectroscopic signatures in the density of states were observed in Nb superconducting films coupled to Ho by proximity effect [88].

In this chapter, we take a step forward in this direction. We focus on one of the simplest hybrid systems: a single magnetic adatom immersed into a conventional s-wave spin-singlet superconductor. Because the impurity breaks both the time-reversal symmetry, it can convert s-wave spin-singlet Cooper pairs into s-wave spin-triplet ones. Focusing on the local pairings at the impurity site, we will show that the locally broken time-reversal symmetry efficiently converts s-wave spin-singlet Cooper pairs into s-wave spin-triplet, hence odd-ω, ones. In addition, we will show that the odd-ω pairing is tightly linked to the existence of superconducting sub-gap states known as Yu-Shiba-Rusinov (YSR) states. Finally, we will establish a proportionality relation between the local density of states measured by STS experiments and the odd-ω pairing and provide experimental evidence for the existence of local odd-ω superconductivity. Before investigating odd-ω around magnetic impurities, we briefly review the basic properties of magnetic impurities immersed in BCS superconductors.

3.2 Magnetic impurities and Yu-Shiba-Rusinov (YSR) states

3.2.1 A brief historical overview

Soon after the advent of the BCS theory, Anderson showed its famous theorem stipulating that time-reversal symmetric perturbation does not alter a *conventional* BCS superconductor [6]. Hence, scalar impurities immersed in a superconductor do not produce any sub-gap states. This result suggests that on the contrary magnetic impurities which break the time-reversal symmetry may strongly affect the superconducting state. Indeed, Abrikosov and Gor'kov early showed that a finite concentration of magnetic impurities in a BCS superconductor is responsible for a decrease in the BCS gap and critical temperature T_C. Later on, L. Yu [8], H. Shiba [9], and A. I. Rusinov [10] independently demonstrated that an isolated *classical* magnetic impurities is responsible for a Cooper pair breaking potential and gives rise to low-energy excited states, named Yu-Shiba-Rusinov states, lying inside the excitation gap of the superconductor. In a nutshell, these states correspond to quasiparticle excitations which are fully spin-polarized and localized around the impurity [8, 9, 10]. Since a single YSR state is a coherent superposition of electron- and hole-like states, it manifests itself in the LDOS as a pair of sub-gap peaks localized at opposite energy with respect to the Fermi level.

While their theoretical prediction dates back to the sixties, the experimental observation of YSR states remained in its infancy until recently, mainly because of the high spatial and energy resolution, at temperatures well below T_c, required. Thanks to the development of *in vacuo* preparation techniques, deposition of magnetic ad-atoms and scanning tunneling microscopy/spectroscopy YSR were first observed in 1997 by Yazdani *et al.* [11].

Since their prediction, our theoretical understanding of the YSR states progressed considerably. Follow-

ing [8, 9, 10], many subsequent theoretical studies focused on *classical* spin model for the impurity (see [89] for a review). These addressed various interesting features of YSR states, including their spectral properties [8, 9, 10, 90, 39], the spatial extent of their wavefunctions [8, 9, 10, 18], and the renormalization of the superconducting gap [90, 91, 92] to list a few. Magnetic impurities were also proposed as a probe of the underlying superconductor [93]. Complexities due to crystal field splitting [94, 91], spin-orbit coupling [95, 93] and, very recently, Fermi surface anisotropy also received attention [19, 96]. Theoretical investigations also predicted the coupling of two impurities long before their experimental investigations [97, 98, 99, 92]. More recently, these theoretical investigations were expanded to the coupling of multiple impurities in 1D chains. The hybridization between YSR states leads to the formation of early predicted Shiba bands [9]. Majorana zero modes were predicted in chains of magnetic atoms with ferromagnetic [12, 100, 101, 102] and spiral [103, 104, 105, 106, 107] magnetic order, as a result of the proximity induced p-wave superconductivity inside Shiba bands. It was also proposed to engineer 2D p-wave topological superconducting phases thanks to 2D arrays of magnetic impurities [108, 109].

It is important to stress that, all the previous results, obtained with *classical* spin models, are only valid when the quantum dynamics of the impurity can be neglected, *i.e.*, when $S_{imp} \gg \hbar$ or in the presence of strong magnetic anisotropy. Despite some early attempts using analytical methods, most of the studies focusing on quantum impurity models appeared later because they require much more demanding calculations. Different techniques were employed to tackle quantum models, such as mean-field approximations [110], perturbation theory [111, 112], or numerical renormalization group theory [113, 114, 115, 116], giving valuable insights into spectral properties around single impurities. Very recently, a simplified model based on the zero-bandwidth approximation for the superconductor was proposed and showed good qualitative agreement with previous results obtained via the numerical renormalization group. This simplified model already provided valuable insights into the spectral properties of single impurities, dimers, and chains of quantum impurities with reduced computational efforts [117, 118, 119].

Since this thesis focuses on the original YSR model of *classical* magnetic impurities [8, 9, 10], we do not discuss the results of quantum models, which are reviewed in [89].

Motivated by the improved resolution of STM/STS techniques and the aspects in connection with topological superconductors, the experimental characterization of YSR states experienced a renewed interest during the last decades and remains an active field of research (see [17] for a detailed review of the field). A decade after the pioneering experiment of Yazdani *et al.* [11], experiments at lower temperatures and the use of superconducting tips allowed a better energy resolution of YSR states, [120, 121, 122, 123, 32]. Before assembling them in more complex structures, a detailed understanding of the properties of single YSR state is necessary. That's why several groups focused on resolving the spatial decay of the YSR wavefunction, and its peculiarities [124, 125, 18], the orbital character of YSR multiplets [124, 125], or the tunneling processes into YSR states [32, 126]. The proposal of building topological superconductors from YSR chains pushed the field even further. Experimental characterization of YSR dimers [127, 128, 129] yields a better understanding of the interaction between impurities. Very recently, the realization of YSR chains reported features suggesting the existence of Majorana edge modes [130].

In the next subsection, we focus on the *classical* model for isolated magnetic impurities originally introduced by L. Yu, H. Shiba, and A. I. Rusinov [8, 9, 10], following the method proposed by L. Yu and A. I. Rusinov, we show the existence of the YSR states and discuss some of their spectral and spatial properties.

3.2.2 The Yu-Shiba-Rusinov model

Let us consider a single isolated magnetic impurity with spin $\boldsymbol{S}_{imp}$ immersed in a conventional s-wave superconductor. Following [8, 9, 10], we assume that the spin of the magnetic impurity is large, $S_{imp} \gg \hbar$, or is subjected to a strong magnetic anisotropy. It is thus legitimate to neglect the quantum fluctuations of the impurity spin and to replace it with a *classical* magnetic moment. For simplicity, we also assume that the superconducting substrate is a single-band superconductor. Finally, we consider a point-like impurity corresponding to Dirac's delta scattering potential in real space. Consequently, the Hamiltonian of the system reads,

$$\begin{aligned}\mathcal{H}_{\mathrm{YSR}} = \int \sum_{\sigma} c^{\dagger}_{S\sigma}(\boldsymbol{r})[\varepsilon_S(\boldsymbol{k}) - \mu]c_{S\sigma} + \Delta[c^{\dagger}_{S\uparrow}(\boldsymbol{r})c^{\dagger}_{S\downarrow}(\boldsymbol{r}) + c_{S\downarrow}(\boldsymbol{r})c_{S\uparrow}(\boldsymbol{r})]\mathrm{d}\boldsymbol{r} \\ + \sum_{\sigma,\sigma'} c_{S\sigma}(\boldsymbol{r}_{\mathrm{imp}})[-J\boldsymbol{\sigma}.\frac{\boldsymbol{S}_{\mathrm{imp}}}{|\boldsymbol{S}_{\mathrm{imp}}|} + U\delta_{\sigma,\sigma'}]c_{S\sigma'}(\boldsymbol{r}_{\mathrm{imp}}),\end{aligned} \tag{3.3}$$

where $c_{S,\sigma}(\boldsymbol{r})$ annihilates an electron of spin σ at the position $\boldsymbol{r}$ in the superconducting substrate. Δ is the BCS gap of the host material, which, without loss of generality, we assume to be real. $\varepsilon_S(\boldsymbol{k})$ is the energy dispersion of the normal electrons in the superconductor, $\hbar\boldsymbol{k} \equiv -i\hbar\nabla_{\boldsymbol{r}}$ the momentum operator. The electrons are coupled to the impurity spin $\boldsymbol{S}_{\mathrm{imp}}$ by a magnetic exchange of strength J and a normal scattering term of strength U.

In the absence of the impurity, the Hamiltonian of the clean superconductor is invariant under spatial translations and $SU(2)$ spin-rotation. Thus, without loss of generality we can choose $\boldsymbol{r}_{\mathrm{imp}} = \boldsymbol{0}$ and $\boldsymbol{S}_{\mathrm{imp}} = S\boldsymbol{e}_z$ to point in the $\boldsymbol{e}_z$ direction. Note that changing the sign of J is equivalent to exchanging the $\uparrow$ and $\downarrow$ spins. Hence, without loss of generality, we can focus on the case of ferromagnetic coupling and assume $J > 0$. One can easily notice that the $\mathcal{H}_{\mathrm{YSR}}$ enjoys a $U(1)$ spin rotation symmetry along the impurity axis. Therefore, we use the *reduced* BdG formalism,

$$\mathcal{H}_{\mathrm{YSR}} = \int \mathrm{d}\boldsymbol{r}\psi^{\dagger}_S(\boldsymbol{r})\{[\varepsilon_S(\boldsymbol{k}) - \mu]\tau_z + \Delta\tau_x - \delta(\boldsymbol{r} - \boldsymbol{r}_{\mathrm{imp}})[-J\tau_0 + U\tau_z]\}\psi_S(\boldsymbol{r}), \tag{3.4}$$

$$= \int \mathrm{d}\boldsymbol{r}\psi^{\dagger}_S(\boldsymbol{r})\hat{H}_{\mathrm{YSR}}(\boldsymbol{r})\psi_S(\boldsymbol{r}), \tag{3.5}$$

where $\psi_S = (c_{\uparrow}(\boldsymbol{r}), c^{\dagger}_{\downarrow}(\boldsymbol{r}))^T$.

In the next subsection, we show that, because the magnetic exchange induced by the impurity acts as a pair breaking potential, $\hat{H}_{\mathrm{YSR}}$ possesses an eigenstate with energy E_0 inside the superconducting gap: the YSR bound-state. Depending on the sign of E_0, the YSR state describes an excited or (spontaneously) occupied *Bogoliubov* quasiparticle.

3.2.3 YSR sub-gap state

The Yu-Shiba-Rusinov bound-state can be found by the Green's function method, as Shiba did in its seminal paper, or by solving the Schrödinger equation governing the dynamics of the Nambu spinor. Here we chose to use the second method and seek for the eigenstates $\phi(\boldsymbol{r})$ of $\hat{H}_{YSR}$ with energy E inside the gap,

$$\hat{H}_{\mathrm{YSR}}(\boldsymbol{r})\phi(\boldsymbol{r}) = E\phi(\boldsymbol{r}), \tag{3.6}$$

with $|E| < \Delta$. Since the single-particle Hamiltonian $\hat{H}_{\mathrm{YSR}}$ is real, we can impose the eigenstates to be real $\phi(\boldsymbol{r}) \in \mathbb{R}^2$. After a Fourier transformation (3.6) reads

$$\{(\epsilon(\boldsymbol{k}) - \mu)\tau_z + \Delta\tau_x - E\tau_0\}\phi(\boldsymbol{k}) = -(-J\tau_0 + U\tau_z)\phi(\boldsymbol{r} = \boldsymbol{0}) \tag{3.7}$$

$$, \Rightarrow \phi(\boldsymbol{k}) = \frac{E + \xi(\boldsymbol{k})\tau_z + \Delta\tau_x}{E^2 - \xi(\boldsymbol{k})^2 - \Delta^2}(U\tau_z - J\tau_0)\phi(\boldsymbol{0}), \tag{3.8}$$

where $\phi(\boldsymbol{k}) = \int \mathrm{d}\boldsymbol{r} e^{-\boldsymbol{k}.\boldsymbol{r}}\phi(\boldsymbol{r})$ and $\xi(\boldsymbol{k}) = \epsilon(\boldsymbol{k}) - \mu$. Therefore, integrating (3.8) over $\boldsymbol{k}$, one obtains a closed equation for $\phi(\boldsymbol{0})$,

$$\phi(\boldsymbol{0}) = \int \frac{\mathrm{d}\boldsymbol{k}}{2\pi^d} \frac{E + \xi(\boldsymbol{k})\tau_z + \Delta\tau_x}{E^2 - \xi(\boldsymbol{k})^2 - \Delta^2}(U\tau_z - J\tau_0)\phi(\boldsymbol{0}), \tag{3.9}$$

with d the dimension of the superconducting substrate. This equation possesses nontrivial solutions if and only if

$$\det\left\{\tau_0 - \int \frac{\mathrm{d}\boldsymbol{k}}{2\pi^d} \frac{E + \xi(\boldsymbol{k})\tau_z + \Delta\tau_x}{E^2 - \xi(\boldsymbol{k})^2 - \Delta^2}(U\tau_z - J\tau_0)\right\} = 0. \tag{3.10}$$

Then we trade the integral over momentum for an integral over energies:

$$\det\left\{\tau_0 - \int_{-\mu}^{\infty} \mathrm{d}\xi\nu(\xi) \frac{E + \xi\tau_z + \Delta\tau_x}{E^2 - \xi^2 - \Delta^2}(U\tau_z - J\tau_0)\right\} = 0. \tag{3.11}$$

We stress that we are interested in energies $|E| < \Delta$. Moreover, for usual BCS superconductors, Δ is much smaller than the Fermi energy, μ. Hence, we can safely assume $\nu(\xi)$ varies slowly on the energy scale Δ around the Fermi level (*i.e.* $\xi = 0$), use the wide-band approximation: $\nu(\xi) \simeq \nu(0) \equiv \nu_0$, and send the integration limits to infinity. With these approximations, the integral can be performed analytically and yields the characteristic equation:

$$\det\left\{\tau_0 + \pi\nu_0 \frac{E + \Delta\tau_x}{\sqrt{\Delta^2 - E^2}}(U\tau_z - J\tau_0)\right\} = 0, \tag{3.12}$$

This equation has a single solution inside the gap:

$$E_0 = \Delta \frac{1 - \alpha^2 + \beta^2}{\sqrt{4\alpha^2 + (1 - \alpha^2 + \beta^2)^2}}, \tag{3.13}$$

with $\alpha \equiv \pi\nu_0 J$, and $\beta \equiv \pi\nu_0 U$. E_0 is the energy of the YSR bound-state. With E_0 in hand, the associated wavefunction $\phi_0(\boldsymbol{r})$ is easily found. Using (3.9) we find,

$$\frac{u(\boldsymbol{0})}{v(\boldsymbol{0})} = \left(\frac{1 + (\alpha + \beta)^2}{1 + (\alpha - \beta)^2}\right)^{1/2}. \tag{3.14}$$

Imposing the normalization condition, $\int \frac{\mathrm{d}\boldsymbol{k}}{(2\pi)^d}\phi_0(\boldsymbol{k})^\dagger\phi_0(\boldsymbol{k}) = 1$, we obtain,

$$\phi_0(\boldsymbol{0}) = \frac{\sqrt{2\pi\nu_0\Delta\alpha}}{\left(4\alpha^2 + (1 + \beta^2 + \alpha^2)^2\right)^{3/4}} \begin{bmatrix} \sqrt{1 + (\beta + \alpha)^2} \\ \sqrt{1 + (\beta - \alpha)^2} \end{bmatrix}. \tag{3.15}$$

Following Rusinov [10], we introduce the scattering phases $\delta^{\pm}$, defined by:

$$\tan\delta^{\pm} \equiv \beta \pm \alpha, \tag{3.16}$$

and finally obtain:

$$E_0 = \Delta\sqrt{\cos(\delta^+ - \delta^-)},\ \phi_0(\mathbf{0}) = \begin{bmatrix}\cos\delta^- \\ \cos\delta^+\end{bmatrix}\sqrt{2\pi\nu_0\Delta\alpha\cos\delta^+\cos\delta^-}. \tag{3.17}$$

Therefore, injecting (3.15) into (3.8), and performing a Fourier transform, we obtain the complete spatial dependence of the YSR wavefunction,

$$\phi_0(\boldsymbol{r}) = \int \frac{\mathrm{d}\boldsymbol{k}}{(2\pi)^d} e^{i\boldsymbol{k}.\boldsymbol{r}} \frac{E_0 + \xi(\boldsymbol{k})\tau_z + \Delta\tau_x}{E_0^2 - \xi(\boldsymbol{k})^2 - \Delta^2}(U\tau_z - J\tau_0).\phi_0(\mathbf{0}). \tag{3.18}$$

Consequently, to obtain the wavefunction in real space, we need to compute the two integrals:

$$f_0(\boldsymbol{r}) = \int \frac{\mathrm{d}\boldsymbol{k}}{(2\pi)^d} e^{i\boldsymbol{k}.\boldsymbol{r}} \frac{1}{E_0^2 - \xi(\boldsymbol{k})^2 - \Delta^2},\ f_1(\boldsymbol{r}) = \int \frac{\mathrm{d}\boldsymbol{k}}{(2\pi)^d} e^{i\boldsymbol{k}.\boldsymbol{r}} \frac{\xi(\boldsymbol{k})}{E_0^2 - \xi(\boldsymbol{k})^2 - \Delta^2} \tag{3.19}$$

These integrals can not be performed analytically exactly. Nevertheless, in the case of an isotropic dispersion, their asymptotic limit when $k_F r \gg 1$ can be obtained analytically, with k_F the Fermi wavevector and $r = |\boldsymbol{r}|$. The results depend on the dimensionality of the superconductor. In 3D, one obtains,

$$f_0(r) = \frac{-\pi\nu_0}{\sqrt{\Delta^2 - E_0^2}} \frac{\exp\{-k_S r\}\sin k_F r}{k_F r},\ f_1(r) = \pi\nu_0 \frac{\exp\{-k_S r\}\cos k_F r}{k_F r}, \tag{3.20}$$

with, $k_S \equiv \sqrt{\Delta^2 - E_0^2}/(\hbar v_F) = \Delta|\sin(\delta^+ - \delta^-)|/(\hbar v_F)$, and v_F the Fermi velocity. Hence, in 3D the YSR wavefunction reads,

$$\phi_{0,3D}(\boldsymbol{r}) \simeq \begin{bmatrix}\sin(k_F r + \delta^-) \\ \sin(k_F r + \delta^+)\end{bmatrix}\sqrt{2\pi\nu_0\alpha\cos\delta^-\cos\delta^+}\frac{\exp\{-r/\xi|\sin(\delta^+ - \delta^-)|\}}{k_F r}, \tag{3.21}$$

with $\xi = \frac{\hbar v_F}{\Delta}$ the coherence length of the superconductor. This result was obtained early by Rusinov in its original article [10]. In the case of a 2D superconducting substrate, the integrals read:

$$f_0(r) = \frac{-\pi\nu_0}{\sqrt{\Delta^2 - E_0^2}}\sqrt{\frac{2}{\pi k_F r}}\cos\Big(k_F r - \frac{\pi}{4}\Big)\exp\{-k_S r\}, \tag{3.22}$$

$$f_1(r) = \pi\nu_0\sqrt{\frac{2}{\pi k_F r}}\sin\Big(k_F r - \frac{\pi}{4}\Big)\exp\{-k_S r\}. \tag{3.23}$$

Therefore, the YSR wavefunction in 2D reads,

$$\phi_{0,2D}(\boldsymbol{r}) \simeq \begin{bmatrix}\sin\big(k_F r + \frac{\pi}{4} - \delta^-\big) \\ \sin\big(k_F r + \frac{\pi}{4} - \delta^+\big)\end{bmatrix}\sqrt{\frac{4\nu_0\Delta\cos\delta^-\cos\delta^+}{k_F r}}\exp\big\{-r/\xi|\sin\big(\delta^+ - \delta^-\big)|\big\}. \tag{3.24}$$

Contrary to the 3D case, the latter result was obtained recently by Guissart *et al.* [18, 131]. We remark that, both in the 3D and 2D cases, the YSR wavefunction is localized around the impurity on a typical length $\xi_S = \frac{\hbar v_F}{\sqrt{\Delta^2 - E_0^2}}$. However, the decay of the YSR wavefunction depends on the dimensionality of the host superconductor. In 3D the wavefunction decays as $\frac{1}{r}$, while in 2D, it decays as $\frac{1}{\sqrt{r}}$. Finally, the electronic and hole components of the wavefunction oscillate with $k_F r$ but with different phase factors, $\delta^{\pm}$. Interestingly, the relative phase $\delta^+ - \delta^-$ is directly related to E_0/Δ by the relation: $E_0/\Delta = \cos(\delta^+ - \delta^-)$.

3.2.4 Physical interpretation

The formation of YSR states has a rather clear physical interpretation: The magnetic exchange tends to align the spin of the electrons of Cooper pairs, hence decreasing their binding energy. The magnetic exchange, therefore, acts as pair-breaking potential, which is the origin of the YSR bound-state. Let us now take a closer look at the evolution of the YSR energy E_0 with the dimensionless parameter α characterizing the magnetic exchange. For $\alpha = \alpha_c \equiv \sqrt{1+\beta^2}$, the YSR energy vanishes and its sign changes, as observed in Fig. 3.1 (a). Indeed, $E_0 > 0$ when $\alpha_c > \alpha > 0$, while $E_0 < 0$ for higher magnetic exchange $\alpha > \alpha_c$.

This sign inversion has profound physical consequences and signals the existence of a quantum phase transition at $\alpha = \alpha_c$. While the YSR bound-state has no dramatic effects on the superconducting groundstate when $\alpha < \alpha_c$, for higher values of $\alpha > \alpha_c$, the system is unstable against spontaneous creation of a local quasiparticle excitation in the YSR state. As a result, the superconductor undergoes a quantum transition which corresponds to a change in the parity and spin polarization of the groundstate.

To explicitly show it let us write the many-body Hamiltonian $\mathcal{H}_{\mathrm{YSR}}$ in its diagonal form:

$$\mathcal{H}_{\mathrm{YSR}} = E_0 a_0^\dagger a_0 + \sum_{|E_n| \geq \Delta} E_n a_n^\dagger a_n, \tag{3.25}$$

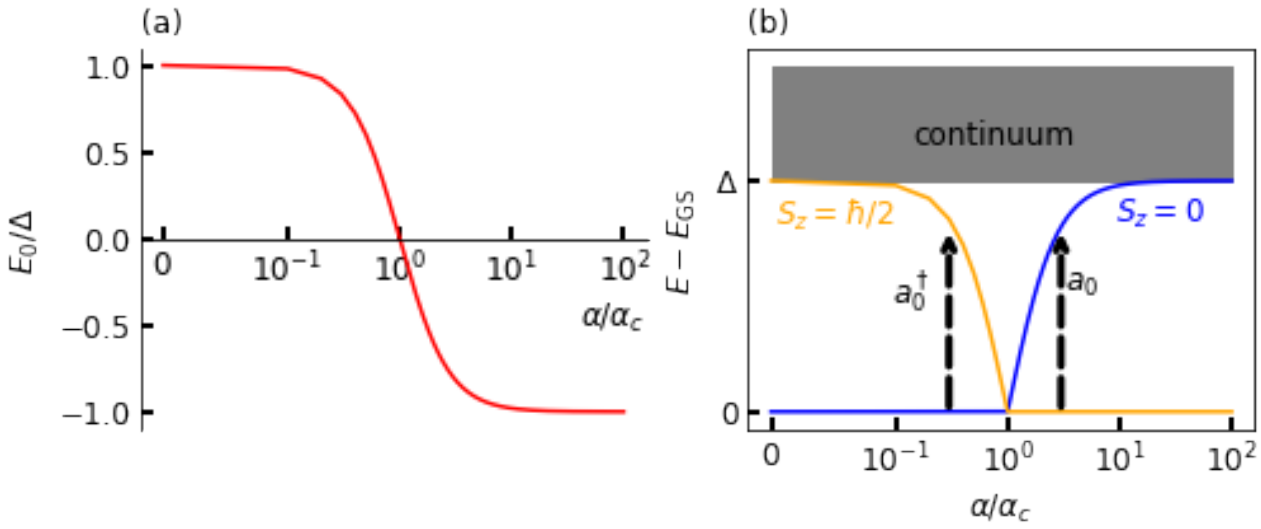

Figure 3.1: Energy of the YSR state and many-body spectrum. (a): Energy of the YSR state E_0/Δ as a function of α/α_c for $\beta = 0$. E_0 vanishes at $\alpha = \alpha_c$, and its sign changes, signaling a change in the many-body groundstate of the system, *i.e.*, a quantum phase transition. (b): Many-body-spectrum of the superconducting electrons in presence of a classical magnetic impurity. Energies are measured with respect to the groundstate energy E_{GS}. The exchange coupling with the impurity J reduces the binding energy of Cooper pairs and generates a low-lying state in the superconducting excitation gap. For $\alpha < \alpha_c$ the groundstate is unpolarized, $S_z = 0$, and has even fermion parity. Adding a quasiparticle in the YSR state transfer the groundstate into the first excited state, which has $S_z = \hbar/2$ and odd fermion parity. At $\alpha = \alpha_c$, a quantum phase transition occurs: the groundstate and first-excited state exchange their role. Higher energy states lie in the quasiparticle continuum with energies $E > E_{\mathrm{GS}} + \Delta$.

with $a_0 = \int \mathrm{d}\boldsymbol{r}\phi_0^\dagger(\boldsymbol{r})\psi(\boldsymbol{r})$ the operator annihilating a fermionic quasiparticle with energy E_0 and spin $\hbar/2$ in the YSR state, and $a_n = \int \mathrm{d}\boldsymbol{r}\phi_n^\dagger(\boldsymbol{r})\psi(\boldsymbol{r})$ the operator annihilating a quasiparticle in the state ϕ_n, with energy E_n outside the superconducting gap ,$|E_n| > \Delta$, and wavefunction $\phi_n(\boldsymbol{r})$. From (3.25), it is obvious that the groundstate of the system depends on the sign of E_0. We stress that the many-body eigenstates of $\mathcal{H}_{\mathrm{YSR}}$ have well-defined fermionic parity and spin projection along the z-axis (S_z) since these quantities are conserved by $\mathcal{H}_{\mathrm{YSR}}$.

Let us first focus on the case $\alpha < \alpha_c$. In that case, the magnetic exchange is not strong enough to effectively bind an electron and $E_0 > 0$. Therefore, the YSR state is an excited state that is unoccupied in the groundstate $|g\rangle$. In that case, the first excited state, $|e\rangle$ of the system corresponds to the occupied YSR state: $|e\rangle = a_0^\dagger |g\rangle$. Because there is no quantum phase transition for $\alpha < \alpha_c$, the groundstate $|g\rangle$ has the same spin projection S_z and fermionic parity as the BCS groundstate. Therefore, $|g\rangle$ has $S_z = 0$ and even fermion parity. Since the YSR state is $\uparrow$-polarized along the z-axis, $|e\rangle$ corresponds to $S_z = \hbar/2$, and odd fermion parity.

On the other hand, when $\alpha > \alpha_c$, the YSR energy E_0 decreases below the Fermi level, and the impurity effectively binds an electron. In this case, the YSR state is occupied in the groundstate $|g'\rangle$. Therefore, a quantum phase transition occurs at the critical point α_c, and the first-excited state and the groundstate exchange their role: $|e'\rangle = |g\rangle$ and $|g'\rangle = |e\rangle$. Hence, the groundstate now corresponds to odd fermionic parity and $S_z = \hbar/2$, while the excited state now corresponds to even fermionic parity and $S_z = 0$. All these results are schematized in Fig. 3.1 (b).

Because the YSR state possesses electron and hole components, it manifests itself in STS experiments performed in the tunneling regime as narrow conductance peaks. Indeed, we have already shown that the

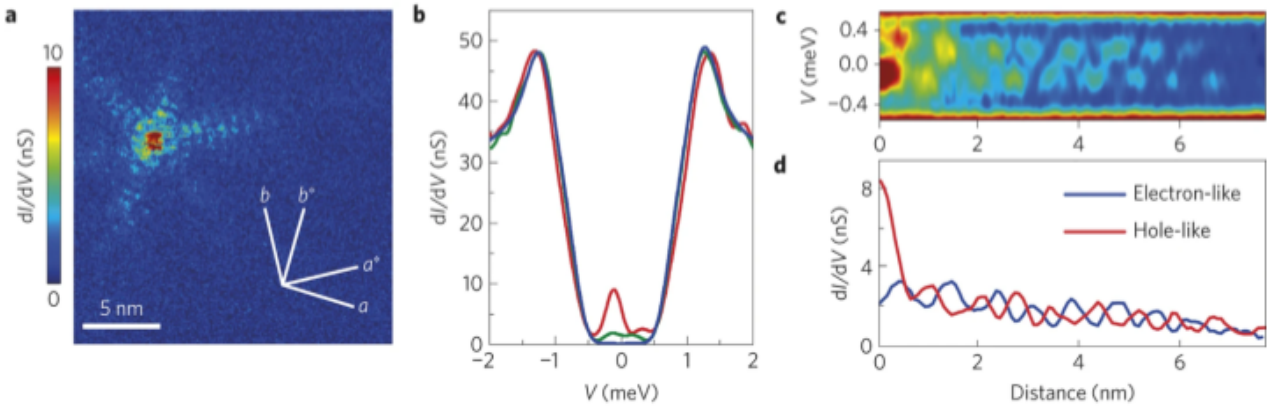

Figure 3.2: Experimental observation of YSR within STS/STM experiments. (a): Experimental conductance map taken at -0.13 meV. The a and b lines indicate the crystallographic axes of 2H–$NbSe_2$, whereas the a^* and b^* lines indicate the directions in the reciprocal space. (b): Characteristic experimental spectra taken on top of the impurity (red solid line), on the right branch, 4 nm from the center of the impurity (green solid line), and far from the impurity (blue solid line). (c): Spatial and energy evolution of the experimental tunneling conductance spectra, $dI/dV(x, V)$ along one branch of the star. The left side of the figure corresponds to the center of the star and the right side to the top-right corner of the scanning area. The color conductance scale is the same as that used in (a). (d): Conductance profiles of the electron- and hole-like YSR states as a function of the distance to the impurity along the same line as for (c). Figure reproduced from [18].

differential conductance measured by STS performed in the tunneling regime is proportional to the local electronic density of states (LDOS), $\rho(\boldsymbol{r_a}, \omega = eV)$, at the position of the tip apex $\boldsymbol{r_a}$. Because the YSR state is the only quasiparticle state lying inside the superconducting gap, for $|\omega| < \Delta$, the LDOS of the superconducting electrons reads:

$$\rho(\boldsymbol{r}, \omega) = u^2(\boldsymbol{r})\delta(\omega - E_0) + v^2(\boldsymbol{r})\delta(\omega + E_0),\ |\omega| < \Delta. \tag{3.26}$$

Here, $u(\boldsymbol{r})$ and $v(\boldsymbol{r})$ are the electron and hole component of the YSR wavefunction ϕ_0, respectively. In other words, $\phi_0(\boldsymbol{r}) = [u(\boldsymbol{r}), v(\boldsymbol{r})]^T$. Therefore, $G(eV = E_0) \propto u^2(\boldsymbol{r_a})$, while $G(eV = -E_0) \propto v^2(\boldsymbol{r_a})$, and the YSR state is manifested as two sub-gap conductance peaks as observed in Fig. 3.2 (b). Moreover, the spatial decay and oscillations of the electron and hole-like component can be observed within STM experiments by measuring the conductance tomography taken at $eV = E_0, -E_0$ respectively, as shown in Fig. 3.2 (c) and (d). Fig. 3.2 (d) shows the out-of-phase nature of the oscillations of the electron and hole components, in agreement with the theoretical predictions of Subsection. 3.2.3.

Lastly, we stress that the height asymmetry of the conductance peaks observed in Figs. 3.2 (b), (c) and (d) is due to the dimensionless parameter β. Indeed, when $\beta = 0$, $u_0^2(\boldsymbol{0}) = v_0^2(\boldsymbol{0})$, and the conductance peaks, measured on top of the impurity, are symmetric. On the contrary, when $\beta > 0$, $u_0^2(\boldsymbol{0}) > v_0^2(\boldsymbol{0})$ and the peak at E_0 is the most pronounced, while when $\beta > 0$, $u_0^2(\boldsymbol{0}) < v_0^2(\boldsymbol{0})$ and the peak at $-E_0$ is the most pronounced.

3.3 Observation of odd-ω pairing around magnetic impurities in a superconductor

In this section, we show that a single magnetic impurity converts even-frequency spin-singlet Cooper pairs to spin-triplet odd-frequency ones. This conversion is a consequence of the time-reversal symmetry breaking at the impurity site and is thus strongly linked to the existence of the YSR bound-state. Indeed, we will show that an odd-frequency pairing function is generated as soon as a YSR state exists inside the gap. Second, we demonstrate that the imaginary part of the odd-ω pairing is proportional to the even-ω component of the LDOS at the impurity site. Finally, by approximating the YSR resonances by Lorentzian functions, we can estimate the proportionality coefficient from the LDOS. Since the LDOS is directly measured in STS experiments, it provides a straightforward method to extract the imaginary part of the odd-ω pairing from STS data. We illustrate our method on STS data measured by our collaborators G. C. Ménard, C. Brun, and T. Cren at the Institut des Nanosciences de Paris. Our results, published in *Physical Review Letters* [30], indicate a significant odd-ω pairing component generated by the magnetic impurity.

3.3.1 Coexistence of odd-ω pairing and YSR state

First, we investigate the properties of the pairing functions around an isolated magnetic impurity in a *conventional* s-wave superconductor. To do so, we use a generalized Yu-Shiba-Rusinov model whose Hamiltonian reads:

$$\begin{aligned}\mathcal{H}_{YSR} = &\int \mathrm{d}\boldsymbol{r}\psi_S^\dagger(\boldsymbol{r}) \begin{bmatrix} \epsilon(\boldsymbol{k}) - \mu & \Delta(\boldsymbol{r}) \\ \Delta^*(\boldsymbol{r}) & -\epsilon(\boldsymbol{k}) + \mu \end{bmatrix} \psi_S(\boldsymbol{r}) \\ &+ \psi_S^\dagger(\boldsymbol{0})(U\tau_z - J\tau_0)\psi_S(\boldsymbol{0}),\end{aligned} \tag{3.27}$$

where $\psi_S^\dagger(\boldsymbol{r}) = [c_\uparrow^\dagger(\boldsymbol{r}), c_\downarrow(\boldsymbol{r})]$, $\epsilon(\boldsymbol{k})$ is the energy dispersion of the normal state substrate, $\hbar\boldsymbol{k} = -i\hbar\nabla_{\boldsymbol{r}}$ the momentum operator, and $\Delta(\boldsymbol{r})$ the pairing potential of the substrate. In principle $\Delta(\boldsymbol{r})$ might depend on $\boldsymbol{r}$ because of the magnetic ad-atom which locally renormalizes the gap. Hereinafter we neglect renormalization effects and spatial dependence of $\Delta(\boldsymbol{r})$, as it was not observed in the experimental data studied below. It implies that we can always choose $\Delta(\boldsymbol{r}) = \Delta$ to be a real positive number without loss of generality.

Within this model, the set of possible pairing functions is reduced. First, (3.27), is a single-band model, therefore $O = 1$. Additionally, the model enjoys a $U(1)$ spin rotation symmetry. Hence equal spin pairing functions vanish. Finally, focusing on the local pairing functions at the impurity site, only $P^* = 1$ pairings are non-zero. As a consequence, there are only two possible types of local pairing functions:

$$1.\ f^r_{\uparrow\downarrow}(\omega) = f^a_{\uparrow\downarrow}(-\omega), \text{Even-}\omega\text{; spin-singlet,} \tag{3.28}$$

$$2.\ f^r_{\uparrow\downarrow}(\omega) = -f^a_{\uparrow\downarrow}(-\omega), \text{Odd-}\omega\text{; spin-triplet.} \tag{3.29}$$

Where we omit the spatial indices for brevity, *i.e.* $f^{r/a}_{\sigma\sigma'}(\omega) \equiv f^{r/a}_{\sigma\sigma'}(\boldsymbol{r} = \boldsymbol{0}, \boldsymbol{r}' = \boldsymbol{0}, \omega)$ Therefore, it is convenient to decompose $f^r_{\uparrow,\downarrow}(\omega)$ into even-ω (spin-singlet) $f_{even}(\omega)$ and odd-ω (spin-triplet) $f_{odd}(\omega)$ components.

Treating the coupling with the impurity as a perturbation, it is easy to show that the local retarded Green's function of the substrate at the impurity site, $\hat{g}^r_S(\omega) \equiv \hat{g}^r_S(\boldsymbol{r} = \boldsymbol{0}, \boldsymbol{r}' = \boldsymbol{0}, \omega)$ obeys the following Dyson equation:

$$\hat{g}^r_S(\omega) = [(\hat{g}^r_0(\omega))^{-1} - (U\tau_z - J\tau_0 - i\Lambda\tau_0)]^{-1}, \tag{3.30}$$

where $\hat{g}^r_0(\omega)$ is the local retarded Green's function of the substrate in the absence of the impurity (also called the bare one). Note that, following [132], we also introduced a phenomenological Dynes broadening Λ accounting for quasiparticle relaxation. This broadening is essential if one wants to establish a direct link with experimental data. The advanced Green's function in Nambu space obeys the adjoint equation:

$$\hat{g}^a_S(\omega) = (\hat{g}^a_0(\omega))^{-1} - (U\tau_z - J\tau_0 + i\Lambda\tau_0)]^{-1}. \tag{3.31}$$

Because of our gauge choice, $\Delta \in \mathbb{R}$, the bare Green's functions satisfy, $g^a_0(\omega) = g^r_0(\omega)^*$. Hence, (3.31) is the complex conjugate of (3.30) and, in presence of the impurity, the perturbed Green's functions still satisfy $g^a_S(\omega) = g^r_S(\omega)^*$. It directly follows that equations (3.28) and (3.29) become:

$$1.\ f^r_{\uparrow\downarrow}(\omega) = f^r_{\uparrow\downarrow}(-\omega)^*, \text{Even-}\omega\text{; spin-singlet,} \tag{3.32}$$

$$2.\ f^r_{\uparrow\downarrow}(\omega) = -f^r_{\uparrow\downarrow}(-\omega)^*, \text{Odd-}\omega\text{; spin-triplet.} \tag{3.33}$$

Hence, $f^r_{even}(\omega) = \frac{1}{2}\left(f_{\uparrow\downarrow}(\omega) + f_{\uparrow\downarrow}(-\omega)^*\right)$ and $f^r_{odd}(\omega) = \frac{1}{2}\left(f^r_{\uparrow\downarrow}(\omega) - f^r_{\uparrow\downarrow}(-\omega)^*\right)$. A non-zero $f^r_{odd}(\omega)$ component is thus a fingerprint of odd-ω superconductivity.

The longstanding difficulty in proving the existence of odd-ω superconductivity relies in extracting the pairing functions from spectral quantities experimentally measurable. Here, the goal is to show that $f^r_{odd}(\omega)$ can be extracted from the local density of states (LDOS) measured with scanning tunneling spectroscopy (STS) on top of the impurity. For this purpose, we first remark that $\hat{g}^r_S(\omega)$ can be written as:

$$\hat{g}^r_S(\omega) = \begin{bmatrix} g^r_\uparrow(\omega) & f^r_{\uparrow\downarrow}(\omega) \\ f^r_{\downarrow\uparrow}(\omega) & -g^r_\downarrow(-\omega)^* \end{bmatrix}, \tag{3.34}$$

where $g^r_\sigma(\omega)$ are the local components of the *normal* retarded Green's functions describing the propagation of electrons with spin σ. Notice that we also used the fact that $g^r_S(\omega)$ is symmetric because of fermionic anticommutation relations. To compute $g^r_S(\omega)$, we only need $\hat{g}^r_0(\omega)$ and to solve the Dyson equation, (3.30). Similarly to $\hat{g}^r_S(\omega)$ the bare superconducting Green's function $g^r_0(\omega)$ can be written as:

$$\hat{g}^r_0(\omega) = \begin{bmatrix} g^0_\uparrow(\omega) & f^0_{\uparrow\downarrow}(\omega) \\ f^0_{\uparrow\downarrow}(\omega) & -g^0_\downarrow(-\omega)^* \end{bmatrix}, \tag{3.35}$$

with $g^0_\sigma(\omega)$ the (local component) of the *normal* electronic Green's functions and $f^r_{\uparrow\downarrow}(\omega)$ the pairing function in the absence of the impurity. Note that (3.35) is valid for any single-band superconducting substrate where spin is locally a good quantum number. Most importantly, our results remain valid in the presence of Rashba spin-orbit coupling (see the Supplementary Material of [30]). Since the clean superconducting substrate is a *conventional* superconductor, the bare pairing function, $f^0_{\uparrow\downarrow}(\omega)$ is spin-singlet and even-ω. Inserting (3.35) into (3.30) we obtain the following set of equations:

$$g^r_\uparrow(\omega) = \frac{1}{D(\omega)}\{g^0_\uparrow(\omega) - (J+U+i\Lambda)\left([f^0_\uparrow(\omega)]^2 + g^0_\downarrow(-\omega)^* g^0_\uparrow(\omega)\right)\}, \tag{3.36}$$

$$g^r_\downarrow(-\omega)^* = \frac{1}{D(\omega)}\{g^0_\downarrow(-\omega)^* + (J-U+i\Lambda)\left([f^0_\uparrow(\omega)]^2 + g^0_\downarrow(-\omega)^* g^0_\uparrow(\omega)\right)\}, \tag{3.37}$$

$$f^r_{\uparrow\downarrow}(\omega) = \frac{1}{D(\omega)} f^0_{\uparrow\downarrow}(\omega), \tag{3.38}$$

with $D(\omega) = \det\{\tau_0 - \Sigma g^r_0(\omega)\}$. Typical YSR states observed in STS experiments exhibit a narrow intrinsic energy-width [32]. It thus seems legitimate to assume that the Dynes broadening Λ is the smallest energy scale in our problem. In the limit $\Lambda \to 0$ the previous set of equations becomes:

$$g^r_\uparrow(\omega) \simeq \frac{1}{D(\omega)}\{g^0_\uparrow(\omega) - (J+U)\left([f^0_\uparrow(\omega)]^2 + g^0_\downarrow(-\omega)^* g^0_\uparrow(\omega)\right)\}, \tag{3.39}$$

$$g^r_\downarrow(\omega)^* \simeq \frac{1}{D(-\omega)}\{g^0_\downarrow(\omega)^* + (J-U)\left([f^0_\uparrow(\omega)]^2 + g^0_\downarrow(\omega)^* g^0_\uparrow(-\omega)\right)\}, \tag{3.40}$$

$$f^r_{\uparrow\downarrow}(\omega) \simeq \frac{1}{D(\omega)} f^0_{\uparrow\downarrow}(\omega), \tag{3.41}$$

$$\begin{aligned} D(\omega) \simeq & 1 - (J^2 - U^2)[f^0_{\uparrow\downarrow}(\omega)^2 + g^0_\downarrow(-\omega)^* g^0_\uparrow(\omega)] + J\left(g^0_\uparrow(\omega) - g^0_\downarrow(\omega)^*\right) - U\left(g^0_\uparrow(\omega) + g^0_\downarrow(\omega)^*\right) \\ & - i\Lambda\{2J[f^0_{\uparrow\downarrow}(\omega)^2 + g^0_\downarrow(-\omega)^* g^0_\uparrow(\omega)] - g^0_(\omega) + g^0_\downarrow(-\omega)^*\} + \mathcal{O}(\Lambda^2). \end{aligned} \tag{3.42}$$

Note that it is necessary to keep the first order in Λ term in $D(\omega)$ because the zeroth order one can vanish, introducing a divergence. Hereinafter, we focus on sub-gap energies, $|\omega| < \Delta$. Because of our gauge choice, the bare Green's functions $g^r_0(\omega)$ and $g^a_0(\omega)$ are real in this regime, and we obtain:

$$\begin{aligned} \rho(\omega) = & -\frac{1}{\pi}\,\mathrm{Im}\left\{\frac{1}{D(\omega)}\right\}\{g^0_\uparrow(\omega) - (J+U)[f^0_{\uparrow\downarrow}(\omega)^2 + g^0_\downarrow(-\omega) g^0_\uparrow(\omega)]\} \\ & + \frac{1}{\pi}\,\mathrm{Im}\left\{\frac{1}{D(-\omega)}\right\}\{g^0_\downarrow(\omega) + (J-U)[f^0_{\uparrow\downarrow}(\omega)^2 + g^0_\downarrow(\omega) g^0_\uparrow(-\omega)]\}, \end{aligned} \tag{3.43}$$

$$\mathrm{Im}\{f^r_{\uparrow\downarrow}\}(\omega) = \mathrm{Im}\left\{\frac{1}{D(\omega)}\right\} f^0_{\uparrow\downarrow}(\omega), \tag{3.44}$$

with $\rho(\omega)$ the LDOS, which is defined as: $\rho(\omega) = -\frac{1}{\pi}\,\mathrm{Im}\Big\{g^r_\uparrow(\omega) + g^r_\downarrow(\omega)\Big\}$. In the $\Lambda \to 0$ limit, $\mathrm{Im}\{g^r_S(\omega)\}$ are narrow peaks located at the sub-gap poles of $[D_0(\omega)]^{-1}$, denoted E_n, with $D_0(\omega) \equiv D(\omega)|_{\Lambda=0}$. E_n are the energies of the spin-polarized YSR sub-gap states. The experimental data analyzed below show a single YSR resonance; hence we assume that $D_0(\omega)$ possesses a single sub-gap pole E_0. Nevertheless, the results of this paragraph remain valid in the case of multiple YSR resonances, as long as they are well-separated in energy. Consequently, if the three functions, $f^0_{\uparrow\downarrow}$, $g^0_\uparrow(\omega)$, and $g^0_\downarrow(\omega)$ vary slowly around $\pm E_0$ on the typical energy scale Λ it is legitimate to simplify (3.43) and (3.44) as:

$$\begin{aligned}\rho(\omega) \simeq &-\frac{1}{\pi}\,\mathrm{Im}\left\{\frac{1}{D(\omega)}\right\}\{g^0_\uparrow(E_0) - (J+U)[f^0_{\uparrow\downarrow}(E_0)^2 + g^0_\downarrow(-\omega)g^0_\uparrow(E_0)]\} \\ &-\frac{1}{\pi}\,\mathrm{Im}\left\{\frac{1}{D(-\omega)}\right\}\{g^0_\downarrow(E_0) + (J-U)[f^0_{\uparrow\downarrow}(E_0)^2 + g^0_\downarrow(-E_0)g^0_\uparrow(E_0)]\},\end{aligned} \tag{3.45}$$

$$\mathrm{Im}\{f^r_{\uparrow\downarrow}\}(\omega) \simeq \mathrm{Im}\left\{\frac{1}{D(\omega)}\right\} f^0_{\uparrow\downarrow}(E_0). \tag{3.46}$$

It is therefore straightforward to write the LDOS as a linear combination of odd/even-ω pairings:

$$\rho(\omega) \simeq C_e(E_0)\,\mathrm{Im}\{f^r_{even}(\omega\}) + C_o(E_0)\,\mathrm{Im}\{f^r_{odd}(\omega)\}, \tag{3.47}$$

$$\text{with, } C_e(E_0) = \frac{2VA(E_0) - g^0_\uparrow(E_0) - g^0_\downarrow(-E_0)}{\pi f^0_{\uparrow\downarrow}(E_0)}, \tag{3.48}$$

$$C_o(E_0) = \frac{2JA(E_0) - g^0_\uparrow(E_0) + g^0_\downarrow(-E_0)}{\pi f^0_{\uparrow\downarrow}(E_0)}, \tag{3.49}$$

We stress that counterintuitively, $\mathrm{Im}\{f^r_{odd}(\omega)\}$ is an even function of ω while $\mathrm{Im}\{f^r_{odd}(\omega)\}$ is odd. Hence, the even and odd component of $\rho(\omega)$, $\rho_{even}(\omega) = \frac{\rho(\omega)+\rho(-\omega)}{2}$ and $\rho_{odd}(\omega) = \frac{\rho(\omega)-\rho(-\omega)}{2}$ satisfy:

$$\rho_{even}(\omega) = C_o(E_0)\,\mathrm{Im}\{f^r_{odd}(\omega)\},\ \rho_{odd}(\omega) = C_e(E_0)\,\mathrm{Im}\{f^r_{even}(\omega)\}. \tag{3.50}$$

Thus, we demonstrated that $\rho_{even}(\omega)$ is proportional to $\mathrm{Im}\{f_{odd}(\omega)\}$ for $|\omega| < \Delta$. The LDOS being a positive quantity, the existence of YSR resonances directly implies a non-zero $\rho_{even}(\omega)$ and hence a non-zero odd-ω pairing. In principle, (3.50) allows to extract $\mathrm{Im}\{f_{odd}(\omega)\}$ from the LDOS measured in STS experiments. However, to obtain quantitative results, reliable knowledge of $C_o(E_0)$ is required. $C_o(E_0)$ is not universal and depends on the microscopic properties of the clean superconductor but also on the impurity parameters J and U, which can not be directly measured. In the next paragraph, we first show that in the wide-band limit $C_o(E_0)$ has a simple expression that only involves the superconducting gap Δ and the normal DOS at the Fermi level, ν_0, two quantities that are easily accessible. However, even within this limit, $C_o(E_0)$ is still not universal and depends on the impurity parameters. Second, we also test the validity of the assumption used to derive (3.50).

Lastly, we stress that (3.50) has the strong physical implication that **as soon as there is a YSR sub-gap state, odd-ω pairing exists locally at the impurity site**. Both the YSR state and odd-ω pairing are consequences of the magnetic impurity locally breaking the time-reversal symmetry.

3.3.2 Evaluation of $C_o(E_0)$ in the wide band limit

The main difficulty preventing us from estimating $C_o(E_0)$ is the exact knowledge of $\hat{g}_0^r(\omega)$ inside the gap. The local retarded Green's function describing the clean BCS superconductor reads:

$$\hat{g}_0^r(\omega) = \int \frac{\mathrm{d}\boldsymbol{k}}{(2\pi)^d} \frac{\omega - \Delta\tau_x - \xi(\boldsymbol{k})\tau_z}{\omega^2 - \xi(\boldsymbol{k})^2 - \Delta^2}, \text{ with } |\omega| < \Delta. \tag{3.51}$$

Introducing $\nu(\xi)$, the DOS of the normal-state superconductor, we can tade the integral over momentum-space for an integral over energy-space:

$$\hat{g}_0^r(\omega) = \int_{-\mu}^{\infty} \nu(\xi) \frac{\omega - \Delta\tau_x - \xi\tau_z}{\omega^2 - \xi^2 - \Delta^2}, \text{ with } |\omega| < \Delta. \tag{3.52}$$

In principle, $\nu(\xi)$ is energy-dependent and the former integral depends on the detailed energy dispersion of the normal-state substrate. Nevertheless, for most physically relevant cases, the Fermi energy is the largest energy scale, and the normal DOS can be approximated by its value at the Fermi energy ν_0. Hence, the integral can be performed exactly, and one obtains,

$$\hat{g}_0^r(\omega) = -\frac{\pi\nu_0(\omega + \Delta\tau_x)}{\sqrt{\Delta^2 - \omega^2}}, \text{ with } |\omega| < \Delta. \tag{3.53}$$

Therefore, the coefficient $C_o(E_0)$ adopts a rather simple expression,

$$C_o(E_0) = -\frac{2}{\Delta}\left\{E_0 + \pi\nu_0 J\sqrt{\Delta^2 - E_0^2}\right\}. \tag{3.54}$$

We have already computed E_0 in the wide band limit and found,

$$E_0 = \Delta\frac{1 - \alpha^2 + \beta^2}{\sqrt{4\alpha^2 + (1 - \alpha^2 + \beta^2)^2}}, \tag{3.55}$$

with $\alpha \equiv \pi\nu_0 J$ Using the analytical expression of $g_0^r(\omega)$, we can compute exactly $g_S^r(\omega)$ via the Dyson equation. Hence, we can also verify the validity of our result (3.50) in the wide-band limit. Indeed, (3.50) was obtained assuming that the components of the bare Green's function, $g_0^r(\omega)$ vary slowly around E_0 the energy of the YSR state on the typical energy scale Λ governing the width of the YSR resonances. To check the validity of this assumption, we computed the exact LDOS $\rho(\omega)$ and the odd-frequency pairing $f_{odd}^r(\omega)$. Then we compare the exact $\rho(\omega)$ with the one obtained from (3.50). We repeat this operation for several sets of impurity parameters. The results, presented in Fig. 3.3 show that for moderate Dynes broadening, $\Lambda < \Delta/10$, our approximation is in quantitative agreement with the exact results, as long as the YSR energy E_0 is well-separated from the gap edges ($|E_0 \pm \Delta| \gg \Lambda$), even if the peaks merges ($|E_0| \sim 0$). The typical value of the Dynes broadening in *conventional* superconductors being $\Lambda \simeq \Delta/10^2$ (see for example [73]), our approximation is applicable in most physically relevant cases. In addition, we stress that in the case of a single YSR state lying inside the gap, (3.50) is valid inside the whole superconducting gap and not only in the vicinity of the YSR peaks. Nevertheless, even if we proved the validity of (3.50), the use of the wide-band limit is not enough to extract $C_o(E_0)$ directly from STS experiments. Indeed, it still depends on the impurity parameters J and U, which are not directly accessible. In the next paragraph, we show how we can circumvent this problem and extract $C_o(E_0)$ from the differential conductance spectrum measured in STS experiments and apply our method to concretely extract $\mathrm{Im}\{f_{odd}^r(\omega)\}$ from experimental STS data.

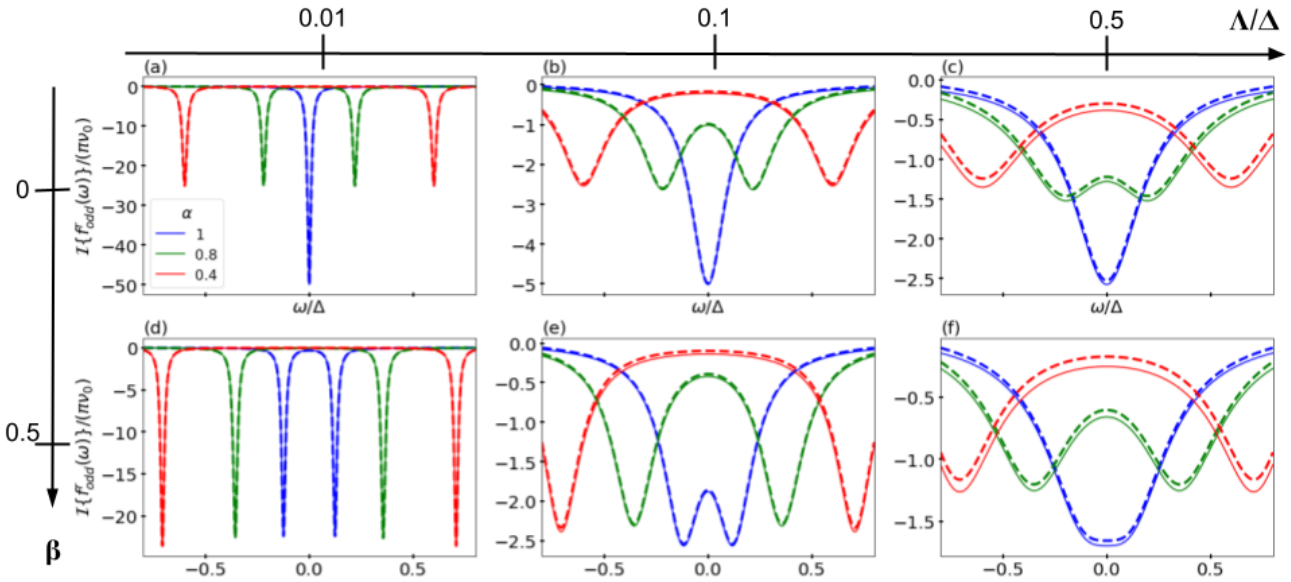

Figure 3.3: Validity of (3.50). In each panels, the solid lines show the exact $\mathrm{Im}\{f^r_{odd}(\omega)\}$, while the dashed lines correspond to $\rho_{even}(\omega)/C_o(E_0)$. The color indicates the value of α as indicated in the legend. The upper panels correspond to $\beta = 0$ and $\Lambda = 0.01,\ 0.1$, and 0.5 respectively for (a),(b), and (c). The bottom panels correspond to $\beta = 0.5$ and $\Lambda = 0.01,\ 0.1$, and 0.5 respectively for (d),(e), and (f).One can observe the quantitative agreement between the solid and dashed lines up to $\Lambda = 0.1\Delta$, indicating the validity of (3.50) for moderate Dynes broadening $\Lambda \lesssim \Delta/10$.

3.3.3 Efficient protocol to extract the odd-ω pairing from scannig tunneling spectrocopy (STS) data

Let us now provide an efficient protocol to extract $\mathrm{Im}\{f^r_{odd}(\omega)\}$ from local measurements of the differential conductance spectrum, $G = dI/dV$, performed in the tunneling regime. In the tunneling regime, we have already shown that $G(V)$ is proportional to the LDOS convoluted with the derivative of the Fermi-Dirac distribution at the experimental temperature (see equation (2.83)). Consequently, after a proper deconvolution, the differential conductance spectrum provides us with the LDOS, $\rho(\omega)$, in arbitrary units. Since $\rho(\omega) \approx \nu_0$, when $\omega \gg \Delta$, we can normalize the data to 1 in the high-voltage limit to obtain $\rho(\omega)$ in units of ν_0. Once the normalized LDOS in hand, it is straightforward to obtain its even component, $\rho_{even}(\omega)$. However, to extract $\mathrm{Im}\{f_{odd}(\omega)\}$ we need to evaluate $C_o(E_0)$. Since J, and U, can not be directly measured, an alternative way to evaluate $C_o(E_0)$ directly from the LDOS is required. The basic idea here is to remark that, provided that $\Lambda \ll \Delta$ and E_0 remain well separated from the gap edges, the imaginary part of $g^r_S(\omega)$ is non-zero only when $\omega \approx E_0$. Therefore, following [32], we expand $g^r_S(\omega)$ around E_0. While the numerators and the imaginary part of the denominator in $g_S(\omega)$ can be evaluated at E_0, the real part has to be evaluated at first order in

$\delta\omega = \omega - E_0$, yielding,

$$g_S^r(\omega) \simeq \frac{1}{\omega + i\eta - E_0}.\begin{bmatrix} u^2 & uv \\ uv & v^2 \end{bmatrix}, \tag{3.56}$$

$$u^2, v^2 = 2\pi\nu_0\Delta\frac{1 + (\alpha^2 \pm \beta^2)}{\sqrt{(1 - \alpha^2 + \beta^2)^2 + 4\alpha^2}^{3/2}}, \tag{3.57}$$

$$\eta = 4\pi\nu_0\Delta\Lambda\alpha\frac{1 + \alpha^2 + \beta^2}{\sqrt{(1 - \alpha^2 + \beta^2)^2 + 4\alpha^2}^{3/2}}. \tag{3.58}$$

Note that $(u, v)^T = \phi_0(\mathbf{0})$, with $\phi_0(\boldsymbol{r})$ the YSR wavefunction in real space. Hence (3.56), is equivalent to $g_S^r(\omega) = \frac{\phi_0(\mathbf{0})\phi_0(\mathbf{0})^\dagger}{\omega + i\eta - E_0}$ which is nothing but the Green's functions of a single YSR state with an intrinsic energy width η. In other words, the approximation (3.56) is equivalent to retaining only the YSR contribution to the Green's function. The YSR state being the only state lying inside the gap, well-separated from the gap edges, it seems legitimate to use (3.56) to compute $\rho(\omega)$ when $|\omega| < \Delta$. Using (3.56), it is straightforward to show that,

$$\rho(\omega) = \frac{\eta u^2/\pi}{(\omega - E_0)^2 + \eta^2} + \frac{\eta v^2/\pi}{(\omega + E_0)^2 + \eta^2}, \tag{3.59}$$

$$\mathrm{Im}\{f_{odd}^r(\omega)\} = -\frac{\eta uv}{2}\{\frac{1}{(\omega - E_0)^2 + \eta^2} + \frac{1}{(\omega + E_0)^2 + \eta^2}\}, \tag{3.60}$$

$$C_o(E_0) = -\frac{u^2 + v^2}{\pi uv}. \tag{3.61}$$

Obviously, provided that $E_0 \gg \eta$, $\rho(E_0) = \frac{u^2}{\pi\eta}$, $\rho(-E_0) = \frac{v^2}{\pi\eta}$, and consequently,

$$C_o(E_0) = \frac{\rho(E_0) + \rho(-E_0)}{\pi\sqrt{\rho(E_0).\rho(-E_0)}}, \tag{3.62}$$

We can use the last equation to evaluate $C_o(E_0)$ directly from the experimental measurement of G, provided the STS experiment is performed in the tunneling regime. Note that $C_o(E_0)$ is invariant under the exchange $u \leftrightarrow v$. Therefore, the sign of E_0 is irrelevant for the present purpose, and we can always assume E_0 to be positive.

Two methods are thus possible to estimate $C_o(E_0)$. We can either fit the measured LDOS with the expression (3.59) to extract the parameters u, v an η and evaluate the coefficient $C_o(E_0)$ from (3.61). Alternatively, if the YSR resonances do not overlap, we can use (3.62) to directly estimate the coefficient and extract $\mathrm{Im}\{f_{odd}^r(\omega)\}$. In the next subsection, we illustrate these methods on the differential conductance spectrum measured on top of magnetic impurities immersed in a $\mathrm{Pb/Si(111)}$ substrate.

3.3.4 Application to magnetic impurities in a $\mathrm{Pb/Si(111)}$ substrate

Here we extract $\mathrm{Im}\{f_{odd}^r(\omega)\}$ from the differential conductance on a magnetic impurity in a $\mathrm{Pb/Si(111)}$ substrate. The clean Pb monolayer was shown to be superconducting below 1.8 K [133]. As expected for a conventional s-wave superconductor, the system does not show any in-gap states in the presence of strong non-magnetic disorder [134]. STM images of the Pb monolayer revealed the presence of magnetic impurities as it can be observed on Fig. 3.4 (a). The corresponding conductance map measured at the Fermi level

by STS at 320 mK is shown on Fig. 3.4 (b). One can observe a red spot on top of the magnetic impurity, indicating the presence of a strong YSR state. The speckles-like pattern surrounding the red spot originates from the decaying YSR wavefunction scattered by the atomic disorder of the monolayer. The comparison

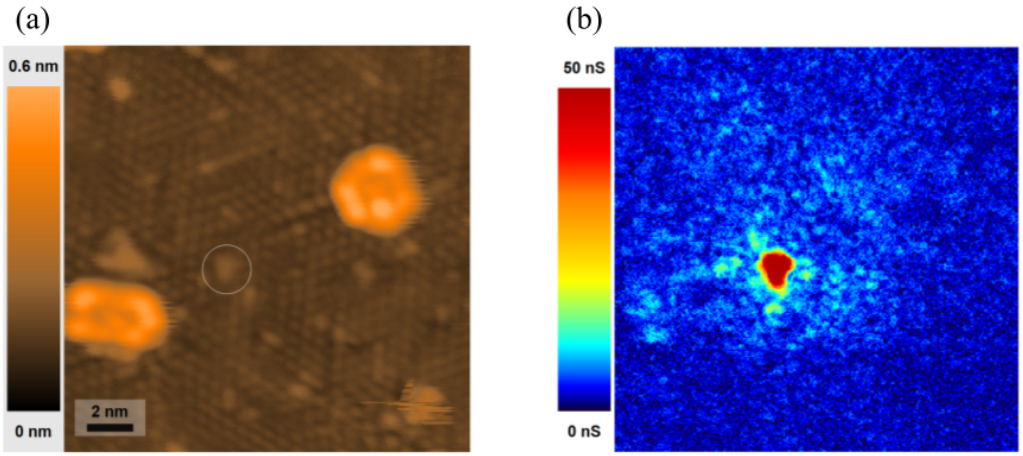

Figure 3.4: Typical YSR state studied. (a): Scanning tunneling microscopy image of the Pb monolayer where a magnetic defect can be identified as the encircled triangular protrusion. (b): Corresponding conductance map measured at the Fermi level by scanning tunneling spectroscopy at 320 mK.

between the differential conductance spectra measured on top of the impurity and far away from it confirms the presence of a YSR state. As it can be observed in Fig. 3.5 (a) far away from the impurity, the differential conductance spectrum does not show any in-gap peaks. The spectrum corresponds to a BCS gap of 0.38 meV with a Dynes broadening of approximately 0.004 meV. On the contrary, the spectrum measured on top of the impurity shows a single pair of strong YSR peaks inside the gap. For all the impurities studied, a single pair of conductance peaks was always observed, indicating that only a single YSR state is present[1]. We stress that because the Pb is a 2D superconductor, YSR states extend very far from the impurities, typically tens of nanometers away. Nevertheless, here we focus on differential conductance spectra measured right on top of the impurities. Following the above-mentioned protocol, we extract the normalized LDOS, $\rho(\omega)$ from the differential conductance spectrum acquired on top of the impurity (Fig. 3.5 (a)). For consistency, we check that the convolution of the obtained LDOS with the Fermi-Dirac derivative at temperature $T = 320$ mK reproduces the conductance data, as it can be observed in Fig. 3.5 (a). Once the LDOS in hand, we normalize it to ν_0, and the results are presented in Fig. 3.5 (b). Then we extract $C_o(E_0)$ from two different methods. First, we measured the YSR energy, finding $E_0 \simeq 0.074$ meV, fit the measured $\rho(\omega)/\nu_0$ with (3.59) and find, $\eta = 0.013$ meV, $u^2/\nu_0 = 0.30$, $v^2/\nu_0 = 0.40$, yielding $C_o(E_0) \approx 0.64$. Second, we used (3.62) to estimate the coefficient without any fitting procedure directly. We found $C_o(E_0) \approx 0.64$ consistently with the fitting method. Finally, using $C_o(E_0)$ we are able to obtain explicit $-\mathrm{Im}\{f^r_{odd}(\omega)\}/\pi$ from (3.50) and present the results, on Fig. 3.5 (c). Note that, because of our gauge choice, $\mathrm{Re}\{f^r_{odd}(\omega)\}$ is linked to $\mathrm{Im}\{f^r_{odd}(\omega)\}$. Hence, $-\mathrm{Im}\{f^r_{odd}(\omega)\}/\pi$ might be interpreted as the analog of the LDOS for the odd-ω pairing function. Fig. 3.5 (c), clearly shows that $-\mathrm{Im}\{f^r_{odd}(\omega)\}/\pi$ has an amplitude comparable to the LDOS, indicating that the impurity efficiently converts even-ω Cooper pairs into odd-ω one, and generates a significant amount of odd-ω pair

[1] or at least that the eventual multiple YSR states are degenerated up to the experimental resolution

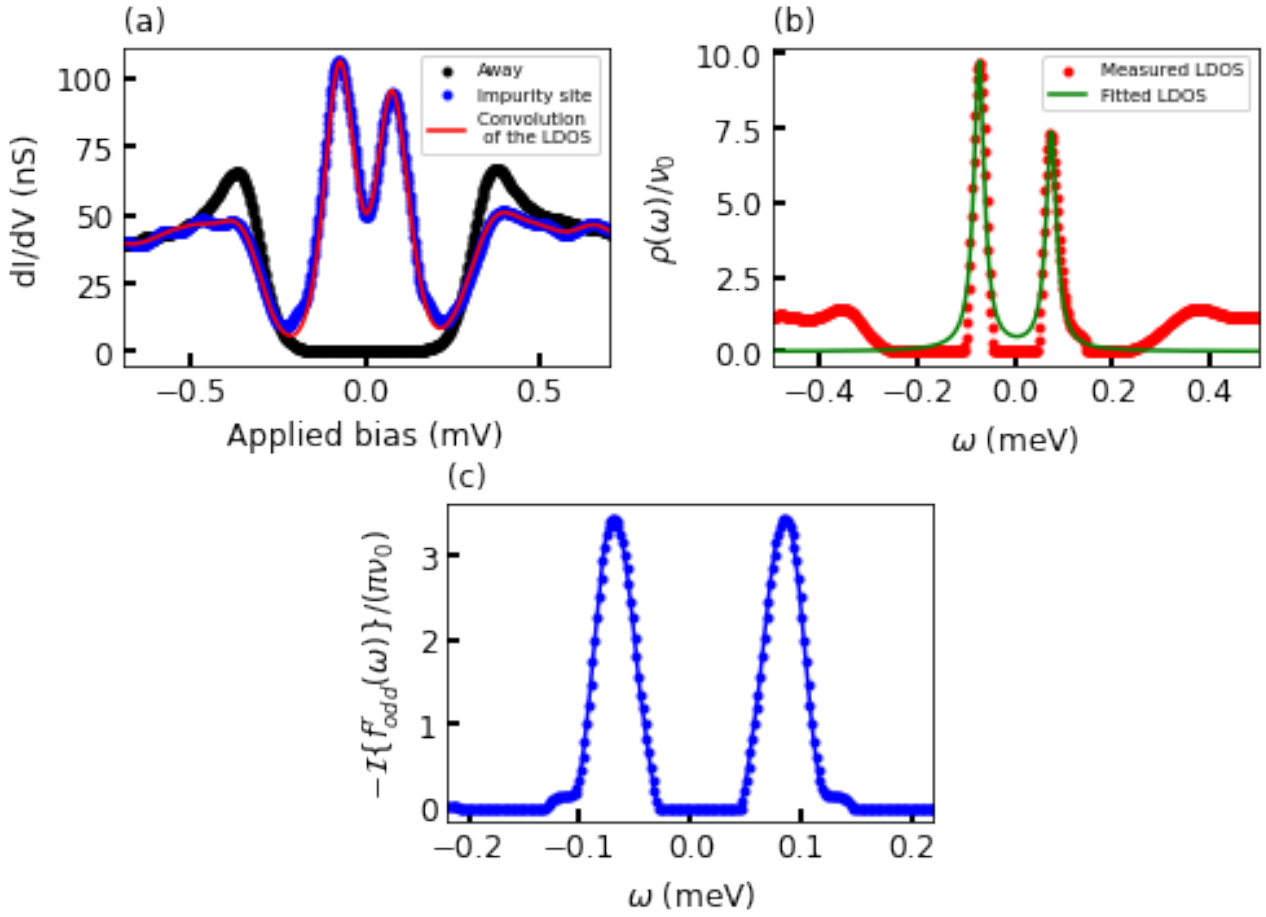

Figure 3.5: Odd-frequency-pairing extracted from STS data. (a): Differential conductance as a function of the applied bias, measured on top of the impurity (blue dots), away from the impurity (black dots), and obtained from the convolution of the extracted LDOS with the Fermi-Dirac derivative with a temperature $T = 320$ mK (solid red line). (b): LDOS obtained after deconvolution taking into account the finite temperature $T = 320$ mK (red dots), along with the LDOS fitted with (3.59) by using the parameter set: $E_0 = 0.074$ meV, $\eta = 0.013$ meV, $u^2/\nu_0 = 0.30$, $v^2/\nu_0 = 0.40$ (green curve). (c): $-\mathrm{Im}\{f^r_{odd}(\omega)/(\pi n u_0)\}$ at the impurity site, extracted from (3.50) with $C_o(E_0) = 0.64$ obtained from the LDOS.

correlations.

3.3.5 Conclusion and perspectives

To conclude, in this chapter, we showed that an isolated magnetic impurity in an *s*-wave superconductor locally breaks the time-reversal symmetry and induces local pairing correlations that are odd in frequency. Using Green's functions technique, we showed that, for energies inside the gap, the imaginary part of the odd-frequency pairing function is proportional to the even component of the local density of states. This result highlights the fact that odd-ω pairing and the YSR state are intimately linked and originate from the time-

reversal symmetry breaking at the impurity site. In addition, since the LDOS is directly accessed in tunneling spectroscopy, based on the former proportionality relation, we provided a protocol to extract these anomalous pairing functions from STS measurements and apply it to data taken from a Pb/Si(111) monolayer with magnetic impurities. Our theoretical analysis of experimental data finally proves the occurrence of odd-ω pairing in the simplest magnetic-superconductor hybrid system.

While finalizing our publication, [30], we learned about the theoretical work of D. Kuzmanovski *et al.* [135], which has partial overlap with the present theoretical analysis. Nevertheless, we stress that, differently from our work, their study mainly focuses on the spatial and frequency dependence on the **spin-resolved** LDOS in relation to odd-ω pairing and that no proportionality relation was established.

Very recently, S. I. Suzuki *et al.* proposed an alternative physical picture to explain why the YSR state has energy below the superconducting gap, and the sign of pair potential changes at the magnetic atom [136]. The authors showed that the analytical expression of Green's function suggests that the magnetic impurity converts spin-singlet s-wave Cooper pairs into odd-frequency Cooper pairs rather than breaking them. In agreement with our analysis, they found that the odd-frequency pairing correlations coexist with the YSR states below the gap. Based on the self-consistent solution of the Eilenberger equation, they conclude that the sign change of the pair potential happens only when the amplitudes of odd-frequency pairing correlations are dominant at the magnetic impurity. These works corroborate our results and show a vivid interest in understanding odd-ω pairing.

A question that naturally arises here is the following one: How these results obtained for a single isolated magnetic atom generalize to the case of a finite concentration of impurity? In collaboration with F. L. N. Santos *et al.* [35], we used a dynamical mean-field theory to tackle this problem. Thanks to a scaling of the YSR-bands and pairing functions with the impurity concentration, we have shown how to extract an odd-frequency component of superconductivity from the Shiba band forming within the bulk superconducting gap following the same strategy as the single impurity case [35].

Chapter 4

Scanning tunneling shot-noise spectroscopy of YSR states

If one applies a constant voltage bias to a mesoscopic junction, between two electronic reservoirs, like in scanning tunneling spectroscopy experiments, a stationary current will typically establish after a transient regime. Nevertheless, after careful analysis, one will discover that the current exhibits time-dependent fluctuations around the stationary average value. These fluctuations arise because of the discreteness of the electron charge combined with the stochastic nature of the electron transport across the junction. For short-enough junctions, as is the case for the STM junction studied throughout this manuscript, inelastic and dephasing effects can be ignored, and the electronic transport through the junction is coherent and determined by elastic scattering of the carriers through the junction.

In this situation, there are two distinct sources of randomness. First, because of thermal agitation, the incident electrons on both sides of the junction occupy states with given energy with a probability given by the Fermi-Dirac distribution. Second, the electronic transport through the junction has to be described quantum mechanically. Hence, incident charge carriers have a finite probability of being transmitted across the junction or reflected into their original reservoir. Notice that, in this case, the noise should also depend on the statistics of the charge carriers. For fermions, the Pauli exclusion principle imposes that a transmitted charge carrier cannot occupy the same state as another carrier incident from the opposite side, which has been reflected.

A common way to characterize the current fluctuations is to study the Fourier transform of the current-current correlations, named the noise. The noise, therefore, carries information about the amplitude and frequency of the current fluctuations.

The noise is particularly suited to study the electronic properties of mesoscopic systems and was intensively investigated during the last decades (see [137] for a review). Indeed the noise is sensitive to both the charge of the carriers q as well as the dynamics of the charge transfer processes.

More precisely, for uncorrelated charge carriers, in the tunneling limit, the shot-noise is Poissonian, *i.e.*, proportional to the current magnitude $|I|$: $S = 2q|I|$. Hence, in the tunneling limit, the Fano factor $F = S/(2e|I|)$ can be used to determine the effective charge of uncorrelated carriers since $F = q/e$. This result has been used to reveal the existence of fractional charges in fractional quantum hall states [138, 139] or the charge doubling due to Andreev reflections in short normal-metal/superconductor junctions [140]. When the transmission probability of charge carriers increases, the shot-noise is no longer Poissonian and depends on

the probability distribution of the charge transfer processes [137]. For systems of independent fermions, the shot-noise is reduced below its Poissonian limit and $F < q/e$, as observed in [141]. For correlated charge carriers, the Fano factor also depends on the interactions and is a powerful tool to study electron correlation in Kondo systems [142, 143] or Coulomb blockade regime [144, 145].

Recently, the development of scanning tunneling shot-noise techniques allowed for the measurement of the shot-noise with atomic-scale resolution and at low currents (< 1 nA) [21, 22]. These recent improvements allow for the experimental study of the shot-noise in YSR states. Nevertheless, to the best of our knowledge, a theoretical description of the shot-noise in YSR states is still lacking. In this chapter, we will fill this gap and show that the shot-noise spectroscopy reveals clear signatures of the resonant Andreev and single-particle processes that carry the current via YSR states.

4.1 Model and methods

4.1.1 Description of the setup

Here we consider a typical STS/STM experiment where a YSR state, supported by a superconducting substrate, is probed by a metallic tip. The tip and sample are coupled via the quantum tunneling effect, and a voltage bias across the tunnel junction is applied, driving the system into an out-of-equilibrium state. The Hamiltonian describing the complete set-up reads :

$$\mathcal{H} = \mathcal{H}_S + \mathcal{H}_T + t\psi_S(\boldsymbol{r}_0)\tau_z\psi_T(\boldsymbol{r}_a) + \text{h.c.}, \tag{4.1}$$

with $\psi_\alpha(\boldsymbol{r}) = [c_{\alpha\uparrow}(\boldsymbol{r}), c_{\alpha\downarrow}(\boldsymbol{r})]^T$ the two-component Nambu spinor in the sub-system $\alpha = S, T$. Here $c_{\alpha\sigma}(\boldsymbol{r})$ annihilates an electron of spin σ in the sub-system $\alpha = S, T$ at position $\boldsymbol{r}$. $\mathcal{H}_S$ describes the isolated superconducting sample, $\mathcal{H}_T$ describes the isolated metallic tip and the last term describes tip-sample tunneling. For simplicity, we only consider local direct tunneling between the tip apex $\boldsymbol{r}_a$ and the substrate position $\boldsymbol{r}_0$ below it with a tunneling amplitude t and neglect any possible mechanical [146, 147, 129], multi-paths related [148, 149, 150, 151], or spin-dependent [152] complications from direct tunneling into the impurity. This approximation is justified, provided that the STM tip probes the tails of the YSR state far away from the core where the above-mentioned effects might be relevant.

The sample consists of an isolated magnetic impurity immersed into a superconducting substrate. We assume that the spin of the magnetic impurity is large, $S_{imp} \gg \hbar$, or is subjected to a strong magnetic anisotropy. Therefore quantum fluctuations of the impurity spin are negligible, and we describe it by a *classical* magnetic moment. As already shown, the magnetic exchange with the spin impurity is responsible for the appearance of a YSR bound-state lying inside the superconducting gap. For the sake of simplicity, we assume that the metallic tip and the normal-state superconducting sample have a single conduction band crossing the Fermi level. Therefore, focusing on the low-energy physics around the Fermi energy, the sample is conveniently described by the single-band YSR model given by (3.27), and $\mathcal{H}_S$ reads:

$$\mathcal{H}_S = \int \frac{\mathrm{d}\boldsymbol{k}}{(2\pi)^{d_S}} \psi_S^\dagger(\boldsymbol{k})[\epsilon_S(\boldsymbol{k})\tau_z + \Delta\tau_x]\psi_S(\boldsymbol{k}) + \psi_S^\dagger(\boldsymbol{r}=\boldsymbol{0})(U\tau_z - J)]\psi_S(\boldsymbol{r}=\boldsymbol{0}), \tag{4.2}$$

with $\psi_\alpha(\boldsymbol{k}) \equiv \int \mathrm{d}\mathbf{r} e^{-i\boldsymbol{k}\boldsymbol{r}}\psi_\alpha(\boldsymbol{r})$, the momentum representation of Nambu spinor in the sample. d_S denotes the dimension of the superconducting substrate. $\epsilon_S(\boldsymbol{k})$ denotes the band dispersion of the normal-state substrate.

Δ is the BCS order parameter of the substrate, which is chosen real, without loss of generality. U is the local electrostatic potential created by the magnetic impurity, and J is the magnetic exchange coupling. Without loss of generality, we choose the impurity position as the substrate coordinates' origin. Lastly, τ_i ($i = x, y, z$) are Pauli matrices acting in Nambu-space and τ_0 the identity in Nambu-space.

Finally, since we are only interested in low voltage bias, $|eV| < \Delta$, the relevant energy range for the transport properties is a narrow window around the Fermi energy with width $\sim \Delta$. For conventional superconductors, Δ is much smaller than the Fermi energy. Therefore we can safely neglect the energy dependence of the normal-state DOS of the tip and sample. Within this wide-band approximation, the tip and normal-state substrate are characterized by their densities of states at the Fermi level, denoted ν_0 and ν_S, respectively.

4.1.2 Description of the transport observables within the Keldysh formalism

The central quantity of interest here is the charge current operator $\hat{I}(t) = -e\partial_t \hat{N}_T(\tau)$, with $\hat{N}_T(\tau)$ the particle number operator in the tip in the Heisenberg picture. Using the equation motion, it is straightforward to show that:

$$\hat{I}(\tau) = \frac{iet}{\hbar}\{\langle\psi_T^\dagger(\tau)\psi_S(\tau) - \psi_S^\dagger(\tau)\psi_T(\tau)\}, \tag{4.3}$$

where we introduced the short-hand notations $\psi_S \equiv \psi_S(\boldsymbol{r}_0)$ and $\psi_T \equiv \psi_T(\boldsymbol{r}_a)$. To evaluate the mean current and its fluctuations, we use the non-equilibrium Green's functions (NEGF) technique on the Keldysh contour c, depicted in Fig. 2.4. Thus, we introduce the following set of contour-ordered Green's functions,

$$\hat{G}^c_{\alpha\beta}(z, z') = -\frac{i}{\hbar}\langle\mathcal{T}_c[\psi_\alpha(z) \otimes \psi^\dagger_\beta(z')]\rangle, \tag{4.4}$$

and the corresponding retarded $\hat{G}^r_{\alpha\beta}(\tau, \tau')$, advanced $\hat{G}^a_{\alpha\beta}(\tau, \tau')$, lesser $\hat{G}^<_{\alpha\beta}(\tau, \tau')$, and greater $\hat{G}^>_{\alpha\beta}(\tau, \tau')$ real-time NEGFs. Here $\alpha, \beta = S, T$ are sub-system index, $\langle ...\rangle$ indicates the non-equilibrium average of operators evolving in the Heisenberg picture, with respect to $\mathcal{H}$, $\mathcal{T}_c$ is time-ordering operator along the Keldysh contour c, finally z, and z' are time arguments lying on c. Focusing our attention on the long-time DC regime, all real-time Green's functions depend only on the relative time difference:

$$\hat{G}^\gamma_{\alpha\beta}(\tau, \tau') = \hat{G}^\gamma_{\alpha\beta}(\tau - \tau'), \tag{4.5}$$

where γ is the index for the Keldysh sub-space *i.e.* $\gamma = r, a, >, <$. Thus, it is convenient to define their Fourier transform:

$$\hat{G}^\gamma_{\alpha\beta}(\omega) \equiv \int \mathrm{d}\tau e^{i\frac{\omega\tau}{\hbar}} \hat{G}^\gamma_{\alpha\beta}(\tau). \tag{4.6}$$

With these definitions, the average charge current flowing from the tip apex, $I(t) = \langle\hat{I}(t)\rangle$, reads:

$$I = \frac{et}{h}\int \mathrm{d}\omega\, \mathrm{Tr}\left\{G^<_{ST}(\omega) - G^<_{TS}(\omega)\right\}, \tag{4.7}$$

where the trace is performed over the Nambu space. The current shot-noise $S(\tau)$ is defined as the zero-frequency limit of the time-symmetric current-current correlation, $C(\tau,\tau')$,

$$C(\tau,\tau') = \langle \delta\hat{I}(\tau)\delta\hat{I}(\tau') + \delta\hat{I}(\tau')\delta\hat{I}(\tau)\rangle, \tag{4.8}$$

$$S(\tau) = \int_{-\infty}^{\infty} \mathrm{d}\tau' C(\tau'+\tau,\tau), \tag{4.9}$$

where $\delta\hat{I}(\tau) \equiv \hat{I}(\tau) - \langle\hat{I}(\tau)\rangle$. Using the Wick theorem and a straightforward Fourier transform, we can express S in terms of Keldysh NEGFs:

$$S = \frac{2e^2t^2}{h}\int \mathrm{d}\omega\, \mathrm{Tr}\big\{G^<_{TT}(\omega)G^>_{SS}(\omega) - G^<_{ST}(\omega).G^>_{ST}(\omega)\big\} + (S \leftrightarrow T). \tag{4.10}$$

In order to compute the NEGFs entering S and I, we treat the tip-sample as a perturbation and use perturbative expansion with respect to the tip-sample coupling. Using the results of Section. 2.3, and more particularly of Subsection. 2.3.2, it is straightforward to show that the contour-ordered Green's functions obey the following equations:

$$\hat{G}^c_{\alpha\beta}(z,z') = \delta_{\alpha\beta}\hat{g}^c_\alpha(z,z') + t\int_c \mathrm{d}z_1 \hat{g}_\alpha(z,z_1)\hat{G}^c_{\delta\beta}(z_1,z'),\ \delta\neq\alpha. \tag{4.11}$$

Here, we introduced the unperturbed contour-ordered Green's functions of the isolated tip and sample:

$$\hat{g}^c_\alpha(z,z') = -\frac{i}{\hbar}\langle \mathcal{T}_c[\psi_\alpha(z)\psi^\dagger_\alpha(z')]\rangle_0,\ \alpha = S,T. \tag{4.12}$$

These contour-ordered Green's function contains the retarded, $\hat{g}^r_\alpha(z,z')$, advanced, $\hat{g}^a_\alpha(z,z')$, lesser, $\hat{g}^<_\alpha(z,z')$, and greater, $\hat{g}^>_\alpha(z,z')$ real-time unperturbed NEGFS describing the tip ($\alpha = T$) and sample ($\alpha = S$). We recall that the notation $\langle ...\rangle_0$ defined in (2.34) denotes equilibrium average with respect to the unperturbed density matrix of operators evolving with respect to the unperturbed Hamiltonian $\mathcal{H}_0$. Using Langreth's rules and after a straightforward Fourier transformation, we obtain the following set of equations:

$$\hat{G}^{r/a}_{\alpha\alpha}(\omega) = \hat{g}^{r/a}_\alpha(\omega) + t^2\hat{g}^{r/a}_\alpha(\omega)\tau_z\hat{g}^{r/a}_\delta(\omega)\tau_z\hat{G}^{r/a}_{\alpha\alpha}(\omega),\ \delta\neq\alpha \tag{4.13}$$

$$\begin{aligned}\hat{G}^{</>}_{mm}(\omega) =& g^{</>}_m(\omega) + t^2\{\hat{g}^{</>}_\alpha(\omega)\tau_z\hat{g}^a_\delta(\omega)\tau_z\hat{G}^a_{\alpha\alpha}(\omega) + \hat{g}^r_\alpha(\omega)\tau_z\hat{g}^{</>}_\delta(\omega)\tau_z\hat{G}^a_{\alpha\alpha}(\omega)\\ &+ \hat{g}^r_\alpha(\omega)\tau_z\hat{g}^r_\delta(\omega)\tau_z\hat{G}^{</>}_{\alpha\alpha}(\omega),\ \delta\neq\alpha\end{aligned} \tag{4.14}$$

$$\hat{G}^{</>}_{ST}(\omega) = t\{\hat{G}^{</>}_{SS}(\omega)\tau_z\hat{g}^a_T(\omega) + \hat{G}^r_{SS}(\omega)\tau_z\hat{g}^{</>}_T(\omega)\} \tag{4.15}$$

$$\hat{G}^{</>}_{TS}(\omega) = t\{\hat{g}^r T(\omega)\tau_z\hat{G}^{</>}_{SS}(\omega) + \hat{g}^{</>}_T(\omega)\tau_z\hat{G}^a_{SS}(\omega)\}. \tag{4.16}$$

The above set of equations is a closed set that allows us to compute all Green's functions entering (4.10) and (4.7) from the sole knowledge of the unperturbed local Green's functions $\hat{g}^{r/a/</>}_\alpha(\omega)$ describing the isolated tip ($\alpha = T$) and sample ($\alpha = S$).

We recall that the isolated green's functions satisfy the following relationships

$$g^a_{T/S}(\omega) = \left[g^r_{T/S}(\omega)\right]^\dagger, \tag{4.17}$$

$$g^<_T(\omega) = \hat{f}_T(\omega)\cdot[\hat{g}^a_T(\omega) - \hat{g}^r_T(\omega)],\ g^>_T(\omega) = -\left(\tau_0 - \hat{f}_T(\omega)\right)\cdot[\hat{g}^a_T(\omega) - \hat{g}^r_T(\omega)], \tag{4.18}$$

$$g^<_S(\omega) = -f(\omega)\cdot[\hat{g}^a_S(\omega) - \hat{g}^r_S(\omega)],\ g^>_S(\omega) = -(1-f(\omega))\cdot[\hat{g}^a_S(\omega) - \hat{g}^r_S(\omega)], \tag{4.19}$$

with $\hat{f}_T(\omega)$ defined by equation (2.77) and $f(\omega)$ the Fermi-Dirac distribution. Therefore, the isolated metallic tip and superconducting substrate are completely characterized by the local retarded Green's functions, $g_T^r(\omega)$ and $g_S^r(\omega)$, respectively. Within our wide-band approximation $g_T^r(\omega)$ reads:

$$g_T^r(\omega) = -i\pi\nu_T\tau_0. \tag{4.20}$$

Hence, $g_T^r(\omega)$ is energy-independent and only involves the DOS of the metallic tip at the Fermi level, ν_T. It follows that the transmission of the STM junction is characterized by an energy-independent tunneling rate $\Gamma = 2\pi\nu_T t^2$.

Let us now turn to the unperturbed Green's function describing the superconducting sample. In realistic systems, it is not possible to isolate the sample from its environment, and quasiparticles undergo relaxation processes. These relaxation processes can have various origins, such as electron-phonon coupling, electron-photon coupling, or quasiparticle poisoning. However, the details of the microscopic relaxation mechanisms are not crucial for the transport properties we are interested in. Hence, for the present purpose, it is enough to assume that the quasiparticle of the substrate can relax into an incoherent quasiparticle bath at equilibrium with the superconducting substrate [1]. In addition, since we are only interested in a narrow energy range of the order Δ around the Fermi energy, we can safely neglect the energy dependence of the relaxation rate and replace it by a constant. Thus, we introduce a phenomenological Dynes broadening, Λ_0, which accounts for quasiparticle relaxation and provides the quasiparticles of the substrate with a finite lifetime. Within this approximation, $g_S^r(\omega)$ obey the following Dyson equation:

$$\hat{g}_S^r(\omega) = \hat{g}_0^r(\boldsymbol{r_0},\omega)\{[\hat{g}_0^r(\omega)]^{-1} - (U\tau_z - J\tau_0 - i\Lambda_0\tau_0)\}^{-1}\hat{g}_0^r(\boldsymbol{r_0},\omega), \tag{4.21}$$

where $\hat{g}_0^r(\boldsymbol{r}-\boldsymbol{r'},\omega)$ is the retarded Green's function of the BCS substrate in the absence of the magnetic impurity. $\hat{g}_0^r(\omega)$ denotes the local Green's function of a clean BCS superconductor $\hat{g}_0^r(\boldsymbol{0},\omega)$. Using the wide-band approximation this Green's function reads: $\hat{g}_0^r(\omega) = -\frac{\pi\nu_0}{\sqrt{\Delta^2-\omega^2}}(\omega\tau_0 + \Delta\tau_x)$, with ν_0 the normal-state density of state at the Fermi level.

In the absence of relaxation, *i.e.* $\Lambda_0 = 0$, $\hat{g}_S^r(\omega)$ possesses a single pole inside the gap at energy $E_0 = \Delta\frac{1-\alpha^2+\beta^2}{\sqrt{(1-\alpha^2+\beta^2)^2+4\alpha^2}}$ signaling the existence of the YSR state of energy E_0, with $\alpha = \pi\nu_0 J$ and $\beta = \pi\nu_0 U$. The wavefunction $\phi_0(\boldsymbol{r}) = [u(\boldsymbol{r}), v(\boldsymbol{r})]^T$ of the YSR state and its properties have been studied in Subsection. 3.2.3.

In the presence of relaxation, because of the Dynes broadening Λ_0, the YSR state becomes a resonance with a finite energy-width Λ. In most superconductors, the Dynes broadening is typically much smaller than the superconducting gap, $\Lambda_0 \ll \Delta$, and one can relate the energy-width Λ to the Dynes broadening: $\Lambda = 4\pi\nu_0\Delta\Lambda_0\alpha\frac{1+\alpha^2+\beta^2}{\sqrt{(1-\alpha^2+\beta^2)^2+4\alpha^2}^{3/2}}$, as shown in Subsection. 3.3.3.

Albeit exact, the retarded Green's function $\hat{g}_S^r(\omega)$, given by (4.21), is too complicated and does not yield insightful results for the current and shot-noise. Nevertheless, we recall that we are only interested in the sub-gap voltage ($eV < \Delta$) and low-temperature regime ($k_BT \ll \Delta$) regime. Fortunately, in this regime, for weak enough tunnel coupling, resonant tunneling processes via the YSR state give the dominant contribution to transport properties, as we will show below. Thus, $\hat{g}_S^r(\omega)$ can be projected onto the YSR subspace. This approximation significantly simplifies our model and allows for semi-analytical treatment.

[1] This incoherent bath can be the continuum of excited quasiparticles of the superconducting substrate in the case of inelastic relaxation mediated by phonons or photons [32], or a reservoir of gapless quasiparticles in the case of quasiparticle poisoning [31].

4.1.3 Relevant tunneling processes

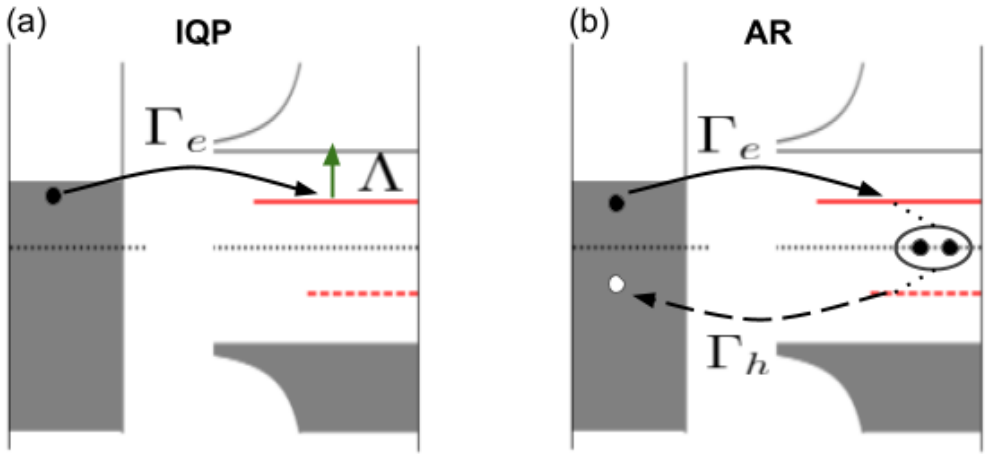

Figure 4.1: Schematic illustration of the fundamental tunneling processes between the metallic tip and the YSR state. The metallic tip and superconducting substrate are represented by their DOS. The vertical axis corresponds to the energy of the states measured from the Fermi substrate level indicated by the horizontal black dotted line. Occupied states are indicated by the grey-shaded region, and blank regions correspond to unoccupied states. The YSR state gives rise to two resonances at $\pm E_0$. The electron-like resonance at E_0, proportional to u^2, is indicated by the red solid line, while the hole-like resonance at $-E_0$, proportional to v^2, is indicated by the red dashed line. We stress that a hole with energy E represents an unoccupied electronic state at energy $-E_0$. (a): Incoherent single quasiparticle process (IQPs): An electron from the occupied states of the metallic tip tunnels into the electron-like YSR resonance at E_0 with probability $\Gamma_e = \Gamma u^2$ (black solid arrow). Subsequently, the YSR state relaxes into an incoherent quasiparticle bath, which might correspond to the quasiparticle continuum of the substrate, with a probability $\propto \Lambda$ (green solid arrow). (b): Resonant Andreev reflection via the YSR state (AR): An electron from the occupied levels of the tip virtually tunnels into the YSR state via its electron-like component with probability $\propto \Gamma_e$. Then it is converted into a hole, adding a Cooper into the condensate of the substrate. This hole is finally reflected back into the metallic tip with probability $\propto \Gamma_h = \Gamma v^2$. Both processes schematized in (a) and (b) are resonant process which become relevant for biases $eV \gtrsim E_0$. Analogous processes with electrons replaced by holes occur for $eV \lesssim -E_0$.

We should now discuss the fundamental tunneling processes that give rise to a continuous current flowing between the tip and superconducting substrate supporting the magnetic impurity. To simplify the discussion we assume a low-temperature regime $E_0 \gg k_B T$ and focus on the sub-gap regime $|eV| < \Delta$.

First, when $eV \gtrsim E_0$ the continuum of occupied electrons in the tip overlaps with E_0, spin-up electrons with energy $\omega \sim E_0$ can tunnel into the YSR state, which subsequently relaxes into the unoccupied states of the incoherent quasiparticle bath. This process corresponds to an incoherent single-particle process (IQP) schematized in Fig. 4.1 (a). Notice that spin-down electrons cannot undergo similar processes since the YSR

state is spin-polarized. Similar processes, where spin-down holes at energy $\omega \sim E_0$ [2] from the tip can tunnel into the unoccupied YSR state that subsequently relaxes occur when the continuum of unoccupied electrons in the tip overlaps with the symmetric energy $-E_0$, *i.e.*, $eV \lesssim -E_0$.

Second, as in the case of a clean BCS superconductor, an incoming electron from, say, the tip can be reflected as a hole in the tip, transferring a Cooper pair into the condensate of the superconducting substrate. This tunneling process is nothing but an *ordinary* Andreev reflection (AR) studied in Subsection. 2.3.5 and schematized in Fig. 2.5 (b). It is important to notice that such *ordinary* Andreev reflections do not involve the YSR state. However, since an Andreev reflection requires the transfer of two charge carriers across the STM junction, they become relevant only for strong tunnel coupling. Thus, *ordinary* Andreev reflections can be safely neglected for weak tunnel coupling.

Third, because of the YSR state, an additional type of Andreev reflection is possible here. Indeed, when $eV \gtrsim E_0$, the continuum of occupied electrons in the tip overlaps E_0. Thus, spin-up electrons from the tip can virtually tunnel into the YSR state, reflect back as spin-up holes and resonantly transfer a Cooper pair into the condensate, as illustrated in Fig. 4.1 (b). Such a process corresponds to a resonant Andreev reflection via the YSR state, which transfers a charge $2e$ across the STM junction. Note that complementary Andreev processes, where spin-up holes are resonantly reflected as electrons via the YSR state, occur when $eV \lesssim -E_0$. Contrary to *ordinary* Andreev reflections, Andreev reflections via the YSR state are resonant processes. Hence, they are resonantly enhanced at energies $\omega \sim E_0$, and they may become relevant at much weaker tunnel coupling than *ordinary* non-resonant Andreev reflections [32]. Thus, there is no *a priori* reasons to neglect, even for weak tunnel coupling.

Finally, we stress that there exists an important difference between resonant ARs and IQPs via the YSR state. Indeed, IQPs change the occupation of the YSR state. Hence, a continuous current supported by IQPs via the YSR state requires relaxation of the YSR state and is necessarily an incoherent process. On the contrary, in an AR, the YSR is an intermediate state that is virtually occupied, and ARs do not change the occupation of the YSR. They are thus coherent processes that are present even in the ideal case of a perfectly isolated YSR.

4.1.4 Simplified model

Throughout this chapter, we assume the tunnel coupling to be weak enough such that we can safely neglect non-resonant Andreev reflections at the superconducting substrate. In this regime, we can focus our attention on the single-particle processes and resonant Andreev reflections via the YSR state, sketched in Fig. 4.1. Therefore, following M. Ruby *et al.* [32], we project the unperturbed retarded Green's function describing the isolated sample, $\hat{g}^r_S(\omega)$ onto the YSR subspace:

$$g^r_S(\omega) \equiv g^r_S(\boldsymbol{r}_0, \boldsymbol{r}_0, \omega) \sim \frac{\phi_0(\boldsymbol{r}_0)\phi_0^\dagger(\boldsymbol{r}_0)}{\omega - E_0 + i\Lambda/2} = \frac{1}{\omega - E_0 + i\Lambda/2} \begin{bmatrix} u^2 & uv \\ uv & v^2 \end{bmatrix}, \tag{4.22}$$

where the YSR components, $u \equiv u(\boldsymbol{r}_0)$, $v \equiv v(\boldsymbol{r}_0)$ depend implicitly on the tip location with respect to the core of the impurity.

Within this simplified model, all tunneling processes are mediated by the YSR state. **Since the YSR state is only coupled to spin-up electrons and spin-down holes of the metallic tip, we will omit the spin indices**

[2] Here, we use the following convention: an occupied hole with energy ω and spin σ is an unoccupied electron with energy $-\omega$ and spin σ

hereinafter. Hence, throughout the rest of this chapter, the term *electron* designates a spin-up electron of energy ω while the term *hole* refers to a spin-down hole. By passing, we point out that within our simplified model, tunneling into YSR states is equivalent to the scattering of spinless particles between three reservoirs connected by a resonant level. The reservoirs correspond to spin-up electrons in the metallic tip, spin-down holes in the metallic tip, and quasiparticles in the incoherent bath, while the resonant level represents the YSR level. Thorough details about this equivalence can be found in the Supplementary Material of [33].

Inserting the low-energy approximation (4.22) in the aforementioned closed set of equations, we obtain exact expressions for the current and shot-noise, which we analyze in the following sections.

4.2 Standard current spectroscopy : a brief review

Before discussing the shot noise spectroscopy in YSR states, which, to the best of our knowledge, was not addressed before, we first briefly review the important features of the standard current and differential spectroscopy in YSR states. This topic has already been investigated in previous works, and a thorough discussion of the differential conductance in YSR states measured with a metallic tip can be found in [31]. Notice that the current and differential conductance has also been measured with a superconducting tip and theoretically analyzed in [32].

4.2.1 Discussion of the average current I

After lengthy but straightforward algebra, we find that the average current passing through the YSR resonance reads:

$$\begin{aligned} I = \frac{e}{h}\int \mathrm{d}\omega 2 &\frac{\Gamma_e\Gamma_h}{(\omega-E_0)^2+\Gamma_t^2/4}[f(\omega^-)-f(\omega^+)] \\ &+\frac{\Gamma_e\Lambda}{(\omega-E_0)^2+\Gamma_t^2/4}[f(\omega^-)-f(\omega)] \\ &+\frac{\Gamma_h\Lambda}{(\omega-E_0)^2+\Gamma_t^2/4}[f(\omega)-f(\omega^+)], \end{aligned} \tag{4.23}$$

where we introduced the shorthand notation $\omega^{\pm} = \omega \pm eV$, and f denotes the Fermi-Dirac distribution. We also defined the notations $\Gamma_e \equiv \Gamma u^2$, $\Gamma_h \equiv \Gamma v^2$ and $\Gamma_t \equiv \Lambda + \Gamma_e + \Gamma_h$. Here $\Gamma \equiv 2\pi\nu_T t^2$, with ν_T the density of states in the metallic tip, is the tunneling rate characterizing the transmission of the STM junction. In the ideal zero-temperature limit, the integrals can be performed exactly and yield:

$$\begin{aligned} I = \frac{2e}{h\Gamma_t}\Bigg\{ &2\Gamma_e\Gamma_h\left[\arctan\left(2\frac{eV-E_0}{\Gamma_t}\right)+\arctan\left(2\frac{eV+E_0}{\Gamma_t}\right)\right] \\ &+\Gamma_e\Lambda\left[\arctan\left(2\frac{eV-E_0}{\Gamma_t}\right)+\arctan\left(2\frac{E_0}{\Gamma_t}\right)\right] \\ &+\Gamma_h\Lambda\left[\arctan\left(2\frac{eV+E_0}{\Gamma_t}\right)-\arctan\left(2\frac{E_0}{\Gamma_t}\right)\right]\Bigg\}. \end{aligned} \tag{4.24}$$

As observed in Fig.4.2, in the ideal $T = 0$ limit, far below the resonance, *i.e.* when $|eV| \ll E_0$, the current is negligible[3] and linear in V. Near the resonances, *i.e.* when $|eV \pm E_0| \lesssim \Gamma_t$, I is non-linear in V and abruptly increases. It rapidly saturated to finite values:

$$I_+ = \lim_{eV \gg E_0} = \frac{e}{\hbar} \frac{2\Gamma_e\Gamma_h + \Gamma_e\Lambda}{\Gamma_t}, \tag{4.25}$$

$$I_- = \lim_{eV \ll -E_0} = -\frac{e}{\hbar} \frac{2\Gamma_e\Gamma_h + \Gamma_h\Lambda}{\Gamma_t}, \tag{4.26}$$

where we assumed $E_0 \gg \Gamma_t$. The staircase shape of the $I - V$ characteristic is a direct consequence of the resonant nature of the single-particle and Andreev processes producing the current. Indeed, these processes become relevant only when there are available electrons or holes in the tip at energy E_0 to tunnel into the YSR resonance, which correspond to the condition $eV \gtrsim E_0$ and $eV \lesssim E_0$, respectively. We stress that this result could be anticipated since (4.23) was obtained by considering only the resonant tunneling processes via the YSR state. It is interesting to remark that, inspecting (4.24), one immediately remark that when $\Lambda = 0$, $|I|$ is an even functions of V, regardless of the model parameters. For finite Λ, the shape of the $I - V$ characteristic is not voltage-symmetric unless $u^2 = v^2$. Interestingly, the asymmetry in the current magnitude $|I|$ depends on G_N or equivalently Γ. Indeed, in the tunneling regime $\Gamma(u^2 + v^2) \ll \Lambda$, the height ratio of the positive and negative plateaus, $|I_+|/|I_-|$ reflects the particle-hole ratio of the YSR wavefunction, $I_+/|I_-| \simeq u^2/v^2$, as observed in Figs. 4.2 (a) and (d). Increasing the tunneling rate Γ the current magnitude $|I|(V)$ becomes more and more symmetric but remains slightly asymmetric. Indeed, $|I_+| > |I_-|$ if $u^2 > v^2$ and vice versa (see Figs. 4.2 (b) and (e)). In the strong tunnel coupling regime, $\Gamma(u^2 + v^2) > \Lambda$, the current magnitude $|I|(V)$ is almost perfectly symmetric, independently of the particle-hole ratio u^2/v^2, as observed in Figs. 4.2 (c) and (f). We will see later in this section that these features are due to the simultaneous presence of single-particle and Andreev processes.

In the realistic finite-temperature case, the integrals entering equation (4.23) are no longer exact and have to be evaluated numerically. In Fig. 4.2 we compare the numerical evaluation of I for a moderate temperature, $E_0 \gg k_B T \simeq 0.06\text{meV}$, corresponding to the typical electronic temperature in STM experiments ([33]) with the above-mentioned zero-temperature limit. Fig. 4.2 clearly shows that finite temperature effects smooth the abrupt steps at $eV = \pm E_0$ whose width is now of order $\sim k_B T$. Other qualitative features observed at $T = 0$ remain unchanged at finite T. More specifically, the values of the asymptotic limit, $I_\pm$ are unaffected by temperature. Indeed, when $E_0 \gg k_B T \gg \Gamma_t$, as typically encountered in the experiment studied at the end of this chapter (see [33]), I can be approximated by:

$$I \simeq \frac{e}{\hbar} \left\{ \frac{2\Gamma_e\Gamma_h}{\Gamma_t}[f(E_0^-) - f(E_0^+)] + \frac{\Gamma_e\Lambda}{\Gamma_t}[f(E_0^-)] - \frac{\Gamma_h\Lambda}{\Gamma_t}[f(E_0^+)] \right\}, \tag{4.27}$$

explicitly showing the above-mentioned statements.

[3] Indeed, in the weak tunnel coupling that we are interested in, below the resonance ($|eV| \ll E_0$), the current magnitude is typically very weak (for example [33] reported $|I| < 1pA$ below the resonances). Hence it is experimentally challenging to measured it accurately.

4.2.2 Discussion of the differential conductance G

Having discussed the qualitative feature of the current, we now turn to the differential conductance $G = \frac{\mathrm{d}I}{\mathrm{d}V}$. In the $T = 0$ limit, the differential conductance adopts an elegant and compact analytical form that reads:

$$G = \frac{G_0}{2}\left\{\frac{\Gamma_e(2\Gamma_h + \Lambda)}{(\omega - E_0)^2 + \Gamma_t^2/4} + \frac{\Gamma_h(2\Gamma_e + \Lambda)}{(\omega + E_0)^2 + \Gamma_t^2/4}\right\}, \tag{4.28}$$

with $G_0 = \frac{2e^2}{h}$ the quantum of conductance. Therefore, the differential conductance exhibits two sub-gap peaks located at the resonances $eV = \pm E_0$, indicating the presence of the YSR sub-gap state. In the $T = 0$ limit, the width of the peaks is given by Γ_t. Notice that in absence of relaxation processes, $\Lambda = 0$, G is an even function of V independently of the tunneling rate Γ. Therefore in the absence of relaxation processes, even for weak tunneling rates, G is not proportional to the LDOS of the YSR state. On the contrary, for finite Λ, the conductance becomes asymmetric, and its asymmetry depends on the tunneling rate Γ. In the tunneling regime,

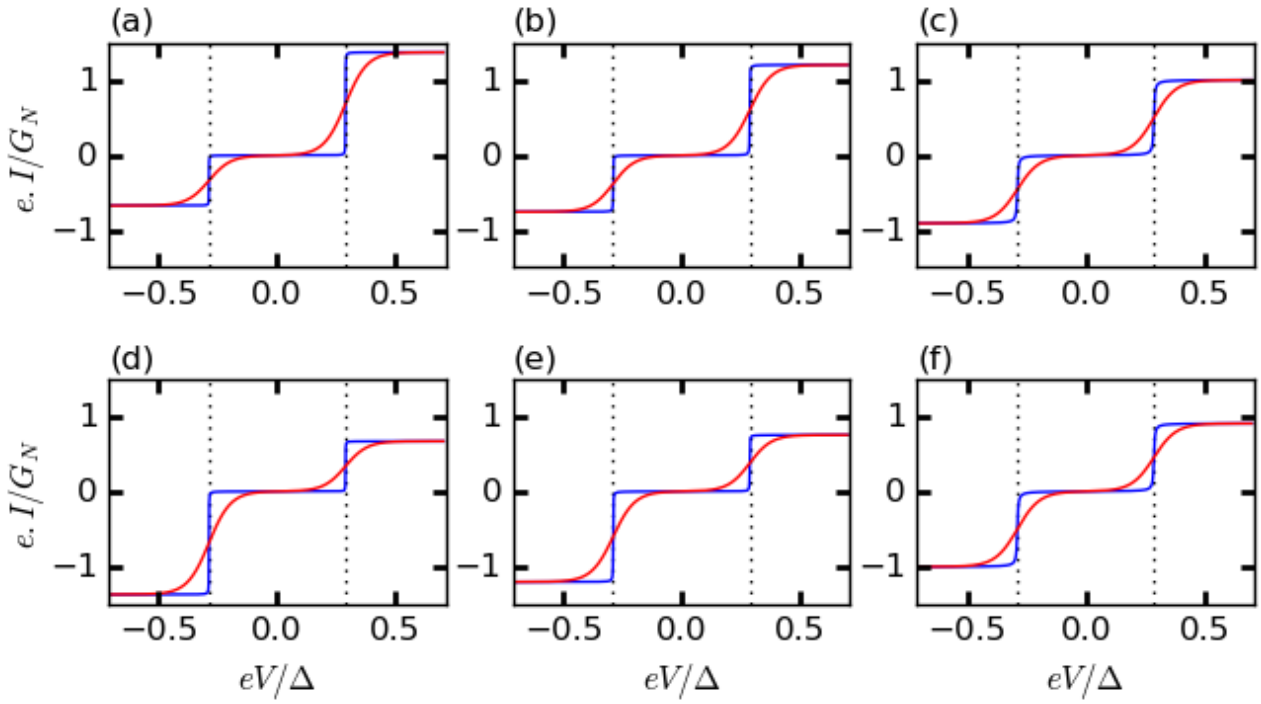

Figure 4.2: Average current I in units of G_N/e as a function of eV/Δ in the sub-gap regime for different normal state conductance G_N and temperature T. Panels (a),(b) and (c) corresponds to $u^2 = 0.09\pi\nu_0$, $v^2 = 0.042\pi\nu_0$, and $G_N/G_0 = 10^{-3}, 10^{-2}, 10^{-1}$ respectively. Panels (d),(e) and (f) corresponds to $u^2 = 0.042\pi\nu_0$, $v^2 = 0.09\pi\nu_0$, and $G_N/G_0 = 10^{-3}, 10^{-2}$, and 10^{-1} respectively. In each panels, the blue solid line corresponds to $T = 0$ while the red solid line corresponds to $k_BT = 0.06\mathrm{meV}$, which satisfies $k_BT \gg \Gamma_t$ in all cases.

$\Lambda \gg \Gamma_e, \Gamma_h$, the differential conductance is approximately given by

$$G \underset{\Lambda \gg \Gamma_e, \Gamma_h}{\simeq} \frac{G_0}{2} \left\{ \frac{\Gamma_e(\Lambda)}{(\omega - E_0)^2 + \Lambda^2/4} + \frac{\Gamma_h(\Lambda)}{(\omega + E_0)^2 + \Lambda^2/4} \right\}. \tag{4.29}$$

and G is proportional to the LDOS of the YSR state as expected in the tunneling regime. In this case, the width of the conductance peaks directly yields the relaxation rate Λ. Moreover as long as $E_0 \gg \Lambda$ the positive and negative resonance does not overlap, and $G_+ = G(E_0) \propto u^2$ while $G_- = G(-E_0) \propto v^2$. Increasing the tunneling rate Γ, the conductance becomes more and more symmetric, as observed in Fig. 4.3 (a). When $\Gamma(u^2 + v^2) \gg \Lambda$, the relaxation rate becomes negligible, and one recovers a perfect symmetry of G.

In the realistic finite-temperature case, the width of the differential conductance peaks is increased by thermal broadening and is no longer directly related to Γ_t. Most importantly, when $k_B T \gg \Gamma_t$, which is the case for the experimental data studied at the end of this chapter, the conductance is approximately given by:

$$\begin{aligned} G \underset{k_B T \gg \Gamma_t}{\simeq} \frac{G_0}{2k_B T} \{ & \frac{2\Gamma_e \Gamma_h}{\Gamma_t} \left[\Phi(E_0 - eV) + \Phi(E_0 + eV) \right] \\ & + \frac{\Gamma_e \Lambda}{\Gamma_t} \Phi(E_0 - eV) + \frac{\Gamma_h \Lambda}{\Gamma_t} \Phi(E_0 + eV) \}, \end{aligned} \tag{4.30}$$

$$\text{with, } \Phi(\omega) = \frac{e^{\beta\omega}}{\left[1 + e^{\beta\omega}\right]^2}. \tag{4.31}$$

Therefore, similarly to the $T = 0$ limit, when $k_B T \gg \Gamma_t$, the differential conductance spectrum exhibits two peaks located at opposite energies $\pm E_0$. When $E_0 \gg k_B T$, they do not overlap, and their width at half maximum does not depend on Γ and is roughly given by $3.5 k_B T$, as observed in Fig. 4.3 (b). We stress that, in this regime, Λ is masked by thermal effects and can not be simply extracted from the width of the conductance peaks at low tunneling rates. On the contrary, the heights of the conductance peaks depend on Γ and, provided that $E_0 \gg k_B T \gg \Gamma_t$, read:

$$G_+ \simeq \frac{G_0}{8k_B T} \left[\frac{\Gamma_e \left(2\Gamma_h + \Lambda\right)}{\Gamma_t} \right], G_- \simeq \frac{G_0}{8k_B T} \left[\frac{\Gamma_h \left(2\Gamma_e + \Lambda\right)}{\Gamma_t} \right] \tag{4.32}$$

Thus, as in the $T = 0$ limit, the asymmetry of the conductance peaks depends on the tunneling rate Γ. For weak tunneling rates, $\Gamma_e, \Gamma_h \ll \Lambda$, the conductance peaks are approximately given by $G_+ \simeq \frac{G_0 \Gamma_e}{8k_B T}$, while $G_- \simeq \frac{G_0 \Gamma_h}{8k_B T}$. Hence, their asymmetry reflects the particle-hole asymmetry of the YSR wavefunction, see the green curve in Fig. 4.3 (b). Hence, the asymmetry of the conductance peaks reflects the particle-hole asymmetry of the YSR wavefunction. Increasing the tunneling rate, the peaks become more and more symmetric, as indicated by the blue curve in Fig. 4.3 (b). In the strong tunneling rate limit, $\Gamma_e, \Gamma_h \gg \Lambda$, the peaks are roughly symmetric independently of u^2/v^2 as observed from the red curve in Fig. 4.3 (b).

4.2.3 Physical interpretation

Let us now show that the above-mentioned feature of the average current and differential conductance result from the competition between single-particle and Andreev processes, which produces the current. To that end, we shall first interpret (4.23) in terms of Andreev reflections and IQPs.

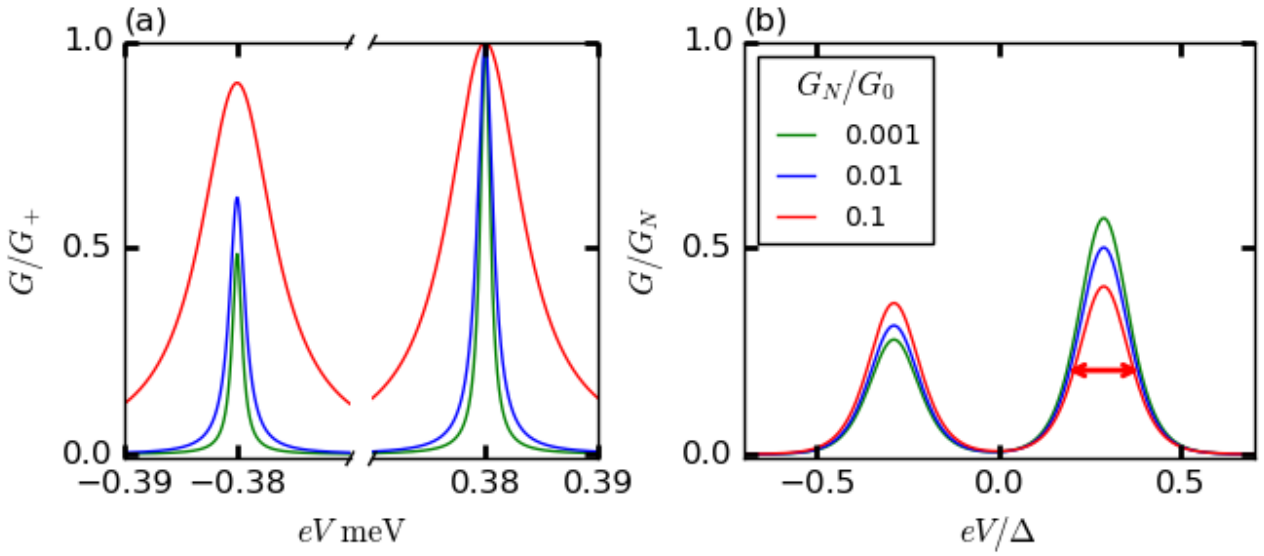

Figure 4.3: Differential conductance spectrum of a YSR state with parameters: $u^2 = 0.09\pi\nu_0$, $v^2 = 0.042\pi\nu_0$ and $\Lambda = 10^{-3}$meV. (a) G as a function of eV in the zero-temperature limit, $T = 0$. The green, blue and red solid lines correspond to $G_N/G_0 = 10^{-3},\ 10^{-2},$ and 10^{-1} respectively. The green solid line corresponds to the tunneling regime, $\Gamma u^2/\Lambda \ll 1$. Therefore for the green curve, the width of the peaks is given by Λ, and the peak height ratio G_+/G_- reflects the particle-hole ratio of the YSR wavefunction, $G_+/G_- \simeq u^2/v^2$. The red solid line corresponds to a strong tunnel coupling regime $\Gamma u^2 \gg \Lambda$. Hence, for the red curve, the relaxation rate is almost negligible, and the width of the peaks is approximately given by tip-induced line-width $\Gamma(u^2 + v^2)$. Moreover, Andreev processes give the dominant contribution to the differential conductance, which is thus almost voltage symmetric. The blue solid line corresponds to an in-between situation between the tunnel limit and the strong tunneling coupling regime. (b) Same as in (a) but for a finite temperature $k_BT = 0.06$ meV. In this case, $k_BT \gg \Gamma_t$ for the green, blue and red solid lines and the width of the conductance peaks is $\sim 3.5k_BT$, as indicated by the red arrow.

Let us start with the first term in (4.23). We immediately remark that the integrand in this has a numerator proportional to $\Gamma_e\Gamma_h$, indicating that this term is due to tunneling processes that require the coherent transfer of two carriers through the STM junction. Moreover, the denominator selects electrons whose energy is resonant with the YSR state. Thus, we interpret the first term in (4.23) as the current carried by resonant Andreev reflections via the YSR, I_A:

$$I_A = \frac{2e}{h}\int d\omega R_A(\omega)[f(\omega^-) - f(\omega^+)],\ \text{with},\ R_A(\omega) = \frac{\Gamma_e\Gamma_h}{(\omega - E_0)^2 + \Gamma_t^2/4}. \tag{4.33}$$

Here, $R_A(\omega)$ corresponds to the probability for charge carriers of energy ω to be resonantly Andreev reflected via the YSR level. Equation (4.33) has a clear physical interpretation. Indeed, there are two complementary Andreev processes transferring charge in opposite direction:

(i) First, an occupied electron at energy ω in the metallic tip can be reflected into an unoccupied hole state of the tip with probability $R_A(\omega)$, transferring a charge $2e$ across the junction. Taking into account the

occupation probabilities of electron and holes and summing over all possible energies these processes gives a contribution $\frac{2e}{h}\int \mathrm{d}\omega R_A(\omega) f(\omega^-)[1-f(\omega^+)]$ to the average Andreev current I_A.

(ii) An occupied hole with energy ω from the metallic tip has the same probability $R_A(\omega)$ to be Andreev reflected into an unoccupied electron state, transferring a charge $-2e$ across the junction. Again, taking into account the occupation probabilities of electron and holes and summing over all possible energies these processes gives a contribution $-\frac{2e}{h}\int \mathrm{d}\omega R_A(\omega) f(\omega^+)[1-f(\omega^-)]$ to the average Andreev current I_A.

Summing the contributions of the above mentioned processes one recovers equation (4.33).

The second and third terms are proportional to Λ and therefore involve relaxation of the YSR level. Hence, these terms correspond to the quasiparticle (or single-particle) current I_{QP} produced by IQPs:

$$I_{QP} = \frac{e}{h}\int \mathrm{d}\omega \frac{\Gamma_e \Lambda}{(\omega - E_0)^2 + \Gamma_t^2/4}[f(\omega^-) - f(\omega)] + \frac{\Gamma_h \Lambda}{(\omega - E_0)^2 + \Gamma_t^2/4}[f(\omega) - f(\omega^+)]. \tag{4.34}$$

The first term in I_{QP} correspond to the tunneling of spin-up electrons between the tip and the YSR state via its electron-like component u. The last term describes the single-particle tunneling of holes between the tip and the YSR state via its hole-like component v. Therefore, we can write I_{QP} as the sum of the single-electron and single-hole currents, I_e, and I_h:

$$I_{QP} = I_e + I_h, \tag{4.35}$$

$$I_e = \frac{e}{h}\int \mathrm{d}\omega T_e(\omega)[f(\omega^-) - f(\omega)], \text{ with } T_e(\omega) = \frac{\Gamma_e \Lambda}{(\omega - E_0)^2 + \Gamma_t^2/4} \tag{4.36}$$

$$I_h = -\frac{e}{h}\int \mathrm{d}\omega T_h(\omega)[f(\omega^+) - f(\omega)], \text{ with } T_h(\omega) = \frac{\Gamma_h \Lambda}{(\omega - E_0)^2 + \Gamma_t^2/4}. \tag{4.37}$$

Here $T_e(\omega)$ and $T_h(\omega)$ are the transmission probability of a single-electron and a single-hole via the YSR state respectively. Like equation (4.33), equations (4.36) and (4.37) have clear physical interpretations in terms of the single-particle processes that electrons and holes may undergo at STM junction. Let us focus on the single electron which results from two complementary processes:

(i) An occupied electron at energy ω coming from the metallic tip can be transmitted into an unoccupied quasiparticle state of the incoherent bath with a probability $T_e(\omega)$, transferring a charge e across the junction. Taking into account the occupation probability and summing other all energies, these processes produce an average current $\frac{e}{\hbar}\int \mathrm{d}\omega T_e(\omega) f(\omega - eV)[1-f(\omega)]$.

(ii) The complementary processes where incoming quasiparticles from the incoherent are transmitted into unoccupied electron states of the metallic tip to produce a current $-\frac{e}{\hbar}\int \mathrm{d}\omega T_e(\omega) f(\omega)[1-f(\omega - eV)]$.

Summing these two contributions, one directly recovers (4.36). A similar discussion holds for I_h, replacing electrons by holes.

To finish, (4.33) obviously indicates that the magnitude of I_A is an even function of V and that $I_A(V) = -I_A(-V)$. On the contrary, (4.34) indicates that the magnitude of the single-particle current $|I_{QP}|$ is not voltage-symmetric in the presence of a finite particle-hole asymmetry of the YSR wavefunction, i.e., $u^2 \neq v^2$. Hence, in the weak tunnel coupling regime, $\Gamma u^2, \Gamma v^2 \ll \Lambda$ the single-particle current gives the dominant

contribution to I, $|I|$ and G are thus not voltage symmetric (except if $u^2 = v^2$). Increasing the tunnel coupling, the contribution of Andreev current increases, and it follows that $|I|$ and G become more and more symmetric. In the opposite strong tunnel coupling regime, $\Gamma u^2, \Gamma v^2 \gg \Lambda$ the single-particle current is negligible in front of the Andreev current; as a consequence, $|I|$ and G are almost perfectly symmetric. Thus, the decrease in the asymmetry of the current and differential conductance spectrum when the tunneling rate Γ, or equivalently the normal-state conductance G_N, increases results from the competition between the Andreev and single-particle current.

4.3 Shot-noise and Fano factor spectroscopy

In this section, we shall demonstrate that the shot noise reveals direct signatures of the Andreev and single-particle processes. To that end, we find it convenient to first discuss two ideal limits. First, we focus our attention on the ideal case $\Lambda = 0$. In this case, the YSR state cannot relax, and single-particle processes are forbidden. The current and shot-noise, therefore, uniquely originate from Andreev reflections via the YSR state. Second, we analyze the opposite limit where Andreev reflections are absent. In that case, the current and shot-noise uniquely originate from single-particle processes. Finally, we studied the realistic case where Andreev reflections and single-particle are simultaneously present (*i.e.*, $\Lambda > 0$).

In each case, we first discuss the ideal zero-temperature limit where current and shot-noise can be calculated analytically, facilitating their analysis. Next, we analyze how this analysis is modified by thermal effects in the realistic finite temperature case. The experimental data studied at the end of this chapter were measured at an electronic temperature $T \simeq 700$ mK. At this temperature, the analysis of the differential conductance data clearly indicates that the width of the YSR conductance peaks is dominated by thermal broadening. Hence, $k_B T \gg \Gamma_e, \Gamma_h, \Lambda$ for all tunneling strengths studied in the experiment. In addition, the YSR energies reported in this experiment are $\sim 200 - 400$ μeV, hence, $E_0 \gg k_B T \sim 60$ μeV. Thus, hereinafter we will focus on the experimentally relevant regime and assume that $E_0 \gg \Gamma_t$ and focus on temperature such that $E_0 \gg k_B T \gg \Gamma_t$.

4.3.1 Results in the absence of single-particle processes, $\Lambda = 0$

To begin, let us focus on the ideal limit $\Lambda = 0$. In this case, the YSR state is isolated and cannot relax. Therefore, single-particle processes are forbidden, and the current is solely carried by resonant Andreev reflections via the YSR state. Consequently, the expression of S is significantly simplified and reads:

$$S = \frac{2e^2}{h} \int \mathrm{d}\omega 4R(\omega)\left[1 - R(\omega)\right]\left[f(\omega^-)f(-\omega^+) + f(\omega^+)f(-\omega^-)\right] \\ +4R^2(\omega)\left[f(\omega^-)f(-\omega^-) + f(\omega^+)f(\omega^-)\right]. \tag{4.38}$$

From this expression, one immediately remarks that, independently of the temperature, the shot-noise S is an even function of the voltage bias V, as observed in Fig. 4.4. This feature was expected since the underlying Andreev reflections do not depend on the direction of the voltage bias.

In the $T = 0$ limit, the last line of (4.38) vanishes, and S reads:

$$S = \frac{2e^2}{h}\mathrm{sign}(V) \int_{-eV}^{eV} \mathrm{d}\omega 4R(\omega)\left[1 - R(\omega)\right]. \tag{4.39}$$

The above expression has a clear-cut physical interpretation. Indeed, in the $T = 0$ limit, focusing on the case of a positive bias $V > 0$[4], an occupied electron with energy $|\omega| < eV$ in the metallic tip can either be Andreev reflected in an unoccupied hole state of the tip with a probability $R_A(\omega)$ or normal reflected as an electron with a probability $1 - R_A(\omega)$. The first process transfers a charge $2e$ across the junction, while the second does not produce any charge transfer. Because of the Pauli exclusion principle, other occupied carriers in the metallic tip are normally reflected with a probability equal to 1 and do not participate in the charge transfer. Hence the charge transferred by carriers of energy ω, $g(\omega)$, is distributed according to a binomial distribution when $|\omega| < eV$,

$$g(\omega) = \begin{cases} 2e, \text{ with probability } R_A(\omega) \text{ if } |\omega| < eV, \\ 0, \text{ with probability } 1 - R_A(\omega) \text{ if } |\omega| < eV, \end{cases} \tag{4.40}$$

and certainly vanishes elsewhere. Thus, it is straightforward to obtain the mean-square deviation of $g(\omega)$, $\langle \delta g^2(\omega) \rangle = 4e^2 R_A(\omega)[1 - R_A(\omega)]$. The shot-noise produced by carriers of energy ω reads $\frac{\mathrm{d}S}{\mathrm{d}\omega} = 2\langle \delta g^2(\omega) \rangle / h$. Summing over all carriers' energy, one directly recovers (4.39). According to this hand-waving argument, the shot noise can be interpreted as the partition noise of Andreev reflections. We can perform the integral of (4.39) analytically and, after straightforward algebra, finally obtain:

$$S = \frac{2e^2}{h} \frac{4\Gamma_e \Gamma_h}{\Gamma_t^3} \mathrm{sgn}(V) \Big\{ \left[2\Gamma_t^2 - 4\Gamma_e \Gamma_h \right] \cdot \left[A(eV - E_0) + A(eV + E_0) \right] \\ - 4\Gamma_e \Gamma_h \cdot \left[B(eV + E_0) + B(eV - E_0) \right] \Big\}, \tag{4.41}$$

$$\text{with, } A(\omega) = \arctan(2\omega/\Gamma_t), \text{ and, } B(\omega) = \frac{2\omega\Gamma_t}{4\omega^2 + \Gamma_t^2}. \tag{4.42}$$

Hence, like the current magnitude $|I|$, the shot-noise linearly vanishes with $|V|$ far below the resonances, when $|eV| \ll E_0$, exhibits abrupt non-linear steps near the resonances, when $|eV \pm E_0| \lesssim \Gamma_t$ and finally saturates at finite values S_+, S_- when $eV \gg E_0$ and $-eV \gg E_0$, respectively. It is important to notice that the non-linear step-like shape of $S(V)$ is a consequence of the resonant nature of the charge transfer via the YSR level and does not depend on the precise type of resonant tunneling considered (*i.e.* Andreev processes, single-particle processes or both). In the absence of single-particle processes, the shot-noise is an even function of V and $S_+ = S_-$. It is straightforward to show that:

$$S_+ = S_- = \frac{e^2}{\hbar} \frac{4\Gamma u^2 v^2}{u^2 + v^2} \left[1 + \frac{(u^2 - v^2)^2}{(u^2 + v^2)^2} \right]. \tag{4.43}$$

Thanks to equations (4.41) and (4.24), we can readily obtain the Fano factor, which reads:

$$F = \frac{S}{2e|I|} = 1 + \frac{(u^2 - v^2)^2}{(u^2 + v^2)^2} - \left[1 - \frac{(u^2 - v^2)^2}{(u^2 + v^2)^2} \right] \frac{B(eV - E_0) + B(eV + E_0)}{A(eV - E_0) + A(eV - E_0)}. \tag{4.44}$$

After a straightforward Taylor expansion, we show that:

$$F_0 = \lim_{|eV|/E_0 \ll 1} F(V) = 2 - \left[1 - \frac{(u^2 - v^2)^2}{(u^2 + v^2)^2} \right] \frac{2\Gamma_t^2}{4E_0^2 + \Gamma_t^2} + \mathcal{O}\left(\left[\frac{eV}{E_0} \right]^2 \right). \tag{4.45}$$

[4] In the case of a negative bias, the following arguments remain valid if one replaces electrons by holes.

Therefore, using the hypothesis $E_0 \gg \Gamma_t$, the Fano factor saturates to 2 in the linear regime, $|eV| \ll E_0$:

$$F_0 \underset{E_0 \gg |eV|}{\simeq} 2 + \mathcal{O}\left(\left[\frac{eV}{E_0}\right]^2\right) + \mathcal{O}\left(\left[\frac{\Gamma_t}{E_0}\right]^2\right). \tag{4.46}$$

These results could have been anticipated from (4.39). Indeed, since Andreev reflections are resonant processes via the YSR state, their probability $R_A(\omega)$ is a narrow peaked function centered around E_0. Most importantly, $R_A \underset{|\omega - E_0| \gg \Gamma_t}{\simeq} \Gamma^2 u^2 v^2 / E_0^2 \ll 1$, if $|eV| \ll E_0$. Therefore, when $|eV| \ll E_0$, and $E_0 \gg \Gamma_t$ the terms proportional to $R_A^2(\omega)$ is negligible in front of $R_A(\omega)$ in (4.39) and we obtain a Poissonian shot-noise, $S = 2q|I|$, with $q = 2e$ the effective charge carried by Andreev reflections. As a consequence, the Fano factor $F = q/e$ gives the effective charge carried by an Andreev reflection, q, and $F = 2$, in this regime. Unfortunately, due to the extremely weak current signal below the resonances, The Fano factor can not be accurately measured, when $|eV| < E_0$. Hnece the above-mentioned Poissonian regime can not be accessed by the experiment studied at the end of this chapter. Thus, in order to make a direct comparison with experimental data we shift our attention to the regime: $|eV| > E_0$.

When $|eV| \gg E_0$ the integral in (4.39) contains contribution from energies $\omega \simeq E_0$. For such energies, Andreev reflections via the YSR state are resonantly enhanced. Most importantly, the probability $R_A(\omega)$ reaches it maximum when $\omega = E_0$, $R_A(E_0) = 1 - \frac{(u^2-v^2)^2}{(u^2+v^2)^2}$, which does not depend on the tunneling strength Γ and can reach unity. Hence, the term proportional to $R_A^2(\omega)$ in (4.39) is no longer negligible and reduces the shot-noise below the Poissonian limit, $S < 2.2e|I|$. As a consequence F decreases below 2 and reads:

$$F_+ = F_- = \lim_{|eV| \gg E_0} F(V) = 1 + \frac{(u^2 - v^2)^2}{(u^2 + v^2)^2} \tag{4.47}$$

Therefore, when $|eV| \gg E_0$, F decreases below its Poissonian limit, $1 \leq F \leq 2$, and only depends on u^2/v^2, regardless of the tunneling rate Γ, as observed in Fig.4.4.

Near the resonances,*i.e.*, when $|eV \pm E_0| \lesssim E_0$, F exhibits sharp nonlinearities which are non-monotonous. As we will show below, these non-monotonous variations are washed out by thermal effects in the experimentally relevant temperature regime. Hence, we do not discuss it further.

The experimental data studied at the end of this chapter were measured at an electronic temperature $T \simeq 700$ mK. Hence $E_0 \gg k_B T$, while $k_B T$ largely dominates the energy width of the YSR state Γ_t for all tunneling strengths studied in the experiment. Therefore, it is necessary to understand how the above results, obtained in the zero-temperature limit, are affected by thermal effects in the low-temperature regime: $E_0 \gg k_B T \gg \Gamma_t$. Since, temperature significantly modifies the Fermi-Dirac distribution $f(\omega)$ only in the energy range $|\omega| \lesssim 2k_B T$, finite-temperature effects are expected to significantly modify S and F only at small biases $|eV| \lesssim 2k_B T$ and near the resonances, $|eV \pm E_0| \lesssim 2k_B T$. To confirm this conjecture, we numerically computed I, S, and F using expressions (4.33) and (4.38), and compare the results to the zero-temperature limit in Fig.4.4.

As expected, Fig.4.4 shows that thermal effects significantly modifies S and F at small biases $|eV| \leq 2k_B T$ and near the resonances, $|eV \pm E_0| < 2k_B T$. Indeed, because of thermal effects, S no longer vanishes in the zero-bias limit. It directly follows that the Fano factor is diverging when $eV \to 0$ as indicated by its rapid increases above 2 when $|eV| \leq 2k_B T$ in Fig.4.4. In the vicinity of the resonances, *i.e.*, when $eV = \pm E_0$, the sharp steps in S become smooth, and their width is of the order of $k_B T$ instead of Γ_t. Moreover, the non-

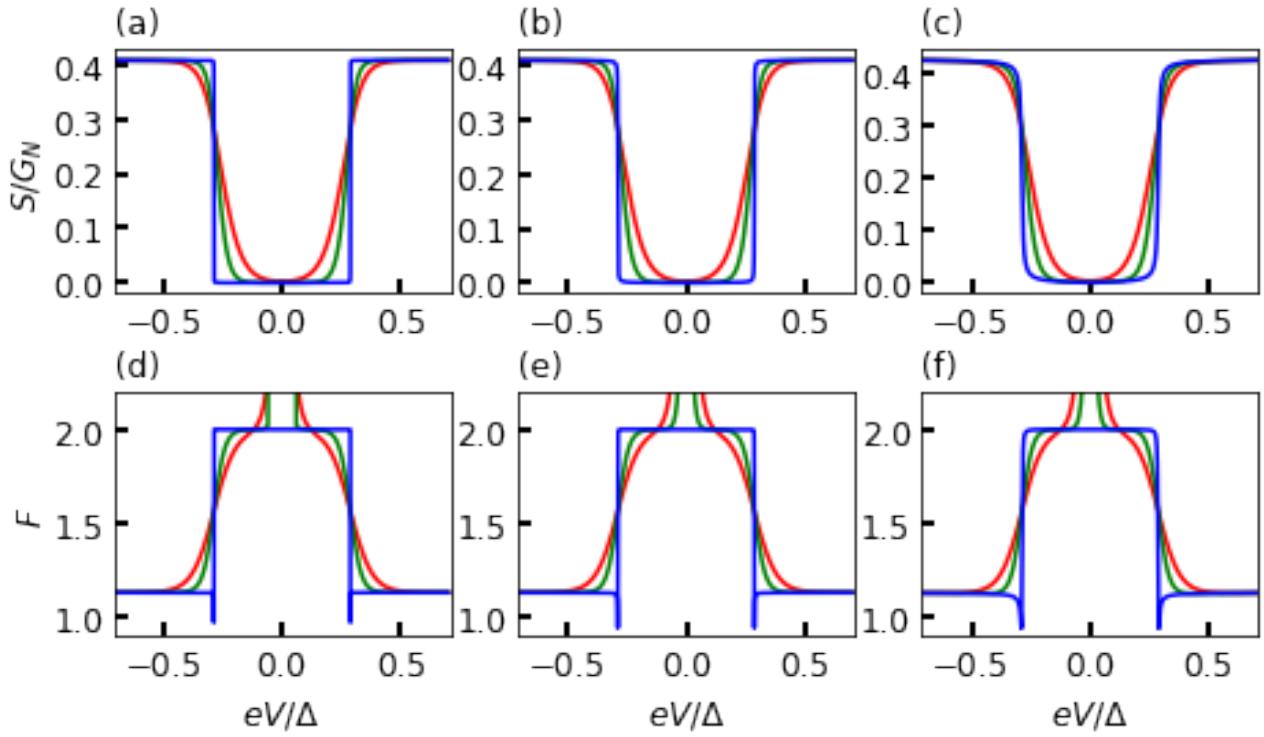

Figure 4.4: Noise and Fano spectroscopy of a YSR state, in the absence of single-particle processes, $\Lambda = 0$. The YSR energy is $E_0 = 0.34$ meV and the superconducting gap is $\Delta = 1.35$ meV. (a): Shot-noise S as a function of eV/Δ for $G_N = 10^{-3}G_0$ $u^2 = 0.09\pi\nu_0$, $v^2 = 0.042\pi\nu_0$ and various temperature $T = 0$ (blue solid line), $k_BT = 0.03$ meV (green solid line), and $k_BT = 0.06$ meV (red solid line). (b) and (c): Same as in (a) for higher normal-state conductances $G_N = 10^{-2}G_0$ and $G_N = 2.10^{-1}G_0$, respectively. (d), (e), and (f): Fano factor F as a function of eV/Δ. The parameters are the same as in (a), (b), and (c), respectively.

monotonous variations of F are replaced by smooth monotonous decreases, and F is a linear function of V when $|eV \pm E_0| < k_BT$.

Elsewhere, the thermal effects are negligible. Indeed, when $|eV| > E_0 + 2k_BT$, Fig. 4.4 shows that F saturates and that the asymptotic limits, F_+ and F_- are not affected by finite temperature, as long as $E_0 \gg k_BT$. Similarly, when $E_0 - 2k_bT > |eV| > 2k_BT$ thermal effects are negligible, and one recover the Poissonian behavior $F = 2$. Nevertheless, for strong temperatures, this behavior can not be observed (see the red solid line in Figs. 4.4 (c), (d), and (e)). Notice that for $|eV| > E_0$ the current signal is extremely weak, and F can not be measured experimentally. Hence we will mainly focus on the asymptotic regime $|eV| \gg E_0$ hereinafter.

To be complete, let us finally show that the finite-temperature expression (4.38) can also be interpreted with simple hand-waving arguments. To that end, we should investigate how the charge transferred by carriers of energy ω, $g(\omega)$, is distributed. Only two possible processes produce a net charge transfer across the junction. First, an electron of the metallic tip is Andreev reflected into an unoccupied hole state of the tip with probability $R_A(\omega)f(\omega^-)[1 - f(\omega^+)]$. This process produces a charge transfer $g(\omega) = 2e$. Second, the reverse process, where a hole is reflected as an electron with probability $R_A(\omega)f(\omega + eV)[1 - f(\omega - eV)]$, produces a charge transfer $g(\omega) = -2e$. All other processes do not produce any charge transfer. Therefore $g(\omega)$ is distributed as

follows:

$$g(\omega) = \begin{cases} 2e, \text{ with probability, } R_A(\omega) f(\omega^-)[1 - f(\omega^+)] \\ -2e, \text{ with probability, } R_A(\omega) f(\omega^+)[1 - f(\omega^-)], \\ -0, \text{ with probability, } 1 - R_A(\omega)\{f(\omega^+)[1 - f(\omega^-)] + f(\omega^-)[1 - f(\omega^+)]\}. \end{cases} \tag{4.48}$$

Using $S = \frac{2}{h} \int \mathrm{d}\omega \langle [g(\omega) - \langle g(\omega) \rangle]^2 \rangle$, one directly recovers (4.38).

4.3.2 Results in the absence of Andreev reflections

Let us now analyze the opposite limit and study the shot-noise and, most importantly, the Fano factor spectroscopy produced by only single-particle processes in the absence of Andreev reflections. To eliminate the Andreev reflections, we suppress the off-diagonal terms in $g_S^r(\omega)$, which mix the electron and hole sectors. The YSR state is therefore replaced by two degenerate electron and hole states of energy E_0, and $g_S^r(\omega)$ reads:

$$g_S^r(\omega) = \frac{1}{\omega - E_0 + i\Lambda} \begin{bmatrix} u^2 & 0 \\ 0 & v^2 \end{bmatrix} . \tag{4.49}$$

Notice that we assumed that the electron and hole states have the same relaxation rate for simplicity. In principle, these two states can have different relaxation rates, but this does not modify the results discussed below. After straightforward algebra, we obtain expressions for the current and shot-noise that read:

$$I = \frac{e}{h} \int \mathrm{d}\omega \tilde{T}_e(\omega) \left[f(\omega - eV) - f(\omega) \right] + \tilde{T}_h(\omega) \left[f(\omega) - f(\omega + eV) \right], \tag{4.50}$$

$$\begin{aligned} S = \frac{2e^2}{h} \int \mathrm{d}\omega & \tilde{T}_e(\omega) \left[1 - \tilde{T}_e(\omega \right] \left[f(\omega^-) f(-\omega) + f(\omega) f(-\omega^-) \right] \\ & + \tilde{T}_h(\omega) \left[1 - \tilde{T}_h(\omega \right] \left[f(\omega^+) f(-\omega) + f(\omega) f(-\omega^+) \right] \\ & + \tilde{T}_e^2(\omega) \left[f(\omega^-) f(-\omega^-) + f(\omega) f(-\omega) \right] \\ & + \tilde{T}_h^2(\omega) \left[f(\omega^+) f(-\omega^+) + f(\omega) f(-\omega) \right] \end{aligned} \tag{4.51}$$

$$\text{with, } \tilde{T}_{e/h}(\omega) = \frac{\Gamma_{e/h} \Lambda}{(\omega - E_0)^2 + (\Gamma_{e/h} + \Lambda)^2/4} \tag{4.52}$$

The above expressions have a clear physical interpretation. To show it let us study the probability distribution of the charge transferred across the junction by carriers of energy ω, $g(\omega)$. In the absence of Andreev processes, holes and electrons are independent charge carriers. Hence, $g(\omega)$ is the sum of two independent random variables $g_e(\omega)$ and $g_h(\omega)$ representing the charge transferred by electrons of energy ω and holes of energy ω, respectively. Let us focus on $g_e(\omega)$. There are only two different single-electron processes transferring charge across the STM junction. First, an occupied electron of energy ω can tunnel into the electronic level that subsequently relaxes, transferring a charge e across the junction. This process has a probability $\tilde{T}_e(\omega) f(\omega^-) f(-\omega)$. Second, the complementary process, where an electron from the incoherent bath is transmitted into an unoccupied electron state with energy ω in the metallic tip, transfers a charge $-e$. This process, has a probability $\tilde{T}_e(\omega) f(-\omega^-) f(\omega)$. Hence, $g_e(\omega)$ is distributed according to:

$$g_e(\omega) = \begin{cases} e, \text{ with probability, } \tilde{T}_e(\omega) f(\omega^-) f(-\omega) \, , \\ -e, \text{ with probability, } \tilde{T}_e(\omega) f(-\omega^-) f(\omega) \, , \\ 0, \text{ with probability, } 1 - \tilde{T}_e(\omega) \left[f(-\omega^-) f(\omega) + f(\omega^-) f(-\omega) \right] \, . \end{cases} \tag{4.53}$$

Along the same line, one readily found that $g_h(\omega)$ is distributed according to :

$$g_h(\omega) = \begin{cases} -e, \text{ with probability, } \tilde{T}_h(\omega) f(\omega^+) f(-\omega) \ , \\ e, \text{ with probability, } \tilde{T}_h(\omega) f(-\omega^+) f(\omega) \ , \\ 0, \text{ with probability, } 1 - \tilde{T}_h(\omega) \left[f(-\omega^+) f(\omega) + f(\omega^+) f(-\omega) \right] \ . \end{cases} \tag{4.54}$$

Using $I = \frac{1}{h} \int \mathrm{d}\omega \langle g(\omega) \rangle$ and $S = \frac{1}{h} \int \mathrm{d}\omega \langle [g(\omega) - \langle g(\omega) \rangle]^2 \rangle$ one recovers equations (4.50) and (4.51).

We first focus our attention on the ideal zero-temperature limit. In this limit, all integrals entering equations (4.50) and (4.51) are exact, and we can obtain exact analytical expressions for I and S that read:

$$\begin{aligned} I = \frac{2e}{h} \Bigg\{ & \frac{\Gamma_e \Lambda}{\Gamma_e + \Lambda} \left[\arctan\left(2 \frac{eV - E_0}{\Gamma_e + \Lambda} \right) + \arctan\left(2 \frac{E_0}{\Gamma_e + \Lambda} \right) \right] \\ & + \frac{\Gamma_h \Lambda}{\Gamma_h + \Lambda} \left[\arctan\left(2 \frac{eV + E_0}{\Gamma_h + \Lambda} \right) - \arctan\left(2 \frac{E_0}{\Gamma_h + \Lambda} \right) \right] \Bigg\} \end{aligned} \tag{4.55}$$

$$\begin{aligned} S = \frac{2e^2}{h} \mathrm{sign(V)} \Bigg\{ & \frac{\Gamma_e \Lambda}{(\Gamma_e + \Lambda)} \left[1 + \frac{(\Gamma_e - \Lambda)^2}{(\Gamma_e + \Lambda)^2} \right] \left[\arctan\left(2 \frac{eV - E_0}{\Gamma_e + \Lambda} \right) + \arctan\left(2 \frac{E_0}{\Gamma_e + \Lambda} \right) \right] \\ & - \frac{\Gamma_e \Lambda}{(\Gamma_e + \Lambda)} \left[1 - \frac{(\Gamma_e - \Lambda)^2}{(\Gamma_e + \Lambda)^2} \right] \left[\frac{2(\Gamma_e + \Lambda)(eV - E_0)}{4(eV - E_0)^2 + (\Gamma_e + \Lambda)^2} + \frac{2(\Gamma_e + \Lambda) E_0}{4(E_0)^2 + (\Gamma_e + \Lambda)^2} \right] \\ & + \frac{\Gamma_h \Lambda}{(\Gamma_h + \Lambda)} \left[1 + \frac{(\Gamma_h - \Lambda)^2}{(\Gamma_h + \Lambda)^2} \right] \left[\arctan\left(2 \frac{eV + E_0}{\Gamma_h + \Lambda} \right) - \arctan\left(2 \frac{E_0}{\Gamma_h + \Lambda} \right) \right] \\ & - \frac{\Gamma_h \Lambda}{(\Gamma_h + \Lambda)} \left[1 - \frac{(\Gamma_h - \Lambda)^2}{(\Gamma_h + \Lambda)^2} \right] \left[\frac{2(\Gamma_h + \Lambda)(eV + E_0)}{4(eV + E_0)^2 + (\Gamma_h + \Lambda)^2} + \frac{2(\Gamma_h + \Lambda) E_0}{4(E_0)^2 + (\Gamma_h + \Lambda)^2} \right] \Bigg\}. \end{aligned} \tag{4.56}$$

Similarly to the current and shot-noise produced by Andreev reflections, here I and S are negligible for $|eV| \ll E_0$, rapidly increase around the resonances when $eV \simeq \pm E_0$ and saturate to finite values I_+, S_+, when $eV \gg E_0$, and I_-, S_- when $eV \ll -E_0$ respectively. Since we assume $E_0 \gg \Gamma_e, \Gamma_h, \Lambda$ throughout this chapter, the asymptotic limits of the current and shot-noise are easily obtained and read:

$$I_+ = \frac{e}{\hbar} \frac{\Gamma_e \Lambda}{\Gamma_e + \Lambda}, \ I_- = -\frac{e}{\hbar} \frac{\Gamma_h \Lambda}{\Gamma_h + \Lambda}, \tag{4.57}$$

$$S_+ = 2eI_+ \left[1 - \frac{2\Gamma_e \Lambda}{(\Gamma_e + \Lambda)^2} \right], \ S_- = 2e|I_-| \left[1 - \frac{2\Gamma_h \Lambda}{(\Gamma_h + \Lambda)^2} \right]. \tag{4.58}$$

Therefore, contrarily to the results obtained in the sole presence of Andreev reflections, here $I_\pm$ and $S_\pm$ are not necessarily identical.

Thanks to the analytical expressions (4.57) and (4.58), it is straightforward to obtain the Fano factor analytically. Nevertheless, the resulting expression is lengthy and not insightful. Therefore, to gain insight into its qualitative features, we evaluate F for different YSR parameters and normal-state conductance. The results are presented in Fig. 4.5. Fig. 4.5 shows that $F \simeq 1$ when $|eV| \ll E_0$, exhibits sharp non-monotonous variations around the resonances $eV \simeq \pm E_0$ and finally saturates to finite values $F_+ < 1$ and $F_- < 1$, when $eV \gg E_0$ and $eV \ll -E_0$, respectively.

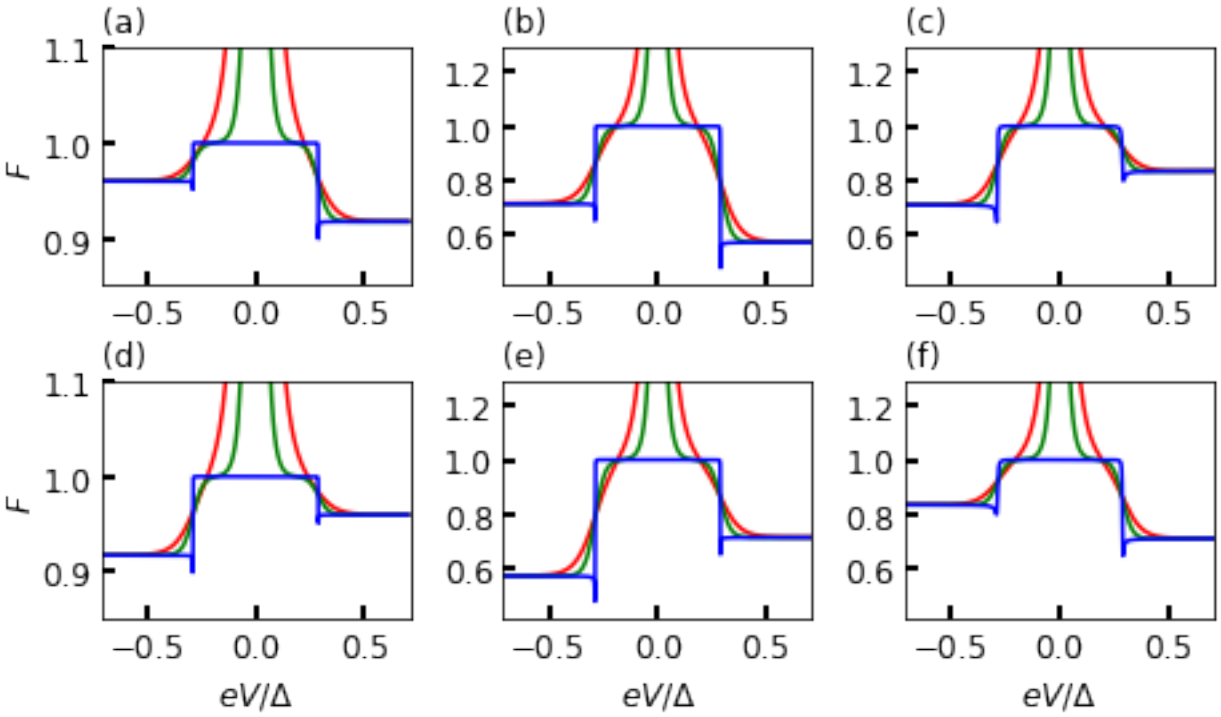

Figure 4.5: Fano factor spectroscopy of a YSR state in the absence of Andreev processes. The YSR energy is $E_0 = 0.34$ meV and the superconducting gap is $\Delta = 1.35$ meV. (a): Fano factor F as a function of eV/Δ for $G_N = 10^{-3}G_0$ $u^2 = 0.09\pi\nu_0$, $v^2 = 0.042\pi\nu_0$ and various temperature $T = 0$ (blue solid line), $k_BT = 0.03$ meV (green solid line), and $k_BT = 0.06$ meV (red solid line). (b) and (c): Same as in (a) for higher normal state conductances $G_N = 10^{-2}G_0$ and $G_N = 2.10^{-1}G_0$, respectively. (d), (e), and (f): Same as (a),(b), and (c) for perfectly mirrored particle-hole asymmetry of the YSR state: $u^2 = 0.042\pi\nu_0$, and $v^2 = 0.09\pi\nu_0$.

When $|eV| \ll E_0$, the charge carriers transferred across the STM junction have energies $\omega \ll E_0$. In this energy range, $\tilde{T}_e(\omega) \sim \dfrac{\Gamma_e\Lambda}{E_0^2} \ll 1$ and $\tilde{T}_h(\omega) \sim \dfrac{\Gamma_h\Lambda}{E_0^2} \ll 1$. Hence, the terms proportional to $\tilde{T}_e^2(\omega)$ and $\tilde{T}_h^2(\omega)$ in (4.51) can be neglected and the shot-noise is Poissonian, $S \sim 2q|I|$, with $q = e$ the effective charge transferred by single-particle processes. It directly follows that $F \simeq 1$.

As already mentioned, the Fano factor can not be measured accurately when $|eV| < E_0$, because of the extremely weak current signal. Hence, we shift our attention on the regime $eV \gg E_0$. Using equations (4.57) and (4.58), and after straightforward algebra, we obtain compact expressions of F_+, and F_- that read:

$$F_+ = 1 - \frac{2\Gamma_e\Lambda}{(\Gamma_e + \Lambda)^2}, \; F_- = 1 - \frac{2\Gamma_h\Lambda}{(\Gamma_h + \Lambda)^2}. \tag{4.59}$$

Therefore, in sharp contrast with the Fano-factor produced by Andreev reflections, in the sole presence of single-particle processes, $F_\pm < 1$, and $F_+ \neq F_-$ if $u^2 \neq v^2$. Moreover, $F_\pm$ depends on the tunneling rate Γ.

It is also interesting to remark that the order of the asymptotic limits, F_+ and F_- depends on the tunneling rate Γ. Indeed, for weak tunneling rates $\Gamma_e, \Gamma_h \ll \Lambda$, $F_\pm \simeq 1 - \frac{2\Gamma_{e/h}}{\Lambda}$. Hence, in this regime, $F_+ < F_-$, if

$u^2 > v^2$ and vice versa. On the contrary, for strong tunneling rates, $\Gamma_e, \Gamma_h \gg \Lambda$, $F_\pm \simeq 1 - \frac{2\Lambda}{\Gamma_{e/h}}$. Therefore, in this regime, $F_+ > F_-$, if $u^2 > v^2$ and vice versa. The order inversion between F_+ and F_- occurs at the special point $\Gamma = \Lambda/\sqrt{u^2v^2}$, where $F_+ = F_-$.

In the more realistic finite-temperature case, as mentioned previously, thermal effects significantly modify the Fano factor spectroscopy only at small biases and near the resonances, as observed in Fig. 4.5. Therefore, the asymptotic limits $F_\pm$ are unaffected by thermal effects, and equations (4.59) remain valid at finite temperature, as long as $k_B T \ll E_0$.

To conclude this subsection, in the absence of Andreev reflections, the asymptotic limits of the Fano factor are always below 1 regardless of the temperature and the tunneling rate Γ. This result sharply contrasts with $2 \geq F_\pm \geq 1$ observed in the absence of single particle processes (see (4.47)).

4.3.3 Interplay between single-particle processes and Andreev reflections

In a realistic sample, one can not perfectly isolate the YSR state from its environment, and relaxation is inevitable. Hence both Andreev reflections and single-particle processes play a role in the transport via YSR states. In this case, the Fano spectroscopy exhibits signatures of these two different processes, as shown below. In the generic case, the shot-noise is given by:

$$\begin{aligned} S = \frac{2e^2}{h}\int d\omega & \frac{4\Gamma_e\Gamma_h\{(\omega-E_0)^2+(\Gamma_e-\Gamma_h)^2/4\}}{\{(\omega-E_0)^2+\Gamma_t^2/4\}^2}[f(\omega^-)f(-\omega^+)+f(\omega^+)f(-\omega^-)] \\ &+\frac{\Gamma_e\Lambda\{(\omega-E_0)^2+(3\Gamma_h-\Gamma_e+\Lambda)^2/4\}}{\{(\omega-E_0)^2+\Gamma_t^2/4\}^2}[f(\omega^-)f(-\omega)+f(-\omega^-)f(\omega)] \\ &+\frac{\Gamma_h\Lambda\{(\omega-E_0)^2+(3\Gamma_e-\Gamma_h+\Lambda)^2/4\}}{\{(\omega-E_0)^2+\Gamma_t^2/4\}^2}[f(\omega)f(-\omega^+)+f(-\omega)f(\omega^+)] \\ &+\frac{\Gamma_e^2(\Lambda+2\Gamma_h)^2 f(\omega^-)f(-\omega^-)+\Gamma_h^2(\Lambda+2\Gamma_e)^2 f(\omega^+)f(-\omega^+)}{((\omega-E_0)^2+\Gamma_t^2/4)^2} \\ &+\frac{\Lambda^2(\Gamma_e-\Gamma_h)^2 f(\omega)f(-\omega)}{((\omega-E_0)^2+\Gamma_t^2/4)^2}. \end{aligned} \tag{4.60}$$

Let us first focus on the zero-temperature limit. In this limit, the two last lines of equation (4.60) vanishes, and S adopts an elegant form:

$$\begin{aligned} S = \frac{2e^2}{h}\text{sign}(V)\Bigg\{ & \int_0^{eV} \mathrm{d}\omega 4R(\omega)[1-R(\omega)] - 4R(\omega)T_e(\omega) + T_e(\omega)[1-T_e(\omega)] \\ & + \int_{-eV}^{0} \mathrm{d}\omega 4R(\omega)[1-R(\omega)] - 4R(\omega)T_h(\omega) + T_h(\omega)[1-T_h(\omega)]\Bigg\} \end{aligned} \tag{4.61}$$

To interpret the above equation, let us investigate the distribution probability of the transferred charge across the junction by carriers of energy ω, $g(\omega)$. Focusing on the case of positive bias, there are only three different processes transferring charge across the junction. First, an electron with energy $|\omega| < eV$ from the tip can be Andreev reflected into an unoccupied hole state of the tip producing a charge transfer $2e$. This process has a probability $R_A(\omega)$. Second, an electron from the tip with energy $0 < \omega < eV$ can be transmitted to the

substrate via an incoherent single-particle process, transferring a charge e across the junction. This process occurs with a probability $T_e(\omega)$. Third, occupied quasiparticles of the incoherent bath can be transmitted into unoccupied holes states of the tip with energy $0 > \omega > -eV$, via an incoherent single-particle process, transferring a charge $-e$ across the junction. Such process has a probability $T_h(\omega)$. Therefore, in the energy range $0 < \omega < eV$, $g(\omega)$ is distributed according to:

$$g(\omega) = \begin{cases} 2e, \text{ with probability } R_A(\omega), \\ e, \text{ with probability } T_e(\omega), \\ 0, \text{ with probability } 1 - \{R_A(\omega) - T_e(\omega)\}. \end{cases} \tag{4.62}$$

In the energy range $-eV < \omega < 0$, $g(\omega)$ is distributed according to:

$$g(\omega) = \begin{cases} 2e, \text{ with probability } R_A(\omega), \\ -e, \text{ with probability } T_h(\omega), \\ 0, \text{ with probability } 1 - \{R_A(\omega) - T_h(\omega)\}, \end{cases} \tag{4.63}$$

and vanishes in the energy range $|\omega| > eV$. Using $S = \frac{2}{h}\int \mathrm{d}\omega \langle g^2 - \langle g \rangle^2 \rangle$, one finally recover equation (4.61).

It is also interesting to remark that the terms $R_A(\omega)[1 - R_A(\omega)]$, $T_e(\omega)[1 - T_e(\omega)]$ and $T_h(\omega)[1 - T_h(\omega)]$, in the integrand of (4.61) could be interpreted as the auto-correlation of the Andreev, single-electron and single-hole currents respectively. On the other hand, the terms $-4R_A(\omega)T_e(\omega)$ and $-4R_A(\omega)T_h(\omega)$ might be viewed as the cross-correlations between the Andreev and single-electron current and the Andreev and single-hole currents respectively. Notice that these terms give a negative contribution to S, indicating that Andreev and single-particle currents are anti-correlated, due to the Pauli exclusion principle. To show it let us assume $V > 0$. Then, Andreev reflections and single-electron processes have the same initial state: an occupied electron in the tip at energy $eV > \omega > 0$. Hence, when Andreev current increases, single-electron current reduces and vice-versa. The anti-correlation between the Andreev and single-hole currents can be understood with similar arguments, replacing electrons by holes and assuming $V < 0$.

The integrals entering (4.61) can be performed analytically, and we finally obtain an analytical expression for S that reads:

$$\begin{aligned} S = \frac{2e^2}{h}\mathrm{sign(V)}\Bigg\{ & \frac{4\Gamma_e\Gamma_h}{\Gamma_t^3}\left[(\Gamma_h - \Gamma_e)^2\left(C(eV - E_0) + C(eV + E_0)\right) + \Gamma_t^2\left(D(eV + E_0) + D(eV - E_0)\right)\right] \\ & + \frac{\Gamma_e\Lambda}{\Gamma_t^3}\left[(3\Gamma_h - \Gamma_e + \Lambda)^2\left(C(eV - E_0) + C(E_0)\right) + \Gamma_t^2\left(D(eV - E_0) + D(E_0)\right)\right] \\ & + \frac{\Gamma_h\Lambda}{\Gamma_t^3}\left[(3\Gamma_e - \Gamma_h + \Lambda)^2\left(C(eV + E_0) - C(E_0)\right) + \Gamma_t^2\left(D(eV + E_0) - D(E_0)\right)\right]\Bigg\}, \end{aligned} \tag{4.64}$$

$$\text{with, } C(\omega) = A(\omega) + B(\omega), \text{ and } D(\omega) = A(\omega) - B(\omega). \tag{4.65}$$

As observed in Fig. 4.6, the shot-noise is negligible when $E_0 - |eV| \gg \Gamma_t$, and vanishes at zero-bias. When $|eV| \sim E_0$, S rapidly increases and saturates to finite values S_+ and S_- when $(eV - E_0) \gg \Gamma_t$ and $(eV + E_0) \ll -\Gamma_t$, respectively. Hence, we mainly focus our attention on biases $|eV| > E_0$.

Contrarily to the shot-noise produced only by Andreev reflections (see Subsection. 4.3.1), the shot-noise is not an even function of the bias and $S_+ \neq S_-$, unless $u^2 = v^2$. This feature is due to the presence of

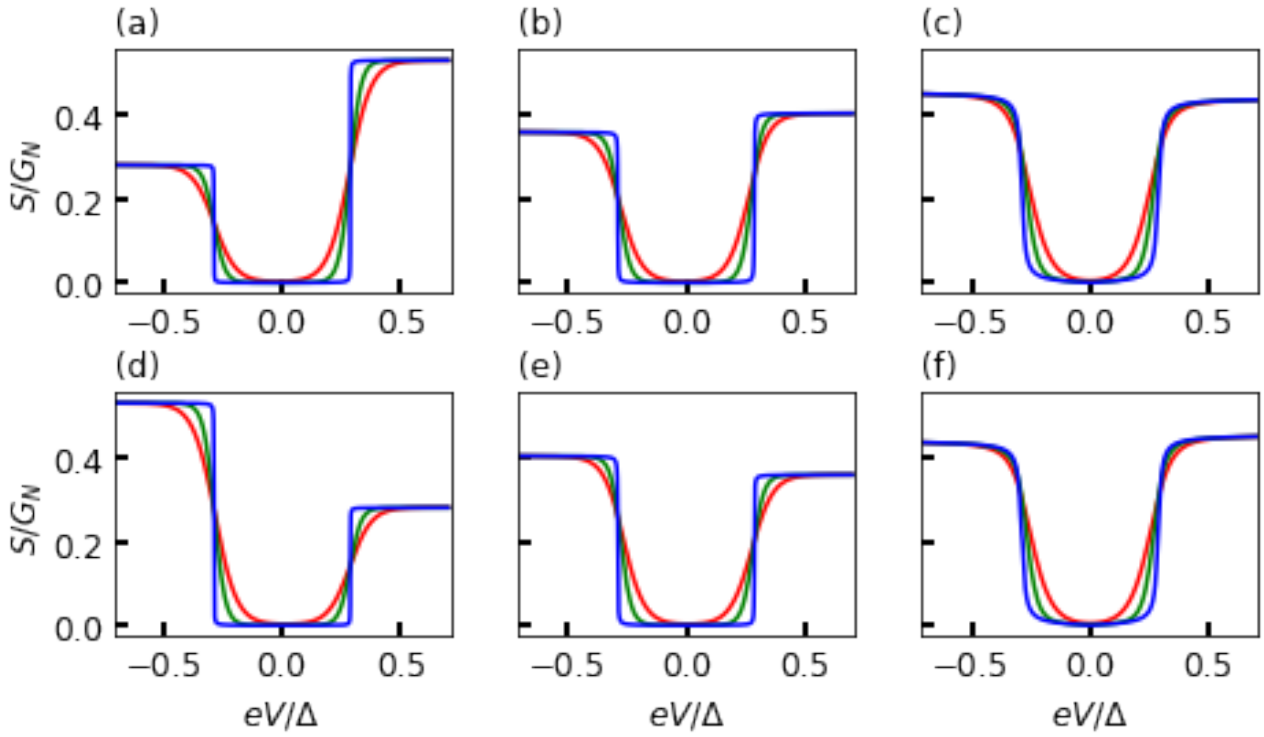

Figure 4.6: Shot-noise spectroscopy of a YSR state for finite relaxation rate $\Lambda = 10^{-3}$ meV. The YSR energy is $E_0 = 0.34$ meV and the superconducting gap is $\Delta = 1.35$ meV. (a): Shot-noise S as a function of eV/Δ for $G_N = 10^{-3}G_0$ $u^2 = 0.09\pi\nu_0$, $v^2 = 0.042\pi\nu_0$ and various temperature $T = 0$ (blue solid line), $k_BT = 0.03$ meV (green solid line), and $k_BT = 0.06$ meV (red solid line). (b) and (c): Same as in (a) for higher normal-state conductances $G_N = 10^{-2}G_0$ and $G_N = 2.10^{-1}G_0$, respectively. (d), (e), and (f): Same as (a),(b), and (c) for perfectly mirrored particle-hole asymmetry of the YSR state: $u^2 = 0.042\pi\nu_0$, and $v^2 = 0.09\pi\nu_0$.

single-particle processes. Moreover, the order of the asymptotic limits S_+ and S_- depends on the tunneling rate Γ, as observed in Fig. 4.6. To understand this feature, we use $E_0 \gg \Gamma_t$ and obtain simple expressions that read:

$$S_+ = \frac{2e^2}{h}\left\{\frac{4\Gamma_e\Gamma_h}{\Gamma_t}\left[1+\frac{(\Gamma_e-\Gamma_h)^2}{\Gamma_t^2}\right]+\frac{\Gamma_e\Lambda}{\Gamma_t}\left[1+\frac{(3\Gamma_h-\Gamma_e+\Lambda)^2}{\Gamma_t^2}\right]\right\}, \tag{4.66}$$

$$S_- = \frac{2e^2}{h}\left\{\frac{4\Gamma_e\Gamma_h}{\Gamma_t}\left[1+\frac{(\Gamma_e-\Gamma_h)^2}{\Gamma_t^2}\right]+\frac{\Gamma_h\Lambda}{\Gamma_t}\left[1+\frac{(3\Gamma_e-\Gamma_h+\Lambda)^2}{\Gamma_t^2}\right]\right\}. \tag{4.67}$$

Therefore, when $\Gamma(u^2+v^2) \ll \Lambda$, single-particle process dominate Andreev reflections, and $S_+ \sim \frac{2e^2}{h}\frac{\Gamma u^2}{\Lambda}$ while $S_- \sim \frac{2e^2}{h}\frac{\Gamma v^2}{\Lambda}$. Hence, $S_+/S_- \sim \frac{u^2}{v^2}$, as observed in Figs. 4.6 (a) and (d). Increasing Γ, S_+ approaches S_-, and the order of the asymptotic is inverted, as observed in Figs. 4.6(b) and (e). Finally, when $\Gamma u^2, \Gamma v^2 \gg \Lambda$, Andreev reflections are dominant, $S_+/S_- \to 1$ and S tend to be symmetric, see Figs. 4.6 (c) and (f).

Let us now turn to the Fano factor spectroscopy. Thanks to equations (4.61) and (4.24) we can readily obtain the Fano factor $F = S/(2e|I|)$ analytically. The analytical expression of F is not insightful. Hence, to gain insight into the qualitative features of F we numerically evaluate it for different tunneling rates Γ and present the results in Fig. 4.7. As observed in Fig. 4.7 F saturates to finite values F_+ and F_- when $eV - E_0 \gg \Gamma_t$ and $eV + E_0 \ll -\Gamma_t$ respectively. When the bias approaches the positive and negative resonances, $eV \sim \pm E_0$, F exhibits abrupt non-monotonous variations. When $|eV| - E_0 \ll \Gamma_t$, F linearly depends on V and takes values between 1 and 2. This sharply contrasts with $F = 2$ observed in the same regime for Andreev reflections or $F = 1$ for single-particle processes. Naively one can interpret this feature as a result of the competition between Andreev and single-particle processes. When $|eV| \ll E_0$, single-particle, and Andreev processes produce Poissonian shot-noise. Hence, the Fano factor lies between 1 and 2 depending on the relative contribution of single-particle and Andreev processes. Unfortunately, we recall that, this regime is not experimentally relevant because of the weak current signal. Hence we shift our attention to the case $|eV| > E_0$ and the asymptotic limits F_+ and F_-.

Fig. 4.7 shows that, due to single-particle processes, F is not an even function of V, and $F_+ \neq F_-$. However, unlike in the absence of Andreev reflections, the order of the asymptotic limits does not depend on the tunneling strength Γ. Namely, $F_+ < F_-$ if $u^2 > v^2$ and vice versa, as observed in Fig. 4.7. Indeed, using the hypothesis, $E_0 \gg \Gamma_t$, we obtain a simple analytical expression for the asymptotic limits F_+ and F_- that read:

$$F_+ \simeq 1 - \frac{2\Gamma_e}{\Gamma_e + \Gamma_h + \Lambda} - \frac{2\Gamma_e(\Gamma_h - \Gamma_e)}{(\Gamma_e + \Gamma_h + \Lambda)^2} + \frac{2\Gamma_h}{2\Gamma_h + \Lambda}\,, \tag{4.68}$$

$$F_- \simeq 1 - \frac{2\Gamma_h}{\Gamma_e + \Gamma_h + \Lambda} - \frac{2\Gamma_h(\Gamma_e - \Gamma_h)}{(\Gamma_e + \Gamma_h + \Lambda)^2} + \frac{2\Gamma_e}{2\Gamma_e + \Lambda}\,, \tag{4.69}$$

$$\text{and, } F_+ - F_- \simeq -\frac{2\Lambda(\Gamma_e - \Gamma_h)(\Gamma_e^2 + 4\Lambda(\Gamma_e + \Gamma_h) + 6\Gamma_e\Gamma_h + \Gamma_h^2 + 2\Lambda^2)}{(2\Gamma_e + \Lambda)(2\Gamma_h + \Lambda)}\,. \tag{4.70}$$

These equations directly prove that $F_+ > F_-$ for $v^2 > u^2$, while $F_- > F_+$ for $u^2 > v^2$. In other words, the Fano factor is stronger for the weaker resonance.

In addition, because of the competition between Andreev and single-particle processes, $F_\pm$ strongly depends on the tunneling rate Γ and, therefore, on G_N. Indeed, for weak tunneling rates $\Gamma(u^2 + v^2) \ll \Lambda$, the single-particle processes dominate, and $F_\pm$ barely deviates from 1, see Figs. 4.7 (a) and (d). When Γ increases, F_+ increases above 1 while F_- decreases below 1 if $u > v^2$, and vice versa when $v^2 > u^2$, as observed in Figs. 4.7 (b) and (e). In the opposite limit, $\Gamma(u^2 + v^2) \gg \Lambda$, Andreev reflections dominate, F is almost symmetric and $F_\pm \simeq 1 + \frac{(u^2-v^2)^2}{(u^2+v^2)^2}$, see Figs. 4.7 (c) and (f).

As expected, in the experimentally relevant temperature regime, $E_0 \gg k_BT \gg \Lambda$, thermal effects significantly modify the shot-noise and Fano factor spectroscopy only for small biases and around the resonances, as observed in Fig. 4.6 and Fig. 4.7. Most importantly, when $k_BT \gg \Gamma_t$, F rapidly increases when $|eV| < 2k_BT$ and diverges at $V = 0$ and linearly depends on V in the vicinity of the resonances, when $|eV \pm E_0| < k_BT$. Namely, for $|eV - E_0| < k_BT$, $F \simeq F(E_0) - \alpha_+ V$, while for $|eV + E_0| < k_BT$ $F \simeq F(E_0) + \alpha_- V$, with:

$$\alpha_+ = \frac{\Gamma_e(2\Gamma_h + \Lambda)}{\Gamma_t^2}\,,\ \alpha_- = \frac{\Gamma_h(2\Gamma_e + \Lambda)}{\Gamma_t^2}\,. \tag{4.71}$$

Hence, contrarily to the results obtained in the absence of single-particle processes (see Subsection. 4.3.1) the

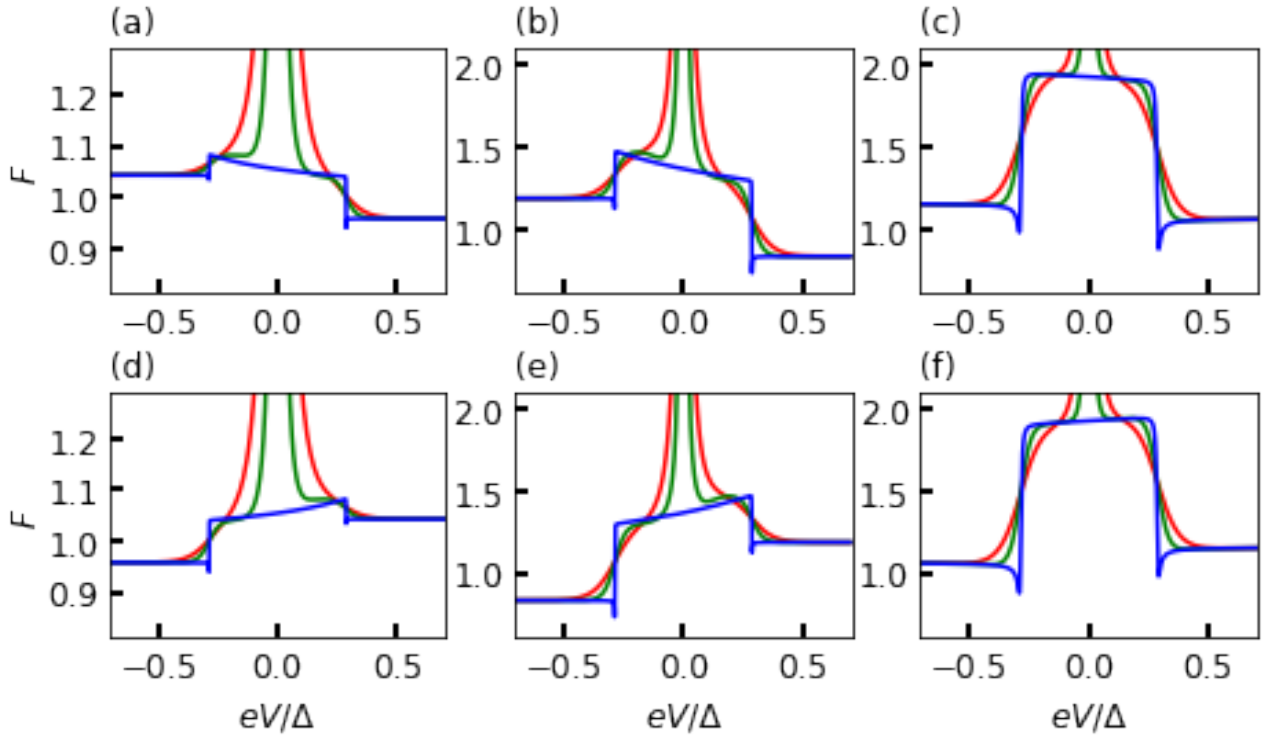

Figure 4.7: Fano factor spectroscopy of a YSR state for finite relaxation rate $\Lambda = 10^{-3}$ meV. The YSR energy is $E_0 = 0.34$ meV and the superconducting gap is $\Delta = 1.35$ meV(a): Fano factor F as a function of eV/Δ for $G_N = 10^{-3}G_0$ $u^2 = 0.09\pi\nu_0$, $v^2 = 0.042\pi\nu_0$ and various temperature $T = 0$ (blue solid line), $k_BT = 0.03$ meV (green solid line), and $k_BT = 0.06$ meV (red solid line). (b) and (c): Same as in (a) for higher normal-state conductances $G_N = 2.10^{-2}G_0$ and $G_N = 2.10^{-1}G_0$, respectively. (d), (e), and (f): Same as (a),(b), and (c) for perfectly mirrored particle-hole asymmetry of the YSR state: $u^2 = 0.042\pi\nu_0$, and $v^2 = 0.09\pi\nu_0$.

slopes are not identical, $\alpha_+ \neq \alpha_-$, except if $u^2 = v^2$. The strongest resonance is associated with the steepest slope: $\alpha_+ > \alpha_-$ is $u^2 > v^2$ and vice-versa.

Elsewhere, thermal effects do not modify the zero-temperature results. Most importantly, the asymptotic limits F_+ and F_- are not affected by thermal effects and equations (4.68), (4.69), which constitute the central results of our theoretical model and remains valid at finite temperature as long as $k_B T \ll E_0$.

To conclude our discussion, we stress that equations (4.68), (4.69), and (4.70) allow us to draw important conclusions that remain valid at finite temperatures[5]:

(i). When $u^2 \neq v^2$, having $F_+ = F_-$ requires the absence of relaxation, *i.e.*, $\Lambda = 0$. Consequently, a voltage-asymmetric Fano factor $F_+ \neq F_-$, clearly indicates the presence of single quasi-particle tunneling events in the current.

(ii). $F_+ > F_-$ for $v^2 > u^2$, while $F_- > F_+$ for $u^2 > v^2$. In other words, the Fano factor is stronger for the weaker resonance.

(iii). Independently of the relaxation rate Λ, $\max[F_+, F_-] \geq 1$. This is a consequence of the presence of Andreev reflections (see Eqs. (4.59)). This proves that a Fano factor larger than 1 is a consequence of Andreev processes.

4.4 Comparison with experimental data

Thanks to a recent collaboration with U. Thupakula, A. Palacio-Morales, L. Cario, M. Aprili, and F. Massee, we were able to make a quantitative comparison between our theoretical model and experimental noise data. In this work, U. Thupakula *et al.* used shot-noise scanning tunneling microscopy to study electron tunneling into superconducting 2H-NbSe2 mediated by YSR states. Despite its simplicity, the theoretical model presented above is able to quantitatively reproduce the Fano factor data measured experimentally by our colleagues. The results of this fruitful collaboration were recently published in *Physical Review Letters* [33]. In this section, we first briefly describe the experimental setup. Then, we present the method used to extract the model parameters from the experimental data. Finally, we compare the experimental Fano factor data to the theoretical predictions of our model and show the quantitative agreement between theory and experiment.

4.4.1 Description of the experimental setup and data

In their experiment, U. Thupakula *et al.* studied the electronic transport into YSR states in 2H-NbSe2. To that end, the current noise was measured at the atomic scale thanks to a home-built scanning tunneling microscope with cryogenic circuitry operating in the MHz regime [21]. Thorough details about the circuitry, its calibration, and the fitting method used to measure the Fano factor can be found in [33]. An etched, atomically sharp, and stable tungsten tip was used for all measurements.

2H-NbSe2 single crystals, grown using an iodine transport method, were unintentionally doped by a few tens of ppm of magnetic species (Fe, Cr, Mn) contained in the Niobium precursor (see [18] for more details). After a mechanical cleaving in a cryogenic vacuum at ~ 20 K, these single crystals were directly inserted into the head of the STM tip at 4.2 K.

[5] as long as $E_0 \gg k_B T$

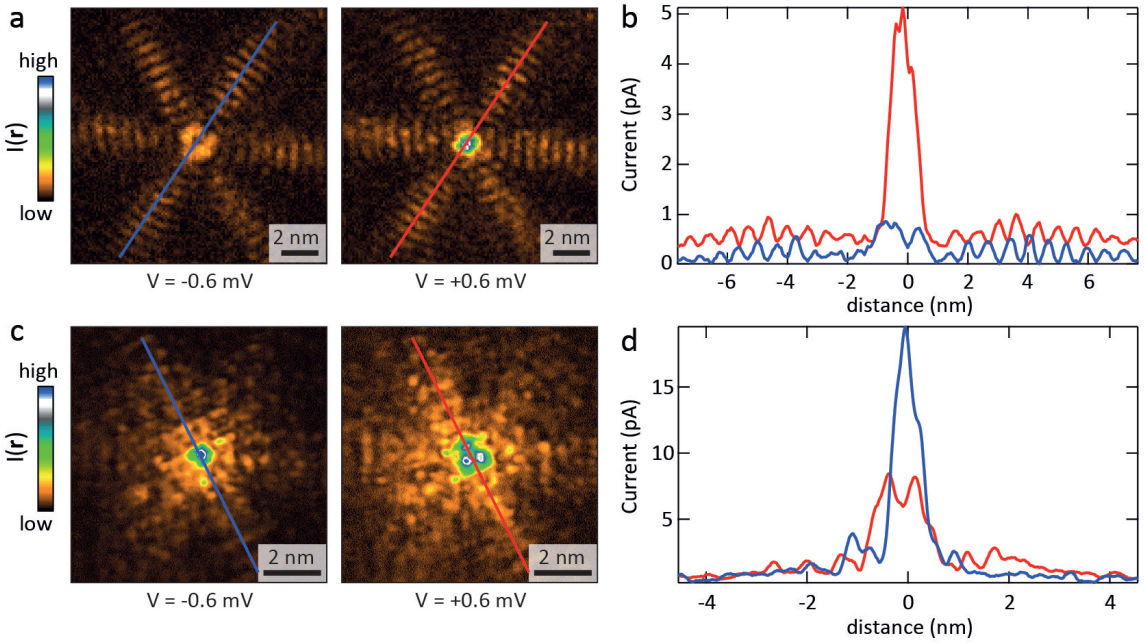

Figure 4.8: YSR spatial profile. (a): Current map of the YSR with a large spatial extent recorded at negative (left) and positive (right) bias. (b): Cuts along the red and blue lines in panel (a) , respectively, highlighting the out-of-phase nature of the particle-hole asymmetry. (c) and (d): As (a) and (b) for a more compact but relatively strong YSR located elsewhere on the same sample. Figure reproduced from [33].

Because of the magnetic impurities, the 2H-NbSe2 samples studied here exhibit YSR sub-gap states localized around the impurities. Here we focus on two YSR states shown in Fig. 4.8. The precise spatial extent of the in-gap resonances, as well as the particle-hole asymmetry of the core, can vary from impurity to impurity as it depends on the impurity type and its location in the crystal structure [18, 153, 154]. Because of the 2D superconductivity in 2H-NbSe2, the YSR wavefunctions have a large spatial extent away from the cores. The electron and hole components oscillate as a function of the distance from the core and are out of phase one with each other, as observed in Fig.4.8.

As we are interested in the tunneling processes through the YSR states, the shot-noise was first measured on top of the impurity's cores. To facilitate comparison, setup parameters were chosen such that they give roughly the same YSR-current, *i.e.* the YSR peaks in differential conductance in Figs. 4.9 (a) and (c) have approximately the same height. Consequently, since the noise is proportional to the current, the simultaneously recorded current noise has a similar magnitude for the two cores, despite the rather different conditions outside the gap, see Figs. 4.9.

It is important to stress that for every normal-state conductance studied experimentally, the current inside the superconducting gap (*i.e.,* for $|eV| < \Delta$) vanishes when the tip probes the clean 2H-NbSe2, away from impurities. This clearly indicates that the contribution of $ordinary$ Andreev reflections to transport observables is negligible. Therefore, the in-gap current solely originates from resonant tunneling via the YSR states, and our low-energy approximation (4.22) is legitimate.

Fig. 4.9 clearly shows that the noise on the YSR cores does not follow $F = 1$. Indeed, for the dominant

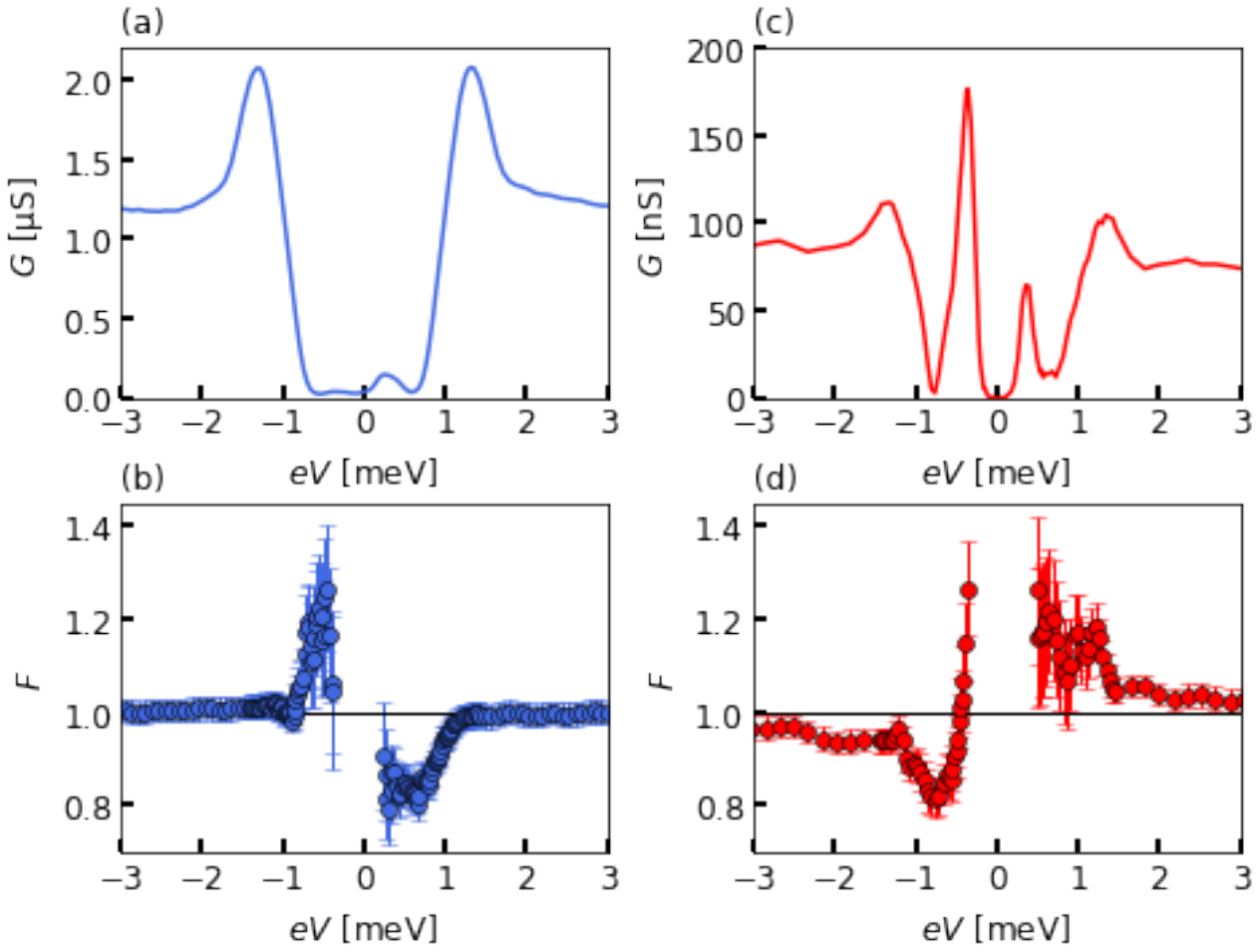

Figure 4.9: Noise on the YSR cores. (a): Differential conductance spectrum taken at the core of the YSR state shown in Fig.4.8 (a). The set-up parameters are chosen such that $G_N \simeq 0.01G_0$. (b): Fano factor spectrum measured at the same location. The black line indicates $F = 1$ and clearly shows that F deviates from 1 inside the gap for positive and negative biases. Outside the gap, F converges to 1, as expected for elastic single-particle tunneling in the quasiparticle continuum of the superconducting substrate. (c) and (d): The same as (a) and (b) for a more compact, but relatively strong, YSR located elsewhere on the same sample and set-up parameters such that $G_N \simeq 0.001G_0$.

resonance, *i.e.* positive bias for Fig. 4.9 (b) and negative bias for Fig. 4.9 (d) the noise is reduced ($F < 1$), whereas for the weak resonance, i.e., negative biases for Fig. 4.9 (b) and positive biases for Fig. 4.9 (d), it is enhanced ($F > 1$). Notice that, although the deviations in absolute numbers are relatively small, they are larger than the experimental error bars due to the high signal-to-noise ratio and the accurate fitting procedure (see Supplementary Information Section 1 of [33]). Thus the qualitative features of the experimental Fano factor data reported here are well captured by our theoretical model. It suggests that, despite its simplicity, our theoretical model contains the necessary ingredients to describe electronic transport into YSR states and can be used to interpret the experimental data. Most importantly, the observation of $F > 1$ indicates the presence

of Andreev processes, while the particle-hole asymmetry of the noise indicates a contribution from incoherent single-particle processes, meaning both processes operate simultaneously.

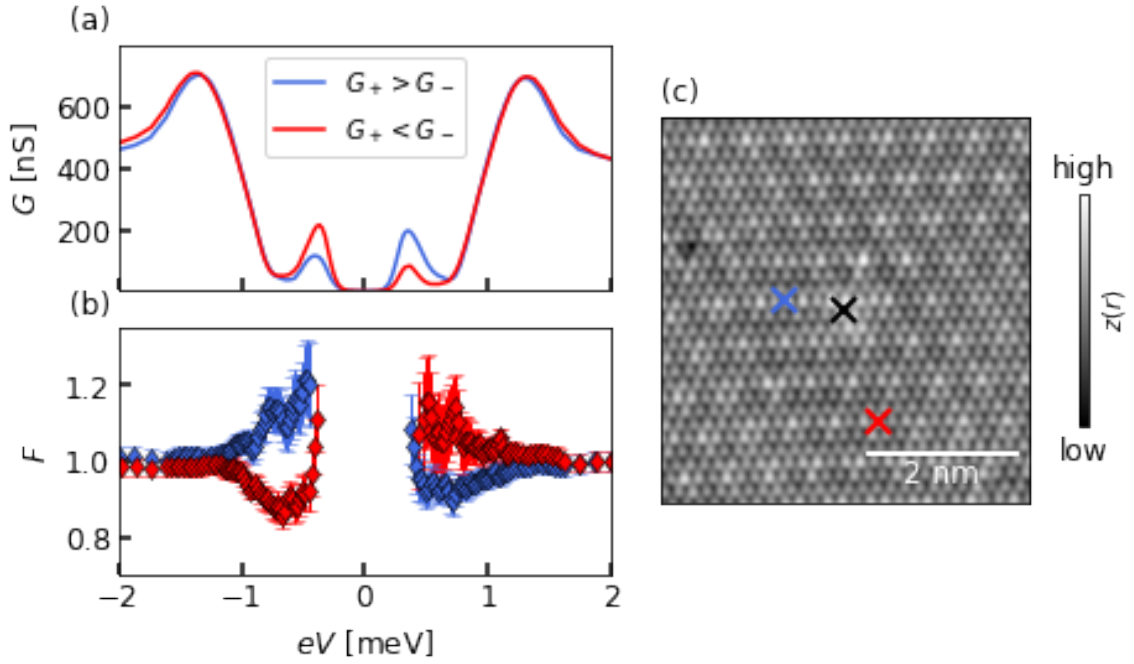

Figure 4.10: Noise on the YSR tails. (a): Differential conductance $G = \frac{\mathrm{d}I}{\mathrm{d}V}$ on two tail locations with opposite particle-hole asymmetry. Set-up parameters are set such that the normal-state conductance is $G_N \simeq 0.055G_0$. (b): Fano factor, F, extracted from the measured shot noise at the same tail locations. It clearly shows deviations from $F = 1$ inside the gap where the current is dominated by the YSR. The points corresponding to $I < 10$ pA have been omitted for clarity. For such small currents, since the fluctuations in the noise are the same for all voltages, the associated error in F becomes relatively large. (c): Constant current image of the 2H-NbSe2 surface around the YSR core of Fig.4.8 (c). The location of the blue and red spectra in (a) and (b) are indicated by the blue and red crosses, respectively. The black cross indicates the location of the YSR core.

To make a more quantitative comparison between the theoretical model described previously and experimental Fano factor data, we shift our attention to the YSR tails in order to avoid possible mechanical [146, 147, 129], multi-paths related [148, 149, 150, 151], or spin-dependent [152] complications from direct tunneling into the impurity, which were not included in our theory. Since the particle-hole asymmetry of the YSR wavefunction oscillates as a function of distance from the core [18], one can probe locations where the particle-hole asymmetry is nearly perfectly mirrored while all other experimental parameters remain identical. Fig.4.10 (c) shows two such locations, both situated at a distance of several atoms from the core of the YSR state presented in Fig. 4.8 (c), ensuring that direct tunneling into the impurity is negligible. Fig. 4.10 (b) shows the noise recorded simultaneously with the differential conductance spectra of Fig. 4.10 (a). Fig. 4.10 (b) shows that, as was the case for the spectra taken on the core (see Fig. 4.9), the noise is reduced, $F < 1$ for the dominant resonance and enhanced, $F > 1$, for the weaker resonance. Notice that F is roughly equally enhanced as it is suppressed and converges to $F = 1$ as soon as the current becomes dominated by the quasi-particles at the

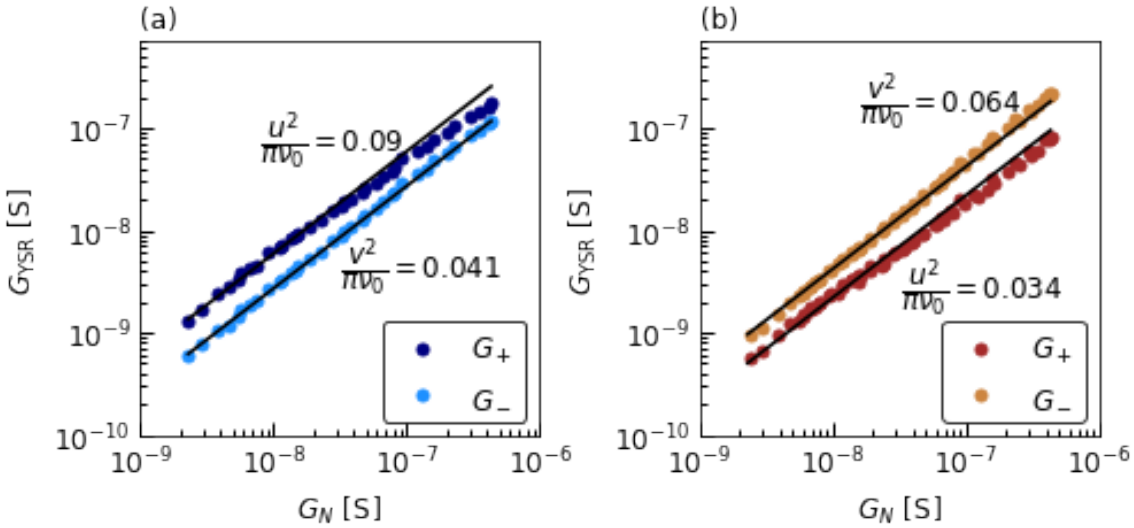

Figure 4.11: Normal-state conductance dependence of the YSR conductance peaks for the tail location indicated by the blue cross in Fig.4.10 (c). (b): Same as in (a) for the location indicated by the red cross in Fig. 4.10 (c). A fit of the linear part of the curves at weak G_N yields $\frac{u^2}{\pi\nu_0}$ and $\frac{v^2}{\pi\nu_0}$ for each location.

coherence peaks, $|eV| \geq \Delta$, as expected for quasi-particle tunneling following Poissonian statistics [155].

4.4.2 Quantitative comparison

Our theoretical model depends on five input parameters that are the electronic temperature, T, the YSR energy, E_0, the electron and hole tunneling rates $\Gamma_e = \Gamma u^2$ and $\Gamma_h = \Gamma v^2$, and finally the YSR relaxation rate, Λ.

The YSR energy can be directly measured from the position of the in-gap conductance peaks. The YSR state in Fig. 3.2 (c), has an energy $E_0 \simeq 0.4\text{meV}$, while the one in Fig. 3.2 (b) has an energy $E_0 \sim 0.28$ meV. Although the base temperature of the STM is ~ 0.3 K, the electron temperature, determined by noise thermometry (see the Supplementary Material in [33]) is actually higher than that, and $T \sim 0.7$ K. This is likely due to limited thermal anchoring and filtering of the current line. Therefore, $k_BT \sim 0.06\text{meV}$ and $E_0 \gg k_BT$.

The dimensionless tunneling rate $\Gamma\pi\nu_0$ can be obtained from the experiment as it is directly related to the normal-state conductance of the STM junction, G_N, thanks to:

$$\frac{G_N}{G_0} = \frac{2\Gamma\pi\nu_0}{(1+\Gamma\pi\nu_0)^2}, \tag{4.72}$$

with $G_0 = 2e^2/h$ the quantum of conductance.

In addition, for weak enough normal-state conductance, such that $G_N \ll G_0$ and $\Gamma(u^2+v^2) \ll \Lambda$, the conductance peaks are given by:

$$G_+ \simeq G_0 \frac{2\Gamma\pi^2\nu_0}{8k_BT}\frac{u^2}{\pi\nu_0},\ G_- \simeq G_0 \frac{2\Gamma\pi^2\nu_0}{8k_BT}\frac{v^2}{\pi\nu_0}. \tag{4.73}$$

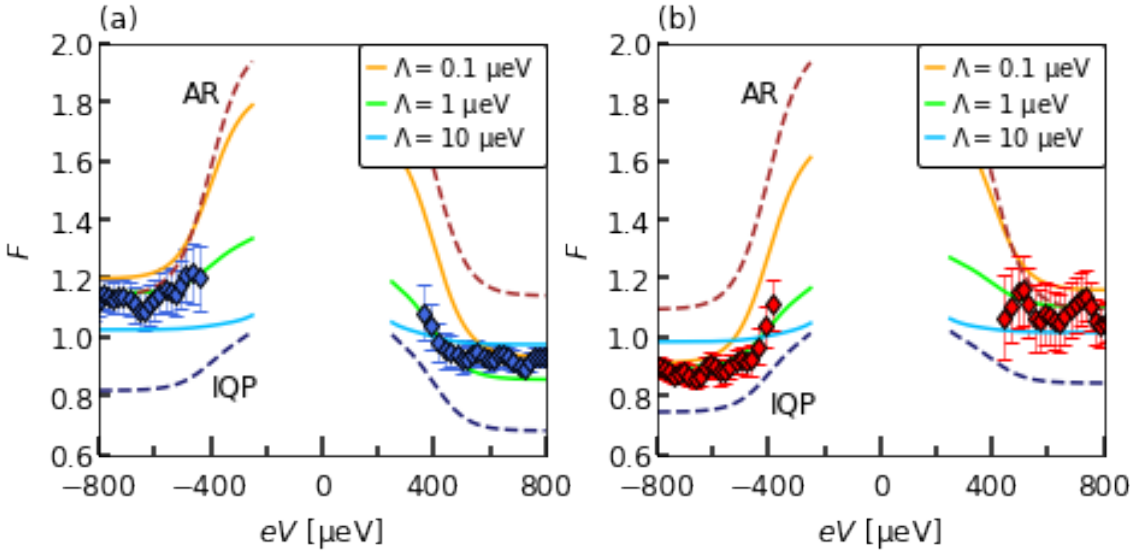

Figure 4.12: Theory experiment comparison for Fano factor data measured on the top of the YSR tails. (a): Sub-gap F for the blue spectrum in Fig. 4.10 (b) (diamonds), compared with theoretical curves (solid lines) for three different values of Λ as indicated in the legend. Theoretical curves in the sole presence of Andreev reflection (AR, $\Lambda = 0$ μeV) and inelastic quasi-particle tunneling (IQP, $\Lambda = 1$ μeV) are also shown for comparison. (b): Same as in (a) for the red data in Fig. 4.10 (b).

In this regime, since $G_N \ll G_0$, $G_N \simeq 2\Gamma\pi\nu_0$, and we finally obtain:

$$G_+ \simeq \frac{\pi G_N}{8k_BT}\frac{u^2}{\pi\nu_0},\ G_- \simeq \frac{\pi G_N}{8k_BT}\frac{v^2}{\pi\nu_0}. \tag{4.74}$$

Therefore, $\frac{u^2}{\pi\nu_0}$ and $\frac{v^2}{\pi\nu_0}$ can be extracted from the normal state conductance (G_N) dependence of the YSR conductance peaks ($G_\pm$), see Figs. 4.11 (a) and (b). Here, we fit the linear part at low conductance to determine $\frac{u^2}{\pi\nu_0}$ and $\frac{v^2}{\pi\nu_0}$. Thus, equations (4.72) and (4.74) allow us to determine Γ_e and Γ_h directly from the experimental conductance data. This enables us to calculate the noise with the YSR relaxation rate Λ, which is masked in the experimental conductance data by thermal broadening.

In Fig. 4.12, we compare the experimental Fano factor data for biases, V, where the tunnelling current is carried exclusively by the YSR states, *i.e.*, $|V| < 0.8$ mV, with theoretical predictions obtained with our model ((4.60) and (4.23)) for several values of the relaxation rate Λ. Fig. 4.12 shows quantitative agreement between theoretical curves and experimental data for $\Lambda \sim 1$ μeV, for both measured tip locations, corresponding to a relaxation time $\tau = \hbar/\Lambda \sim 0.7$ ns. It is worth noticing that we extracted u^2 and v^2 from the linear part of Figs. 4.11 (a) and (b) while all experimental noise data was recorded in the non-linear part of Figs. 4.11 (a) and (b), highlighting the robustness of our results. We stress that increasing values of Λ, meaning shorter relaxation times, incoherent single-particle tunneling increasingly dominates the tunneling process. Indeed, for $\Lambda = 10$ μeV, the calculated Fano factor is already nearly $F = 1$, for all biases, presented in Fig. 4.12. This puts a strong lower limit on the relaxation time extracted from the noise data. The sub-nanosecond relaxation time

$\tau \sim 0.7$ ns at 0.7 K, extracted from the noise data, is similar to that reported for Mn atoms on a Pb(111) surface [32] and not incompatible with the electron-phonon relaxation time in 2H-NbSe2 [156]. More importantly, the energy scale of the relaxation that we extracted, $\Lambda \sim 1$ μeV is much smaller than the electron temperature and masked by thermal broadening in the differential conductance spectroscopy. This clearly shows that scanning tunneling shot-noise spectroscopy is a powerful technique that allows one to access energy/time scale inaccessible to conventional spectroscopy techniques.

To be complete, we also included theoretical curves of the Fano factor produced by only Andreev reflection (AR) or only incoherent single-particle processes (IQP). Both curves fail to reproduce the data for any Λ, as the former always has $F > 1$ for both polarities and the latter $F < 1$.

4.4.3 Limits of the model and discussion

Let us now come back to the experimental data measured on the YSR cores and analyze the experimental Fano factor data of Figs. 4.9 (b) and (d) using our theoretical model. As for the tail locations, we extract the input parameters $\frac{u^2}{\pi\nu_0}$ and $\frac{u^2}{\pi\nu_0}$ from the linear part of $G_+(G_N)$ and $G_-(G_N)$ at low normal-state conductance, respectively, see Figs. 4.13 (a) and (c). With these parameters in hand, we can readily calculate the Fano factor for various relaxation rates Λ and compare the theoretical curves to the experimental data. The results of this comparison are presented in Fig. 4.13 (b) and (d).Fig. 4.13 (b) and (d) show that, although still in qualitative agreement, the theoretical curves slightly deviate quantitatively from the experimental points. The slight quantitative inaccuracy of our model suggests that tip- or current-induced effects, which are not included in our theory, do play a role when the current is measured directly on top of the YSR cores. The non-equilibrium Green's functions method being a versatile framework, these effects could be included in our theory and studied in the next future. Despite the less accurate fit, the Fano factor measured on the YSR cores of Fig. 4.8 (a) and (c) agree best with the theory curves that use a relaxation rate $\Lambda \sim 1$ μeV, similar to that obtained on the YSR tail. This highlights the simultaneous presence of Andreev processes and incoherent single-particle. This suggests that for roughly equal YSR currents, the YSR lifetime in 2H-NbSe2 is independent of the particular details of the magnetic impurity and the measurement location.

4.5 Conclusion and perspectives

To conclude, we presented a theoretical analysis of the electronic transport into YSR sub-gap states. Our model includes a phenomenological relaxation rate of the YSR state Λ that allows for resonant single-particle tunneling processes in addition to resonant Andreev processes via the YSR state. Using the Keldysh technique, we extracted analytical expressions of the asymptotic values F_+ and F_- reached by the Fano factor in the saturated regimes $eV \gg E_0$ and $eV \ll -E_0$, respectively (see (4.68) and (4.68)). These expressions allow us to draw important conclusions:

(*i*). $F_+ \neq F_-$ clearly indicates the presence of incoherent single-particle processes.

(*ii*). F is stronger on the weaker resonance.

(*iii*). Independently of the relaxation rate, $F > 1$ for the weaker resonance, indicating the presence of Andreev reflections.

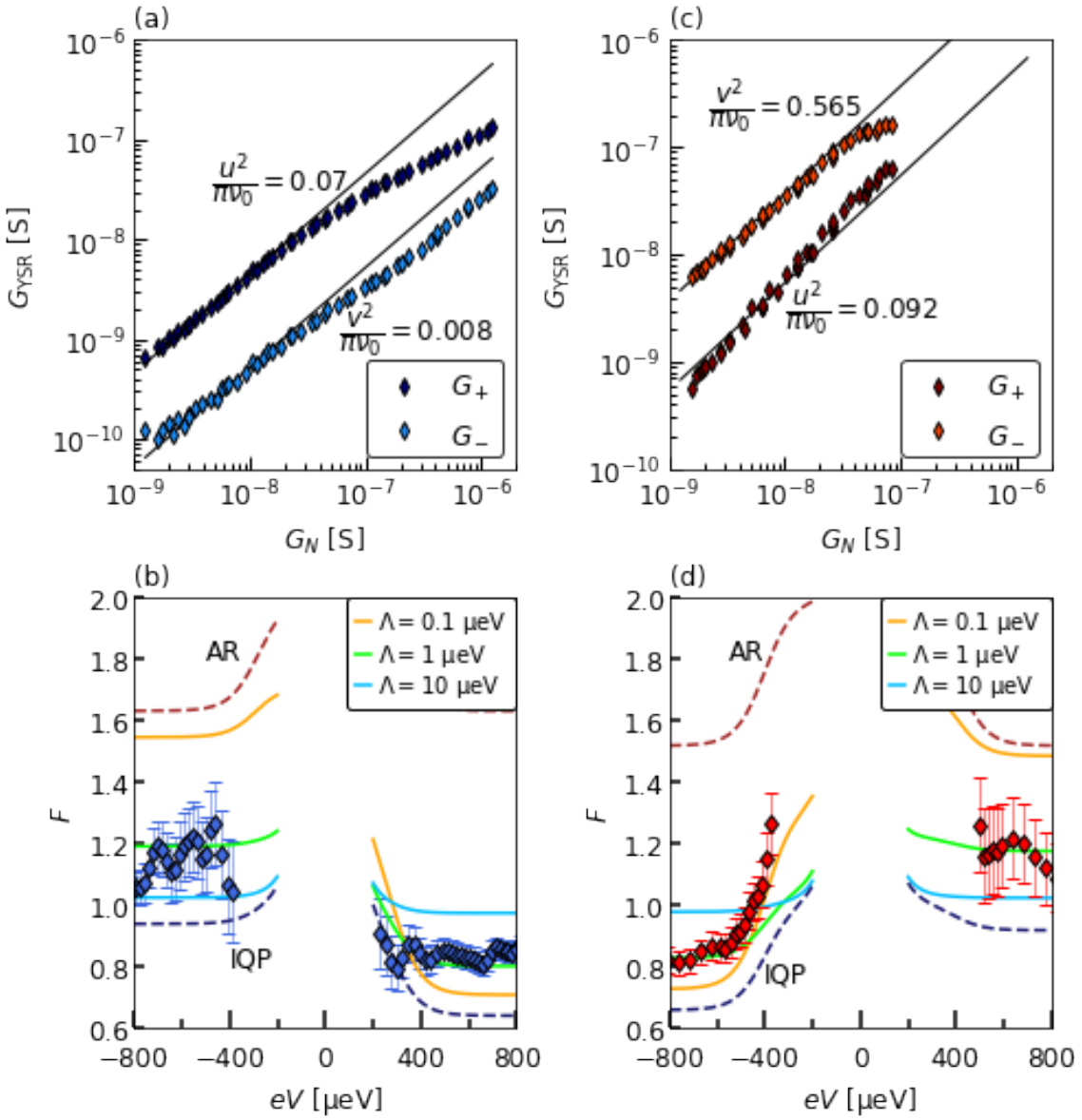

Figure 4.13: Theory experiment comparison for Fano factor data measured on the top of the YSR cores of Fig.3.2 (a) and (c). (a): Normal-state conductance dependence of the YSR conductance peaks measured on top of the YSR core shown in Fig.3.2 (a). A fit of the linear part of the curves at weak G_N yields $\frac{u^2}{\pi\nu_0}$ and $\frac{v^2}{\pi\nu_0}$. Sub-gap F for the blue spectrum in Fig. 4.9 (b) (dots), compared with theoretical curves (solid lines) for three different values of Λ as indicated in the legend. Theoretical curves in the sole presence of Andreev reflection (AR, $\Lambda = 0$ μeV) and inelastic quasi-particle tunneling (IQP, $\Lambda = 1$ μeV) are also shown for comparison. (c) and (d): Same as in (a) and (b) for the blue data in Fig. 4.9 (d).

Then, we used our theoretical model to analyze the experimental data measured by U. Thupakula *et al.*. The theory/experiment comparison shows that our model correctly captures the main features of F. In agreement

with our theoretical predictions, experimental data show the persistent enhancement of F above 1 for the smaller of the two YSR resonances, which directly proves the presence of Andreev processes. The measured asymmetry in F reveals the presence of single-particle processes. With Λ as the only adjustable parameter, we are able to obtain a quantitative agreement between theory and experiment. From this quantitative agreement, we extracted the relaxation rate $\Lambda \sim 1\ \mu\mathrm{eV}$.

Although qualitatively still in agreement, the theoretical curves for the data taken on the cores Fig. 4.13 slightly deviate quantitatively. It suggests that tip and/or current induced effects, which are currently not included in our theory, may indeed play a role when the STM tip is right on top of the YSR core. These effects could be included in the theory and studied in the next future. Also, it would be interesting to understand how the present results generalize to the case of a quantum spin impurity. This point could be addressed in the next future, but would require state-of-the-art technique adapted to strongly-correlated systems with local interactions, like non-equilibrium dynamical mean-field theory [36].

We stress that the YSR relaxation rate estimated from comparison with theoretical curves, $\Lambda \sim 1\ \mu\mathrm{eV}$, is much smaller than $k_B T = 0.7$ K. Thus, shot-noise spectroscopy allows one to probe energy/time scales inaccessible to conventional spectroscopy.

Although experimentally challenging, the measurements presented here show the feasibility of using atomic-scale shot-noise to elucidate the transport dynamics through superconducting sub-gap states. Hence, it is legitimate to wonder how the above-mentioned results could be generalized to other types of superconducting sub-gap states, such as Andreev bound-states and/or topological Majorana zero modes. In the next chapter, we will address this point and shows that shot-noise tomography can be used to distinguish trivial fermionic states from Majorana zero modes [34].

Chapter 5

Shot-noise tomography: a new tool to identify Majorana zero modes (MZM)

In the precedent chapter, we have shown that the recently developed scanning tunneling shot-noise spectroscopy is a powerful experimental technique that provides valuable insights into the properties of superconducting sub-gap states. More especially, we showed that the Fano factor in the YSR state is sensitive to both their intrinsic lifetime and particle-hole asymmetry. It seems, therefore, natural to wonder if the measurement of the current fluctuations with an atomic-scale resolution could help us to distinguish highly desirable Majorana bound-states from trivial zero-energy fermions. Indeed the unambiguous identification of MBS remains a difficult issue because of the concomitant competition with other topologically trivial fermionic states, which poison their detection in most spectroscopic probes. In this chapter, we will show that shot-noise tomography reveals key distinctive features that allow one to distinguish trivial zero-energy fermionic states, like YSR states, from Majorana zero modes.

This chapter is organized as follows: First, we briefly describe the most promising and mature solid-state platform supporting MZMs: hybrid semiconductor/superconductor nanowires. Then, we briefly review the experimental signatures of MZMs and explain why the distinction between MBS and trivial zero-energy fermions remains a difficult task. Finally, by employing numerical and analytical methods, we show that the Fano factor in the vicinity of Majorana zero modes is spatially constant and equal to one. In sharp contrast, the Fano factor of trivial fermionic bound-states is strongly spatially dependent and exceeds one. These sharp differences have a universal character that is rooted in the intrinsic particle-hole symmetry of the MBS wavefunction and can be used to as a key tool for discerning MBS from trivial fermionic bound-states.

5.1 Superconducting Rashba nanowires: a solid-state platform supporting MZMs

5.1.1 Motivation

Non-degenerate Majorana zero-modes arise at the ends of one-dimensional (1D) spinless p-wave superconductors (described by the Kitaev chain) [16] or at the vortex cores of two-dimensional (2D) $p_x + ip_y$ superconductors [60, 61, 62]. However, these models are somewhat unrealistic for the following two reasons. First, they

consider spinless fermions while electrons are spinful. This first problem can be easily circumvented if the spin degeneracy of the electrons is lifted such that the fermion doubling is effectively eliminated at low energy.

Second, spin-triplet p-wave superconductivity is rather rare in nature. Strontium ruthenate Sr_2RuO_4 have long been the main candidate for intrinsic p-wave superconductor. Nevertheless, recent nuclear magnetic resonance (NMR) results call into question the existence of a spin-triplet order parameter. These results were corroborated by recent theoretical studies and other experiments, suggesting the absence of p-wave superconductivity in this material. Besides Sr_2RuO_4, iron-based superconductors of the family $FeTe_xSe_{1-x}$, and the compound $(Li_{0.84}Fe_{0.16})$OHFeSe which possibly exhibit MZMs localized at the core of vortices, motivating further studies.

To circumvent this problem, a possibility would be to artificially engineer *exotic* p-wave superconductors by fabricating appropriate heterostructures with abundant *ordinary* s-wave. It was early shown that a spin-triplet p-wave pairing could be generated from the combination of s-wave superconductivity spin-orbit coupling and magnetic fields [157, 158]. Following this idea, theoretical studies showed that MZMs arise in 1D and 2D heterostructures made of a spin-orbit coupled semiconductor, in contact with an ordinary s-wave superconductor and subjected to a magnetic field [159, 15, 160, 161]. In 1D, MZMs do not require the presence of a vortex and are thus simpler to produce. Therefore, in this manuscript, we focus on the 1D case. A detailed theoretical study of the 2D case is provided in [159, 15]. In the 1D case, the proposed heterostructure, named the *superconducting Rashba nanowire* consists of a spin-orbit coupled nanowire (a Rashba nanowire) in contact with a s-wave superconductor subjected to a magnetic field applied perpendicular to the direction of the spin-orbit coupling. Theoretical studies showed that as the chemical potential or magnetic field is tuned, the *superconducting Rashba nanowire* undergoes a topological phase transition from a topological phase supporting MZMs at the ends of the wire and a trivial superconducting phase with no MZMs [160, 161]. The *superconducting Rashba nanowire* has the advantage of being a simple heterostructure that does not require any specialized materials and is feasible in the lab. Thereby, the first experimental realization and characterization of *superconducting Rashba nanowire* came soon after their theoretical proposition[162]. In the next subsections, we review the properties of the superconducting Rashba nanowire from the theoretical point of view.

5.1.2 The Oreg-Lutchyn model

Following Oreg and Lutchyn [161, 160], our starting point is an ideal single-channel semi-conducting nanowire with parabolic dispersion and Rashba SOC characterized by a SOC vector $\boldsymbol{\alpha}_R = \alpha_R \boldsymbol{e}_y$ pointing in the y-direction, perpendicularly to the nanowire axis. Without loss of generality, we can assume $\alpha_R > 0$. We choose the spin quantization axis as the z-axis. In addition, a magnetic field $\boldsymbol{B}$ is applied along the nanowire and points in the x-direction, $\boldsymbol{B} = B\boldsymbol{e}_x$. Finally, we assume that the nanowire is tunnel-contacted with a s-superconductor, which induces s-wave superconductivity in the nanowire itself by proximity effects. The induced superconductivity is characterized by the induced s-wave gap Δ, which, without loss of generality, we choose to be real and positive. Therefore the system is described by the Oreg-Lutchyn minimal model [161, 163],

$$\mathcal{H} = \frac{1}{2}\int \mathrm{d}x \psi^\dagger(x)\hat{H}\psi(x), \text{ with } \hat{H} = \left[\frac{-\hbar^2\partial_x^2}{2m^*} - \mu - i\alpha_R\sigma_y\partial_x\right]\tau_z + \Delta\tau_x + V_Z\sigma_x, \tag{5.1}$$

where we introduced the Nambu spinor $\psi^\dagger(x) = [c_\uparrow^\dagger(x), c_\downarrow^\dagger(x), c_\downarrow(x), -c_\uparrow(x)]$, $c_\sigma^\dagger(x)$ is the operator creating an electron of spin σ (along the z-axis) at position x in the nanowire, σ_i are the Pauli matrices acting in spin

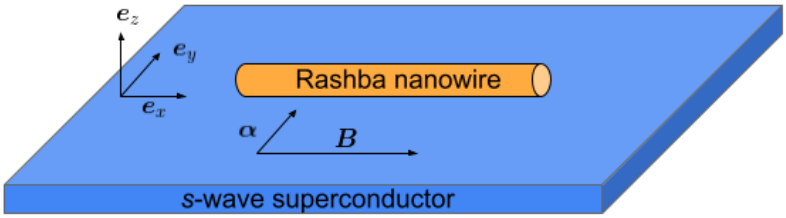

Figure 5.1: Schematic illustration of the superconducting Rashba nanowire set-up. A semi-conducting nanowire (in orange) is deposited on a s-wave superconducting substrate (in blue). Because of the broken inversion symmetry breaking at the semiconductor-superconductor interface and the intrinsically broken symmetry inversion of the semiconductor crystal lattice, a finite Rashba-type spin-orbit coupling is present in the nanowire, characterized by the SOC vector $\boldsymbol{\alpha}$. A magnetic field, $\boldsymbol{B}$, is applied along the nanowire axis and breaks the time-reversal symmetry.

space, and τ_i are the Pauli matrices acting in particle-hole space. m^* is the effective mass of the semiconducting nanowire, μ its chemical potential, and V_Z the Zeeman energy due to the magnetic field, given by $V_Z = g\mu_B B$. Focusing on the bulk properties of the nanowire, we can define the Fourier transform $\psi(x) = \int \frac{\mathrm{d}k}{2\pi} e^{ikx}\psi(x)$, and obtain,

$$\mathcal{H} = \frac{1}{2}\int \frac{\mathrm{d}\boldsymbol{k}}{2\pi}\psi^\dagger(k)\hat{H}(k)\psi(k), \text{ with } \hat{H}(k) = \left[\frac{\hbar^2 k^2}{2m^*} - \mu + \alpha_R\sigma_y k\right]\tau_z + \Delta\tau_x + V_Z\sigma_x. \tag{5.2}$$

For latter convenience, we parametrize the BdG Hamiltonian $\hat{H}(k)$ as,

$$\hat{H}(k) = \begin{bmatrix} \hat{h}_0(k) & \Delta\sigma_0 \\ \Delta\sigma_0 & -\sigma_y\hat{h}_0^*(-k)\sigma_y \end{bmatrix}, \text{ with } \hat{h}_0(k) = \frac{\hbar^2 k^2}{2m^*} - \mu + \alpha_R\sigma_y k + V_Z\sigma_x, \tag{5.3}$$

where $\hat{h}_0(k)$ is the single-particle Hamiltonian describing the electrons in the normal-state nanowire.

5.1.3 Induced p-wave superconductivity

To understand how p-wave superconducting is effectively induced in the nanowire, it is insightful first to study the effect of SOC and successively add the magnetic field and the proximity-induced superconductivity to the model.

Hence, we first focus on the normal-state nanowire. In the absence of superconductivity, $\Delta = 0$, electron and hole sectors are decoupled, and the BdG Hamiltonian $\hat{H}$ is block-diagonal. Hence we can focus on the electronic sector described by $\hat{h}_0(k)$. The energies of the electrons are given by the spectrum of $\hat{h}_0(k)$, while the energies of the holes are simply obtained via the particle-hole symmetry.

When $V_Z = 0$, $\hat{h}_0(k) = \frac{\hbar^2 k^2}{2m^*} - \mu + \alpha_R\sigma_y k$, hence it is straightforward to diagonalize it and obtain its eigenvalues $E_\pm^0(k)$ and the associated eigenvectors $\phi_\pm^0(k)$,

$$E_\pm^0(k) = \frac{\hbar^2 k^2}{2m^*} - \mu \pm \alpha_R k, \ \phi_\pm^0(k) = \begin{bmatrix} 1 \\ \pm i \end{bmatrix}. \tag{5.4}$$

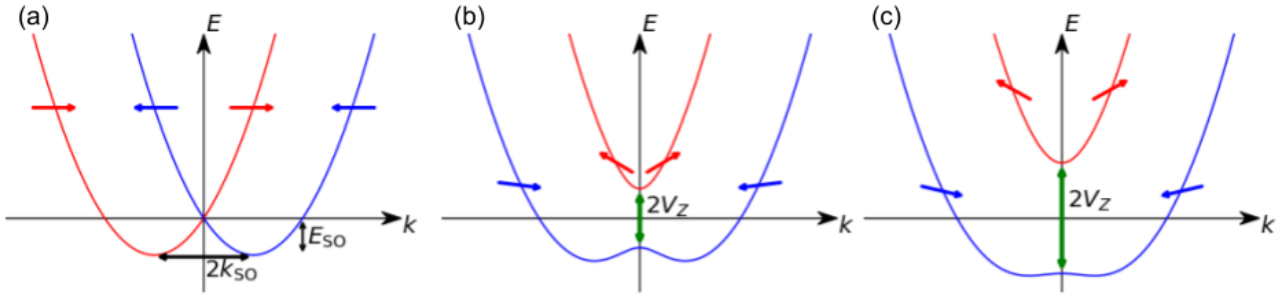

Figure 5.2: Schematic spectra of the normal-state Rashba nanowire $\hat{h}^0(k)$ at $\mu = 0$. The red solid line corresponds to $E^0_+(k)$ and the blue one to $E^0_-(k)$, given in (5.6). (a): Electronic bands in absence of Zeeman energy ($V_Z = 0$). In this case, the $\pm$ band corresponds to electrons with spin locked in the $\pm y$-direction respectively, as indicated by the arrows. (b): Electronic bands in presence of a Zeeman energy $V_Z > 0$ dominated by SOC, $E_{SO} > V_Z$. (c): Electronic bands in presence of a dominant Zeeman energy $V_Z > E_{SO}$. In these two cases, the $+(-)$ band corresponds to electrons with spin aligned (anti-aligned) with the effective field $\boldsymbol{b}(k)$, as indicated by the arrows. Increasing the Zeeman energy, the double-well structure of the $-$ band flattens.

Therefore, the electronic spectrum consists of two shifted parabolas crossing at $k = 0$ represented in Fig. 5.2 (a). The $+/-$ band corresponds to states with spin locked in $\pm$-y direction, respectively. The spin-orbit coupling does not break the time-reversal symmetry, but spin is coupled to the momentum: electrons with the same energy and opposite momenta have opposite spins as indicated in Fig. 5.2(a).

In the presence of a finite magnetic field $B > 0$, $\hat{h}_0(k)$ becomes,

$$\hat{h}_0(k) = \frac{\hbar^2 k^2}{2m^*} - \mu + \boldsymbol{b}(k) \cdot \boldsymbol{\sigma}, \tag{5.5}$$

where $\boldsymbol{b}(k) = V_Z \boldsymbol{e}_x + \alpha_R k \boldsymbol{e}_y$ is an effective magnetic field which is momentum-dependent. Intuitively we expect that the spin of the electron of momentum k aligns with the effective magnetic field $\boldsymbol{b}(k)$. Defining the unit vector, $\boldsymbol{u}(k) = \frac{\boldsymbol{b}(k)}{|\boldsymbol{b}(k)|}$, the spin operator $\hat{s}(k) = \boldsymbol{u}(k) \cdot \hat{\sigma}$ commutes with $\hat{h}_0(k)$. Therefore, the two electronic bands are eigenfunctions of $\hat{s}(k)$ with eigenvalues ± 1,

$$E^0_\pm(k) = \xi(k) \pm \sqrt{V_Z^2 + \alpha_R^2 k^2}, \; \phi^0_\pm(k) = \frac{1}{\sqrt{2 \pm 2u_z(k)}} \begin{bmatrix} 1 \pm u_z(k) \\ \pm u_x(k) \pm i u_y(k) \end{bmatrix}, \tag{5.6}$$

with $\xi(k) = \dfrac{\hbar^2 k^2}{2m^*} - \mu$. As it can be observed in Fig. 5.2 (b) and (c), the magnetic field completely lifts the spin-degeneracy and opens a gap $2V_Z$ at $k = 0$. Time-reversal symmetry is broken: electrons with the same energy and opposite momenta have different spins, as indicated by the arrows in Fig. 5.2 (b) and (c). Each band can be considered spinless, and by tuning the chemical potential inside the gap at $k = 0$, the system is effectively spinless at low energies. Notice that the number of Fermi momenta depends on the different energy scales set by the Zeeman energy.

In presence of the proximity-induced superconductivity ($\Delta > 0$), the nanowire exhibits all ingredients required to effectively realize a spinless p-wave topological superconductor, namely the presence of spin-orbit

coupling, the absence of time-reversal symmetry and the presence of s-wave superconductivity. Thus we expect that the superconducting gap Δ induces p-superconductivity in the nanowire. Indeed,in the basis diagonalizing the normal-state Hamiltonian $\hat{h}_0(k)$, the model (5.1) reads,

$$\mathcal{H} = \int \frac{\mathrm{d}\boldsymbol{k}}{2\pi} \sum_{\nu=\pm} \left\{ c_\nu^\dagger(k) E_\nu^0(k) c_\nu(k) + \frac{1}{2}(\Delta_\nu(k) c_\nu^\dagger(k) c_\nu^\dagger(-k) + \text{h.c.}) \right\} \tag{5.7}$$
$$+ (\Delta_c(k) c_+^\dagger(k) c_-^\dagger(-k) + \text{h.c.}),$$

$$\text{with, } \Delta_\nu(k) = \Delta \frac{i\nu\alpha_R k}{V_Z^2 + \alpha_R^2 k^2}, \ \Delta_c(k) = -\Delta \frac{V_Z}{V_Z^2 + \alpha_R^2 k^2}, \tag{5.8}$$

where we introduced the operator $c_\nu(k)$ annihilating an electron in the $\nu = \pm$ band (5.6). The proximity-induced superconductivity generates an interband s-wave pairing $\Delta_c(k)$ and an intraband p-wave pairing $\Delta_\pm(k)$.

Therefore, if we tune the chemical potential such that only the lower band is partially filled, the upper band can be neglected at low energy, and the model (5.1) is equivalent to a spinless p-wave topological superconductor and can exhibit a non-trivial topological phase supporting MZMs. In addition, we remark that when $k \sim 0$, $\Delta_- \sim \Delta \frac{-i\alpha_R k}{V_Z}$, hence the nanowire is equivalent to the Kitaev chain. As a last remark, $\Delta_-(k \sim 0)$ depends on the Rashba SOC, the Zeeman energy, and the proximity-induced gap Δ, illustrating that these three ingredients are indispensable for realizing a topological superconductor.

5.1.4 Topological properties of the nanowire

Since the nanowire is effectively equivalent to a spinless p-wave superconductor, it might realize a topological phase supporting MZMs at its ends. Here, we rigorously prove that it is indeed the case and study the topological properties of the superconducting Rashba nanowire (5.1).

The first step is to find the symmetry class of (5.1). At first sight, the model belongs to the D class. Indeed, $\hat{H}$ possesses particle-hole symmetry,

$$C^{-1}\hat{H}(k)C = -\hat{H}(-k), \text{ with } C = \sigma_y\tau_y\mathcal{K}. \tag{5.9}$$

However, the Zeeman energy breaks the physical time-reversal symmetry,

$$T^{-1}V_Z\sigma_x T = -T^{-1}V_Z\sigma_x T, \text{ with } T = i\sigma_y\mathcal{K}, \tag{5.10}$$

hence $\hat{H}$ breaks the time-reversal symmetry, $T^{-1}\hat{H}(k)T \neq \hat{H}(-k)$. Additionally, $\hat{H}$ also breaks the chiral symmetry $S = TC = i\tau_y$. Nevertheless, considering the symmetry classification of the *ten-fold way*, the time-reversal symmetry is not necessarily the physical one, and any *artificial* time-reversal symmetry defined by an anti-unitary operator T' has to be considered. Thus, remarking that $\hat{H}(k)$ is a real matrix, it possesses the *artificial* time-reversal symmetry defined by the operator $T' = \mathcal{K}$, and the *artificial* chiral symmetry defined by $S' = \tau_y\sigma_y$,

$$T'^{-1}\hat{H}(k)T' = \hat{H}(-k), \ S'^{-1}\hat{H}(k)S' = -\hat{H}(k). \tag{5.11}$$

Since, $C^2 = 1$ and $T'^2 = 1$, the BdG Hamiltonian $\hat{H}$ belongs to the BDI class.

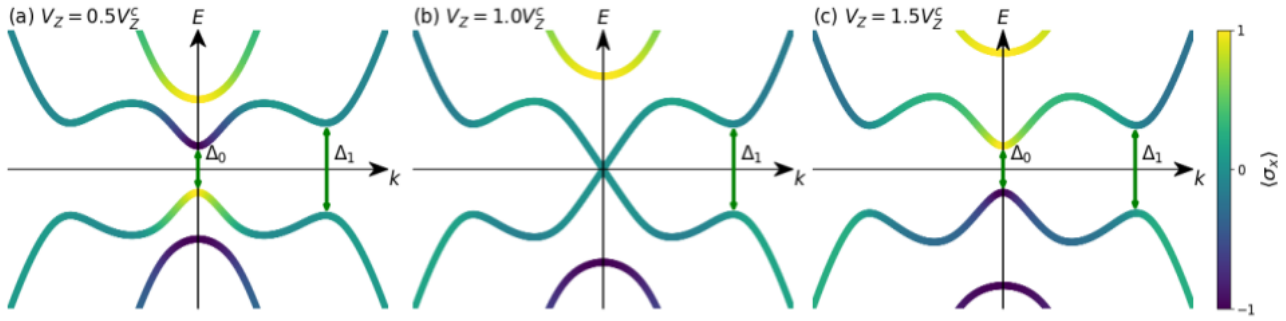

Figure 5.3: Schematic quasiparticle spectra of the superconducting Rashba nanowire in different regimes. The quasiparticle energy bands are colored according to the spin projection of the state along $\boldsymbol{e}_x$, $\langle\sigma_x\rangle = \phi^\dagger(k)\sigma_x\phi(k)$, with $\phi(k)$ the eigenvector of the relevant band. The central gap Δ_0 is open at low Zeeman energies, $V_Z < V_Z^c = \sqrt{\mu^2+\Delta^2}$ (a), closes at the critical point $V_Z = V_Z^c$ (b), and reopens for large Zeeman energy $V_Z > V_Z^c$ (c). Notice that a band inversion occurs when the central gap closes.

Let us now construct the topological phase diagram of the nanowire in the (V_Z, μ) plane. Reminding that a topological phase transition requires the quasiparticle gap to close, we first investigate the quasiparticle spectrum. The quasiparticle spectrum of $\hat{H}(k)$ consists of four dispersion bands: two positive energy bands $\pm E_\pm(k)$. After straightforward algebra, we obtain,

$$E_\pm(k) = \sqrt{\xi^2(k) + \boldsymbol{b}^2(k) + \Delta^2 \pm \sqrt{\xi^2(k)\boldsymbol{b}^2(k) + \Delta^2 V_Z^2}}. \tag{5.12}$$

As it can be observed in Fig.5.3(a) and (c) the quasiparticle gap $\Delta_{ph}(k) = 2E_-(k)$ possess two local minima one at finite k named Δ_1 and another one at $k = 0$, named Δ_0. The gap Δ_1 never vanishes. On the contrary, Δ_0 can vanish. Indeed,

$$\Delta_0 = 2E_-(0) = 2|V_Z - \sqrt{\mu^2+\Delta^2}|, \tag{5.13}$$

hence if $V_Z = \sqrt{\mu^2+\Delta^2}$, $\Delta_0 = 0$ and the quasiparticle gap closes, allowing for a topological transition, as it can be observed in Fig. 5.3 (b). Moreover, when $V_Z^2 > \mu^2 + \Delta^2$, Δ_0 is a spin gap due to the Zeeman energy, while when $V_Z^2 < \mu^2+\Delta^2$, Δ_0 is a superconducting gap. Therefore the gap closing of Δ_0 for $V_Z = \sqrt{\mu^2+\Delta^2}$ is associated with band inversion (see Fig. 5.3) that signals a quantum phase transition [161].

This quantum phase transition is a topological phase transition from a topologically trivial phase to a non-trivial one supporting a single pair of MZMs localized at each end of the nanowire [161, 160, 164]. To prove it, we show that the topological invariant characterizing the Oreg-Lutchyn model changes when the gap closes. In principle, the Oreg-Lutchyn model belongs to the BDI class. Therefore it is characterized by a $\mathbb{Z}$ topological invariant, the winding number ν, and can support 2ν MZMs.

However, in realistic systems, the *artificial* time-reversal symmetry is inevitably broken by magnetic disorder, misalignment of the magnetic field with the nanowire axis, or multi-band effects. In these cases, the Oreg-Lutchyn model falls into the D symmetry class, and its topological properties are classified by the pfaffian $\mathbb{Z}_2$. Thus, we discuss the topological properties of the model in the D class and use the pfaffian invariant.

To define topological invariant, the momentum space has to be a smooth, compact manifold [165]. Therefore, we discretize the continuum model given by (5.1) on a 1D lattice and obtain a tight-binding Hamiltonian that reads:

$$\mathcal{H} = \frac{1}{2}\sum_{l=0}^{N-1} \psi_l^\dagger[(2t - \mu + V_Z\sigma_x]\psi_l + \frac{1}{2}\sum_{l=0}^{N-2} \psi_{l+1}^\dagger[-t\tau_z - i\alpha\sigma_y\tau_z]\psi_l + \text{h.c.},$$

where we defined the Nambu spinor $\psi_l = [c_{\uparrow l}, c_{\downarrow l}, c_{\downarrow l}^\dagger, -c_{\uparrow l}^\dagger]^T$, with $c_{\sigma l}$ the operator annihilating an electron of spin σ at site l of the chain, $t = \frac{\hbar^2}{2ma^2}$ the hopping parameter, $\alpha = \frac{\alpha_R}{2a}$ the spin-flip hopping parameter, a the lattice constant of the discrete model and N the number of sites of the chain. Since the typical length scales (the nanowire length, the superconducting coherence length ξ, the spin-orbit length $l_{SO} = k_{SO}^{-1}$) are much larger than the atomic length scales, the lattice parameter a needs not to coincide with the microscopic atomic lattice parameter. It is usually chosen to be much larger, allowing for efficient numerical simulations.

Imposing periodic boundary conditions, and defining the discrete Fourier transform:

$$\psi_l = \frac{1}{\sqrt{N}}\sum_k e^{ikla}\psi_k, \tag{5.14}$$

where k belongs to the first Brillouin zone ($k = \frac{2m\pi}{Na}$, with $m = 0, 1, ..N-1$), (5.14) becomes:

$$\mathcal{H} = \sum_k \psi_k^\dagger \hat{H}(k)\psi_k, \text{ with } \hat{H}(k) = (\xi(k) + 2\alpha\sin(ka)\sigma_y)\tau_z + \Delta\tau_x + V_Z\sigma_x, \tag{5.15}$$

where $\xi(k) = 2t + \mu - 2t\cos(ka)$ Analogously to the continuum case, the quasiparticle spectrum is therefore given by (5.12), and the quasiparticle gap closes at $k = 0$ when $V_Z = \sqrt{\mu^2 + \Delta^2}$. It is important to note that, contrary to the continuum case, in the discrete case, the quasiparticle gap closes at $ka = \pi$ if $V_Z^2 = (4t - \mu)^2 + \Delta^2$, allowing for a topological transition. However, in the physically relevant regime where $t \gg \mu,\ b,\ \Delta$, the gap at $ka = \pi$ remains open. Hence we disregard this transition.

Since the Brillouin zone is now well-defined, we can now compute the $\mathbb{Z}_2$ pfaffian invariant $(-1)^\nu$ of $\hat{H}(k)$, which is defined as [165, 164]:

$$(-1)^\nu = \text{sgn}\{\text{pf}\left[\hat{H}(k=0)\sigma_y\tau_y\right]\text{pf}\left[\hat{H}(k=\pi/a)\sigma_y\tau_y\right]\}. \tag{5.16}$$

Note that the antisymmetry of $\hat{H}(k)\sigma_y\tau_y$ at the real momenta $ka = 0, \pi$, is guaranteed by the particle-hole symmetry. Straightforward algebra yields,

$$(-1)^\nu = \text{sgn}\{\left[\Delta^2 + \mu^2 - V_Z^2\right]\left[\Delta^2 + (4t-\mu)^2 - V_Z^2\right]\}. \tag{5.17}$$

The second term is always positive in the physically relevant regime, $t \gg \mu,\ b,\ \Delta$. Consequently, we obtain:

$$(-1)^\nu = \begin{cases} 1, & \text{if } V_Z < \sqrt{\mu^2 + \Delta^2}, \\ -1, & \text{if } V_Z > \sqrt{\mu^2 + \Delta^2}, \end{cases} \tag{5.18}$$

and the gap closing at $V_Z = \sqrt{\mu^2 + \Delta^2}$ is indeed a topological transition from a topologically trivial phase when $V_Z < \sqrt{\mu^2 + \Delta^2}$ to a non-trivial phase when $V_Z > \sqrt{\mu^2 + \Delta^2}$ supporting MZMs. The corresponding phase diagram is depicted in Fig. 5.4. As we will show in the next subsection, in the non-trivial phase, the nanowire supports a single pair of MZMs localized at its end.

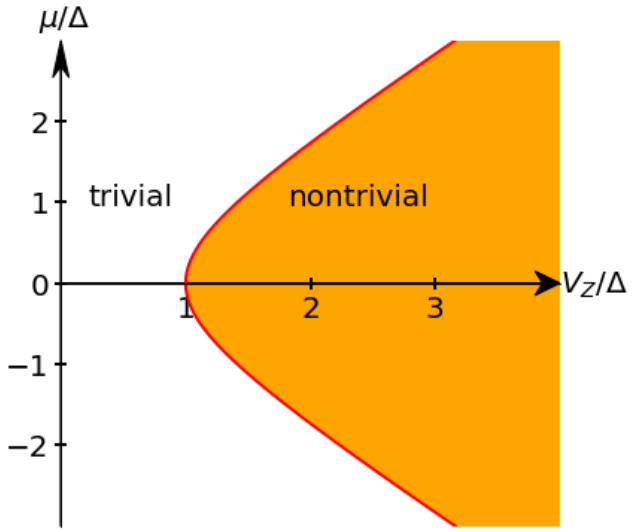

Figure 5.4: Topological phase diagram of the Oreg-Lutchyn model given by (5.1) as a function of the Zeeman energy V_Z and chemical potential μ. The nanowire is in a trivial phase for weak Zeeman energy $V_Z < \sqrt{\mu^2 + \Delta^2}$ (white region) and enters a nontrivial phase for strong Zeeman energy $V_Z > \sqrt{\mu^2 + \Delta^2}$ (orange region). The system is gapless at the topological transition $V_Z = \sqrt{\mu^2 + \Delta^2}$ (indicated by the red solid line).

5.1.5 Properties of the Majorana zero modes

Let us now show how MZMs emerge in finite-size superconducting Rashba nanowires. To that end, we numerically diagonalize the BdG Hamiltonian $\hat{H}$ given by (5.14). The results are presented in Fig. 5.5. As it can be observed, when V_Z crosses $\sqrt{\mu^2 + \Delta^2}$ the quasiparticle gap closes and reopens, and a single pair of particle-hole conjugated eigenstates ϕ_+ and $\phi_- = C\phi_+$ sticks to zero energy. This pair corresponds to a single fermionic operator $a_0 = \sum_j \phi_+^\dagger(j)\psi(j)$ that annihilates a zero-energy *bogoliubon* in the state ϕ_+. Notice that ϕ_+ is non-zero at both sides of the wire, as observed in Fig. 5.5 (d). Therefore, a_0 is a nonlocal operator delocalized on both sides of the nanowire. As already mentioned, any zero-energy fermionic bound-state can eb decomposed into a pair of Majorana modes $\gamma_A = (a_0 + a_0^\dagger)/\sqrt{2}$ and $\gamma_B = -i(a_0 - a_0^\dagger)/\sqrt{2}$. The Majorana wavefunctions describing these Majorana operators reads $\phi_A = (\phi_+ + \phi_-)/\sqrt{2}$ and $\phi_B = -i(\phi_+ - \phi_-)/\sqrt{2}$, and are also zero-energy eigenstates of $\hat{H}$. As it can be observed in Fig. 5.5 (g), ϕ_A is localized at one end of the nanowire while ϕ_B is localized at the opposite end. Consequently, as expected from the bulk-edge correspondence, the nonlocal quasiparticle a_0 is a Majorana bound-state (MBS) which corresponds to the superposition of two unpaired MZMs.

Nevertheless, the above statement is strictly valid for infinitely long wire, *i.e.*, when $L/\xi_M \gg 1$, with ξ_M the typical localization length of the MZMs ϕ_A and ϕ_B. Indeed, the Majorana wavefunctions decay exponentially towards the bulk with fast oscillations, $\phi_{A/B}(j) \propto e^{-x/\xi_M} e^{\pm I k_M x}$, where $x = ja$. Therefore, when the length of the nanowire is comparable to the localization of the MZMs, $L \geq \xi_M$, the Majorana wavefunctions ϕ_A and ϕ_B are partially overlapping (see Fig. 5.5 (b), (e), (g) and (c), (f), (i)) and hybridize. As a consequence, the Majorana wavefunctions are no longer exact eigenstates of the BdG Hamiltonian, and the non-local MBS

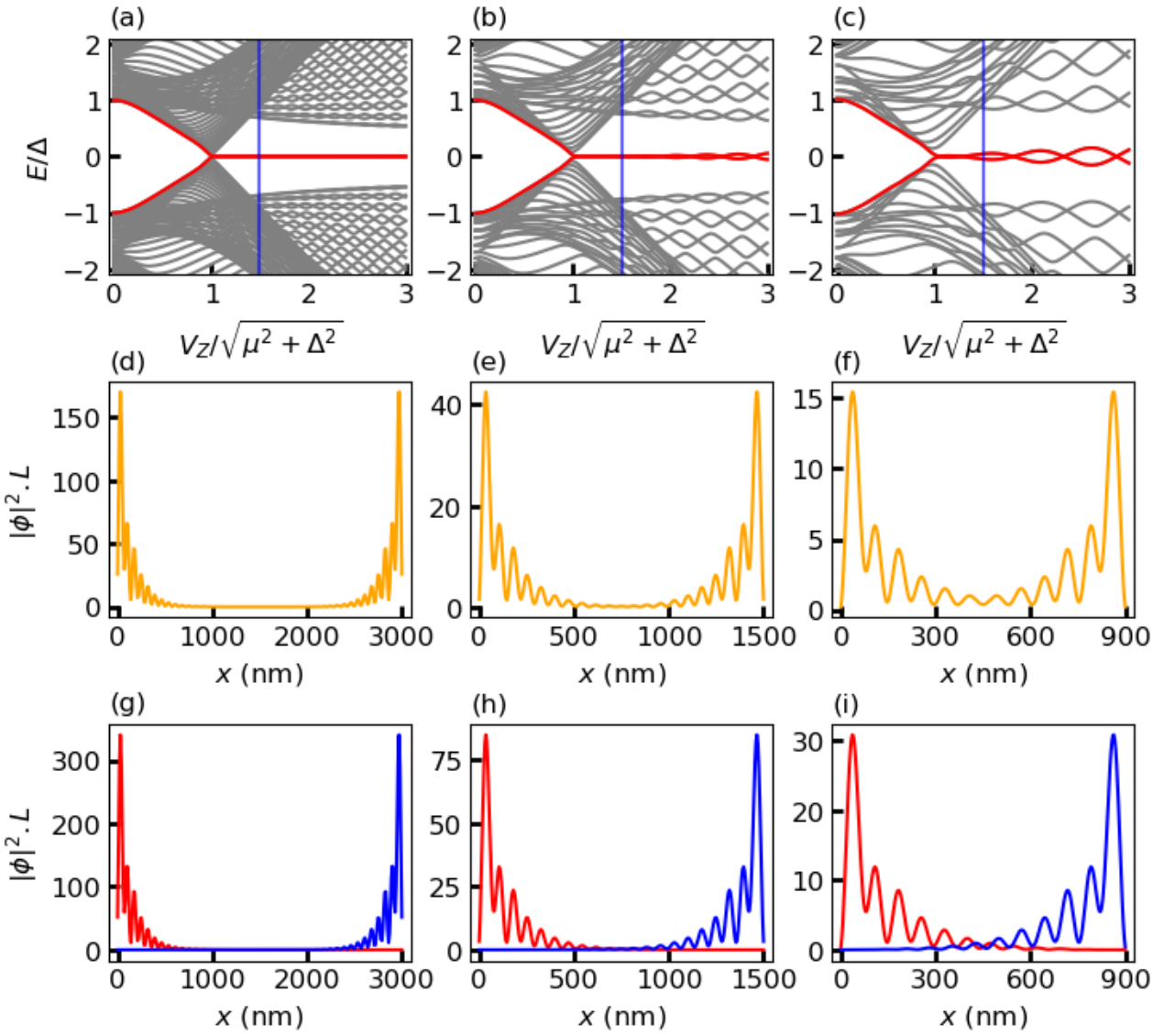

Figure 5.5: Majorana bound-states in hybrid semiconductor/superconductor nanowires. (a): Quasiparticle spectrum of a finite-size nanowire described by the Oreg-Lutchyn model (5.1) as a function of the Zeeman energy V_Z. The length of the nanowire is $L = 3000$ nm. (d): Majorana bound-state wavefunction weight $|\phi(x)|^2.L$ as a function of the position x for $V_Z = 1.5\sqrt{\mu^2+\Delta^2}$. (g): Weights of the wavefunction of the left (red solid line) and right (blue solid line) Majorana zero-mode as a function of the position x. (b), (e), (h): Same as (a), (d), (g) for $L = 1500$ nm. (c), (f), (i): Same as (a), (d), (g) for $L = 900$ nm.

a_0 acquire a finite energy E_M, approximately given by:

$$E_M = \frac{\hbar^2 k_F}{m\xi_M} |\cos(k_M L)| e^{\xi_M/L}. \tag{5.19}$$

Because k_M depends on V_Z and μ, the energy splitting $2E_M$ oscillates as a function of V_Z, as can be observed

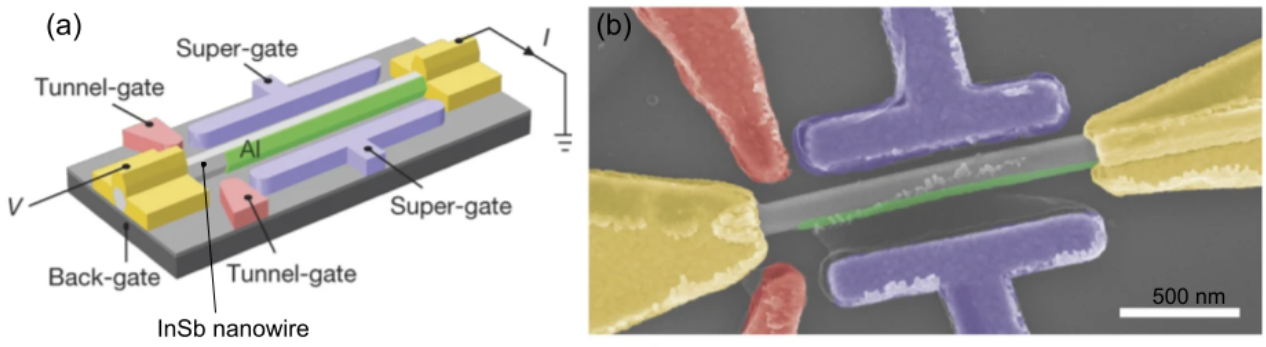

Figure 5.6: Realistic superconducting Rashba nanowires. (a) Schematic illustration of a superconducting Rashba nanowire device. An InSb nanowire (light grey) is partially coated with a thin shell of superconducting Al (green). The tunnel gates (red) are used to induce a tunnel barrier in the non-coated segment. A voltage bias is applied across the tunnel junction thanks to the left electrical contact (yellow). The right electrical contact is used as a current drain. (b) False-color STM image of a typical fabricated device. Figures extracted and adapted from [166]

in Fig. 5.5 (c) and (d).

5.2 Experimental signatures of MZMs

5.2.1 A brief overview

A first indication of the presence of MZMs is the measurement of a zero-bias peak (ZBP) in the differential conductance. Indeed, as we have already shown, at low temperatures and in the customary tunneling regime, the differential conductance is given by:

$$G(V) = \frac{\mathrm{d}I}{\mathrm{d}V} \propto \rho(\omega), \tag{5.20}$$

with I the dc current flowing through the system, V the applied bias, and ρ the electronic DOS of the analyzed sample.

Soon after the theoretical proposition of Oreg and Lutchyn, ZBP has been observed in InAs and InSb nanowires partially coated with the conventional superconductor Al subjected to a magnetic field, represented in Fig. 5.6 [162, 167, 168]. Nanowires fully coated with Al have also been realized. In that case, the topological phase emerges because of orbital effects. More recently, a new generation of nanowires has been fabricated where the nanowire is partially coated with superconducting Al and ferromagnetic EuS. In these set-ups, the presence of an external magnetic field is no longer necessary.

Even if the nanowire platform is currently the most mature and promising MZMs platform, numerous alternative platforms have been proposed and realized during the last decade. An exhaustive list of these platforms is beyond the scope of this manuscript. Instead, we focus on two promising examples: phase-controlled 2D Josephson junctions (see Fig. 5.7) and 1D chains of magnetic ad-atoms on top of s-wave superconducting substrate (see Fig. 5.8).

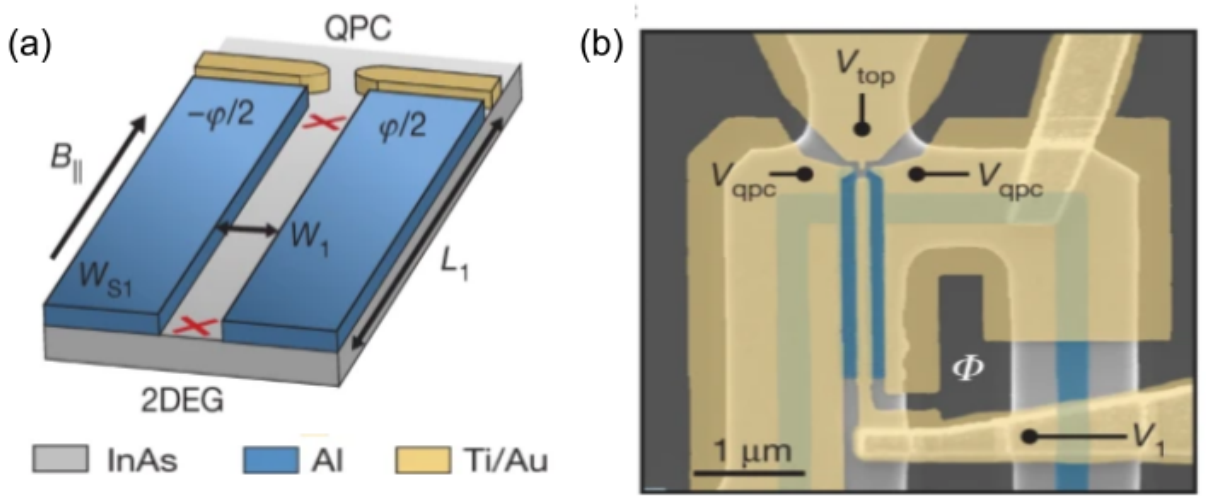

Figure 5.7: Planar Josephson junctions exhibiting MZMs. (a) Schematic illustration of a Planar Josephson junction made of two epitaxial superconducting Al layers on top of a InAs 2D electron gas (2DEG) exhibiting SOC. The 1D channel, defined in between the two superconducting leads, can be tuned into a topologically non-trivial phase with MZMs (red crosses) by tuning the chemical potential, the parallel magnetic field $B_{||}$ and the phase difference φ. The MZMs can be probed by tunneling spectroscopy using a QPC located at one end of the device. (b) False-colour STM image of the top part of a typical device. Figures extracted from [169]

Planar Josephson junctions have been recently fabricated, and ZBPs have been measured at the edge of the junction suggesting the existence of MZMs [169, 170]. Because of the additional control parameter offered by the superconducting phase-bias planar, Josephson junctions seem a promising alternative platform exhibiting MZMs.

In 1D chains of magnetic atoms deposited on s-wave superconductors, the YSR states generated by each atom hybridize and form a Shiba band inside the superconducting gap [9], which can be gapped. It has been theoretically proposed that topological superconductivity can be induced in ferromagnetic chains, in the presence of spin-orbit coupling [12, 100, 101, 102], or in helical ordered chains [105, 171, 103, 104, 106, 172, 107]. Recently, scanning tunneling spectroscopy on self-assembled or artificially constructed chains of magnetic atoms on top of s-wave superconductors revealed the existence of ZBP spatially localized at the edge of these chains, suggesting the presence of MZMs [20, 173, 174, 175].

Nevertheless, the presence of ZBP is not sufficient to claim the existence of MZMs in a system since any zero-energy quasiparticle will also produce a ZBP. Hence, to confirm the existence of MZMs in a system, additional experimental pieces of evidence have to be observed.

A first experimental signature of MZM is the quantization of the conductance peak at zero bias. Indeed, in the presence of a MZM, the zero-bias conductance is quantized such that $G(V = 0) = (2e^2)/\hbar$ [176, 177, 178, 179, 180, 181]. Quantized zero-bias peaks have been observed in nanowires. However, because of the lack of reproducibility, these measurements can not be interpreted as unambiguous proofs of MZMs [182, 183, 184]. Moreover, a quantized zero-bias peak is a necessary but not sufficient condition for the existence of MZMs, and several other mechanisms can produce a nearly quantized zero-bias peak, such as trivial zero-energy bound-states due to disorder or inhomogeneities [185, 186, 187]. Note that conductance tomography has also been

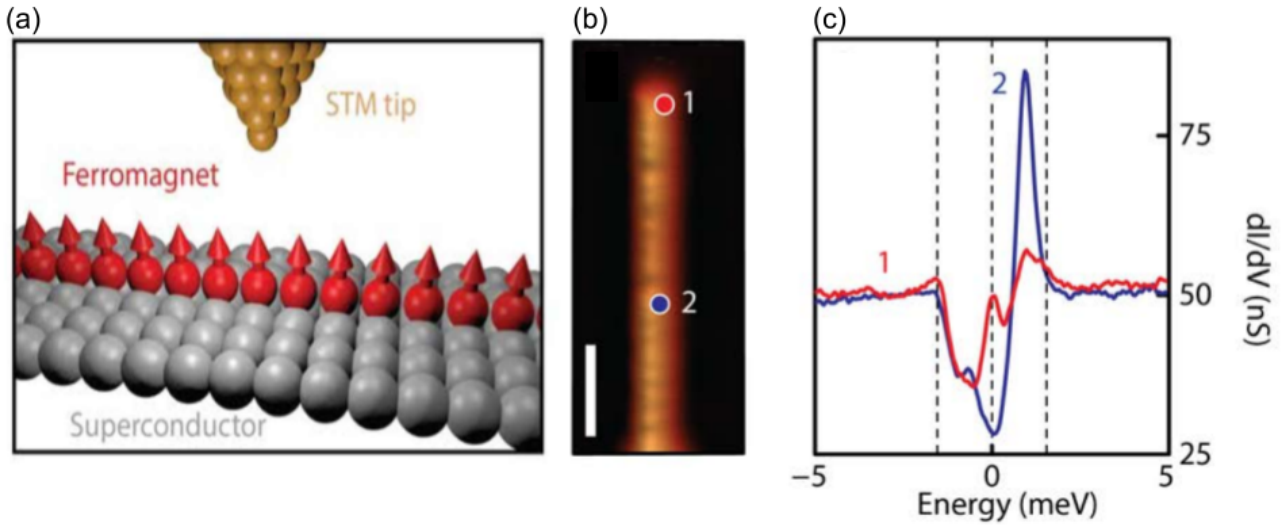

Figure 5.8: MZMs signature in 1D chains of magnetic atoms deposited on conventional superconductors. (a) Schematic picture of the ferromagnetic chain of magnetic atoms placed on top of a conventional superconductor exhibiting SOC. The system is probed by a STM tip. (b) STM image of the ferromagnetic chain. (c) Differential conductance spectra. The red solid line corresponds to differential conductance measured on top of position 1, indicated on (b), while the blue solid line corresponds to position 2. The red solid line exhibits a zero-bias peak, interpreted as a sign of a MZM localized at the end of the chain. Figures extracted from [20].

proposed as a signature of MZMs since the conductance exhibits a quantized plateau in the case of MZMs while spatial dependence is expected for trivial bound-states [181]. However, numerical simulations have shown that the oscillations of the Majorana wavefunctions ultimately spoil the conductance plateau and that a strong tunneling regime is required to recover a distinctive saturation plateau in the differential conductance near a MZM [188].

Another experimental signature of MZMs is the so-called fractional Josephson effect. A Josephson junction is a hybrid structure made of two superconducting regions separated by a thin non-superconducting region (insulating, metallic, ferromagnetic,...). Let us focus on the case of an insulating central region. In the presence of a superconducting phase difference, φ, between the two superconductors, a charge current flows through the junction without voltage bias [42, 189, 190]. This phenomenon is known as the DC Josephson effect (see [42, 191] for a review of the Josephson effect). For a trivial Josephson junction, *i.e.*, between two trivial superconductors, the Josephson current $I(\varphi)$ is carried by Cooper pairs (charge $2e$) and is described by the Josephson equations,

$$I(\varphi) = I_c \sin(\varphi), \tag{5.21}$$

with I_c the so-called critical current. Therefore, the Josephson current is a 2π-periodic function of φ. On the contrary, in a topological Josephson junction, *i.e.*, between two non-trivial topological superconductors, the Josephson current is carried by the MZMs localized at the junction. Consequently, the current-phase relation, $I(\varphi)$, is no longer 2π-periodic but 4π-periodic[16, 192]. The doubling of the current-phase periodicity can be understood as an effect of fractionalization since MZMs can be interpreted as *half* a fermionic degree of free-

dom. The 4π-periodic Josephson effect has been observed in Josephson junctions between $\mathrm{InAs/Al}$ [193] and $\mathrm{InSb/Nb}$ [194] hybrid nanowires. Nevertheless, the 4π-periodic effect is not sufficient to claim the existence of MZMs. Indeed, in a realistic set-up, the 4π-periodicity is hard to achieve because Coulomb energy, finite-size effects, or quasiparticle poisoning can restore the 2π-periodic effect [195, 196, 197, 198, 199]. Therefore, in order to observe the fractional Josephson effect, the current-phase relation should be performed by sweeping the phase bias φ on time scales shorter than the quasiparticle poisoning time. However, sweeping the phase rapidly can drive the junction out of equilibrium. In this case, Landau-Zener transitions into higher energy levels can produce the 4π-periodicity even in absence of MZMs [198, 196, 200].

Many experiments focusing on zero-bias conductance peak and Josephson effects are consistent with the existence of MZMs from topological origin. These signatures have been observed in a variety of experimental platforms, including nanowires-based set-ups, planar Josephson junctions, and magnetic chains, to list a few. Despite the significant advances made in the fabrication techniques and the improved quality of the heterostructures studied, definitive proof of the existence of MZMs remains elusive. Indeed, so far, the observed experimental signatures can have alternative origins to MZMs. In particular, trivial zero-energy bound-states can be induced in the trivial phase by magnetic impurities, disorder, partial proximitization, or smooth potential. As we explain below, a smooth cross-over exists between topologically trivial zero-energy bound-state and topological MZMs. Therefore, there exist trivial zero-energy bound-states with an almost perfect Majorana character mimicking most of the experimental signatures of MZMs.

5.2.2 The challenging distinction between trivial bound-states and MBS

In the literature, the discussion of the experimental pieces of evidence for MZMs often opposes the term *true* MBS, used to designate pair of MZMs induced by non-trivial bulk topology, to *false* MBS or *trivial* bound-states, designating any kind of zero-energy bound-states induced in a superconductor with trivial bulk-topology. Hence the term *Majorana* is nowadays often incorrectly used as a synonym of non-trivial bulk topology. Actually, a Majorana zero mode is defined as any spatially isolated self-conjugate zero-energy eigenmode, and a MBS is nothing but a pair of MZMs. These two definitions are not at all related to the topological properties of the underlying bulk system. Consequently, unambiguous proof of the existence of MBS (or MZMs) does not constitute unambiguous proof of non-trivial bulk topology and vice-versa. Indeed, the MZMs localized at the extremities of 1D topological superconductors have a finite overlap scaling as e^{-L/ξ_M}, with L the length of the system and ξ_M the localization length of the Majorana modes. Therefore, as already mentioned, the zero-energy edge modes of topological origin do correspond to MZMs only when the system is sufficiently large, $L \gg \xi_M$. Otherwise, the edge modes have a finite overlap and do not exhibit the desired properties of Majorana qubits.

Moreover, even if the bulk-edge correspondence guaranteed the existence of MZMs in large topological superconductors, it is not impossible to find MZMs in trivial superconductors. Indeed, as already pointed out, regardless of its origin, any zero-energy fermionic bound-state a_0 can be formally decomposed into a pair of Majorana modes γ_A and γ_B

$$a_0 = \frac{\gamma_A + i\gamma_B}{\sqrt{2}}. \tag{5.22}$$

The wavefunctions ϕ_A and ϕ_B describing the operator γ_A and γ_B, respectively are named the Majorana components of the bound-state. If the underlying bulk system is topologically trivial, the operators γ_A and γ_B have

no *a priori* reasons for being spatially separated. Hence, the zero-energy bound-state is not necessarily a perfect MBS formed by unpaired MZMs. The overlap of the Majorana components of a zero-energy bound-state depends on the underlying mechanism at its origin. Consequently, it is necessary to understand the formation and properties of zero-energy superconducting sub-gap states.

Focusing on semiconductor/superconductor hybrid nanowires, this includes conventional Andreev bound-states (ABS) appearing at normal-superconducting (NS) interface or in superconducting-normal-superconducting (SNS) junctions, zero-energy states induced by localized impurities such as Yu-Shiba Rusinov (YSR) bound-states or zero-energy states induced by smooth confining potential, smooth inhomogeneities or smooth NS and SNS junctions, to list a few (see [186] for a recent and comprehensive review of the topic).

In general, zero-energy ABS and impurity bound-states possess highly overlapping Majorana components. On the contrary, zero-energy bound-states appearing in smoothly confined nanowires, or smooth NS and SNS junctions, exhibits partially separated Majorana components [187, 186]. That is why they are named quasi-Majorana states (QMS), partially-separated Majorana bound states (ps-MBS), or trivial Majorana-bound states (trivial MBS), depending on the context. In fact, the mechanism at the origin of all these states is the same. Hence, in this manuscript, we will indifferently name them quasi-Majorana states (QMS). The overlap of the Majorana modes forming a QMS can be highly suppressed for sufficiently smooth potentials. In this case, the QMS corresponds to a MBS, and exhibits a full Majorana[187] character despite its trivial origin. In consequence, in non-uniform nanowires, a continuous crossover exists between MBS and QMS.

Lastly, we stress that the desired properties of perfect MBS (made of unpaired MZMs), like immunity to local noise, and non-Abelian braiding, are rooted in their non-local nature and require an exponentially suppressed Majorana overlap. In addition, some properties, like parametric non-Abelian braiding [187], only require the Majorana modes to be partially separated. Hence QMS might be good enough for such kinds of applications. Therefore, the absence of Majorana overlap seems to be the most relevant criterion for selecting zero-energy bound-states that are good candidates for quantum computation. On the contrary, non-trivial bulk topology does not guarantee the existence of truly unpaired MZMs.

In conclusion, since zero-energy states mimicking Majorana properties are ubiquitous in real nanowire-based devices, the reported signatures of MZMs should be interpreted with caution, and experimental protocols providing a clearer distinction between truly unpaired MZMs and partially overlapping ones are highly desirable. It is important to stress that unpaired MZMs does not necessarily have a topological origin and that edge-states of topological origin does not necessarily corresponds to true unpaired MZMs because of finite-size effects. Hence, the identification of MBS and non-trivial bulk topology are two disconnected problems, and a non-ambiguous proof of the bulk topology requires the use of non-local probes. In this respect, multi-terminal conductance measurements seem a promising route [201, 202, 203].

5.3 Fano factor tomography of *trivial* zero-energy states and MZMs

Definitive unambiguous proof of the existence of perfectly isolated MZMs in solid-state platforms, therefore, requires experimental protocols able to distinguish truly unpaired MZMs from overlapping ones is highly desirable. In this respect, numerous protocols have been studied. For example, it has been proposed to use conductance tomography since the zero-bias conductance peak associated with a perfectly isolated MZM is quantized and does not depend on the position of the tip. Nevertheless, the quantized plateau is ultimately spoiled by the oscillations of the Majorana wavefunctions in spin-orbit coupled nanowires [188]. Moreover,

a strong tunneling regime is necessary to observe a distinctive conductance saturation plateau in the proximity of a MZM [188]. Other theoretical predictions proposed to use non-trivial spin signatures of MZM [204, 205, 206, 207, 208, 209] and spin-selective Andreev reflection [210, 211] as distinctive tools. Based on those propositions, Jeon *et al.* used spin-polarized STS to identify MZM in self-assembled Fe chains on the surface of Pb [212]. However, discerning some local excess of polarization over a magnetic background remains a difficult task. Other theoretical studies proposed to use current shot-noise [177, 213, 214, 215], spin-resolved shot-noise measurements [205, 216], finite-frequency current shot-noise [31], or time-resolved transport spectroscopy [217] to identify *unpaired* MZMs. All the above-mentioned protocols require more involved setups than the usual local spectroscopic probes used in the lab. Here we show the current shot-noise spatial tomography with a metallic tip, nowadays realized within scanning tunneling microscopy (STM) [21, 22, 33], can distinguish *unpaired* MZMs from other zero-energy bound-states. More precisely, we prove below that in the vicinity of a perfectly isolated MZM, the Fano factor is spatially constant and equals one, the Poissonian limit. This result is a consequence of the local particle-hole symmetry of the Majorana wave function. However, for *trivial* zero-energy bound states, like YSR or ABS, the overlap of the Majorana wavefunctions breaks the local particle-hole symmetry of the wavefunction and implies a strongly spatially dependent Fano factor. Even for the case of QMS, we shall show that the Fano factor oscillates above 1 in the superconducting part of the wire. Even if our proposal is not able to determine whether MZMs have a topological origin [186], the spatially unity Fano factor is a clear distinguishing signature of the Majorana wave function.

5.3.1 System and model

Here we focus on the most typical MZM platform, the Rashba nanowire set-up. The typical system we consider consists of a semiconducting nanowire deposited on top of a *conventional* s-wave BCS superconductor in the presence of spin-orbit coupling (SOC) and a magnetic field applied along the nanowire axis (see Fig. 5.9). As shown above, for strong Zeeman energies, $V_Z > \sqrt{\mu^2 + \Delta^2}$, the system enters into a topologically nontrivial phase supporting a MBS corresponding to unpaired MZMs. We compare the shot-noise tomography of such MBS to three different types of zero-energy bound-state, used as reference cases. First, we study a zero-energy Yu-Shiba-Rusinov (YSR) state induced by a magnetic impurity located at one end of the wire. Second, we assume that the proximity-induced gap Δ is not uniform and vanishes in a small portion of the nanowire located at one of its extremities. This situation might happen if the extremity of the nanowire is in contact with a normal substrate or if the nanowire is not coated with a superconductor on its entire length. In that case, a normal-superconducting interface is present in the nanowire, and an Andreev bound-state (ABS), localized in the normal region, can be induced. Lastly, in this situation, if an additional smooth potential barrier is present at the interface, a quasi-Majorana bound-state (QMS) can be induced at the interface. All these situations are conveniently described by the tight-binding BdG Hamiltonian $\mathcal{H}_S$, given by,

$$\begin{aligned}\mathcal{H}_S =& \frac{1}{2}\sum_{l=0}^{N-1} \psi^\dagger_{l,S}[(2w - \mu + V(l))\tau_z + \Delta(l)\tau_x + V_Z\sigma_x]\psi_{l,S} \\ &+ \frac{1}{2}\sum_{l=0}^{N-2} \psi^\dagger_{l+1,S}[-w\tau_z - i\alpha\sigma_y\tau_z]\psi_{l,S} + \text{(h.c.)} \\ &- \frac{1}{2}\psi^\dagger_{0,S} J\sigma_z\psi_{0,S},\end{aligned} \tag{5.23}$$

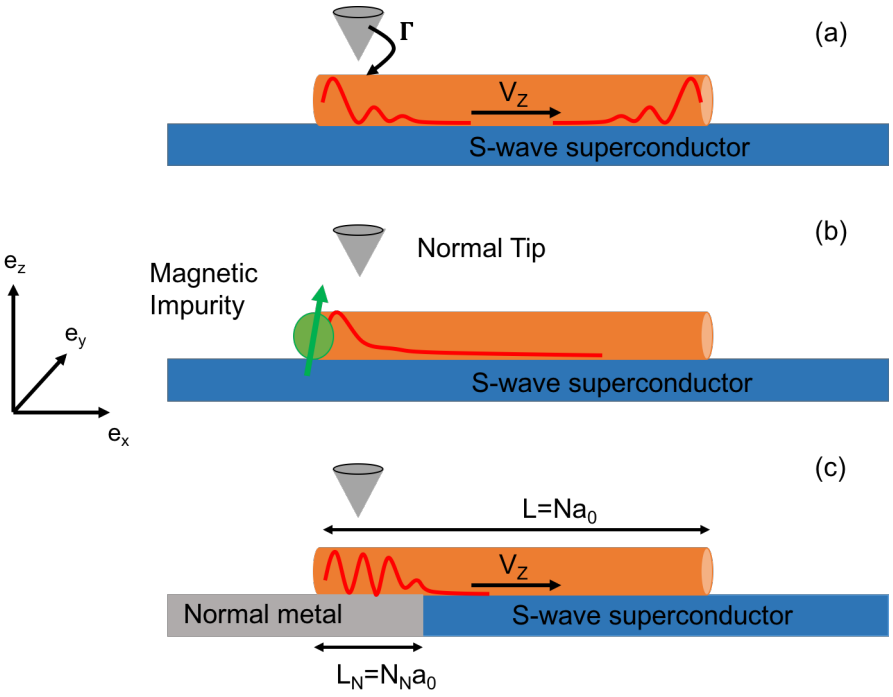

Figure 5.9: Schematic representation of the typical experimental setup considered here. (a): A semiconducting nanowire placed on top of an s-wave superconductor, subject to an external Zeeman field V_Z along the wire $\boldsymbol{e}_x$ axis. This system can host a pair of MZMs localized at its ends, as indicated by the red solid lines. (b): A semiconducting nanowire terminated by a magnetic impurity on top of an s-wave superconductor. This system hosts a YSR bound-state at its left end (red solid line). (c): Same as in (a), except that the left end of the nanowire is in contact with a normal substrate. In that case, the system can host an ABS (red solid lines). In each case, the fermionic bound-state is probed by a metallic tip via the tunneling effect of strength Γ.

with $N = L/a$ the number of sites in the nanowire, L the physical length of the nanowire, and a the lattice constant of the tight-binding model. We defined the Nambu spinor $\psi_{l,S} = \left[c_{\uparrow,l}, c_{\downarrow,l}, c^\dagger_{\downarrow,l}, -c^\dagger_{\uparrow,l}\right]^T$, where the operator $c_{\sigma,l}$ annihilates an electron of spin σ at site l of the nanowire. $\Delta(l) = \Theta(l + 1 - N_N)$ is the pairing potential induced by the superconducting substrate, with Θ the Heaviside step function and $N_N a$ the size of the normal region in the nanowire. $V(l) = V_0 \exp\left(\dfrac{(l - N_N)^2}{2s^2}\right)$ is a smooth Gaussian potential barrier centered at the NS interface. μ denotes the chemical potential of the nanowire and w the nearest-neighbor hopping. $V_Z = g\mu_B B$, with g the gyromagnetic factor, is the Zeeman energy induced by a magnetic field $\boldsymbol{B} = B\boldsymbol{e}_x$ applied along the nanowire axis. J is the exchange coupling induced by a magnetic impurity with spin $\boldsymbol{S}_{imp} = S_{imp}\boldsymbol{e_z}$ localized at the left end of the nanowire. Finally, σ_i and τ_i are Pauli matrices acting in the spin and particle-hole space, respectively. This model is rather general. However, we focus on six different physically relevant cases listed in Table. 5.1. In all cases, we consider a finite SOC, $\alpha > 0$.

First, we focus on cases where the nanowire is entirely superconducting, $N_N = 0$. In this case, when $J = 0$ and $V(l) = 0$, the model is equivalent to the Oreg-Lutchyn model (5.14). Therefore it undergoes a topological transition at $V_Z = \sqrt{\mu^2 + \Delta^2}$ from a trivial phase when $V_Z < \sqrt{\mu^2 + \Delta^2}$ to a topological phase

	Case	μ	w	Δ	V_Z	α	J	N	N_N	V_0	s	Δ_{eff}
a	MBS 1	0.5	10	1	2	1.2	0	80	0	0	X	0.63
b	YSR	0.5	10	0.6	0	1.2	11.23	80	0	0	X	0.6
c	MBS 2	0.5	10	1	1.4	2	0	100	20	0	X	0.31
d	ABS	0.5	10	1	0.38	2	0	100	20	0	X	0.27
e	MBS 3	1	10	2	3.2	3	0	100	20	4.5	5	0.27
f	QMS	3	10	1	2.75	3	0	100	20	4.5	5	0.27

Table 5.1: Table summarizing 6 different parameter sets of experimentally relevant situations. Δ_{eff} is the effective gap separating the zero-energy bound-state from other states.

for $V_Z < \sqrt{\mu^2 + \Delta^2}$ (see Fig. 5.4). In the topological phase, the nanowire exhibits MZMs localized at its ends. The superposition of these unpaired MZMs forms a perfect MBS. As a reference case, we compare this case to a trivial zero-energy YSR bound-state localized at the left end of the wire. This state appears in the trivial regime $V_Z < \sqrt{\mu^2 + \Delta^2}$ when $J > 0$ appears because of the exchange coupling with the impurity (case *b*).

Second, we consider a partially proximitized nanowire, $N_N > 0$. In that case, the left part of the wire is in the normal state. In the topological regime, $V_Z > \sqrt{\mu^2 + \Delta^2}$, because they are topologically protected, MZMs are still present on each side of the wire (case *c*). On the contrary, in the trivial regime, $V_Z < \sqrt{\mu^2 + \Delta^2}$, the presence of the NS interface induces a trivial ABS. This ABS is localized in the normal region and has zero energy because of fine-tuning of the parameters (case *d*).

Finally, we consider the effect of a smooth potential barrier, $V_0 > 0$, at the NS interface. Again, in the topological phase, $V_Z > \sqrt{\mu^2 + \Delta^2}$, the MZMs can not be removed by local perturbation. hence, a pair of MZMs remains localized at each side of the wire (case *e*). In the trivial regime, $V_Z < \sqrt{\mu^2 + \Delta^2}$, the smooth potential partially separate the Majorana modes forming the ABS state which becomes a zero-energy QMS (case *f*) [187, 186].

In all cases mentioned above, a zero-energy bound-state does appear in the system. This state is well-separated from the higher energy states by an energy gap Δ_{eff}. This can be observed in the insets of Fig. 5.11, where we plotted the LDOS at the left side of the wire as a function of energy. In addition, we explicitly check that cases *a*, *b*, and *c* do correspond to perfect MBS with negligible Majorana overlap. To that end, we numerically computed the eigenstates of the BdG Hamiltonian describing the system in each case of Table. 5.1. In each case, the zero-energy bound-state a_0 can be decomposed into two Majorana modes $\gamma_A = \dfrac{a_0 + a_0^\dagger}{\sqrt{2}}$ and $\gamma_B = -i\dfrac{a_0 - a_0^\dagger}{\sqrt{2}}$ described by the wavefunctions ϕ_A and ϕ_B respectively. The obtained Majorana wavefunctions are presented in Fig. 5.10. As it can be observed in Figs. 5.10 (a), (c), and (d), all the MBS considered indeed correspond to truly unpaired MZMs. On the contrary, the YSR bound-state, case *b*, corresponds to a pair of perfectly overlapping Majorana eigenstates, as observed in Fig. 5.10 (b). Fig. 5.10 (e) shows that the ABS of case *d* is composed of two Majorana modes with almost perfect overlap. Lastly, the QMS of case *f* corresponds to two Majorana modes localized on each side of the smooth potential barrier, as observed in Fig. 5.10 (f). Nevertheless, the overlap of these Majorana modes is not exponentially suppressed with the nanowire length (since they are not localized at opposite sides), and a small overlap exists at the NS interface.

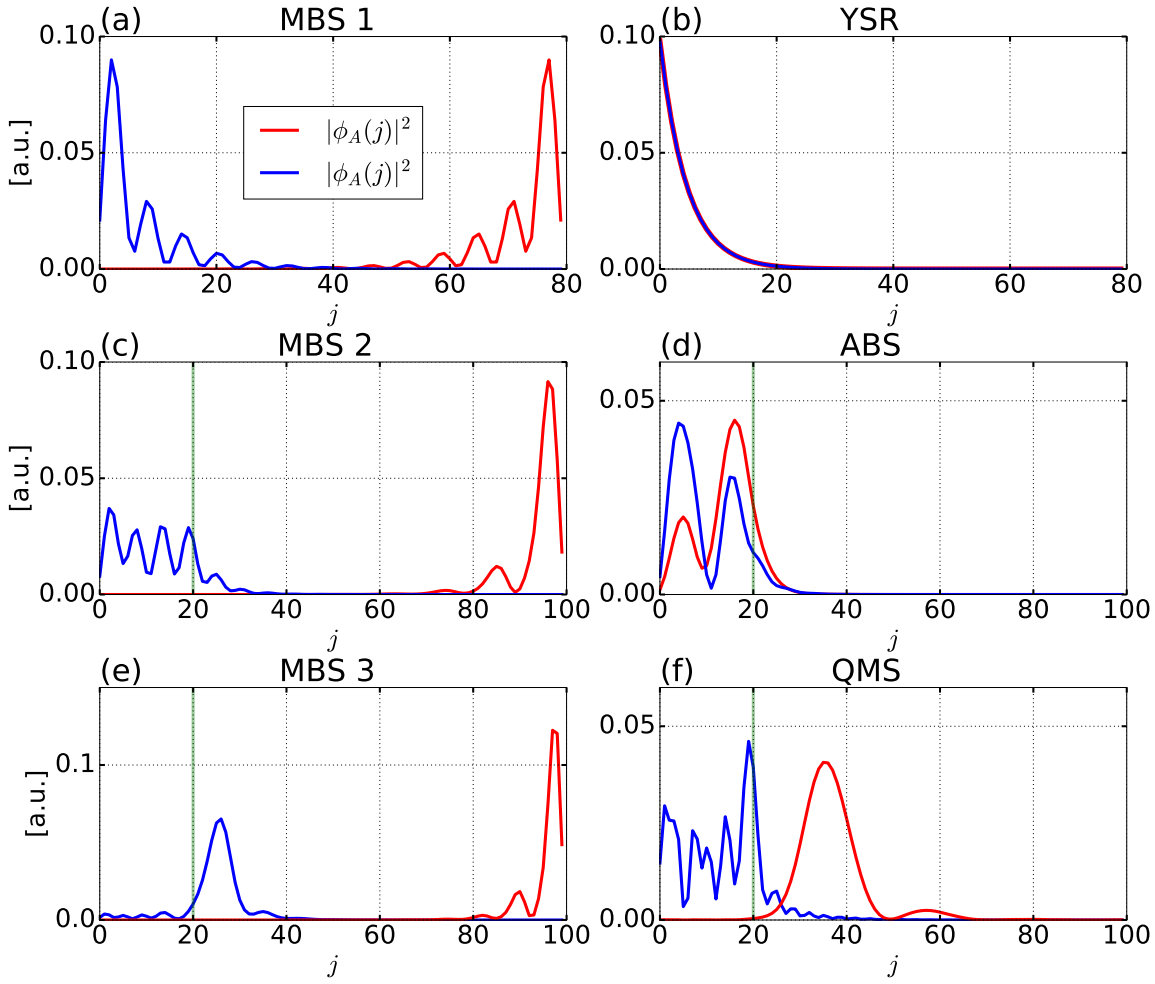

Figure 5.10: Majorana modes composing the six zero-energy fermionic bound-states of Table.5.1.(a)-(f) The square amplitude of the two Majorana modes associated with the zero-energy fermionic mode for case *a-f* of Table. 5.1.

5.3.2 Theoretical description of the shot-noise tomography experiment

To model the STS tomography, we proceed along the same line as in Section. 2.3, and define the complete Hamiltonian,

$$\mathcal{H} = \mathcal{H}_S + \mathcal{H}_T + t\psi^\dagger_{S,j}\tau_z\psi_T + (\text{h.c.}), \tag{5.24}$$

where $\mathcal{H}_S$, given by (5.23), describes the isolated sample, $\mathcal{H}_T$ describes the isolated metallic tip, and the last term describes the coupling between tip and sample. Here we introduced the Nambu spinor $\psi_T = [d_\uparrow, d_\downarrow, d^\dagger_\downarrow, -d^\dagger_\uparrow]^T$, with d_σ the operator annihilating an electron with spin σ at the apex of the tip. For the sake of simplicity, the tip-sample tunneling is assumed to be purely local. t is the tip-sample hopping amplitude, and j denotes the site of the wire coupled to the tip apex. Since we are considering a tomography experiment, j can be varied.

For simplicity, we assume that the metallic tip has a single conducting band. Therefore the Hamiltonian describing the isolated tip reads:

$$\mathcal{H}_T = \sum_{\boldsymbol{k}} \psi^\dagger_{T,\boldsymbol{k}} \left[\epsilon_T(\boldsymbol{k}) - \mu_T \tau_z\right] \psi_{T,\boldsymbol{k}}, \tag{5.25}$$

with $\epsilon_T(\boldsymbol{k})$ the energy dispersion characterizing the metallic tip and $\mu_T = \mu_S + eV$, the chemical potential of the tip, with $\mu_S = \mu$ the chemical potential of the sample. The chemical potential difference $\mu_T - \mu_S = eV$ takes into account the voltage bias across the junction.

The electronic current flowing through the STM junction is defined as $\hat{I}(j,\tau) = -e\dfrac{\mathrm{d}\hat{N}_T(\tau)}{\mathrm{d}\tau}$, with $\hat{N}_T(\tau)$ the particle number operator of the tip at time τ, evolving in the Heisenberg picture. Using the equation of motion in the Heisenberg, we directly obtain:

$$\hat{I}(j,\tau) = \frac{iet}{\hbar}\{\psi^\dagger_T(\tau)\psi_{S,j}(\tau) - \psi^\dagger_{S,j}(\tau)\psi_T(\tau)\}. \tag{5.26}$$

The average current, $I(j,\tau)$, therefore reads:

$$I(j,\tau) = \langle \hat{I}(j,\tau)\rangle = \frac{iet}{2\hbar}\langle \psi^\dagger_T(\tau)\psi_{S,j}(\tau) - \psi^\dagger_{S,j}(\tau)\psi_T(\tau)\rangle, \tag{5.27}$$

where $\langle ...\rangle$ denotes the non-equilibrium average of operators evolving in the Heisenberg picture with respect to $\mathcal{H}$.

We recall that the current shot-noise $S(\tau)$ is defined as the zero-frequency limit of the time-symmetric current-current correlation, $C(\tau_1,\tau_2)$,

$$C(\tau_1,\tau_2) = \langle \delta\hat{I}(\tau_1)\delta\hat{I}(\tau_2) + \delta\hat{I}(\tau_2)\delta\hat{I}(\tau_1)\rangle, \tag{5.28}$$

$$S(\tau) = \int_{-\infty}^{\infty} \mathrm{d}\tau' C(\tau'+\tau,\tau), \tag{5.29}$$

where $\delta\hat{I}(\tau) \equiv \hat{I}(\tau) - \langle\hat{I}(\tau)\rangle$.

To compute the current and shot-noise, we use the Keldysh formalism and introduce the set of local contour-ordered Green's functions,

$$\hat{G}^c_{S,S}(z,z') = -\frac{i}{\hbar}\langle \mathcal{T}_c[\psi_{S,j}(z)\otimes\psi^\dagger_{S,j}(z')]\rangle, \tag{5.30}$$

$$\hat{G}^c_{S,T}(z,z') = -\frac{i}{\hbar}\langle \mathcal{T}_c[\psi_{S,j}(z)\otimes\psi^\dagger_{T}(z')]\rangle, \tag{5.31}$$

$$\hat{G}^c_{T,S}(z,z') = -\frac{i}{\hbar}\langle \mathcal{T}_c[\psi_{T}(z)\otimes\psi^\dagger_{S,j}(z')]\rangle, \tag{5.32}$$

$$\hat{G}^c_{T,T}(z,z') = -\frac{i}{\hbar}\langle \mathcal{T}_c[\psi_{T}(z)\otimes\psi^\dagger_{T}(z')]\rangle, \tag{5.33}$$

and the corresponding retarded, advanced, and lesser Green's functions. We stress that the above Green's functions are matrices 4×4 matrices acting in the particle-hole$\otimes$spin space. z and z' are time arguments lying on the Keldysh contour c (see Fig. 2.4) while τ and τ' time arguments lying on the real axis.

It is then straightforward to show that the average current $I(j,\tau)$ reads,

$$I(j,\tau) = \frac{et}{2}\left[G^{<}_{S,T}(\tau,\tau) - G^{<}_{T,S}(\tau,\tau)\right]. \tag{5.34}$$

Thanks to the Wick theorem and after straightforward algebra (see the Supplementary Materials in [34] for details), the shot-noise is given by:

$$\begin{aligned} S(\tau) =& \frac{e^2t^2}{2}\int \mathrm{d}\tau' \,\mathrm{Tr}\Big\{G^{<}_{T,T}(\tau,\tau+\tau')G^{>}_{S,S}(\tau+\tau',\tau) - G^{<}_{S,T}(\tau,\tau+\tau')G^{>}_{S,T}(\tau+\tau',\tau)\Big\} \\ &+ (S\leftrightarrow T) + (\tau \leftrightarrow \tau+\tau'). \end{aligned} \tag{5.35}$$

Focusing on the dc regime, the current and shot-noise are stationary, $I(j,\tau) = I(j)$, $S(j,\tau) = S(j)$ and all Green's functions depends only on the relative time difference $\tau - \tau'$. Hence, we can define their Fourier representation,

$$G^{\gamma}_{\alpha,\beta}(\omega) = \int \mathrm{d}\tau e^{\frac{i}{\hbar}\omega\tau} G^{\gamma}_{\alpha,\beta}(\tau-\tau'), \tag{5.36}$$

where $\gamma \in a, r, >, <$ denotes the type of Green's functions while $\alpha,\beta = S,T$ are the sub-system indices. After a straightforward Fourier transformation of equations (5.34) and (5.35), the current and shot-noise are therefore given by:

$$I(j,V) = \frac{et}{2\hbar}\int \frac{d\omega}{2\pi}\,\mathrm{Tr}\Big\{G^{<}_{S,T}(\omega) - G^{<}_{T,S}(\omega)\Big\}, \tag{5.37}$$

$$S(j,V) = \frac{e^2t^2}{\hbar}\int \frac{d\omega}{2\pi}\,\mathrm{Tr}\Big\{G^{<}_{T,T}(\omega)G^{>}_{S,S}(\omega) - G^{<}_{S,T}(\omega)G^{>}_{S,T}(\omega)\Big\} + (jS\leftrightarrow T). \tag{5.38}$$

Finally, we recall that the Fano factor $F(j,V)$ is defined by:

$$F(j,V) = \frac{S(j,V)}{2e|I(e,V)|}. \tag{5.39}$$

To compute the local Green's functions entering $S(j,V)$ and $I(j,V)$, we use a perturbative expansion with respect to the tip-sample coupling. Using the results of Section. 2.3, it is straightforward to show that $\hat{G}^{c}_{\alpha\beta}(z,z')$ obeys the following Dyson equations:

$$\hat{G}^{c}_{\alpha\beta}(z,z') = \delta_{\alpha\beta}\hat{g}^{c}_{\alpha}(z,z') + t\int_{c}\mathrm{d}z_1 \hat{g}_{\alpha\delta}(z,z_1)\tau_z\hat{G}^{c}_{\delta\beta}(z_1,z'),\ \text{with}\ \delta\neq\alpha, \tag{5.40}$$

where we defined the local unperturbed contour-ordered Green's functions describing the isolated tip and sample:

$$\hat{g}^{c}_{S}(z,z') = -\frac{i}{\hbar}\langle\mathcal{T}_c\left[\psi_{Sj}(z)\otimes\psi^{\dagger}_{Sj}(z')\right]\rangle_0, \tag{5.41}$$

$$\hat{g}^{c}_{T}(z,z') = -\frac{i}{\hbar}\langle\mathcal{T}_c\left[\psi_{T}(z)\otimes\psi^{\dagger}_{T}(z')\right]\rangle_0. \tag{5.42}$$

Here we used the notation $\langle ... \rangle_0$, which is defined in (2.34). Therefore, using Langreth's rules and after a straightforward Fourier transformation, we obtain the following set of equations on the real-time axis:

$$\hat{G}^{r/a}_{S,S}(\omega) = \hat{g}^{r/a}_{S}(\omega) + t^2 \hat{g}^{r/a}_{S}(\omega)\tau_z \hat{g}^{r/a}_{T}(\omega)\tau_z \hat{G}^{r/a}_{S,S}(\omega), \tag{5.43}$$

$$\begin{aligned}\hat{G}^{</>}_{S,S}(\omega) =& t^2 \hat{g}^{</>}_{S}(\omega)\tau_z \hat{g}^{a}_{T}(\omega)\tau_z \hat{G}^{a}_{S,S}(\omega) \\ &+ t^2 \hat{g}^{r}_{S}(\omega)\tau_z \hat{g}^{</>}_{T}(\omega)\tau_z \hat{G}^{a}_{jS,jS}(\omega) + t^2 \hat{g}^{r}_{S}(\omega)\tau_z \hat{g}^{r}_{T}(\omega)\tau_z \hat{G}^{</>}_{S,S}(\omega),\end{aligned} \tag{5.44}$$

$$\begin{aligned}\hat{G}^{</>}_{T,T}(\omega) =& \hat{g}^{</>}_{T}(\omega) + t^2 \hat{g}^{</>}_{T}(\omega)\tau_z \hat{G}^{a}_{S,S}(\omega)\tau_z \hat{g}^{a}_{T}(\omega) \\ &+ t^2 \hat{g}^{r}_{T}(\omega)\tau_z \hat{G}^{</>}_{S,S}(\omega)\tau_z \hat{g}^{a}_{T}(\omega) + t^2 \hat{g}^{r}_{T}(\omega)\tau_z \hat{G}^{r}_{S,S}(\omega)\tau_z \hat{g}^{</>}_{T}(\omega),\end{aligned} \tag{5.45}$$

$$\hat{G}^{</>}_{S,T}(\omega) = t\hat{G}^{</>}_{S,S}(\omega)\tau_z \hat{g}^{A}_{T}(\omega) + t\hat{G}^{R}_{S,S}(\omega)\tau_z \hat{g}^{</>}_{T}(\omega), \tag{5.46}$$

$$\hat{G}^{</>}_{T,S}(\omega) = t\hat{g}^{</>}_{T}(\omega)\tau_z \hat{G}^{A}_{S,S}(\omega) + t\hat{g}^{</>}_{T}(\omega)\tau_z \hat{G}^{A}_{S,S}(\omega). \tag{5.47}$$

Here we introduced the retarded, $\hat{g}^r_S(\tau,\tau')$, $\hat{g}^r_T(\tau,\tau')$, advanced $\hat{g}^a_S(\tau,\tau')$, $\hat{g}^a_T(\tau,\tau')$ lesser $\hat{g}^<_S(\tau,\tau')$, $\hat{g}^<_T(\tau,\tau')$ and greater $\hat{g}^>_S(\tau,\tau')$, $\hat{g}^>_T(\tau,\tau')$ unperturbed Green's functions describing the isolated sample and tip respectively. In the absence of the tip-sample coupling, the sub-systems are decoupled and at equilibrium at their respective chemical potential. Hence, the unperturbed Green's functions obey the fluctuation-dissipation theorem:

$$g^<_S(\omega) = f(\omega)\left[g^a_S(\omega) - g^r_S(\omega)\right], \tag{5.48}$$

$$g^>_S(\omega) = (f(\omega)-1)\left[g^a_S(\omega) - g^r_S(\omega)\right], \tag{5.49}$$

$$g^<_T(\omega) = \left[g^a_T(\omega) - g^r_T(\omega)\right].\hat{f}_T(\omega, eV), \tag{5.50}$$

$$g^>_T(\omega) = \left[g^a_T(\omega) - g^r_T(\omega)\right].\left[\hat{f}_T(\omega, eV) - \mathbb{1}\right], \tag{5.51}$$

$$\text{with } \hat{f}_T(\omega, eV) = f(\omega - eV)\frac{\tau_0 + \tau_z}{2} + f(\omega + eV)\frac{\tau_0 - \tau_z}{2}, \tag{5.52}$$

where $f(\omega)$ is the Fermi-Dirac distribution, which depends on the temperature T. Moreover, by definition, the retarded and advanced Green's functions are related one to each other according to $\hat{g}^r_\alpha(\omega) = \hat{g}^a_\alpha(\omega)$. Consequently, with the unperturbed retarded Green's functions $\hat{g}^r_{Sj}(\omega)$ and $\hat{g}^r_T(\omega)$ in hands, we can readily compute the current $I(j,V)$, shot-noise $S(j,V)$ and Fano factor $F(j,V)$.

Hereinafter, we focus on the sub-gap voltage regime $|eV| < \Delta_{\text{eff}} < \Delta$. Remembering that Δ is typically much weaker than the Fermi energy and the bandwidth, the relevant energy range for our purpose is a narrow window around the Fermi energy. It is, therefore, legitimate to use the wide-band approximation to describe the metallic tip. Within this approximation, the Green's function of the tip reads:

$$g^r_T(\omega) = -i\pi\nu_T \tau_0 \otimes \sigma_0, \tag{5.53}$$

and the tunnel junction is characterized by the tunneling rate $\Gamma = 2\pi\nu_T t^2$.

At this point, the only missing quantity to determine the current $I(j,V)$, shot-noise $S(j,V)$, and Fano factor $F(j,V)$ is $\hat{g}^r_S(\omega)$. In principle, $\hat{g}^r_S(\omega)$ has to be computed numerically and depends on the details of $\hat{H}_S$, the BdG Hamiltonian of the isolated sample. Nevertheless, using a low-energy approximation for $\hat{g}^r_S(\omega)$, we are able to obtain an insightful analytical model describing the spatial dependence of the shot-noise and Fano factor.

5.3.3 Insights from a low-energy effective theory

Within our tight-binding BDG model, applied to a one-band Hamiltonian, a general zero-energy state, regardless of the bulk-topology, is associated to the 4 particle-hole component wave-function $\phi_+(j) = [u_\uparrow(j), u_\downarrow(j), v_\uparrow(j), -v_\downarrow(j)]$ and its particle-hole partner $\phi_-(j) = C\phi_+(j)$, where $C = \sigma_y\tau_y\mathcal{K}$, with $\mathcal{K}$ the complex conjugation. Since we focus on the sub-gap voltage regime $eV < \Delta_{\text{eff}}$ and low-temperature regime $T \sim 0$, the dominant contribution to transport properties stem from $|\omega| < eV < \Delta_{\text{eff}}$. Because of the effective gap in the sample Δ_{eff}, the zero-energy state is the only state available in the above-mentioned energy range. Therefore, it seems legitimate to neglect the higher-energy states in the sample and approximate the unperturbed retarded Green's function by the retarded Green's function of a single zero-energy bound-state:

$$g_S^R(\omega) \approx \frac{\phi_+(j)\phi_+^\dagger(j) + \phi_-(j)\phi_-^\dagger(j)}{\omega + i0^+}. \tag{5.54}$$

Under the general assumption that the sample Hamiltonian is real [1], $u_\sigma(j)$ and $v_\sigma(j)$ can be safely chosen as real numbers. Under this assumption, injecting (5.54) into our closed set of equations (5.43), (5.44), (5.45), (5.46), and (5.47), and using (5.37) and (5.38), we are able to obtain an exact analytical expression of $S(j,V)$ and $I(j,V)$. In the generic case of a finite temperature, the integrals entering these expressions can not be performed analytically. Hence we focus on the $T = 0$ limit. Even in this limit, for finite voltage, the resulting expressions turn out to be lengthy and not insightful and can be found in the Supplementary Material of [34]. However, in the zero-temperature limit and saturated voltage regime, $eV \gg \Gamma_j$, with $\Gamma_j = \Gamma\sum_\sigma(|u_\sigma(j)|^2 + |v_\sigma(j)|^2)$, we obtain

$$S(j) \simeq 8e^2\Gamma\frac{(\sum_\sigma u_\sigma^2)(\sum_\sigma v_\sigma^2)[(\sum_\sigma u_\sigma^2)^2 + (\sum_\sigma v_\sigma^2)^2]}{(\sum_\sigma u_\sigma^2 + \sum_\sigma v_\sigma^2)^3}, \tag{5.55}$$

$$I(j) \simeq 2e\Gamma\frac{(\sum_\sigma u_\sigma^2)(\sum_\sigma v_\sigma^2)}{(\sum_\sigma u_\sigma^2 + \sum_\sigma v_\sigma^2)}, \tag{5.56}$$

$$F(j) \simeq 1 + \left(\frac{\sum_\sigma(|u_\sigma|^2 - |v_\sigma|^2)}{\sum_\sigma(|u_\sigma|^2 + |v_\sigma|^2)}\right)^2 = 1 + \delta_{\text{ph}}^2(j),. \tag{5.57}$$

Notice that $\delta_{\text{ph}}(j)$ corresponds to the local electric charge of the bound-state normalized by its local square amplitude (also named intensity). Here we interpret this quantity as a local measure of the particle-hole asymmetry of the bound-state. Consequently $F(j)$ does not depend on the tunneling strength and $1 \leq F(j)$. Furthermore, and most importantly, we prove that $F(j) - 1$ is in direct correspondence with $\delta_{\text{ph}}(j)$ and can thus display strong spatial variations. Interestingly it was recently proposed to identify Majorana vortex modes using non-local transport measurements [38]. The proposed protocol provides a spatial map of the quantity $\delta_{\text{ph}}(j)$ (see [38]). It suggests that our FFT protocol, based on local probes, might provide equivalent results to more sophisticated protocols based on non-local transport.

In sharp contrast, a perfectly isolated MZM is described by a Majorana wavefunction $\phi_M(j)$ satisfying the pseudo-reality condition $\phi_M(j) = C\phi_M(j)$. Hence $\phi_M(j)$ is particle-hole symmetric for any position. This imposes strong constraints on the spatial dependence of $F(j)$. Indeed, neglecting the contribution of high energy states above the gap, the unperturbed retarded Green's function of the substrate can be approximated by

[1] We numerically check that our results remain valid for complex Hamiltonian, see Fig. 5.15

the retarded Green's function of a single perfectly isolated MZM,

$$g^R_{S,j,j}(\omega) = \frac{\phi_M(j)\phi_M^\dagger(j)}{\omega + i0^+}, \tag{5.58}$$

with $\phi_M(j) = (u_\uparrow, u_\downarrow, u_\downarrow^*, -u_\uparrow^*)^T$. Focusing on the $T = 0$ limit, the shot-noise and current can be obtained exactly (see Supplementary Material of [34] for details) and adopt a compact form even for finite voltage. The resulting Fano factor reads:

$$F(j, eV) = 1 - \frac{\Gamma_j}{\arctan\left(\frac{eV}{\Gamma_j}\right)} \frac{eV}{(eV)^2 + \Gamma_j^2}. \tag{5.59}$$

Therefore, for sufficiently high voltage, $eV \gg \Gamma_j$, the Fano factor saturates, $F(j) \approx 1$, and does not depend on j. Moreover, the leading order corrections in $\frac{\Gamma_j}{eV}$ reads $F(j) \simeq 1 - \frac{2\Gamma_j}{\pi eV}$. Thus, the Fano factor in the vicinity of a MZM weakly decreases with increasing tunneling strength Γ, reaching values lower than the Poissonian limit 1.

In fact, this result could have already been anticipated from equation (5.57). Notice that nonzero $\delta_{\mathrm{ph}}(j)$ obviously requires finite overlap of Majorana wavefunctions describing the zero-energy fermion. Indeed, decomposing ϕ_+ into a linear superposition of two Majorana wavefunctions, $\phi_A = C\phi_A$ and $\phi_B = C\phi_B$, with $\phi_+ = e^{i\varphi}\frac{\phi_A(j)+\phi_B(j)}{\sqrt{2}}$, we readily obtain:

$$\delta_{ph}(j) = 2i\frac{\phi_A^\dagger(j)\tau_z\phi_B(j)}{|\phi_A^\dagger(j)|^2 + |\phi_B(j)|^2} \;\Rightarrow\; F(j) = 1 + 4\left(\frac{\mathrm{Im}\left\{\phi_A^\dagger\tau_Z\phi_B\right\}}{|\phi_A^\dagger(j)|^2 + |\phi_B(j)|^2}\right)^2. \tag{5.60}$$

In consequence, the FFT of a perfect MBS necessarily consists of a flat plateau $F(j) = 1$ over the entire extent of the zero-energy bound-states. Equation (5.60) does not imply that the presence of a finite Majorana overlap necessarily produces oscillations of F above one. Nevertheless, it seems unlikely that the presence of Majorana overlap does not produce any local charge of the bound-state and could not be detected by FFT. Thus, we expect F to be sensitive to Majorana overlap.

Consequently, even if our FFT protocol is not able to provide any direct signature of the topology of the bulk substrate, it is of great practical interest to develop Majorana-based qubits. Indeed, FFT should be sensitive to Majorana overlap and used to select zero-energy bound-states with suppressed Majorana overlap, which is therefore resilient to local noise and good candidates for quantum computation [186].

As a last remark, we stress that all the above arguments are general and rely only on the existence of a zero-energy bound state in an effective single-band Hamiltonian.

5.3.4 Numerical simulations of Fano factor tomography

In order to verify the validity of the previous results obtained from an effective low-energy theory, we numerically calculated the FFT of the wire. To do so, we first numerically computed the eigenvalues E_n and eigenvectors ϕ_n of $\hat{H}_S$, the BdG Hamiltonian of the sample. Second, we used Lehmann's representation of $\hat{g}^r_S(\omega)$:

$$\hat{g}^r_S(\omega) = \sum_n \frac{\phi_n(j)\phi_n^\dagger(j)}{\omega - E_n + i0^+}, \tag{5.61}$$

with $\phi_n(j)$ the wavefunction of ϕ_n in the Nambu basis at evaluated at site j. Then, we inserted $\hat{g}^r_{Sj}(\omega)$ in the set of equations (5.43), (5.44), (5.45), (5.46), and (5.47). Finally, the obtained local non-equilibrium Green's functions are inserted into (5.37) and (5.38), and the integrals are performed numerically. We performed numerical simulations of the FFT for different configurations of the sample indicated in Table I and many values of the tunneling amplitude. Here we present results for $\Gamma/\Delta_{\text{eff}} = 0.1, 0.3$, which corresponds to strong tunneling strength. Since we are interested in the low-temperature quantum regime, we set $k_B T = \frac{\Delta_{\text{eff}}}{200}$. Typically, the shot-noise increases with voltage and rapidly saturates to a finite value for higher voltage. Therefore, we set $eV = 0.7\Delta_{\text{eff}}$, which ensures that the signal has reached saturation. The results of our numerical simulation are presented in Fig. 5.11. Figs. 5.11 (a), (b, (c), (d), (e), and (f) correspond to case *a*, *b*, *c*, *d*, *e*, and *f* respectively, in Table. 5.1.

First, Figs. 5.11 (a), (c), and (e) show that in the vicinity of a MBS, $F(j)$ does not significantly deviate from the Poissonian limit, $F = 1$ and does not depend strongly on the tip position, j. In addition, the low-energy approximation (5.59) is in quantitative agreement with the exact FFT. This behavior is observed for any tunneling rate. Notice that for the first sites of the wire, $j < 5$, $F(j)$ weakly decreases below one when tunneling strength increases, as expected from the low-energy approximation (5.59).

In sharp contrast, Fig. 5.11(b) shows that in the vicinity of YSR bound-states, the Fano factor can reach values significantly greater than 1, oscillating strongly as a function of the tip position, j. This behavior is again observed for any tunneling regime and does not significantly depend on Γ. Those qualitative results are also found in the vicinity of an ABS, as plotted in Fig. 5.11 (d). In the vicinity of the QMS, case (*f*) of Table. 5.1, the FFT exhibits a flat plateau $F = 1$ extending over the whole normal part of the wire ($j < 20$) and starts oscillating in the superconducting region, where the Majorana wavefunctions overlap. Therefore, the difference with the FFT of an isolated MZM is less pronounced but still visible. Finally and most importantly, in all these cases, our low-energy approximation (5.57) is in quantitative agreement with the exact FFT.

The analysis of the FFT in the vicinity of the QMS (Fig. 5.11 (f)) suggests that the FFT is sensitive to Majorana overlap. This is indeed expected from equation (5.60). More precisely, (5.60) shows that F can exceed one only in the presence of a finite Majorana overlap, and we expect that a finite Majorana overlap produces $F(j) > 1$ in the FFT. To confirm it and further analyze the role of the Majorana overlap in the FFT profile, we performed additional simulations of the FFT in the vicinity of imperfect MBS with overlapping Majorana modes. In short nanowires, due to the finite length of the wire, the Majorana modes localized at the edges of Rashba nanowires in the topological phase can overlap each other. Generally, the finite overlap of Majorana wavefunctions leads to finite energy of the MBS. However, there exist fine-tuning points of the Zeeman energy where a zero-energy bound-state exists with a strong Majorana overlap (see Fig. 5.12). We computed the Fano factor $F(j)$ as a function of the position of the tip, j, for a perfect MBS without Majorana overlap and compared it to two of these fine-tuning points. The corresponding wire parameters are listed in Table. 5.2. In each case, the nanowire is in the topologically non-trivial regime and harbors MZMs localized at each end, as can be observed in Fig. 5.12. While case *a* corresponds to truly unpaired MZMs with negligible overlap, as observed in Fig. 5.12 (a), in case *b* and *c* the Majorana localization length ξ_M increases because of the increase in the Zeeman energy, as observed in Figs. 5.12 (b) and (c). Therefore, a substantial Majorana overlap is observed even at the extremities of the nanowire. The results of the FFT in each case are presented in Fig. 5.13.

Fig. 5.13 shows that the plateau $F = 1$, observed in the absence of overlap, disappears in the presence of finite overlap, which is responsible for an increase in F above 1. Indeed, in case *a*, the absence of Majorana

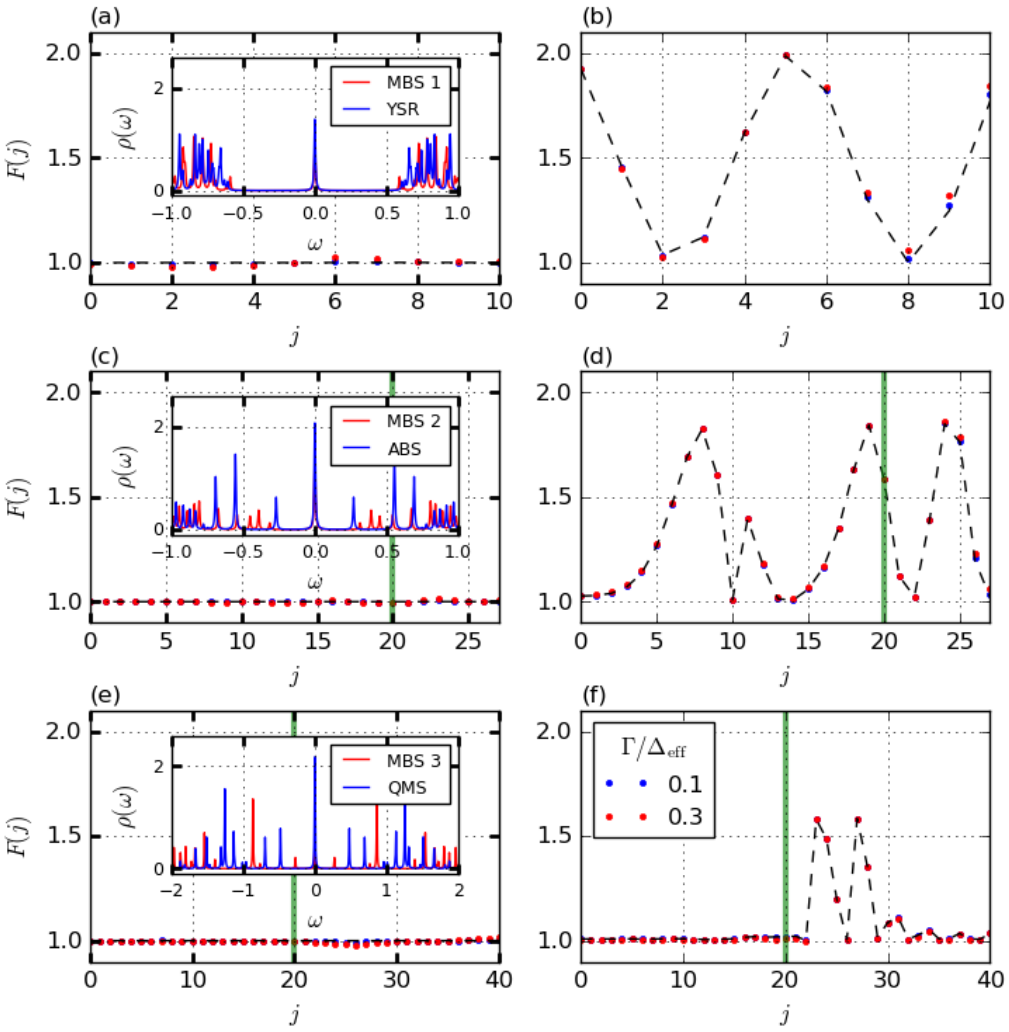

Figure 5.11: Fano factor tomography in the vicinity of trivial fermions and MBS. Dots: Fano factor as a function of the tip position (j) at fixed voltage $eV = 0.7\Delta_{\rm eff}$ for increasing tunneling strengths ($\Gamma/\Delta_{\rm eff} = 0.1, 0.3$) in the vicinity of various types of zero-energy bound-states: MBS 1 (a), YSR (b), MBS 2 (c), ABS (d), MBS 3 (e), and QMS (f) (see Table. 5.1). In the vicinity of unpaired MZMs, cases (a), (c), and (e), a flat plateau $F(j) = 1$ is observed in sharp contrast with trivial cases (b) and (d), where strong oscillations of F well above 1 are obtained. In the vicinity of a QMS, case (f), $F(j) = 1$ in the whole metallic region, where the Majorana wavefunctions do not overlap, however as they start overlapping in the SC region, $20 < j < 40$, (see Fig. 5.12 (f)) spatial oscillations of F above one are found, allowing for a distinction with the MBS of case (e). Dashed line: Analytical approximation obtained from the low-energy model, given by (5.57). The low-energy approximation is in excellent agreement with numerical points. The green vertical line indicates the NS interface when it exists. The three insets show the DOS for the six cases considered here.

overlap leads to the observation of a plateau $F = 1$ for the first sites of the wire where the MBS is localized ($j \leq 10$), as observed in Fig. 5.13 (a). For position further in the bulk, ($j > 10$), the Majorana wave-function

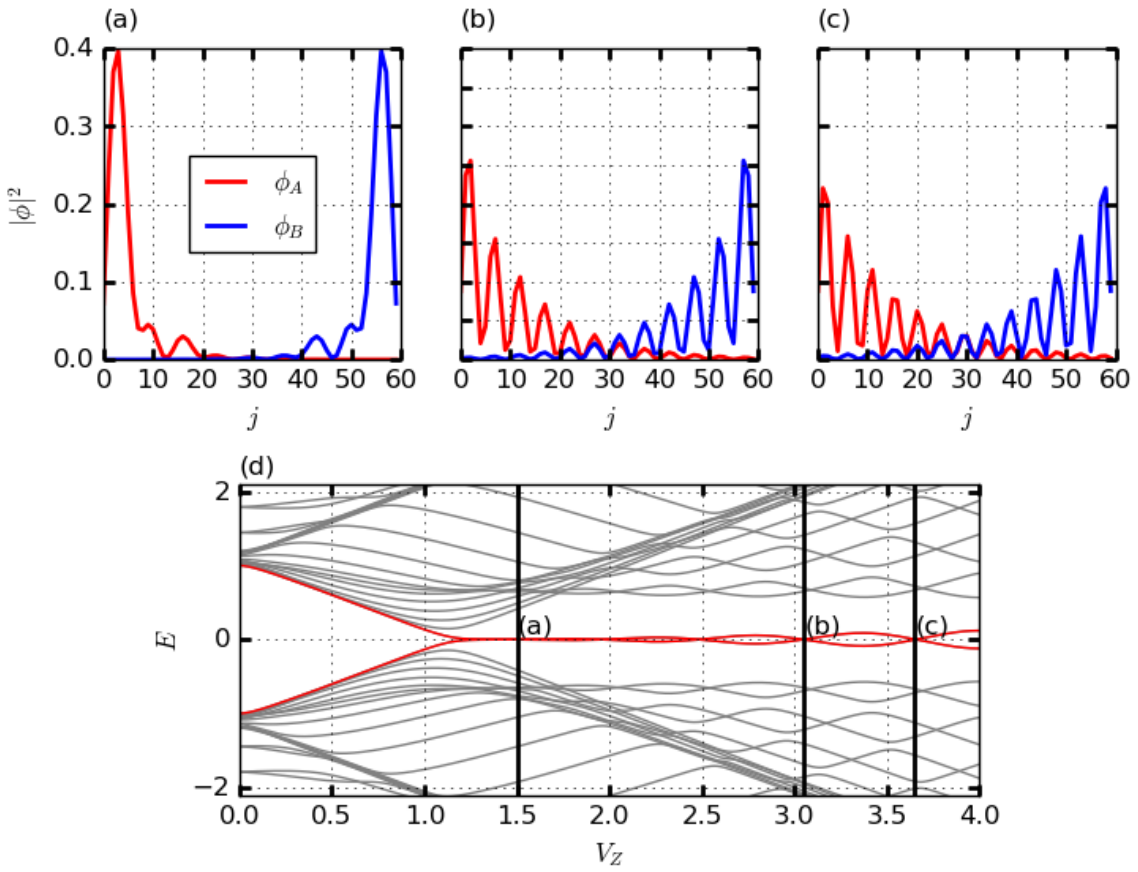

Figure 5.12: Overlapping Majorana modes in short topological nanowires. (a), (b), (c): Square amplitude of the Majorana wave-functions associated to the zero-energy fermionic states for $V_Z = 1.5,\ 3.05,$ and 3.65, respectively. In case (a), the MBS overlap at the edges of the wire ($j \leq 10$) is zero. In cases (b) and (c), the Majorana wavefunctions are not confined to one edge of the wire, and a finite overlap exists at each end of the wire. (d): Spectrum of the wire as a function of the Zeeman coupling V_Z. The vertical lines indicate the value of V_Z corresponding to cases *a*, *b*, and *c* respectively in Table. 5.2. In all cases, the spectrum exhibits a single pair of zero-energy eigenmodes corresponding to a single zero-energy fermion. Notice that in cases *b* and *c*, due to the fine-tuning of the Zeeman energy, the overlapping Majorana end modes do not hybridize. In all figures the other parameters are ($\mu = 0.5, w = 10, \Delta = 1, \alpha = 1.2, N = 60$)

ϕ_A is weak (see Fig. 5.12 (a)) and non-universal contributions are responsible for the increase in $F(j)$ above 1. Those effects are of two types. First, when ϕ_A is almost vanishing, it becomes comparable to ϕ_B. Hence the quantity: δ^2_{ph} can take non-zero values, increasing F above one. Indeed, one can see from the dashed dark line that $\delta^2_{ph}(j)$ is non-zero for such positions. Such contributions are then finite-size effects. Second, due to the weak weight of the MBS wavefunctions ϕ_A and ϕ_B at positions $j > 10$, the non-resonant Andreev reflections on bulk states, neglected in the low-energy approximation, become a relevant charge transfer process and increase F. This is especially true for $j = 13$ where the Majorana wavefunctions are almost exactly vanishing. However, the current at this position is also infinitesimally small, and then the Fano factor may not be experimentally accessible here, and one should observe a plateau extending from $j = 0$ to $j = 20$.

	μ	w	Δ	V_Z	α	N	Δ_{eff}
a	0.5	10	1	1.5	1.2	60	0.41
b	0.5	10	1	3.5	1.2	60	0.65
c	0.5	10	1	3.65	1.2	60	0.67

Table 5.2: Table summarizing the three sets of parameters used to study the effect of Majorana overlap on the FFT. In each case, the nanowire is in the topological regime and exhibits a pair of Majorana edge modes. While case *a* corresponds to non-overlapping Majorana modes realizing MZMs, cases *b* and *c* correspond to overlapping Majorana-edge modes. These modes do not correspond to true MZMs and are not protected against local noise. Δ_{eff} denotes the effective gap separating the zero-energy fermionic bound-state from other states.

On the contrary, in cases *b* and *c*, the presence of a finite overlap of the MBS at the edges washes out the Fano plateau $F = 1$, and MBS overlap is responsible for finite particle-hole asymmetry of the zero-energy states (as it can observe from the dashed dark line), increasing $F(j)$ above one even at the edges of the nanowire. Therefore, (5.57), (5.60), and the above results suggest that the FFT is sensitive to Majorana overlap and might be used to distinguish truly unpaired MZMs from partially overlapping ones.

In summary, we have shown that the recently developed STM shot-noise techniques can provide a key discerning tool MBS from other zero-energy fermionic states. In particular, we evidenced that the Fano factor strongly oscillates spatially for ABS and YSR bound states around the impurity location, greatly exceeding one, *i.e.*, the Poissonian limit. This must be sharply contrasted with the behavior of the MBS Fano factor, which barely deviates from one. These sharp differences have a universal character that is rooted in the intrinsic particle-hole symmetry of the wavefunction describing a single MZM. Such signature in the FFT in the vicinity of a zero-bias conductance peak thus constitutes an additional necessary condition to identify true MBS. Moreover, a finite Majorana overlap is necessary to increase the Fano factor above one. In principle, it is possible that an overlapping pair of Majorana modes does not produce a finite particle-hole asymmetry. Nevertheless, this situation seems rather unlikely in realistic setups and is not observed in our simulations. Hence this suggests that FFT is a promising tool to study and estimate the Majorana overlap of zero-bias peaks.

5.3.5 Discussion

To obtain the insightful result (5.57) from our low-energy effective model, we set $T = 0$ and additionally assumed that the BdG Hamiltonian describing the hybrid sample is real. Moreover, the numerical simulations were performed at a very low temperature $k_B T = \Delta_{\text{eff}}/200$ and all the cases studied in Table. 5.1 correspond to purely real BdG Hamiltonians. Therefore, it is legitimate to wonder how the above results are modified when temperature increases and/or when the BdG Hamiltonian describing the sample contains complex terms.

First, we study the effect of temperature. To do so, we performed numerical simulations of the FFT in the vicinity of the MBS, case *a* in Table. 5.1 and in the vicinity of the YSR, case *b* in Table. 5.1. Our results, presented in Fig. 5.14, show that, independently of the tunneling rate Γ, the FFT is not significantly modified by thermal effects for temperature $k_B T < 0.1\Delta_{\text{eff}}$. Most importantly, Fig. 5.14 shows that, as long as $k_B T < 0.1\Delta_{\text{eff}}$, the $T = 0$ limit of our low-energy model, (5.57), remains in good agreement with the exact FFT obtained numerically.

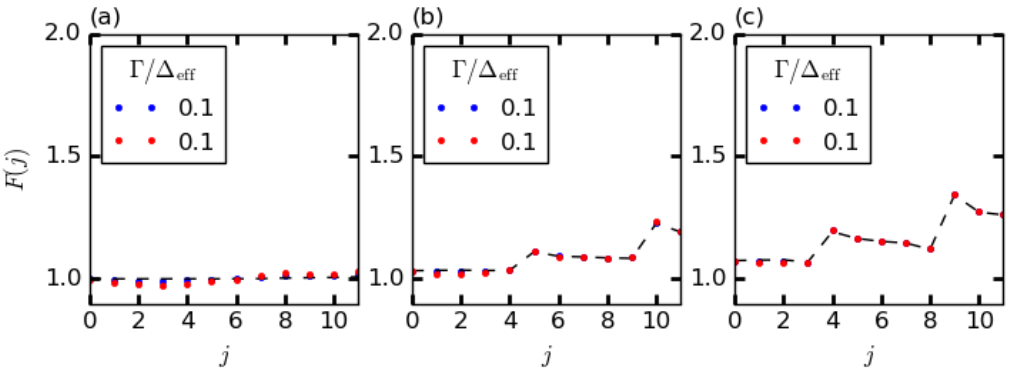

Figure 5.13: Fano factor F as a function of the tip position, j for $V_Z = 1.5$(a), $V_Z = 3.05$(b) and $V_Z = 3.5$(c). Other parameters are set to ($\mu = 0.5, t_w = 10, \Delta = 1, \alpha = 1.2, N = 6$). In case (a) the absence of Majorana wave-functions overlap leads to the observation of a plateau $F = 1$ for the first sites of the wire where the MZM is localized ($j \leq 10$). In cases (b) and (c), the presence of a finite overlap of the MBS at the edges washes out the Fano plateau $F = 1$, and the finite Majorana overlap is responsible for a finite particle-hole asymmetry δ_{ph} of the zero-energy states (as it can be observed from the dashed dark line), increasing $F(j)$ above one even at the edges ($j \leq 10$). In all cases, the analytical approximation given by (5.57) (black dashed line) is in quantitative agreement with the numerical results. For all cases, the voltage and temperature are $eV = 0.7\Delta_{\text{eff}}$ and $k_BT = \Delta_{\text{eff}}/200$.

For higher temperature, $k_BT \geq 0.1\Delta_{\text{eff}}$, thermal contributions to shot-noise are responsible for an increase of the factor which weakly spoils the Poissonian plateau in the vicinity of MBS. However, the qualitative behavior of $F(j)$ in the vicinity of the zero-energy state ($j < 12$) is still well described by our analytical approximation given by (5.57) (black-dashed line) for all temperatures studied here. Temperature effects are more pronounced in the tails of the zero-energy states where the pure quantum contributions (non-vanishing at $T = 0$) to the shot-noise are weaker and more easily dominated by temperature contributions. Our results suggest that as long as $k_BT \ll \Delta_{\text{eff}}$ and $k_BT < eV - \Delta_{\text{eff}}$, such that bulk contributions do not play a key role, the low-temperature results are not modified, and the FFT is well captured by the simple model (5.57). Consequently, the proposed Fano tomography could be performed in the current state-of-the-art experimental setups based on hybrid semiconductor/superconductor nanowires. Indeed, as an example, in [167] authors reported $k_BT \simeq 100$mK and $\Delta_{\text{eff}} \simeq 200\mu$eV, leading to $(k_BT)/\Delta_{\text{eff}} \simeq 0.05$, where the low-temperature regime is still valid.

Let us now investigate how complex terms in the BdG Hamiltonian describing the sample affect the FFT. To derive (5.57) we assumed that the BdG Hamiltonian of the sample is purely real, up to a global gauge transformation. In that case, the complex conjugation $\mathcal{K}$ plays the role of an artificial time-reversal symmetry, and the system belongs to the BDI symmetry class of the ten-fold way. When the BdG Hamiltonian contains complex terms, which can not be removed by a global gauge transformation, the artificial time-reversal symmetry is broken, and the system falls into the D symmetry class. Moreover, the eigenvectors of the BdG Hamiltonian can no longer be written exclusively with real numbers. Hence our derivation of (5.57) is no longer valid. Here we show that the relation (5.57) is still valid for complex Hamiltonians. To that end, we performed numerical

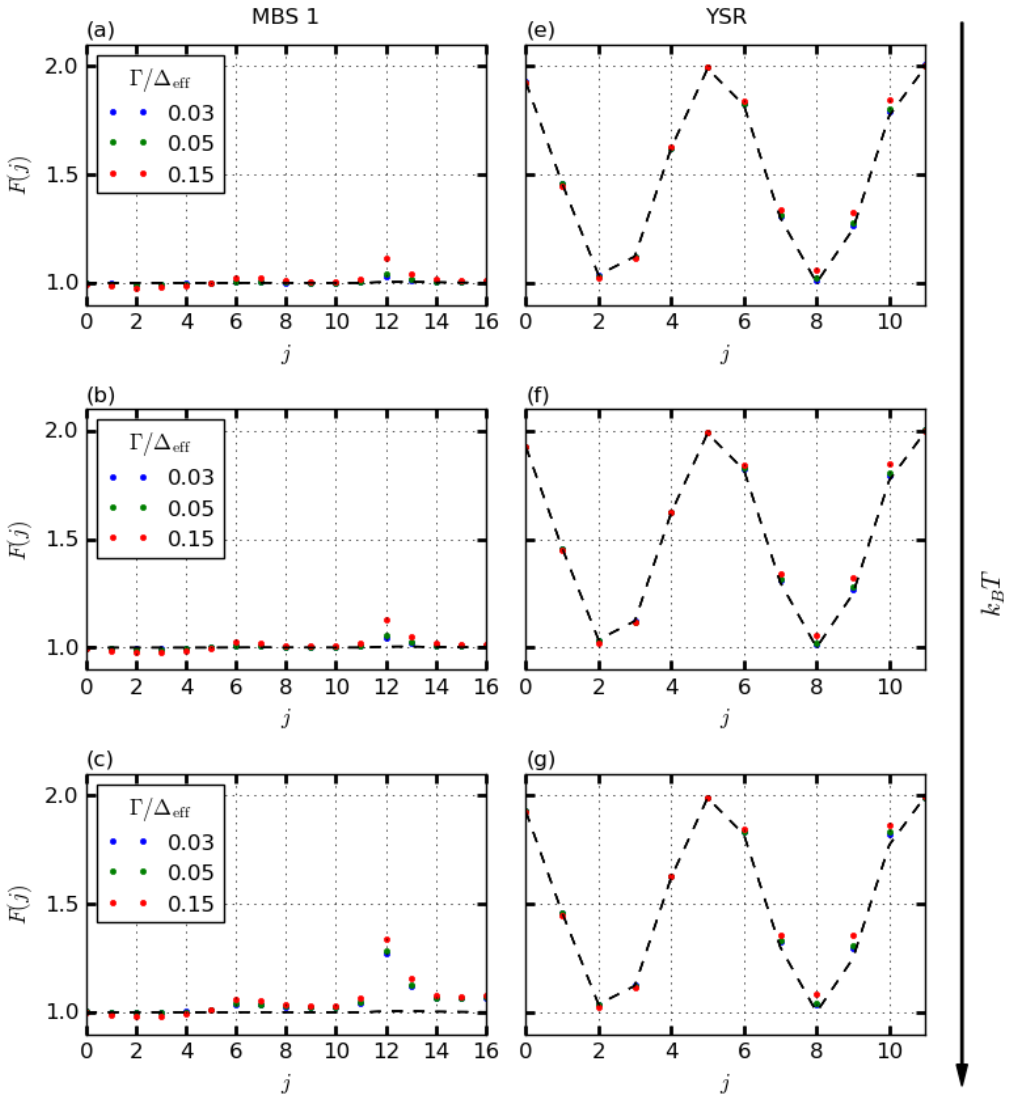

Figure 5.14: Effects of temperature on the FFT of zero-energy bound-states. (a), (b) and (c): $F(j)$ as a function of the tip position, j, for a nanowire in the configuration a of Table. 5.1 at various temperatures $\frac{k_BT}{\Delta} = 0.03,\ 0.05,$ and, 0.1, respectively. The blue, green and red dots corresponds to $\frac{k_BT}{\Delta} = 0.03,\ 0.05,$ and, 0.15, respectively. The black dashed line indicates the low-energy approximation (5.57) obtained at $T = 0$. (e)-(g): same as (a)-(c) for a nanowire in configuration a. The numerical simulation results (colors dots) and the $T = 0$ and low-energy approximation (5.57) (black dashed line) are in quantitative agreement up to $k_BT = 0.1\Delta_{\text{eff}}$, where weak quantitative deviations are observed. All simulations have been performed setting $eV = 0.7\Delta_{\text{eff}}$.

simulations of the FFT for three additional cases, described by the following Hamiltonian,

$$\begin{aligned}\mathcal{H}_S =& \frac{1}{2}\sum_{l=0}^{N-1}\psi^\dagger_{l,S}[(2w-\mu)\tau_z + \Delta(l)\tau_x + \boldsymbol{V}_Z.\boldsymbol{\sigma}]\psi_{l,S} \\ &+\frac{1}{2}\sum_{l=0}^{N-2}\{\psi^\dagger_{l+1,S}[-w\tau_z - i\alpha\sigma_y\tau_z]\psi_{l,S} + \text{h.c.}\} - \frac{1}{2}\psi^\dagger_{0,S}J\sigma_y\psi_{0,S}\ ,\end{aligned} \tag{5.62}$$

with $\boldsymbol{V}_Z = V_Z(\cos\theta \boldsymbol{e}_x + \sin\theta \boldsymbol{e}_y)$. We investigate 3 specific set of parameters(a, b,and c) detailed in Table. 5.3. In all cases, the Hamiltonian contains complex terms and can not be made real. First, in case a we consider a

	Configuration	μ	w	Δ	V_Z	θ	α	J	N	N_N	Δ_{eff}
a	MBS 4	0.5	10	1	1.5	$\pi/6$	2	0	100	20	0.26
b	ABS 2	0.5	10	1	0.26	$\pi/6$	2	0	100	20	0.27
c	YSR 2	0.5	10	0.6	0	0	1.2	11.23	80	0	0.6

Table 5.3: Table summarizing the three additional sets of parameters studied here. In each case, the BdG Hamiltonian describing the sample is not real, and the complex terms can not be removed by a global gauge transformation. Δ_{eff} denotes the effective gap separating the zero-energy fermionic bound-state from other states.

partially-proximitized nanowire and suppose that the external magnetic field is not perfectly aligned with the nanowire axis but tilted by an angle θ from $\boldsymbol{e}_x$. This case is particularly relevant since a perfect alignment can not be achieved in realistic setups. In that case, the nanowire belongs to the D class, and we already showed that when $V_Z > \sqrt{\mu^2 + \Delta^2}$ the nanowire is in the topological phase supporting a single pair of MZMs at its ends. We compare this perfect MBS to two trivial zero-energy bound-states used as reference cases. In case b, we assume that the nanowire is partially-proximitized. Due to fine-tuning of the parameter, a zero-energy ABS localized in the normal part of the nanowire appears. In case c, we assume that a magnetic impurity is localized at the left end of the wire. As the magnetic impurity points along the y axis, the BdG Hamiltonian contains complex terms that cannot be removed because of the presence of SOC. In the absence of an external magnetic field, a zero-energy YSR state appears localized at the left end of the nanowire due to the fine-tuning of the exchange energy J. Again we numerically computed $F(j)$ as a function of the tip's position, j. The results of the FFT are presented in Fig. 5.15. Fig. 5.15 (a), shows that even in the presence of complex terms in the Hamiltonian, $F(j)$ still shows a plateau $F(j) = 1$ in the vicinity of a MBS. This was expected since equation (5.59) relies only on the form of MBS wavefunction without any other additional assumptions about the Hamiltonian. Fig. 5.15 (b) shows that, even in the presence of complex terms in the Hamiltonian, equation (5.57) obtained with the assumption of a real Hamiltonian, is still valid. Indeed, F obtained from equation (5.57) (black dashed line) is in quantitative agreement with the numerical results (colored dots) for the first sites of the wire. Moreover, $F(j)$ still significantly exceeds one in the vicinity of trivial states.

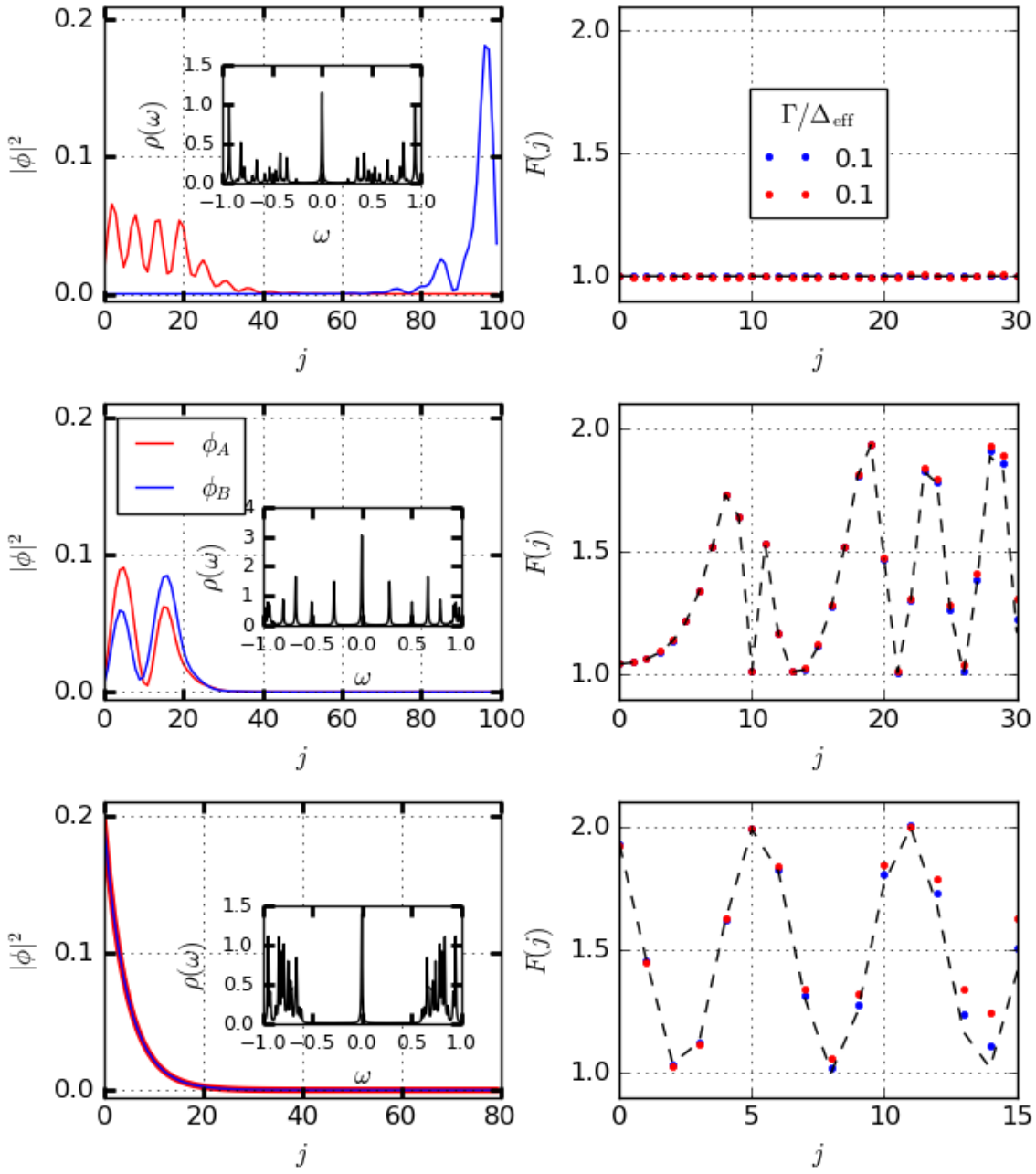

Figure 5.15: Numerical simulations of FFT for complex BdG Hamiltonians. (a), (b), and (c): Square amplitude of the Majorana modes associated to the zero-energy bound-state in case a, b and$c$ respectively in Table.5.3. Insets: LDOS $\rho(\omega)$ in the vicinity of the zero-energy bound-states. (d), (e), and (f): (Dots) Fano factor (F) as a function of the tip position, j, at fixed voltage $eV = 0.7\Delta_{\text{eff}}$ and temperature $k_BT = \frac{\Delta_{\text{eff}}}{200}$ for increasing tunneling rates $\Gamma/\Delta_{\text{eff}} = 0.1, 0.3$ and configuration a, b and c respectively in Table. 5.3. In the vicinity of a MBS, case a, a flat plateau $F(j) = 1$ is observed in sharp contrast with trivial cases b and c, where strong oscillations of F well above 1 are observed. (Dashed line) Analytical approximation obtained from the low-energy model, given by (5.57). In each case, the low-energy approximation is in excellent agreement with numerical points. The weak disagreement for $j > 10$ in panel (f) is due to the contribution of bulk states which is neglected in (5.57) and becomes relevant when the tip moves away from the YSR location.

5.4 Conclusion and perspectives

Majorana bound-states are promising building blocks for future fault-tolerant topological quantum computers. However, the promising developments in using MBS for quantum computing are nowadays limited by the difficulties in detecting and discerning MBS from other zero-energy bound-states. The desired properties of MBS are rooted in their non-local nature. Hence experimental protocols able to quantify the Majorana overlap of zero-energy bound-states are highly desirable. Here, we showed that recently developed scanning tunneling shot-noise microscopy/spectroscopy techniques constitute relevant tools to identify perfect MBS.

In particular, we showed that:

(i) In the vicinity of a spatially isolated MZM, the Fano factor barely oscillates below one. This universal feature is rooted in the intrinsic particle-hole symmetry of the wavefunction describing a single MZM.

(ii) On the contrary, in the vicinity of trivial zero-energy bound-states, the Fano factor can strongly oscillate in space with amplitudes greatly exceeding one, the Poissonian limit. These strong oscillations are rooted in the local particle-hole asymmetry (*i.e* the local charge) of trivial bound-states.

(iii) Finite Majorana overlap is necessary to produce oscillations of the Fano factor above one.

Therefore, the presence of quantized Fano plateau, $F = 1$, in the FFT constitutes an additional necessary condition to identify MBS. In addition, it seems unlikely that a finite Majorana overlap does not produce a Fano factor exceeding one, and we did not encounter such a case in all the numerical simulations performed. Hence, the Fano factor seems a promising tool sensitive to the Majorana overlap, which might be used to identify MBS. Thus, even if the proposed Fano factor tomography protocol is not able to directly access the bulk topology, it should play a key role in the development of Majorana-based technologies. Indeed, we already stressed that the definition of a MBS is directly related to its non-local character but not to bulk topology.

The FFT signature of MBS is rooted in the intrinsic particle-hole symmetry inherent to MZM. Hence it should be universal. Our work, therefore, paves the way for additional theoretical studies of shot-noise around MBS in alternative platforms such as 1D magnetic chains, planar Josephson junctions, or iron-based superconductors. Indeed, even if recent studies investigated shot-noise in MBS localized at the core of vortices [218], numerical simulations of the shot-noise tomography in these systems are still lacking. Finally, the present results should foster further experimental developments of STM shot-noise experiments in the field of Majorana fermions and, more generally, in the topological matter.

Chapter 6

General Conclusion

In this thesis, we revisited electronic transport in superconducting sub-gap states. More particularly, we showed that standard scanning tunneling spectroscopy and the recently developed scanning tunneling shot-noise spectroscopy techniques provide invaluable insights into the properties of superconducting sub-gap states and their host materials. This includes the presence of unconventional pairing, the intrinsic lifetime of the bound-states, or the particle-hole asymmetry of their wavefunction.

First, we have shown that a single classical spin, immersed in a conventional s-wave superconductor, locally induces unconventional odd-frequency pair correlations at the impurity location. Analyzing the local Green's functions at the impurity site, we showed that the imaginary part of the odd-frequency pairing function is proportional to the even component of the local density of state, a quantity directly measured in standard tunneling spectroscopy. This result has the important physical consequence that as soon as a YSR state exists inside the superconducting gap, odd-ω pairing is locally induced around the impurity. Based on the above-mentioned proportionality relation, we proposed a method to extract the unconventional pairing function from scanning tunneling spectroscopy data. Then we applied it to STS data measured on a Pb/Si(111) monolayer and extracted the unconventional pairing function from the conductance data. The results of our analysis clearly proved the occurrence of odd-frequency pairing around YSR states [30]. In collaboration with F. L. N. Santos *et al.* we extended those results in presence of a finite impurity concentration and provided a method to extract the imaginary part of the odd-frequency pairing function from the local density of states in the dilute limit [35].

Second, motivated by the recent development of scanning tunneling spectroscopy, we used the Keldysh techniques to calculate the current shot-noise in YSR states. Based on a minimal model, we showed that the shot-noise contains clear signatures of resonant Andreev reflections and incoherent single-particle tunneling processes in YSR states. We compared our theoretical predictions with experimental data measured by our LPS colleagues and showed that our simple theoretical model correctly captures the important features of shot noise. From the quantitative agreement between theory and experiment, we extracted the intrinsic relaxation rate of the YSR state, which is inaccessible by differential conductance spectroscopy. Using our theory, we also showed that the persistent enhancement of the Fano factor above 1 on the weakest YSR resonance observed in the experimental is a clear signature of resonant Andreev processes via the YSR state. On the other hand, the measured asymmetry of the Fano factor indicates the presence of incoherent single-particle processes. Hence, our results clearly show the concomitant presence of Andreev and single-particle processes in YSR states.

Lastly, we extend the former model to analyze the scanning tunneling shot-noise in the vicinity of any superconducting sub-gap states, including YSR impurity states, Andreev bound-states, and topological Majo-

rana zero-modes. Based on a low-energy model, we showed that in the strong tunnel coupling regime where the contribution of incoherent single-particle processes can be neglected in front of Andreev reflections, we showed that the Fano factor is essentially determined by the local particle-hole asymmetry of the bound-state wavefunction. This encouraging result suggests that the Fano factor tomography can be used to distinguish trivial fermions from Majorana zero modes. By means of numerical methods, we demonstrated that shot-noise tomography indeed reveals key distinctive features that allow one to distinguish trivial zero-energy fermions from Majorana zero-modes. More precisely, we showed that in the vicinity of a spatially isolated MZM, the Fano factor barely oscillates below 1 in sharp contrast with the strong oscillations exceeding 1 observed in the vicinity of trivial states. According to our low-energy model, strong oscillations are rooted in the local particle-hole asymmetry (*i.e* the local charge) of trivial bound-states. Even if the proposed Fano factor tomography protocol is not able to directly access the bulk topology, it is sensitive to the Majorana wavefunction overlap. Thus, it could play a key role in the development of Majorana-based technologies and foster further experimental developments of STM shot-noise experiments in the field of Majorana fermions and, more generally, in the topological matter.

Our numerical investigation was restricted to a minimal model describing hybrid semiconductor/superconductor nanowires. Nevertheless, since the Fano factor tomography (FFT) signature of MBS is rooted in the intrinsic particle-hole symmetry inherent to MZM wavefunctions, our results should not depend on the precise details of the system and be applicable to any topological superconductors. More precisely, FFT should be relevant to study the putative MZMs localized at the vortex cores in iron-based superconductors, which are intensively scrutinized experimentally. Very recently, shot-noise has been measured at the vortex core in $FeTe_{0.55}Se_{0.45}$ [37], paving the way to shot-noise tomography around the vortex core. Hence, in the near future, it will be interesting to perform numerical simulations of the Fano factor in the vicinity of MZMs localized at the vortex cores in iron-based superconductors using realistic multi-band models. Indeed, while recent theoretical studies studied the current and shot-noise in the vortex core [218], a detailed, comprehensive study of the shot-noise tomography is still lacking.

As a final remark, I would like to mention that this manuscript does not constitute an exhaustive review of all the topics I studied during the past three years of my PhD thesis. Although this manuscript focused on electronic transport in sub-gap bound-states, which are determined by the dynamics of charge carriers, another promising route to study the properties of YSR states would be to directly probe the spin dynamics of the impurity. During the last months of my PhD I studied the spin-wave dynamics in a 1D chain of magnetic atoms placed on top of a s-wave superconductor with spin-orbit coupling. Such a system exhibits MZMs localized at its extremities that can influence the spin-wave dynamics of the magnetic moments. Using perturbation theory, I showed that the absorption of the uniform spin-wave mode depends on the parity of the *Majorana qubit* and might be used to determine it. These preliminary results motivate further investigations that can be pursued in the next future.

Bibliography

[1] H. K. Onnes. The superconductivity of mercury. *Comm. Phys. Lab. Univ. Leiden*, 122:122–124, 1911.

[2] W. Meissner and R. Ochsenfeld. Ein neuer effekt bei eintritt der supraleitfähigkeit. *Naturwissenschaften*, 21:787–788, 1933.

[3] J. Bardeen, L. N. Cooper, and J. R. Schrieffer. Microscopic theory of superconductivity. *Phys. Rev.*, 106:162–164, Apr 1957.

[4] J. Bardeen, L. N. Cooper, and J. R. Schrieffer. Theory of superconductivity. *Phys. Rev.*, 108:1175–1204, Dec 1957.

[5] L P Gor'kov. Microscopic derivation of the ginzburg–landau equations in the theory of superconductivity. *Sov. Phys. - JETP (Engl. Transl.); (United States)*.

[6] P. W. Anderson. Theory of dirty superconductors. *Journal of Physics and Chemistry of Solids*, 11(1):26–30, 1959.

[7] A. A. Abrikosov and L. P. Gor'Kov. Superconducting alloys at finite temperatures. *Sov. Phys. JETP*, 9(1):220–221, 1959.

[8] L. Yu. Bound state in superconductors with paramagnetic impurities. *Acta Physica Sinica*, 21(1):75, 1965.

[9] H. Shiba. Classical spins in superconductors. *Progress of Theoretical Physics*, 40(3):435–451, 1968.

[10] A. I. Rusinov. Superconductivity near a Paramagnetic Impurity. *Sov. Phys. JETP Lett.*, 9:85, January 1969.

[11] A. Yazdani, B. A. Jones, C. P. Lutz, M. F. Crommie, and D. M. Eigler. Coherent long-range magnetic bound states in a superconductor. *Science*, 275:1767, 1997.

[12] S. Nadj-Perge, I. K. Drozdov, B. A. Bernevig, and Ali Yazdani. Proposal for realizing majorana fermions in chains of magnetic atoms on a superconductor. *Phys. Rev. B*, 88:020407, Jul 2013.

[13] K. v. Klitzing, G. Dorda, and M. Pepper. New method for high-accuracy determination of the fine-structure constant based on quantized hall resistance. *Phys. Rev. Lett.*, 45:494–497, Aug 1980.

[14] Q. Niu, D. J. Thouless, and Y. S. Wu. Quantized hall conductance as a topological invariant. *Phys. Rev. B*, 31:3372–3377, Mar 1985.

[15] J. Alicea. Majorana fermions in a tunable semiconductor device. *Phys. Rev. B*, 81:125318, Mar 2010.

[16] A. Y. Kitaev. Unpaired majorana fermions in quantum wires. *Physics-Uspekhi*, 44(10S):131, 2001.

[17] B. W. Heinrich, J. I. Pascual, and K. J. Franke. Single magnetic adsorbates on s-wave superconductors. *Progress in Surface Science*, 93(1):1 – 19, 2018.

[18] G. Ménard *et al.* Coherent long-range magnetic bound states in a superconductor. *Nature Physics*, 11:1013, 2015.

[19] M. Uldemolins, A. Mesaros, and P. Simon. Quasiparticle focusing of bound states in two-dimensional s-wave superconductors. *Phys. Rev. B*, 105:144503, Apr 2022.

[20] S. Nadj-Perge, I. K. Drozdov, Jian L., Hua C., Sangjun J., Jungpil S., A. H. MacDonald, B. A. Bernevig, and Yazdani A. Observation of majorana fermions in ferromagnetic atomic chains on a superconductor. *Science*, 346(6209):602–607, 10 2014.

[21] F. Massee, Q. Dong, A. Cavanna, Y. Jin, and M. Aprili. Atomic scale shot-noise using cryogenic mhz circuitry. *Review of Scientific Instruments*, 89(9):093708, 2018.

[22] K. M. Bastiaans, T. Benschop, D. Chatzopoulos, D. Cho, Q. Dong, Y. Jin, and M. P. Allan. Amplifier for scanning tunneling microscopy at mhz frequencies. *Review of Scientific Instruments*, 89(9):093709, 2018.

[23] M. Sigrist. Introduction to unconventional superconductivity. *AIP Conference Proceedings*, 789(1):165–243, 2005.

[24] C.-K. Chiu, J. C. Y. Teo, A. P. Schnyder, and S. Ryu. Classification of topological quantum matter with symmetries. *Rev. Mod. Phys.*, 88:035005, Aug 2016.

[25] R. Aguado. Majorana quasiparticles in condensed matter. *La Rivista del Nuovo Cimento*, 40(11):523–593, 2017.

[26] L. V. Keldysh. Diagram technique for nonequilibrium processes. *Zh. Eksp. Teor. Fiz.*, 47:1515–1527, 1964.

[27] G. Stefanucci and R. Van Leeuwen. *Nonequilibrium many-body theory of quantum systems: a modern introduction*. Cambridge University Press, 2013.

[28] J. C. Cuevas. *Electronic transport in normal and superconducting contacts*. PhD thesis, Universidad autonoma de Madrid, 1999. Thèse de doctorat dirigée par P. Simon Physique Université Paris-Saclay (ComUE) 2016.

[29] J. Linder and A. V. Balatsky. Odd-frequency superconductivity. *Rev. Mod. Phys.*, 91:045005, Dec 2019.

[30] V. Perrin, F. L. N. Santos, G. C. Ménard, C. Brun, T. Cren, M. Civelli, and P. Simon. Unveiling odd-frequency pairing around a magnetic impurity in a superconductor. *Phys. Rev. Lett.*, 125:117003, Sep 2020.

[31] I. Martin and D. Mozyrsky. Nonequilibrium theory of tunneling into a localized state in a superconductor. *Phys. Rev. B*, 90:100508, Sep 2014.

[32] M. Ruby, F. Pientka, Y. Peng, F. von Oppen, B. W. Heinrich, and K. J. Franke. Tunneling processes into localized subgap states in superconductors. *Phys. Rev. Lett.*, 115:087001, Aug 2015.

[33] U. Thupakula, V. Perrin, A. Palacio-Morales, L. Cario, M. Aprili, P. Simon, and F. Massee. Coherent and incoherent tunneling into yu-shiba-rusinov states revealed by atomic scale shot-noise spectroscopy. *Phys. Rev. Lett.*, 128:247001, Jun 2022.

[34] V. Perrin, M. Civelli, and P. Simon. Identifying majorana bound states by tunneling shot-noise tomography. *Phys. Rev. B*, 104:L121406, Sep 2021.

[35] F. L. N. Santos, V. Perrin, F. Jamet, M. Civelli, P. Simon, M. C. O. Aguiar, E. Miranda, and M. J. Rozenberg. Odd-frequency superconductivity in dilute magnetic superconductors. *Phys. Rev. Research*, 2:033229, Aug 2020.

[36] Hideo Aoki, Naoto Tsuji, Martin Eckstein, Marcus Kollar, Takashi Oka, and Philipp Werner. Nonequilibrium dynamical mean-field theory and its applications. *Rev. Mod. Phys.*, 86:779–837, Jun 2014.

[37] Jian-Feng Ge, Koen M. Bastiaans, Damianos Chatzopoulos, Doohee Cho, Willem O. Tromp, Tjerk Benschop, Jiasen Niu, Genda Gu, and Milan P. Allan. Determination of the charge transfer when tunneling into putative majorana modes in individual vortices in fete$_{0.55}$se$_{0.45}$. 2022.

[38] B. Sbierski, M. Geier, A.-P. Li, M. Brahlek, R. G. Moore, and J. E. Moore. Identifying majorana vortex modes via nonlocal transport. *Phys. Rev. B*, 106:035413, Jul 2022.

[39] M. Uldemolins, A. Mesaros, and P. Simon. Effect of van hove singularities on shiba states in two-dimensional s-wave superconductors. *Phys. Rev. B*, 103:214514, Jun 2021.

[40] David Pines. Superconductivity in the periodic system. *Physical Review*, 109(2):280, 1958.

[41] G. Rickayzen. *Theory of Superconductivity*. Interscience monographs and texts in physics and astronomy. Interscience Publishers, 1965.

[42] M. Tinkham. *Introduction to Superconductivity*. International series in pure and applied physics. McGraw Hill, 1996.

[43] G. Rickayzen. *Theory of Superconductivity*. Interscience monographs and texts in physics and astronomy. Interscience Publishers, 1965.

[44] P. A. Frigeri, D. F. Agterberg, A. Koga, and M. Sigrist. Superconductivity without inversion symmetry: Mnsi versus $\mathrm{cept_3Si}$. *Phys. Rev. Lett.*, 92:097001, Mar 2004.

[45] L. D. Landau, E. M. Lifshitz, and M. Pitaevskii. *Statistical Physics*. Butterworth-Heinemann, New York, 1999.

[46] D. J. Thouless, M. Kohmoto, M. P. Nightingale, and M. den Nijs. Quantized hall conductance in a two-dimensional periodic potential. *Phys. Rev. Lett.*, 49:405–408, Aug 1982.

[47] D. J. Thouless. Quantization of particle transport. *Phys. Rev. B*, 27:6083–6087, May 1983.

[48] C. Nayak, S. H. Simon, A. Stern, M. Freedman, and S. Das Sarma. Non-abelian anyons and topological quantum computation. *Rev. Mod. Phys.*, 80:1083–1159, Sep 2008.

[49] A. Altland and M. R. Zirnbauer. Nonstandard symmetry classes in mesoscopic normal-superconducting hybrid structures. *Phys. Rev. B*, 55:1142–1161, Jan 1997.

[50] A. Y. Kitaev. Periodic table for topological insulators and superconductors. *AIP Conf. Proc.*, 1134:22, 2009.

[51] Xiao-Liang Qi, Taylor L. Hughes, and Shou-Cheng Zhang. Topological field theory of time-reversal invariant insulators. *Phys. Rev. B*, 78:195424, Nov 2008.

[52] S. Ryu, A. P. Schnyder, A. Furusaki, and A. W. W. Ludwig. Topological insulators and superconductors: tenfold way and dimensional hierarchy. *New Journal of Physics*, 12(6):065010, jun 2010.

[53] A. P. Schnyder, S. Ryu, A. Furusaki, and A. W. W. Ludwig. Classification of topological insulators and superconductors in three spatial dimensions. *Phys. Rev. B*, 78:195125, Nov 2008.

[54] E. Majorana. Teoria simmetrica dell'elettrone e del positrone. *Il Nuovo Cimento (1924-1942)*, 14(4):171–184, 1937.

[55] D. A. Ivanov. Non-abelian statistics of half-quantum vortices in p-wave superconductors. *Phys. Rev. Lett.*, 86:268–271, Jan 2001.

[56] J.-N. Fuchs. An introduction to symmetries and quantum field theory, 2017.

[57] F. Wilczek. Emergent majorana mass and axion couplings in superfluids. *New Journal of Physics*, 16, August 2014.

[58] G. W. Semenoff and P. Sodano. Stretched quantum states emerging from a majorana medium. *Journal of Physics B: Atomic, Molecular and Optical Physics*, 40(8):1479–1488, mar 2007.

[59] C. Nayak and F. Wilczek. 2n-quasihole states realize 2n1-dimensional spinor braiding statistics in paired quantum hall states. *Nuclear Physics B*, 479(3):529–553, 1996.

[60] G. E. Volovik. Monopole, half-quantum vortex, and nexus in chiral superfluids and superconductors. *Journal of Experimental and Theoretical Physics Letters*, 70(12):792–796, Dec 1999.

[61] G. E. Volovik. Fermion zero modes on vortices in chiral superconductors. *Journal of Experimental and Theoretical Physics Letters*, 70(9):609–614, Nov 1999.

[62] N. Read and D. Green. Paired states of fermions in two dimensions with breaking of parity and time-reversal symmetries and the fractional quantum hall effect. *Phys. Rev. B*, 61:10267–10297, Apr 2000.

[63] N. Read and D. Green. Paired states of fermions in two dimensions with breaking of parity and time-reversal symmetries and the fractional quantum hall effect. *Phys. Rev. B*, 61:10267–10297, Apr 2000.

[64] H. S. Roising. Topological superconductivity and majorana fermions. Master's thesis, University of Oslo, 2016.

[65] M. Wagner. Expansions of nonequilibrium green's functions. *Physical Review B*, 44(12):6104, 1991.

[66] R. P. Feynman. Space-time approach to quantum electrodynamics. *Phys. Rev.*, 76:769–789, Sep 1949.

[67] G. C. Wick. The evaluation of the collision matrix. *Phys. Rev.*, 80:268–272, Oct 1950.

[68] P. Danielewicz. Quantum theory of nonequilibrium processes, i. *Annals of Physics*, 152(2):239–304, 1984.

[69] E. Perfetto, G. Stefanucci, and M. Cini. Correlation-induced memory effects in transport properties of low-dimensional systems. *Physical review letters*, 105(15):156802, 2010.

[70] E. Perfetto. Time-dependent evolution of two coupled luttinger liquids. *Physical Review B*, 74(20):205123, 2006.

[71] E. Perfetto and G. Stefanucci. On the thermalization of a luttinger liquid after a sequence of sudden interaction quenches. *EPL (Europhysics Letters)*, 95(1):10006, 2011.

[72] B. Dóra, M. Haque, and G. Zaránd. Crossover from adiabatic to sudden interaction quench in a luttinger liquid. *Physical Review Letters*, 106(15):156406, 2011.

[73] S. B. Kaplan, C. C. Chi, D. N. Langenberg, J. J. Chang, S. Jafarey, and D. J. Scalapino. Quasiparticle and phonon lifetimes in superconductors. *Phys. Rev. B*, 14:4854–4873, Dec 1976.

[74] V. L. Berezinskii. New model of the anisotropic phase of superfluid he3. *Jetp Lett*, 20(9):287–289, 1974.

[75] A. Balatsky and E. Abrahams. New class of singlet superconductors which break the time reversal and parity. *Phys. Rev. B*, 45:13125–13128, Jun 1992.

[76] E. Abrahams, A. Balatsky, J. R. Schrieffer, and Philip B. Allen. Interactions for odd-ω-gap singlet superconductors. *Phys. Rev. B*, 47:513–514, Jan 1993.

[77] E. Abrahams, A. Balatsky, D. J. Scalapino, and J. R. Schrieffer. Properties of odd-gap superconductors. *Phys. Rev. B*, 52:1271–1278, Jul 1995.

[78] Y. Fuseya, H. Kohno, and K. Miyake. Realization of odd-frequency p-wave spin–singlet superconductivity coexisting with antiferromagnetic order near quantum critical point. *Journal of the Physical Society of Japan*, 72(11):2914–2923, 2003.

[79] P. Coleman, E. Miranda, and A. Tsvelik. Possible realization of odd-frequency pairing in heavy fermion compounds. *Phys. Rev. Lett.*, 70:2960–2963, May 1993.

[80] P. Coleman, E. Miranda, and A. Tsvelik. Odd-frequency pairing in the kondo lattice. *Phys. Rev. B*, 49:8955–8982, Apr 1994.

[81] P. Coleman, A. Georges, and A. Tsvelik. Reflections on the one-dimensional realization of odd-frequency pairing. *Journal of Physics: Condensed Matter*, 9(2):345–356, jan 1997.

[82] F. S. Bergeret, A. F. Volkov, and K. B. Efetov. Long-range proximity effects in superconductor-ferromagnet structures. *Phys. Rev. Lett.*, 86:4096–4099, Apr 2001.

[83] F. S. Bergeret, A. F. Volkov, and K. B. Efetov. Odd triplet superconductivity and related phenomena in superconductor-ferromagnet structures. *Rev. Mod. Phys.*, 77:1321–1373, Nov 2005.

[84] M. Eschrig. Spin-polarized supercurrents for spintronics: a review of current progress. *Reports on Progress in Physics*, 78(10):104501, sep 2015.

[85] J. Linder and J. W. A. Robinson. Superconducting spintronics. *Nature Physics*, 11:307, 2015.

[86] J. Cayao, C. Triola, and A. M. Black-Schaffer. Odd-frequency superconducting pairing in one-dimensional systems. *The European Physical Journal Special Topics*, 229(4):545–575, Feb 2020.

[87] Y. Tanaka, M. Sato, and N. Nagaosa. Symmetry and topology in superconductors –odd-frequency pairing and edge states–. *Journal of the Physical Society of Japan*, 81(1):011013, 2012.

[88] A. Di Bernardo, S. Diesch, Y. Gu, J. Linder, G. Divitini, E. Scheer, M. G. Blamire, and J. W. A. Robinson. Signature of magnetic-dependent gapless odd frequency states at superconductor/ferromagnet interfaces. *Nature Communications*, 6:8053, 2015.

[89] A. V. Balatsky, I. Vekhter, and Jian-Xin Zhu. Impurity-induced states in conventional and unconventional superconductors. *Rev. Mod. Phys.*, 78:373–433, May 2006.

[90] M. I. Salkola, A. V. Balatsky, and J. R. Schrieffer. Spectral properties of quasiparticle excitations induced by magnetic moments in superconductors. *Phys. Rev. B*, 55:12648–12661, May 1997.

[91] M. E. Flatté and J. M. Byers. Local electronic structure of defects in superconductors. *Phys. Rev. B*, 56:11213–11231, Nov 1997.

[92] T. Meng, J. Klinovaja, S. Hoffman, P. Simon, and D. Loss. Superconducting gap renormalization around two magnetic impurities: From shiba to andreev bound states. *Phys. Rev. B*, 92:064503, Aug 2015.

[93] V. Kaladzhyan, C. Bena, and P. Simon. Characterizing p-wave superconductivity using the spin structure of shiba states. *Phys. Rev. B*, 93:214514, Jun 2016.

[94] C.P. Moca, E. Demler, B. Jankó, and G. Zaránd. Spin-resolved spectra of shiba multiplets from mn impurities in mgb_2. *Phys. Rev. B*, 77:174516, May 2008.

[95] Y. Kim, J. Zhang, E. Rossi, and R. M. Lutchyn. Impurity-induced bound states in superconductors with spin-orbit coupling. *Phys. Rev. Lett.*, 114:236804, Jun 2015.

[96] J. Ortuzar, S. Trivini, M. Alvarado, M. Rouco, J. Zaldivar, A. L. Yeyati, J. I. Pascual, and F. S. Bergeret. Yu-shiba-rusinov states in two-dimensional superconductors with arbitrary fermi contours. *Phys. Rev. B*, 105:245403, Jun 2022.

[97] M. E. Flatté and D. E. Reynolds. Local spectrum of a superconductor as a probe of interactions between magnetic impurities. *Phys. Rev. B*, 61:14810–14814, Jun 2000.

[98] D. K. Morr and N. A. Stavropoulos. Quantum interference between impurities: Creating novel many-body states in s-wave superconductors. *Phys. Rev. B*, 67:020502, Jan 2003.

[99] D. K. Morr and J. Yoon. Impurities, quantum interference, and quantum phase transitions in s-wave superconductors. *Phys. Rev. B*, 73:224511, Jun 2006.

[100] J. Li, H. Chen, I. K. Drozdov, A. Yazdani, B. A. Bernevig, and A. H. MacDonald. Topological superconductivity induced by ferromagnetic metal chains. *Phys. Rev. B*, 90:235433, Dec 2014.

[101] H.-Y. Hui, P. M. R. Brydon, J. D. Sau, S. Tewari, and S. Das Sarma. Majorana fermions in ferromagnetic chains on the surface of bulk spin-orbit coupled s-wave superconductors. *Sci. Rep.*, 5:8880, 2015.

[102] K. Pöyhönen, A. Westström, and T. Ojanen. Topological superconductivity in ferromagnetic atom chains beyond the deep-impurity regime. *Phys. Rev. B*, 93:014517, Jan 2016.

[103] F. Pientka, L. I. Glazman, and F. von Oppen. Unconventional topological phase transitions in helical shiba chains. *Phys. Rev. B*, 89:180505, May 2014.

[104] Y. Kim, M. Cheng, B. Bauer, R. M. Lutchyn, and S. Das Sarma. Helical order in one-dimensional magnetic atom chains and possible emergence of majorana bound states. *Phys. Rev. B*, 90:060401, Aug 2014.

[105] B. Braunecker and P. Simon. Interplay between classical magnetic moments and superconductivity in quantum one-dimensional conductors: Toward a self-sustained topological majorana phase. *Phys. Rev. Lett.*, 111:147202, Oct 2013.

[106] K. Pöyhönen, A. Westström, J. Röntynen, and T. Ojanen. Majorana states in helical shiba chains and ladders. *Phys. Rev. B*, 89:115109, Mar 2014.

[107] A. Westström, K. Pöyhönen, and T. Ojanen. Topological properties of helical shiba chains with general impurity strength and hybridization. *Phys. Rev. B*, 91:064502, Feb 2015.

[108] S. Nakosai, Y. Tanaka, and N. Nagaosa. Two-dimensional p-wave superconducting states with magnetic moments on a conventional s-wave superconductor. *Phys. Rev. B*, 88:180503, Nov 2013.

[109] J. Röntynen and T. Ojanen. Topological superconductivity and high chern numbers in 2d ferromagnetic shiba lattices. *Phys. Rev. Lett.*, 114:236803, Jun 2015.

[110] A. Martín-Rodero and A. Levy Yeyati. The andreev states of a superconducting quantum dot: mean field versus exact numerical results. *Journal of Physics: Condensed Matter*, 24(38):385303, sep 2012.

[111] M. Žonda, V. Pokorný, V. Janiš, and T. Novotný. Perturbation theory of a superconducting 0 π impurity quantum phase transition. *Scientific Reports*, 5(1):8821, Mar 2015.

[112] M. Žonda, V. Pokorný, V. Janiš, and T. Novotný. Perturbation theory for an anderson quantum dot asymmetrically attached to two superconducting leads. *Phys. Rev. B*, 93:024523, Jan 2016.

[113] H. Shiba, K. Satori, O. Sakai, and Y. Shimizu. Numerical renormalization group study of the kondo effect in superconductors. *Physica B: Condensed Matter*, 186-188:239–241, 1993.

[114] J Bauer, A Oguri, and A C Hewson. Spectral properties of locally correlated electrons in a bardeen–cooper–schrieffer superconductor. *Journal of Physics: Condensed Matter*, 19(48):486211, nov 2007.

[115] R. žitko, O. Bodensiek, and T. Pruschke. Effects of magnetic anisotropy on the subgap excitations induced by quantum impurities in a superconducting host. *Phys. Rev. B*, 83:054512, Feb 2011.

[116] R. Žitko. Quantum impurity models for magnetic adsorbates on superconductor surfaces. *Physica B: Condensed Matter*, 536:230–234, 2018.

[117] F. von Oppen and K. J. Franke. Yu-shiba-rusinov states in real metals. *Phys. Rev. B*, 103:205424, May 2021.

[118] H. Schmid, J. F. Steiner, K. J. Franke, and F. von Oppen. Quantum yu-shiba-rusinov dimers. *Phys. Rev. B*, 105:235406, Jun 2022.

[119] J. F. Steiner, C. Mora, K. J. Franke, and F. von Oppen. Quantum magnetism and topological superconductivity in yu-shiba-rusinov chains. *Phys. Rev. Lett.*, 128:036801, Jan 2022.

[120] M. Ternes, W.-D. Schneider, J.-C. Cuevas, C. P. Lutz, C. F. Hirjibehedin, and A. J. Heinrich. Subgap structure in asymmetric superconducting tunnel junctions. *Phys. Rev. B*, 74:132501, Oct 2006.

[121] S.-H. Ji, T. Zhang, Y.-S. Fu, Xi C., X.-C. Ma, J. Li, W.-H. Duan, J.-F. Jia, and Q.-K. Xue. High-resolution scanning tunneling spectroscopy of magnetic impurity induced bound states in the superconducting gap of pb thin films. *Phys. Rev. Lett.*, 100:226801, Jun 2008.

[122] B. W. Heinrich, L. Braun, J. I. Pascual, and K. J. Franke. Protection of excited spin states by a superconducting energy gap. *Nature Physics*, 9(12):765–768, Dec 2013.

[123] N. Hatter, B. W. Heinrich, M. Ruby, J. I. Pascual, and K. J. Franke. Magnetic anisotropy in shiba bound states across a quantum phase transition. *Nat. Comm.*, 6:8988, 2015.

[124] M. Ruby, Y. Peng, F. von Oppen, B. W. Heinrich, and K. J. Franke. Orbital picture of yu-shiba-rusinov multiplets. *Phys. Rev. Lett.*, 117:186801, Oct 2016.

[125] D.-J. Choi, C. Rubio-Verdú, J. de Bruijckere, M. M. Ugeda, N. Lorente, and J. I. Pascual. Mapping the orbital structure of impurity bound states in a superconductor. *Nature Communications*, 8(1):15175, May 2017.

[126] H. Huang, C. Padurariu, J. Senkpiel, R. Drost, A. L. Yeyati, J. C. Cuevas, B. Kubala, J. Ankerhold, K. Kern, and C. R. Ast. Tunnelling dynamics between superconducting bound states at the atomic limit. *Nature Physics*, 16(12):1227–1231, Dec 2020.

[127] S.-H. Ji, T. Zhang, Y.-S. Fu, X. Chen, X.-C. Ma, J. Li, W.-H. Duan, J.-F. Jia, and Q.-K. Xue. High-resolution scanning tunneling spectroscopy of magnetic impurity induced bound states in the superconducting gap of pb thin films. *Phys. Rev. Lett.*, 100:226801, Jun 2008.

[128] D.-J. Choi, C. G. Fernández, E. Herrera, C. Rubio-Verdú, M. M. Ugeda, I. Guillamón, H. Suderow, J. I. Pascual, and N. Lorente. Influence of magnetic ordering between cr adatoms on the yu-shiba-rusinov states of the $\beta-\mathrm{bi_2Pd}$ superconductor. *Phys. Rev. Lett.*, 120:167001, Apr 2018.

[129] S. Kezilebieke, M. Dvorak, T. Ojanen, and P. Liljeroth. Coupled yu–shiba–rusinov states in molecular dimers on nbse2. *Nano Letters*, 18(4):2311–2315, 2018. PMID: 29533636.

[130] B. Jäck, Y. Xie, J. Li, S. Jeon, B. A. Bernevig, and A. Yazdani. Observation of a majorana zero mode in a topologically protected edge channel. *Science*, 364(6447):1255–1259, 2019.

[131] S. Guissart. *De l'impureté Kondo aux états liés dans les supraconducteurs*. PhD thesis, 2016. Thèse de doctorat dirigée par P. Simon Physique Université Paris-Saclay (ComUE) 2016.

[132] A. Mishra, S. Takei, P. Simon, and M. Trif. Dynamical torque from shiba states in s-wave superconductors. *Phys. Rev. B*, 103:L121401, Mar 2021.

[133] T. Zhang and et al. Superconductivity in one-atomic-layer metal films grown on si(111). *Nature Physics*, 6:104, 2010.

[134] C. Brun and et al. Remarkable effects of disorder on superconductivity of single atomic layers of lead on silicon. *Nature Physics*, 10:444–450, 2014.

[135] D. Kuzmanovski, R. S. Souto, and A. V. Balatsky. Odd-frequency superconductivity near a magnetic impurity in a conventional superconductor. *Phys. Rev. B*, 101:094505, Mar 2020.

[136] S.-I. Suzuki, T. Sato, and Y. Asano. Odd-frequency cooper pair around a magnetic impurity. *Phys. Rev. B*, 106:104518, Sep 2022.

[137] Y. M. Blanter and M. Büttiker. Shot noise in mesoscopic conductors. *Physics Reports*, 336(1):1–166, 2000.

[138] R. de Picciotto, M. Reznikov, M. Heiblum, V. Umansky, G. Bunin, and D. Mahalu. Direct observation of a fractional charge. *Nature*, 389(6647):162–164, Sep 1997.

[139] A. Bid, N. Ofek, M. Heiblum, V. Umansky, and D. Mahalu. Shot noise and charge at the $2/3$ composite fractional quantum hall state. *Phys. Rev. Lett.*, 103:236802, Dec 2009.

[140] X. Jehl, M. Sanquer, R. Calemczuk, and D. Mailly. Detection of doubled shot noise in short normal-metal/ superconductor junctions. *Nature*, 405(6782):50–53, May 2000.

[141] R. Cron, M. F. Goffman, D. Esteve, and C. Urbina. Multiple-charge-quanta shot noise in superconducting atomic contacts. *Phys. Rev. Lett.*, 86:4104–4107, Apr 2001.

[142] Y. Meir and A. Golub. Shot noise through a quantum dot in the kondo regime. *Phys. Rev. Lett.*, 88:116802, Mar 2002.

[143] T. Delattre, C. Feuillet-Palma, L. G. Herrmann, P. Morfin, J.-M. Berroir, G. Fève, B. Plaçais, D. C. Glattli, M.-S. Choi, C. Mora, and T. Kontos. Noisy kondo impurities. *Nature Physics*, 5(3):208–212, Mar 2009.

[144] A. N. Cleland, J. M. Schmidt, and John Clarke. Charge fluctuations in small-capacitance junctions. *Phys. Rev. Lett.*, 64:1565–1568, Mar 1990.

[145] Carles Altimiras, Olivier Parlavecchio, Philippe Joyez, Denis Vion, Patrice Roche, Daniel Esteve, and Fabien Portier. Dynamical coulomb blockade of shot noise. *Phys. Rev. Lett.*, 112:236803, Jun 2014.

[146] B. W. Heinrich, L. Braun, J. I. Pascual, and K. J. Franke. Tuning the magnetic anisotropy of single molecules. *Nano Letters*, 15(6):4024–4028, 2015. PMID: 25942560.

[147] M. Ormaza, P. Abufager, B. Verlhac, N. Bachellier, M.-L. Bocquet, N. Lorente, and L. Limot. Controlled spin switching in a metallocene molecular junction. *Nature Communications*, 8(1):1974, Dec 2017.

[148] J. Figgins and D. K. Morr. Differential conductance and quantum interference in kondo systems. *Phys. Rev. Lett.*, 104:187202, May 2010.

[149] S. Cocklin and D. K. Morr. Scanning tunneling shot-noise spectroscopy in kondo systems. *Phys. Rev. B*, 100:125146, Sep 2019.

[150] B. Bryant, R. Toskovic, A. Ferrón, J. L. Lado, A. Spinelli, J. Fernández-Rossier, and A. F. Otte. Controlled complete suppression of single-atom inelastic spin and orbital cotunneling. *Nano Letters*, 15(10):6542–6546, 2015. PMID: 26366713.

[151] L. Farinacci, G. Ahmadi, M. Ruby, G. Reecht, B. W. Heinrich, C. Czekelius, F. von Oppen, and K. J. Franke. Interfering tunneling paths through magnetic molecules on superconductors: Asymmetries of kondo and yu-shiba-rusinov resonances. *Phys. Rev. Lett.*, 125:256805, Dec 2020.

[152] S. Pradhan and J. Fransson. Shot noise as a probe of spin-correlated transport through single atoms. *Phys. Rev. B*, 97:115409, Mar 2018.

[153] J. Senkpiel, C. Rubio-Verdú, M. Etzkorn, R. Drost, L. M. Schoop, S. Dambach, C. Padurariu, B. Kubala, J. Ankerhold, C. R. Ast, and K. Kern. Robustness of yu-shiba-rusinov resonances in the presence of a complex superconducting order parameter. *Phys. Rev. B*, 100:014502, Jul 2019.

[154] E. Liebhaber, S. Acero González, R. Baba, G. Reecht, B. W. Heinrich, S. Rohlf, K. Rossnagel, F. von Oppen, and K. J. Franke. Yu–shiba–rusinov states in the charge-density modulated superconductor nbse2. *Nano Letters*, 20(1):339–344, 2020. PMID: 31842547.

[155]

[156] A. Anikin, R. D. Schaller, G. P. Wiederrecht, E. R. Margine, I. I. Mazin, and G. Karapetrov. Ultrafast dynamics in the high-symmetry and in the charge density wave phase of $2h-\mathrm{Nbse}_2$. *Phys. Rev. B*, 102:205139, Nov 2020.

[157] V. M. Edelstein. Characteristics of the cooper pairing in two-dimensional noncentrosymmetric electron systems. *Soviet Physics - JETP (English Translation)*, 68(6):1244–1249, 1989.

[158] L. P. Gor'kov and E. I. Rashba. Superconducting 2d system with lifted spin degeneracy: Mixed singlet-triplet state. *Phys. Rev. Lett.*, 87:037004, Jul 2001.

[159] J. D. Sau, R. M. Lutchyn, S. Tewari, and S. Das Sarma. Generic new platform for topological quantum computation using semiconductor heterostructures. *Phys. Rev. Lett.*, 104:040502, Jan 2010.

[160] R. M. Lutchyn, J. D. Sau, and S. Das Sarma. Majorana fermions and a topological phase transition in semiconductor-superconductor heterostructures. *Phys. Rev. Lett.*, 105:077001, Aug 2010.

[161] Y. Oreg, G. Refael, and F. von Oppen. Helical liquids and majorana bound states in quantum wires. *Phys. Rev. Lett.*, 105:177002, Oct 2010.

[162] A. Das, Y. Ronen, Y. Most, Y Oreg, M. Heiblum, and H Shtrikman. Zero-bias peaks and splitting in an al–inas nanowire topological superconductor as a signature of majorana fermions. *Nat. Phys.*, 8:887, 2012.

[163] J. Klinovaja and D. Loss. Composite majorana fermion wave functions in nanowires. *Phys. Rev. B*, 86:085408, Aug 2012.

[164] S. Tewari and J. D. Sau. Topological invariants for spin-orbit coupled superconductor nanowires. *Phys. Rev. Lett.*, 109:150408, Oct 2012.

[165] J. C. Budich and E. Ardonne. Topological invariant for generic one-dimensional time-reversal-symmetric superconductors in class diii. *Phys. Rev. B*, 88:134523, Oct 2013.

[166] H. Zhang and et al. Retracted article: Quantized majorana conductance. *Nature*, 556(7699):74–79, Apr 2018.

[167] V. Mourik, K. Zuo, S. M. Frolov, S. R. Plissard, E.P.A.M. Bakkers, and L. P. Kouwenhoven. Signatures of majorana fermions in hybrid superconductor-semiconductor nanowire devices. *Science*, 336(6084):1003–1007, 2012.

[168] M. T. Deng, S. Vaitiekenas, E. B. Hansen, J. Danon, M. Leijnse, K. Flensberg, J. Nygård, P. Krogstrup, and C. M. Marcus. Majorana bound state in a coupled quantum-dot hybrid-nanowire system. *Science*, 354(6319):1557–1562, 2016.

[169] A. Fornieri and et al. Evidence of topological superconductivity in planar josephson junctions. *Nature*, 569:89, 2019.

[170] H. Ren, F. Pientka, S. Hart, and et al. Topological superconductivity in a phase-controlled josephson junction. *Nature*, 569:93, 2019.

[171] M. M. Vazifeh and M. Franz. Self-organized topological state with majorana fermions. *Phys. Rev. Lett.*, 111:206802, Nov 2013.

[172] I. Reis, D. J. J. Marchand, and M. Franz. Self-organized topological state in a magnetic chain on the surface of a superconductor. *Phys. Rev. B*, 90:085124, Aug 2014.

[173] R. Pawlak, M. Lisiel, J. Klinovaja, T. Meier, S. Kawai, T. Gladzel, D. Loss, and E. Meyer. Probing atomic structure and majorana wavefunctions in mono-atomic fe chains on superconducting pb surface. *npj Quantum Information*, 2:16035, 2016.

[174] M. Ruby, F. Pientka, Y. Peng, F. von Oppen, B. W. Heinrich, and K. J. Franke. End states and subgap structure in proximity-coupled chains of magnetic adatoms. *Phys. Rev. Lett.*, 115:197204, Nov 2015.

[175] H. Kim, A. Palacio-Morales, T. Posske, L. Rózsa, K. Palotás, L. Szunyogh, M. Thorwart, and R. Wiesendanger. Toward tailoring majorana bound states in artificially constructed magnetic atom chains on elemental superconductors. *Science Advances*, 4(5), 2018.

[176] T. D. Stanescu, R. M. Lutchyn, and S. Das Sarma. Majorana fermions in semiconductor nanowires. *Phys. Rev. B*, 84:144522, Oct 2011.

[177] K. T. Law, P. A. Lee, and T. K. Ng. Majorana fermion induced resonant andreev reflection. *Phys. Rev. Lett.*, 103:237001, Dec 2009.

[178] K. Flensberg. Tunneling characteristics of a chain of majorana bound states. *Phys. Rev. B*, 82:180516, Nov 2010.

[179] E. Prada, P. San-Jose, and R. Aguado. Transport spectroscopy of ns nanowire junctions with majorana fermions. *Phys. Rev. B*, 86:180503, Nov 2012.

[180] D. E. Liu and H. U. Baranger. Detecting a majorana-fermion zero mode using a quantum dot. *Phys. Rev. B*, 84:201308, Nov 2011.

[181] Y. Peng, F. Pientka, Y. Vinkler-Aviv, L. I. Glazman, and F. von Oppen. Robust majorana conductance peaks for a superconducting lead. *Phys. Rev. Lett.*, 115:266804, Dec 2015.

[182] H. Zhang and et al. Ballistic superconductivity in semiconductor nanowires. *Nature Comm.*, 8:16025, 2017.

[183] S. Frolov. Quantum computing's reproducibility crisis: Majorana fermions. *Nature*, 592:350, April 2021.

[184] D. Castelvecchi. Evidence of elusive majorana particle dies — but computing hope lives on. *Nature*, 591:354, March 2021.

[185] S. Das Sarma and H. Pan. Disorder-induced zero-bias peaks in majorana nanowires. *Phys. Rev. B*, 103:195158, May 2021.

[186] E. Prada, P. San-Jose, M. W. A. de Moor, A. Geresdi, E. J. H. Lee, J. Klinovaja, D. Loss, J. Nygård, R. Aguado, and L. P. Kouwenhoven. From andreev to majorana bound states in hybrid superconductor–semiconductor nanowires. *Nature Reviews Physics*, 2(10):575–594, 2020.

[187] A. Vuik, B. Nijholt, A. Akhmerov, and M. Wimmer. Reproducing topological properties with quasi-majorana states. *SciPost Physics*, 7(5), Nov 2019.

[188] D. Chevallier and J. Klinovaja. Tomography of majorana fermions with stm tips. *Phys. Rev. B*, 94:035417, Jul 2016.

[189] B.D. Josephson. Possible new effects in superconductive tunnelling. *Physics Letters*, 1(7):251–253, 1962.

[190] B. D. Josephson. Supercurrents through barriers. *Advances in Physics*, 14(56):419–451, 1965.

[191] Y.V. Nazarov and Y.M. Blanter. *Quantum Transport: Introduction to Nanoscience*. Cambridge University Press, 2009.

[192] P. Falko, R. Alessandro, M. Duckheim, O. Yuval, and F. von Oppen. Signatures of topological phase transitions in mesoscopic superconducting rings. *New Journal of Physics*, 15(2):025001, feb 2013.

[193] D. Laroche, D. Bouman, D. J. van Woerkom, A. Proutski, C. Murthy, D. I. Pikulin, C. Nayak, R. J. J. van Gulik, J. Nygård, P. Krogstrup, L. P. Kouwenhoven, and A. Geresdi. Observation of the 4π-periodic josephson effect in indium arsenide nanowires. *Nature Communications*, 10(1):245, Jan 2019.

[194] L. P. Rokhinson, X. Liu, and J. K. Furdyna. The fractional a.c. josephson effect in a semiconductor-superconductor nanowire as a signature of majorana particles. *Nature Physics*, 8(11):795–799, November 2012.

[195] B. van Heck, F. Hassler, A. R. Akhmerov, and C. W. J. Beenakker. Coulomb stability of the 4π-periodic josephson effect of majorana fermions. *Phys. Rev. B*, 84:180502, Nov 2011.

[196] D. I. Pikulin and Yuli V. Nazarov. Phenomenology and dynamics of a majorana josephson junction. *Phys. Rev. B*, 86:140504, Oct 2012.

[197] J. Cayao, P. San-Jose, A. M. Black-Schaffer, R. Aguado, and E. Prada. Majorana splitting from critical currents in josephson junctions. *Phys. Rev. B*, 96:205425, Nov 2017.

[198] P. San-Jose, E. Prada, and R. Aguado. ac josephson effect in finite-length nanowire junctions with majorana modes. *Phys. Rev. Lett.*, 108:257001, Jun 2012.

[199] L. Fu and C. L. Kane. Josephson current and noise at a superconductor/quantum-spin-hall-insulator/superconductor junction. *Phys. Rev. B*, 79:161408, Apr 2009.

[200] P.-M. Billangeon, F. Pierre, H. Bouchiat, and R. Deblock. ac josephson effect and resonant cooper pair tunneling emission of a single cooper pair transistor. *Phys. Rev. Lett.*, 98:216802, May 2007.

[201] A. Grivnin, E. Bor, M. Heiblum, Y. Oreg, and H. Shtrikman. Concomitant opening of a bulk-gap with an emerging possible majorana zero mode. *Nature Communications*, 10(1):1940, Apr 2019.

[202] G. L. R. Anselmetti, E. A. Martinez, G. C. Ménard, D. Puglia, F. K. Malinowski, J. S. Lee, S. Choi, M. Pendharkar, C. J. Palmstrøm, C. M. Marcus, L. Casparis, and A. P. Higginbotham. End-to-end correlated subgap states in hybrid nanowires. *Phys. Rev. B*, 100:205412, Nov 2019.

[203] D. Puglia, E. A. Martinez, G. C. Ménard, A. Pöschl, S. Gronin, G. C. Gardner, R. Kallaher, M. J. Manfra, C. M. Marcus, A. P. Higginbotham, and L. Casparis. Closing of the induced gap in a hybrid superconductor-semiconductor nanowire. *Phys. Rev. B*, 103:235201, Jun 2021.

[204] D. Sticlet, C. Bena, and P. Simon. Spin and majorana polarization in topological superconducting wires. *Phys. Rev. Lett.*, 108:096802, Mar 2012.

[205] A. Haim, E. Berg, F. von Oppen, and Y. Oreg. Signatures of majorana zero modes in spin-resolved current correlations. *Phys. Rev. Lett.*, 114:166406, Apr 2015.

[206] K. Björnson, S. S. Pershoguba, A. V. Balatsky, and A. M. Black-Schaffer. Spin-polarized edge currents and majorana fermions in one- and two-dimensional topological superconductors. *Phys. Rev. B*, 92:214501, Dec 2015.

[207] P. Kotetes, D. Mendler, A. Heimes, and G. Schön. Majorana fermion fingerprints in spin-polarised scanning tunnelling microscopy. *Physica E: Low-dimensional Systems and Nanostructures*, 74:614 – 624, 2015.

[208] F. Setiawan, K. Sengupta, I. B. Spielman, and Jay D. Sau. Dynamical detection of topological phase transitions in short-lived atomic systems. *Phys. Rev. Lett.*, 115:190401, Nov 2015.

[209] P. Szumniak, D. Chevallier, D. Loss, and J. Klinovaja. Spin and charge signatures of topological superconductivity in rashba nanowires. *Phys. Rev. B*, 96:041401, Jul 2017.

[210] J. J. He, T. K. Ng, Patrick A. Lee, and K. T. Law. Selective equal-spin andreev reflections induced by majorana fermions. *Phys. Rev. Lett.*, 112:037001, Jan 2014.

[211] H.-H. Sun, K.-W. Zhang, L.-H. Hu, C. Li, G.-Y. Wang, H.-Y. Ma, Z.-A. Xu, C.-L. Gao, D.-D. Guan, Y.-Y. Li, C. Liu, D. Qian, Y. Zhou, L. Fu, S.-C. Li, F.-C. Zhang, and J.-F. Jia. Majorana zero mode detected with spin selective andreev reflection in the vortex of a topological superconductor. *Phys. Rev. Lett.*, 116:257003, Jun 2016.

[212] S. Jeon, Y. Xie, J. Li, Z. Wang, B. A. Bernevig, and A. Yazdani. Distinguishing a majorana zero mode using spin-resolved measurements. *Science*, 358(6364):772–776, 2017.

[213] Johan Nilsson, A. R. Akhmerov, and C. W. J. Beenakker. Splitting of a cooper pair by a pair of majorana bound states. *Phys. Rev. Lett.*, 101:120403, Sep 2008.

[214] Anatoly Golub and Baruch Horovitz. Shot noise in a majorana fermion chain. *Phys. Rev. B*, 83:153415, Apr 2011.

[215] C. J. Bolech and Eugene Demler. Observing majorana bound states in p-wave superconductors using noise measurements in tunneling experiments. *Phys. Rev. Lett.*, 98:237002, Jun 2007.

[216] P. Devillard, D. Chevallier, and M. Albert. Fingerprints of majorana fermions in current-correlation measurements from a superconducting tunnel microscope. *Phys. Rev. B*, 96:115413, Sep 2017.

[217] R. Tuovinen, E. Perfetto, R. van Leeuwen, G. Stefanucci, and M. A. Sentef. Distinguishing majorana zero modes from impurity states through time-resolved transport. *New Journal of Physics*, 21(10):103038, oct 2019.

[218] K. H. Wong, E. Mascot, V. Madhavan, D. J. Van Harlingen, and D. K. Morr. Shot noise and differential conductance as signatures of putative topological superconductivity in $\mathrm{fese}_{0.45}\mathrm{te}_{0.55}$. *Phys. Rev. B*, 105:L220504, Jun 2022.